The Methanol Economy Project

Final Technical Report
DOE-USC-00435

Start Date: September 30, 2009
End Date: December 31, 2013

Principal Authors:
George A. Olah (PI)
G. K. Surya Prakash (Co-PI)

February 2014

DOE Award Number: DE-FE0000435

Submitted by:

Loker Hydrocarbon Research Institute
University of Southern California
837 Bloom Walk
Los Angeles, CA 90089-1661

Disclaimer

Acknowledgements

This project was supported by the National Energy Technology Laboratory (NETL) under the U.S. Department of Energy (DOE) under the award number DE-FE0000435. The support of the DOE is gratefully acknowledged. The Loker Hydrocarbon Research Institute, where the work was performed, and the many graduate students, postdoctoral researchers, and senior scientists, who contributed to the efforts are also gratefully acknowledged.

Abstract

The Methanol Economy Project is based on the concept of replacing fossil fuels with methanol generated either from renewable resources or abundant natural (shale) gas. The full methanol cycle was investigated in this project, from production of methanol through bromination of methane, bireforming of methane to syngas, CO_2 capture using supported amines, co-electrolysis of CO_2 and water to formate and syngas, decomposition of formate to CO_2 and H_2, and use of formic acid in a direct formic acid fuel cell. Each of these projects achieved milestones and provided new insights into their respective fields.

- Direct electrophilic bromination of methane to methyl bromide followed by hydrolysis to yield methanol was investigated on a wide variety of catalyst systems, but hydrolysis proved impractical for large-scale industrial application.
- Bireforming the correct ratio of methane, CO_2, and water on a NiO / MgO catalyst yielded the right proportion of H_2:CO (2:1) and proved to be stable for at least 250 hours of operation at 400 psi (28 atm).
- CO_2 capture utilizing supported polyethyleneimines yielded a system capable of adsorbing CO_2 from the air and release at nominal temperatures with negligible amine leaching.
- CO_2 electrolysis to formate and syngas showed considerable increases in rate and selectivity by performing the reaction in a high pressure flow electrolyzer.
- Formic acid was shown to decompose selectively to CO_2 and H_2 using either Ru or Ir based homogeneous catalysts.
- Direct formic acid fuel cells were also investigated and showed higher than 40% voltage efficiency using reduced loadings of precious metals.

A technoeconomic analysis was conducted to assess the viability of taking each of these processes to the industrial scale by applying the data gathered during the experiments to approximations based on currently used industrial processes. Several of these processes show significant promise for industrial scale up and use towards improving our nation’s energy independence.

Table of Contents

List of Tables

List of Figures

List of Schemes

Executive Summary

The Methanol Economy Project at the University of Southern California (USC) centered on developing fundamental science to convert abundant natural (shale) gas and/or anthropogenic carbon dioxide into methanol (and related dimethyl ether, DME) as a fuel and feed-stock beyond oil and gas. The project involved many areas of focused research.

Direct electrophilic bromination (chlorination) of methane to methyl bromide (chloride) followed by hydrolysis of methyl bromide to methanol/DME was probed over a variety of heterogeneous catalysts. By screening a diverse array of catalysts from supported metals and metal halides, zeolite HZSM-5, SAPO 34 and sulfated zirconia, we were able to systematically follow halogenations of methane and find optimized conditions to channel the reactions for monohalogenation of methane more selectively with good conversions. As another important step towards methane functionalization and homologation, direct conversion of methane to higher hydrocarbons over SAPO-34 was also achieved at relatively modest temperatures. Furthermore, we found that polymer bound amines were very efficient catalyst-scavengers for the hydrolysis and methanolysis of methyl bromide to methanol and dimethyl ether, respectively, under moderate conditions. With high PVP catalyst loadings, conversions in the high eighties range can be obtained but proved to be impractical for large-scale industrial adoption.

A successful procedure termed Bireforming to reform methane, carbon dioxide and water mixtures (in a 3:1:2 ratio) to the right ratio of H_2 and CO (2:1) over stable NiO/MgO based heterogeneous catalytic systems for subsequent methanol conversion. A flow reactor system adapted to the study of dry- and bi-reforming of methane and natural gas at high pressures and high temperatures was designed and built. Initially technical issues were experienced, including coking and degradation of the reactor material (metal dusting) due mainly to the high carbon activity of the gas mixtures used. The utilization of an alumina sleeve and alumina filling material in particular proved to be an essential step toward enabling reliable operation. A number of catalysts based on nickel and cobalt deposited on various supports were tested. Among them, NiO / fumed alumina, NiO / MgO, NiO / PURAL MG30 as well as CoO / MgO were found to have a stable activity for the bi-reforming reaction of methane under pressure. Reactions at pressures up to 500 psi (35 atm) were performed. NiO / fumed alumina and NiO / MgO with NiO content from 10% to 35% were successfully tested for the Bireforming of natural gas for up to 250 hours of stable activity on stream. A desired H_2/CO ratio of 2 could be obtained by varying the amount of water added in the gas feed. The bireforming procedure was combined with initial oxidation of methane as a source of water and CO_2 in a novel process termed "Oxidative Bireforming" to effectively utilize the abundant natural (shale) gas as the sole source in a thermoneutral fashion for producing syngas for methanol synthesis.

Nano structured precipitated and fumed silica (nano-silica) were found to be superior supports for the immobilization of varied organo-amines for CO_2 capture. The easily prepared solids were found to be regenerable and effective CO_2 adsorbents at moderate temperatures from room temperature up to 100°C. PEI based adsorbents were able to adsorb CO_2 efficiently and repeatedly even at concentrations as low as 400 ppm CO_2 in air. Supported polyethylenimines (PEIs), especially branched low molecular weight and high molecular weight PEIs were particularly suitable as CO_2 adsorbents. Amines with lower molecular weights and lower boiling points such as pentaethylenehexamine (PEH), tetraethylenepentamine (TEP), monoethanolamine

(MEA) and diethanolamine (DEA) showed sorbent leaching from the solid adsorbents. The addition of polyethylene glycol was found to significantly enhance desorption of CO_2 from PEI based solid adsorbents. The particle size of the nano-silica was found to be advantageous compared to other solid supports having similar or higher surface area, but larger particle size. As solids, the novel nano-silica / PEI adsorbents circumvent many of the difficulties encountered in the currently used technology employing liquid amines. They are promising candidates for the capture of CO_2 from flue gases of fossil fuel burning power plants, cement factories and other industrial sources, and eventually even from the atmosphere itself.

A high-pressure flow electrolyzer cell was successfully built from the ground up to study the effects of flow and pressure on CO_2 electrolysis to formate and CO. We managed to improve the current density of CO_2 reduction to formate from our initial conditions at 1.76 mA/cm^2 to 24.2 mA/cm^2 for similar electrodes, a 13.8 fold improvement. Based on extensive system development and testing, we are able to offer suggestions on achieving either high efficiency CO_2 reduction (Nafion-H membrane) or high rate electrolysis (Nafion-Na) coupled with some CO_2 reduction to either formate or CO. Our high efficiency conditions gave 89% CO_2 reduction efficiency, however this was essentially split evenly between formate and CO. Our high rate electrolysis gave 132.4 mA/cm^2, however the CO_2 reduction efficiency dropped to 23%. Increased pressure will likely not give better results, and we have ruled out most of the engineering-related possibilities for increasing selectivity or rate. Success of this project will likely require significant development towards improving the catalysts so that they are more selective at high rates, or improving the electrolyte for increased performance and conductivity.

In an effort to utilize the electrochemical reduction product of carbon dioxide, formate (formic acid), methods were developed for the catalytic decomposition of formic acid to H_2 or CO. Utilization of formic acid in indirect as well as direct oxidation fuel cells were explored. $RuCl_3$ in the absence of any ligand has good catalytic activity for the decarboxylation of FA and the reaction rate is first order with respect to the catalyst concentration. A tetranuclear Ru-complex, $[Ru_4(CO)_{12}H_4]$ formed *in situ* and was found to be an active and selective catalyst. The catalyst that formed *in situ* from $IrCl_3$ and an isoindoline-based ligand decomposed formic acid to H_2 and CO_2 selectively. The hydrogen produced from formic acid decomposition was utilized in a hydrogen fuel cell to produce electrical energy. Thermal decomposition of formic acid to CO and water over many heterogeneous catalysts proved to be not so effective. Direct formic acid fuel cells (DFAFC) were also constructed and studied utilizing a variety of anode catalysts on Nafion®-H. Five anode catalytic systems based on palladium and other metals performed effectively, exceeding our goal of operating a DFAFC at 40% voltage efficiency. Of the supported catalysts tested, PdAu is the only catalyst that outperforms state-of-the-art Pd black, but PdFe and PdSn on carbon supports perform comparably and show promise for the development of non-precious metal based catalysts. In addition, voltage efficiencies higher than 40% were achieved with Pd on rGO (reduced graphene oxide), reducing the amount of precious metal required for an effective catalyst.

Techno-Economic analysis of each project was also performed, and led to the conclusion that pilot-plant scale work needs to be taken up before the developed chemistry can achieve practical industrial importance for the implementation of the Methanol Economy concept utilizing natural (shale) gas and CO_2.

Project Overview

Task 1: Project Management Planning
Task 2: Direct Conversion of Methane to Methanol
Task 3: Bireforming of CO_2 with Methane
Task 4: Efficient Ways to Capture CO_2 and Its Electrochemical Conversion
Task 5: Utilization of Formic Acid as a Feed-Stock and Fuel in Fuel Cells
Task 6: Techno-Economic Analysis

Scope of Work and Tasks Performed

Task 1: Program Coordination, Resource Planning, Reports, Reviews and Meetings

Task 2: Direct Conversion of Methane to Methanol (10-01-09 to 3-31-2011)
Title: Bromination of Methane (Subtask 2.1)
Executed Date: 10-01-2009 to 3-31-2011
Verification Method: Conversion and selectivity; catalyst life and turnover

Title: Hydrolysis of Methyl Bromide (Subtask 2.2)
Executed Date: 4-01-2010 to 3-31-2011
Verification Method: Conversion and selectivity; catalyst life and turnover

Task 3: Bireforming of CO_2 with Methane (4-01-2010- 3-31-2012)
Title: Catalyst Screening for Bireforming (Subtask 3.1)
Executed Date: 4-01-2010 to 8-31-2011
Verification Method: Conversion and selectivity; catalyst life and turnover

Title: Bireforming of Methane and Related Hydrocarbons (Subtask 3.2)
Executed Date: 4-01-2010 to 3-31-2012
Verification Method: Conversion and selectivity

Task 4: Efficient Ways to Capture CO_2 and Its Electrochemical Conversion (4-01-2010- 9-30-2013)
Title: Adsorbents for CO_2 Capture (Subtask 4.1)
Executed Date: 4-01-2010 to 9-30-2012
Verification Method: Efficacy, ease of regeneration

Title: Electrochemical Reduction of CO_2 to syngas and formic acid (subtask 4.2)
Executed Date: 4-01-2010 to 9-30-2013
Verification Method: Columbic efficiency, current density, catalytic activity
Task 5.0: Utilization of formic acid as a feed-stock and fuel in fuel cells
Executed Date: 4-01-2010 to 9-30-2013
Verification Method: catalytic activity, voltage efficiency, fuel efficiency
fuel cell efficiency

Task 6.0: Techno-Economic Analysis (Task 6.0)

Planned Date: 1-01-2013 to 12-31-2013 (pushed by 3 months)
Verification Method: Estimates and Modeling

As a part of Task 1, the project was coordinated and led by Professors Olah and Prakash with the assistance of Research Scientists, Postdoctoral Fellows and Graduate Students. There was also participation from undergraduate students as well as few High School Interns. The reporting involved Regular Quarterly Reports, Timely Milestone Reports as well as Special Technical Reports as required by the DOE-NETL Sponsors and the Program Manager, Mr. Jason Hissam. Technical Presentations to the Sponsors were also made at the NETL Laboratory at the Morgantown, WV as well as at the Loker Institute at USC Campus. There were also routine phone conferences as well as WEBEX meetings with the Program Manager. Apart from Scientific Reports, regular quarterly Financial Reports were also made. The efforts in the program were quite successful as shown in the scientific results of various tasks elaborated below.

Task 2: Direct Conversion of Methane to Methanol

Subtask 2.1: Study of Efficacy and Compatibility of Various Catalysts for Methane Halogenations

Various Catalyst systems shown below were screened for halogenations of methane

a) Metal bromides ($PtBr_2$, $HgBr_2$ and $PdBr_2$)
b) Noble metals (Rh, Pt) on fumed silica and alumuina
c) Zeolites: H-Beta, USY, HZSM-5, silicalite and SAPO-34
e) Sulfated zirconia (SO_4^{2-}/ZrO_2)
f) Silica supported metal bromides ($LaBr_3/SiO_2$, $InBr_3/SiO_2$, $CdBr_3/SiO_2$)
g) Superacidic systems ($AlBr_3$, $AlBr_3$-HBr, $AlBr_3$-$CuBr_2$, $AlBr_3$-$CuBr_2$-HBr, $AlBr_3$-CBr_4, $AlBr_3$-$CuSO_4$, CF_3SO_3H-SbF_5)

Selective Halogenation of Methane to Methyl Halide

Thermal halogenation (chlorination, bromination) generally proceeds with the formation of all halogen derivatives by sequential halogenation process (Scheme 2.1). The main objective of the work has been selective monohalogenations. As in usual cases, it was found that the conversion and the product distribution were dependent on the nature of the reaction and various reaction parameters applied. Direct oxidative conversion of methane to higher hydrocarbons was also observed at relatively low temperatures in some cases.

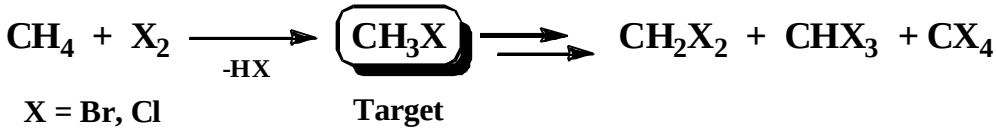

Scheme 2.1. Halogenation of methane

In most of the cases studied (mainly bromination), catalysts suffered considerable loss of activity on-stream over a period of operation. For the batch reactions $PtBr_2$ gave good results (Table 2.1). However, heterogeneity, low conversion under shorter reaction time, low selectivity during longer period, stability of the catalyst and corrosion were the major issues during reactions under batch conditions. Therefore, further reactions were carried out in a quartz flow reactor. Generally, the various catalyst loadings for chlorinations were in the range of 3-7 grams for brominations in the 1 to 10 gram for brominations. Catalyst contact times for chlorinations were 4.4 -60 s and for brominations, 16-81 s.

Table 2.1. Bromination of methane over $PtBr_2$ under batch conditions

Catalyst (mmol)	2	2
CH_4/Br_2 (mol ratio)	4.3	4.2
Temp. (°C)	180	200
Time (h)	3	15
Conversion (Br_2 mol%)	20	39.6
Yield (mol%)		
CH_3Br	17.9	30.4
CH_2Br_2	2.1	4.6
$CHBr_3$	-	4.6

Among flow reactions with noble metals, alumina/fumed silica supported Rh gave significant results. High yield of methyl bromide as well as high Br_2 conversion were achieved. Rhodium on fumed silica exhibited the highest activity and a good selectivity for methyl bromide (Table 2.2). Due to leaching of the metal, sublimation of the support (especially in the case of alumina), and formation of carbon deposits noticed during the reactions, zeolites were considered for further screening.

Table 2.2 Bromination of methane over Rh on silica and alumina

Catalyst	Rh (2%) on silica	Rh (5%) on alumina
Weight (g)	3	3
CH_4/Br_2 (mol ratio)	2.94	2.94
CH_4 Flow rate (mL/min)	5	5
Temp. (°C)	435	435
Br_2 Conversion (mol %)	59.8	34.7
Yield (mol %)		
CH_3Br	53.2	30.5
CH_2Br_2	6.6	4.2
$CHBr_3$	-	-

GHSV ($mL.g^{-1}.h^{-1}$) = 100

HZSM-5 zeolites are known to be stable catalysts for the oxychlorination of methane. For this reason, zeolites were tested and the results are presented in Table 2.3. The high density of the acid sites and the cage structure of these silicoaluminate microporous materials have also been beneficial on the activity and the selectivity upon 3 h on-stream. All zeolites were very active and provided selective bromination of methane. H-Beta was the most active among the tested zeolites. However, decrease in the activity of the catalyst (HZSM-5 and Silicalite in particular) was noticed over a longer period possibly due to the dealumination of the framework by the action of HBr.

Table 2.3. Bromination of methane over various zeolites

Catalyst	H-Beta	USY	HZSM-5
Weight (g)	1	3	5
CH_4/Br_2 (mol ratio)	10	10	10
CH_4 Flow rate (mL/min)	7.3	7.2	7.0
Temp. (°C)	370	370	370
Br_2 Conversion (mol %)	61.0	46.4	63
Yield (mol %)			
CH_3Br	61	46.4	63
CH_2Br_2	-	-	-
$CHBr_3$	-	-	-

GHSV ($mL.g^{-}1.h^{-1}$) = 438 for H-Beta, 144 for USY, 84 for HZSM-5

Among all the catalysts tested, SAPO-34 (a silicoaluminophosphate) was shown to be a good and stable catalyst for bromination and chlorination of methane under continuous flow reaction conditions. Unlike other zeolites, no permanent structural damage of SAPO-34, by hydrogen halide produced during the reaction, was observed even after several reaction-regeneration cycles. This was attributed to the reversibility of the bond dissociation in Al-O-P framework. The thermal chlorination of methane was carried out at 350 ºC in the presence and absence of moisture. When the reaction was conducted in the presence of moisture, high conversion (based on chlorine), selectivity, and stability of the catalyst were observed (Table 2.4). Bromination was carried out in the absence of moisture gave good results (Table 2.5).

Table 2.4. Chlorination of methane over SAPO-34[a] at 350 ºC

Catalyst (3g)	With Moisture			Without Moisture		
CH_4/Cl_2 (mol ratio)	10	10	10	10	10	10
CH_4 Flow rate (mL/min)	40	40	40	40	40	40
Time (h)	4	7	27	1	6	22
Cl_2 Conversion (mol %)	76.8	78	73.1	92.3	73.5	71.5
Yield (mol %)						
CH_3Cl	76	77	72.1	92.3	67.5	65.2
CH_2Cl_2	0.8	1.0	1	-	6	6.3
$CHCl_3$	-	-	-	-	-	-

[a] Reactor feed $CH_4/Cl_2/N_2/H_2O$ in a molar ratio = 10:1:1.3:0.3.GHSV ($mL.g^{-}1.h^{-1}$) = 1000

Table 2.5 Bromination of methane over SAPO-34

Catalyst (g)	3g	3g	10	10	10
CH_4/Br_2 (mol ratio)	10.3	10.3	10.3	10.3	10.3
CH_4 Flow rate (mL/min)	7.2	7.2	7.2	7.2	7.2
Temp (^oC)	345	345	365	365	365
Time (h)	3	10	3	7	15
Br_2 Conversion (mol %)	38.6	38.6	48.9	48.4	48.9
Yield (mol %)					
CH_3Br	38.6	38.6	48.9	48.4	48.9
CH_2Br_2	-	-	-	-	-
$CHBr_3$	-	-	-	-	-

GHSV ($mL.g^{-}1.h^{-1}$) = 43.2 to 144

Bromination of methane with superacidic sulfated zirconia catalysts provided higher conversion but with rather low selectivity (Table 2.6). Elevation of temperature resulted in carbon deposits and leaching of Zr.

Table 2.6 Bromination of methane over sulfated zirconia at 375 ^oC

Catalyst (2g)		
X%/SO_4^{2-}/ZrO_2	5	15
CH_4/Br_2 (mol ratio)	10.3	10.3
CH_4 Flow rate (mL/min)	9.6	9.6
Time (h)	2	7
Br_2 Conversion (mol %)	46.0	68.2
Yield (mol %)		
CH_3Br	42.8	55.7
CH_2Br_2	3.2	9.3
$CHBr_3$	-	3.1

GHSV ($mL.g^{-1}.h^{-1}$) = 43.2 to 144

Reactions with silica supported metal bromides ($LaBr_3/SiO_2$, $InBr_3/SiO_2$, $CdBr_3/SiO_2$) and superacidic systems ($AlBr_3$, $AlBr_3$-HBr, $AlBr_3$-$CuBr_2$, $AlBr_3$-$CuBr_2$-HBr, $AlBr_3$-CBr_4, $AlBr_3$-$CuSO_4$, CF_3SO_3H-SbF_5) were not sustainable and promising as in the other cases.

Direct Oxidative Conversion of Methane to Higher Hydrocarbons

Direct conversion of methane to higher hydrocarbons can be achieved above 1000-1200 ^oC. Low temperature conversion of methane to higher hydrocarbons during the halogenation of methane involves more than one step. But, direct oxidative conversion of methane to higher hydrocarbons was achieved at 350-365 ^oC during the chlorination and bromination of methane over SAPO-34. As shown in Table 2.7, the conversion and product distribution depends on the nature of halogen feed and experimental conditions. Further studies are needed to improve the selectivity and conversion.

Table 2.7 Oxidative conversion of methane to higher hydrocarbons over SAPO-34

	X = Cl*		X = Br†
Amount of Catalyst (g)	7g		10
CH_4/X_2 (mol ratio)	10	10	10
CH_4 Flow rate (mL/min)	39.2	39.2	7.2
Temp (^oC)	350	350	365
Time (h)	18	22	4
X_2 Conversion (mol %)	83	81	61.8
Yield (mol%)			
CH_3X	50.0	42.8	22.5
CH_2X_2	0.3	0.2	0
C_2H_4	16.0	18.4	9.3
C_2H_6	0	0	1.1
C_3H_6	9.6	11.0	17.1
C_3H_8	2.1	2.6	5.1
C_4	3.8	4.7	3.6
C_5	0.4	0.5	2.1
C_{5+}	0.7	0.7	1.0

* Reactor feed $CH_4/Cl_2/N_2/H_2O$ in a molar ratio = 10:1:1.3:0.3. GHSV ($mL.g^{-1}.h^{-1}$) = 420 for Cl_2 and 43.2 for Br_2. † In the absence of N_2 and moisture

Subtask 2.2: Efficient Hydrolysis and Methanolysis of Methyl bromide to Methanol and Dimethyl Ether Using Solid Amines

Methyl bromide can be converted to methanol and dimethyl ether by hydrolysis or methanolysis (Scheme 2.2). The reaction is not thermodynamically favorable. But under batch conditions it was found that poly (4-vinyl pyridine) (PVP) can act as a very efficient catalyst as well as an acid scavenger for selective hydrolysis and selective methanolysis of methyl bromide. The high catalyst loadings seemed untenable in a long run and therefore various other solid polymer/silica-bound amines (Figure 2.1) were tested and found more useful and reusable catalysts for the hydrolysis or methanolysis of methyl bromide (Tables 2.8-2.10). Solid amines acted also as HBr scavenger helping to drive the reaction towards the formation of cleaner products with decreasing hazardous wastes and pollution.

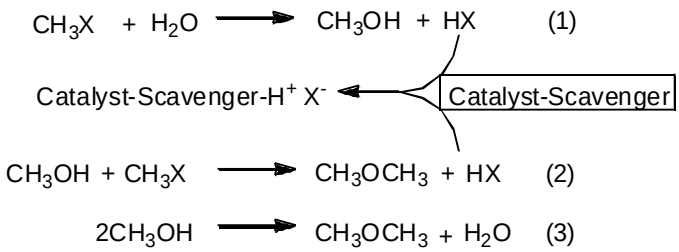

Scheme 2.2 Hydrolysis of methyl bromide to methanol and related reactions in the presence of amine based solid catalysts

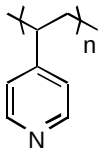

1 PVP, Poly(4-vinyl pyridine)
(2% cross-linked with DVB)

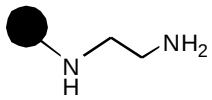

2 EDPB
Polymer-bound Ethylenediamine

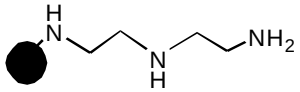

3 PBDETA
Polymer-bound Diethylenetriamine

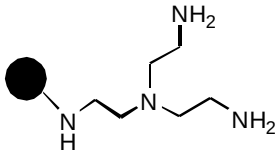

4 PBTAEA
Polymer-bound Tris(2-aminoethyl)amine
(1% cross-linked with DVB)

Figure 2.1 Nitrogen-containing solid catalysts

Table 2.8. Hydrolysis of methyl bromide using poly(4-vinyl pyridine)

Entry	Molar Ratio (CH_3Br:PVP)	Conversion of CH_3Br (%)	Selectivity (%) DME	MeOH
1	1:0	29.9	48.4	51.6
2	1:0.125	67.2	59.8	40.2
3	1:0.2	87.6	43.0	57.0
4	1:0.33	86.8	30.0	70.0
5	1:1	85.6	29.0	71.0

Reaction conditions: 2 h at 100ºC with H_2O:CH_3Br molar ratio of 10:1.

Table 2.9 Methanolysis of methyl bromide using poly(4-vinyl pyridine)

Entry	*Molar ratio (CH_3OH:CH_3Br:PVP)*	*Temp (^oC)*	*Conversion of CH_3Br (%)*	*Selectivity of DME (%)*	*Yield (%)*
1	3:3:1	75	0.0	0.0	0.0
2	3:3:1	100	23.8	100.0	23
3	3:3:1	125	35.3	100.0	35.3
4	3:3:0	125	0.0	0.0	0.0

* Reaction time 2h

Table 2.10 Methanolysis of methyl bromide over polymer containing nitrogen catalysts

Temperature: 100 °C. Catalysts: [a] EDPB: Polymer-bound Ethylenediamine, [b] DETAPB-2.55: Polymer-bound

CH_3OH:CH_3Br:Catalyst Molar ratio	Time (hr)	Conversion CH_3Br (mol %)	Yield of DME (mol %)	DME (mol %) from CH_3Br	DME (mol %) from CH_3OH
Catalyst: PBED[a]					
10.4 : 1 : 0.34	5	37.8	40.9	77.7	22.3
10.2 : 1 : 0.33	16	42.4	133.1	32.3	67.7
10.3 : 1 : 0.34	24	50.7	163.7	31.0	69.0
Catalyst: PBDETA-2.55[b]					
10.3 : 1 : 0.33	5	34.2	50.8	67.3	32.7
Catalyst: PBDETA-4.67[c]					
10 : 1 : 0.35	5	39.2	48.3	81	19
10.4 : 1 : 0.36	16	42.3	128.2	33	67
Catalyst: PBTAEA[d]					
10.5 : 1 : 0.32	5	34.8	34.8	70.5	29.5

Diethylenetriamine, 2% cross-linked with 2.55 mmol N/g; [c] DETAPB-4.67: Polymer-bound Diethylenetriamine, 1% cross-linked with 4.67 mmol N/g; [d] TAEAPB: Polymer-bound tris (2-aminoethyl) amine.

Conclusions

By screening a diverse array of catalysts ranging from supported metals and metal halides, zeolite HZSM-5, SAPO 34 and sulfated zirconia, halogenations of methane were carried out and optimized conditions were found to channel the reactions for monohalogenation of methane more selectively with good conversions. As another important step towards methane functionalization and homologation, direct conversion of methane to higher hydrocarbons over SAPO-34 was also achieved at relatively lower temperatures. Furthermore, polymer bound amines were found to be very efficient catalyst-scavenger system for the hydrolysis and

methanolysis of methyl bromide to methanol and dimethyl ether, respectively, under moderate conditions. With high PVP catalyst loadings, conversions in the high eighties range can be obtained but proved to be untenable for practical, industrial scale conversions.

Task 3: Bireforming of CO_2 with Methane (Subtask 3.1 and 3.2 are combined together as one report)

Methane Dry Reforming and Bi-Reforming at High Pressures

By choosing the right proportions of CO_2, water and CH_4, a combination of steam and dry reforming would generate syn-gas with an ideal H_2/CO ratio of 2 for the synthesis of methanol (Scheme 3.1)

Steam reforming	$2CH_4 + 2H_2O \longrightarrow 2CO + 6H_2$	$\Delta H_{298K} = 49.1$ kcal.mol^{-1}	Eq. 1
Dry reforming	$CH_4 + CO_2 \longrightarrow 2CO + 2H_2$	$\Delta H_{298K} = 59.1$ kcal.mol^{-1}	Eq. 2
Bireforming	$3CH_4 + 2H_2O + CO_2 \longrightarrow 4CO + 8H_2 \longrightarrow 4CH_3OH$		Eq. 3

Scheme 3.1 Various methane reforming reactions

This combination could be advantageous in the use of natural gas sources containing substantial CO_2 concentrations. This CO_2 would, otherwise, have to be removed to allow further processing of the natural gas. Some natural gas sources contain CO_2 concentration from 5 to 50%. Bi-reforming could also be used to recycle CO_2 emissions from sources such as flue gases from fossil fuel (coal, petroleum, natural gas, etc.) burning power plants, exhaust of cement factories and other industries.

The two reactions in bi-reforming could be performed in two separate reactors, one for the dry reforming and another for steam reforming, combining both effluent streams before sending them to the methanol synthesis unit. However, it would be preferable to run both reactions (dry and steam reforming) in a single reformer to lower capital and operational cost as well as complexity of the system. The catalyst for such a reaction should therefore be active and stable over extended durations for both reactions.

The advantage of operating bi-reforming under high pressure is that the gases produced (CO and H_2) could be directly sent to the methanol producing unit without need for further compression to reach the operating pressure of 30 to 60 bars.

In the framework of the Methanol Economy project, a number of catalysts for dry- and bi-reforming under pressure in a high pressure flow reactor system specially built for this purpose were studied. The highlights of the research are presented in this report.

Construction and improvement on the high pressure flow reactor

Based on a design provided, the Parr Instrument company constructed a high pressure flow reactor system able to run simultaneous reactions in three independent tubular reactors. The tubular reactors are made of a special alloy (H230) able to withstand pressures of up to 50 bars at 890 °C and pressures up to 100 bars at lower temperatures. The reactor system is placed in a fume hood to avoid any potentially dangerous accumulation of gases in the laboratory. The entire

system including the gas handling unit, temperature and pressure controller, liquid feed pump is controlled by a process controller connected to a computer. The gaseous products of the reactions are analyzed using an online gas chromatograph and the data collected on an attached computer (Figures 3.1 and 3.2).

Figure 3.1 High pressure and temperature flow reactor system

Initial technical difficulties with the high pressure reactor solved

In the course of the studies on high pressure reforming of methane, some technical difficulties were experienced. After using the high pressure reactors for several months, some small holes started to appear on the inner reactor surfaces, on the spools and thermowell in the temperature region between about 500°C and 700°C. After investigation on the nature of the reactor's metallic composition which happened to be Haynes-230 Alloy (H230), the observed phenomenon turned out to be so-called metal "dusting". This effect is due to the high carbon activity of the entering gas mixtures as well as gas products present during the dry reforming reaction. Although the H230 alloy is very resistant to metal dusting it still underwent this degradation after prolonged exposure under our conditions. Metal dusting also lead to the formation of coke, which had the effect of clogging the reactor after a short runtime. To overcome these problems, the contact of reaction gases with any metallic parts of the reactor at temperatures above 400°C should be avoided. This was achieved by inserting an alumina tube inside the tubular reactor. This alumina tube acts like a protecting lining for the metals which would otherwise be in contact with reactive gases. Between the inner reactor wall and the outer

alumina tube a flow of nitrogen was added to protect the metallic reactor walls. The spools and other support, diluent and filler material were also replaced by inert alumina with no porosity and very low surface area (see Appendix 3.1 for more details). These measures successfully solved the side reactions and metal dusting problems. Using the modified system, reforming of methane with CO_2 as well as bi-reforming with CO_2 and water were reliably studied with no unwanted side reactions.

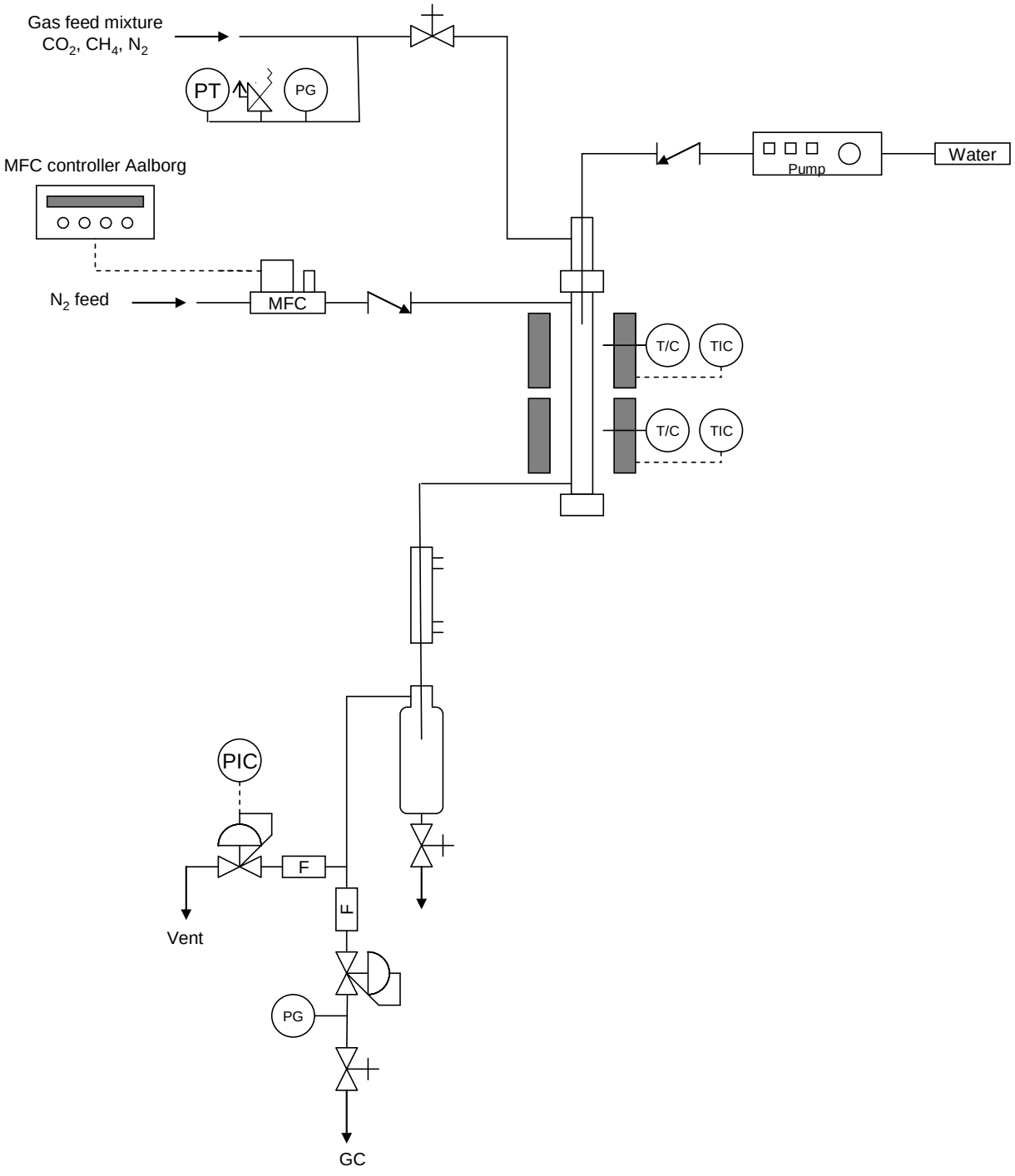

Figure 3.2 Schematics of the experimental set-up for high-pressure methane bi-reforming

Catalyst tested for dry- and bi-reforming

A number of catalysts were prepared for the dry reforming and bi-reforming reactions. All of them were tested for dry reforming at atmospheric pressure. The most promising were also screened for their performance for dry-and/or bi-reforming at high pressure. The catalysts prepared included,

- NiO/fumed alumina, NiO/MgO, NiO/nano MgO, NiO/PURAL MG30, NiO/PURAL MG70, NiO/ PURAL MG5, NiO/PURAL MG20, NiO/CeO_2, NiO/yttrium oxide, NiO/lanthanum oxide
- NiO/V_2O_5/fumed silica, NiO/V_2O_5/MgO/fumed silica
- CoO/fumed alumina, CoO/fumed silica, CoO/MgO, CoO/PURAL MG70, CoO/PURAL MG30
- NiO-WO_3 on alumina
-Tungsten carbide

Catalyst preparation

The catalysts were prepared by deposition of the Ni precursor on a solid support. Typically nickel nitrate hexahydrate, $Ni(NO_3)_2 \cdot 6H_2O$ was used as a precursor and dissolved in methanol. This solution was then added to a suspension of the solid support in methanol. After stirring overnight, the solvent was removed by rotary evaporation, followed by drying under high vacuum for 2 to 3 hours. The obtained powder was transferred to a crucible and placed in an oven at 120°C overnight. The solid was then placed in a box furnace and calcinated at 550 °C for 5 hours under air. Finally, the powder was crushed in a crucible and transferred to a glass vial for storage.

Further details about the materials used are given in Appendix 3.2.

Testing of catalyst for dry- and bi-reforming

The catalyst (generally 100 mg) was mixed with 900 mg tabular alumina (60-200 mesh) and placed on top of tabular alumina (Figure 3.3) in an alumina tube inserted in the metallic tubular reactor. After closing the reactor and placing it in the furnace, the system was checked for leaks by pressurizing it to 150 psi with N_2. If the pressure was stable for 15 minutes, the activation step was initiated. During activation, the catalyst was heated under a hydrogen/nitrogen mixture from room temperature to 850°C in 1.5 hours and kept at this temperature for 3 hours. The carrier gas was then switched to nitrogen, set to the desired reaction pressure and the catalyst maintained at 830 °C. The reaction gas mixture composed of CO_2, CH_4 and N_2 used as a reference was then introduced. For bi-reforming, water was also introduced into the system using a high pressure pump. Downstream of the reaction, the products were analyzed by online GC using a TCD detector (Argon UHP used as carrier gas): Varian 450 series GC equipped with a gas handling valve system from Lotus Consulting. Two packed columns were used in series for the gas analysis: a 5 Å molecular sieve column and a Hayesep N column.

In a typical bi-reforming experiment the gas feed composition was: N_2 (26.3 mL/min), CH_4 (35.0 mL/min), CO_2 (13.7 mL/min), for a total gas flow of 75 mL/min. Liquid water was also added (0.021 mL/min) and vaporized (~28 mL/min steam).

A total gas feed of about 103 mL/min was therefore flown through the catalyst. Nitrogen in the feed gas was used as an internal standard.

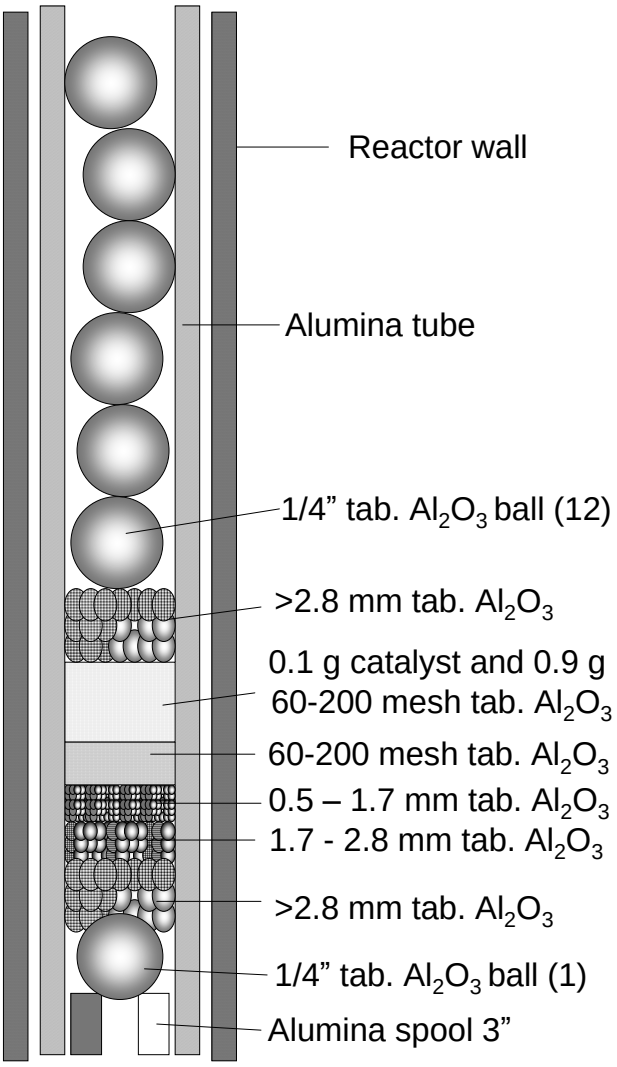

Figure 3.3 Arrangement of the catalyst and filling material in the alumina tube

The bi-reforming reactions are:

Steam reforming $2CH_4 + 2H_2O \longrightarrow 2CO + 6H_2$

Dry reforming $CH_4 + CO_2 \longrightarrow 2CO + 2H_2$

Bireforming $3CH_4 + 2H_2O + CO_2 \longrightarrow 4CO + 8H_2 \longrightarrow 4CH_3OH$

Considering these equations, one molecule of CO_2 is necessary for three molecules of CH_4. In the study, a slight excess of CO_2 (1.18) compared to the theoretical amount needed was

utilized. Water is also in slight excess at (1.2) compared to the theoretical amount needed. In bi-reforming 2 molecules of water are theoretically needed for each three molecules of methane.

A typical exit stream (at 100 psi) is composed of

H_2 67.53 mL/min
N_2 26.3 mL/min (internal standard)
CO 34.59 mL/min
CH_4 8.86 mL/min
CO_2 5.11 mL/min

Total 142.4 mL/min

All the gases were measured by on-line GC. The water was collected at the exit but could not be analyzed in real time with the used setup. In the case of natural gas a slightly higher excess of water compared to CO_2 was needed to reach a H_2/CO ratio of 2. Usually, 0.023 mL/min of water was introduced (instead of 0.021 mL/min in the case of methane)

Dry reforming of methane at high pressure

The insertion of an alumina tube to protect the walls of the metallic tubular reactor from deterioration due to reactive gases essentially eliminated undesired side reactions affecting the gas composition of the product and shortening the apparent life-time of the catalyst. With this new configuration the real reactivity of the catalyst was studied. NiO (15%) on fumed alumina was found to be a stable catalyst for dry reforming of methane under pressure. At 100 psi, the conversion of methane and CO_2 as well as the H_2/CO ratio remained constant for more than 100 hours on stream (Figure 3.4 and 3.5).

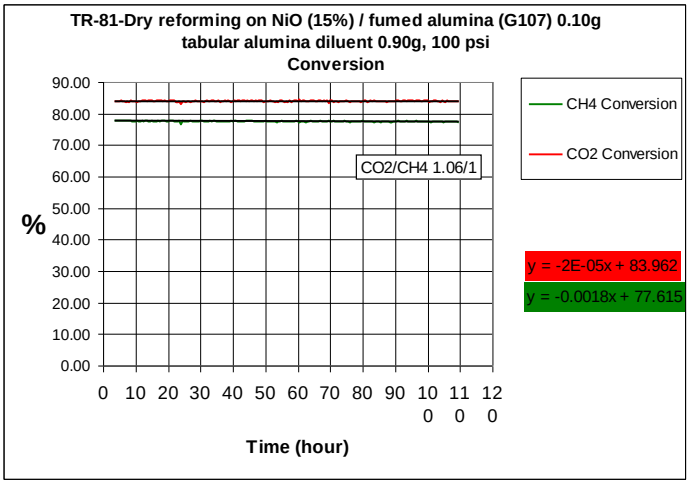

Figure 3.4

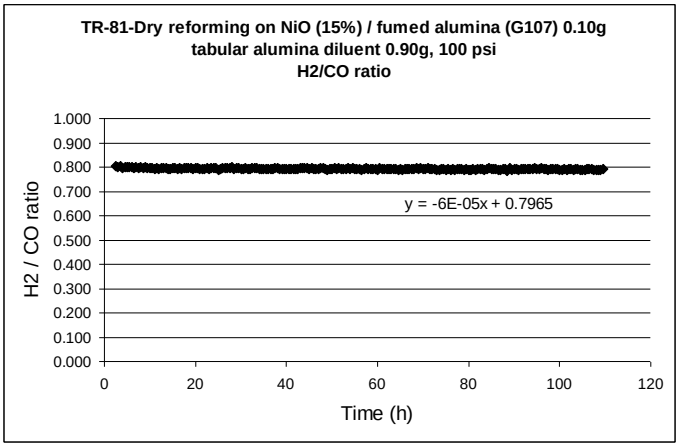

Figure 3.5

Bi-reforming of methane at high pressure

Nickel based catalysts

NiO (15%)/fumed alumina, NiO (15%)/MgO and NiO (15%)/PURAL MG 30 were shown to be active for the bi-reforming reaction for extended periods of time at 100 psi as well as higher pressures. The conversion of methane as well as carbon dioxide was stable over the length of the experiments (Figures 3.6 to 3.8). The H_2 / CO ratio was close to the desired value of 2 (Figures 3.9 to 3.11). The conversion at different pressures was similar for NiO (15%) / MgO and NiO(15%)/PURAL MG 30. As expected from a thermodynamic point of view of the reaction, with an increase in the number of moles, the conversion of CH_4 decreased with increasing pressure (Le Chatelier's principle) (Figures 3.12 and 3.13). In the case of NiO (15%) / MG30, methane conversion decreased from 75% at 100 psi to less than 45% at 500 psi.

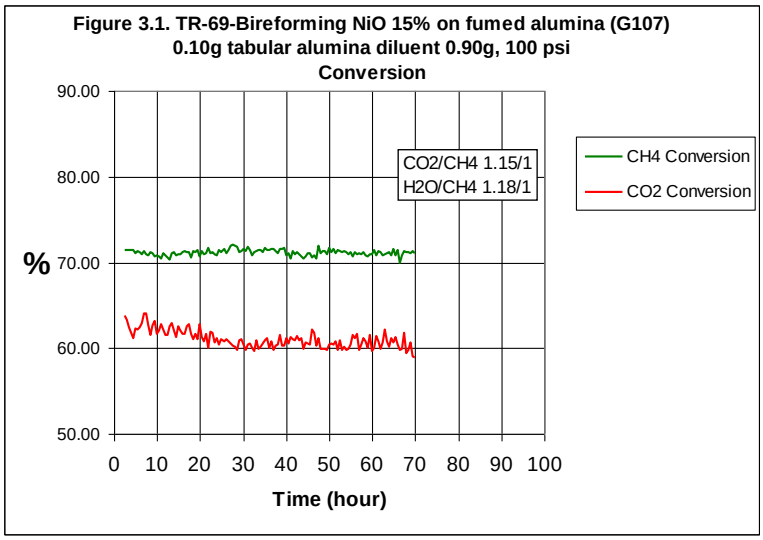

Figure 3.6

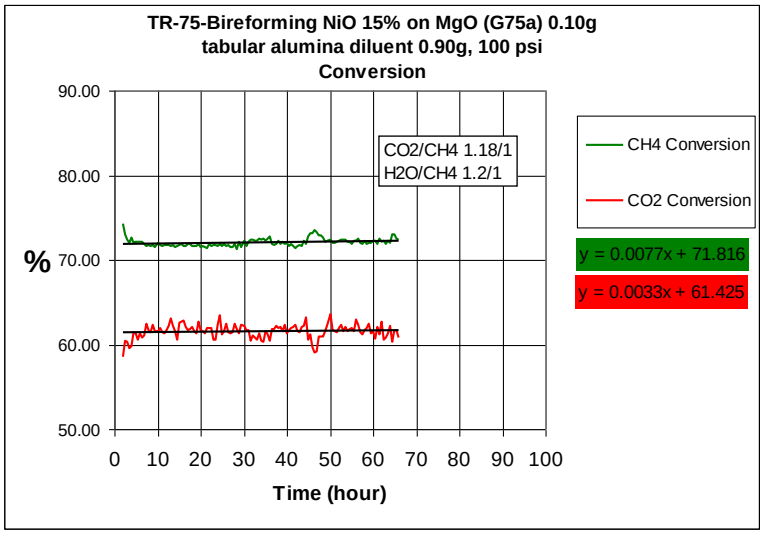

Figure 3.7

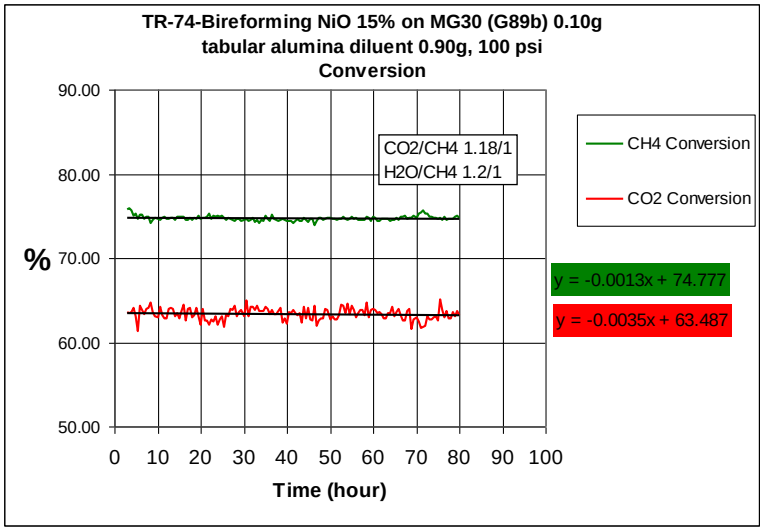

Figure 3.8

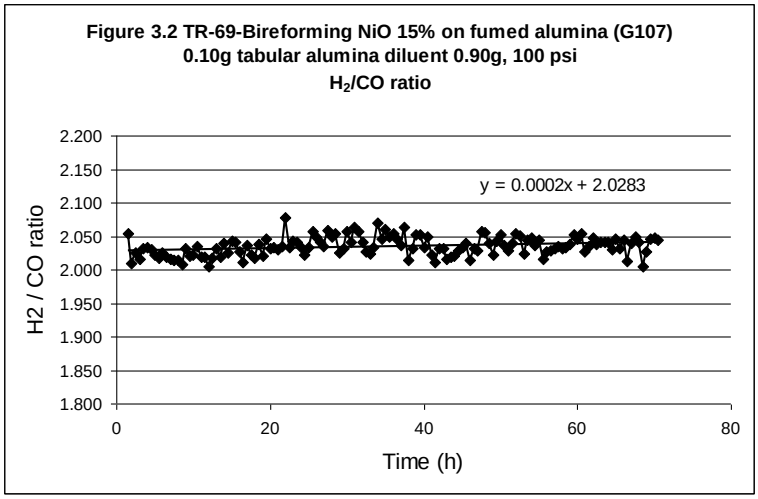

Figure 3.9

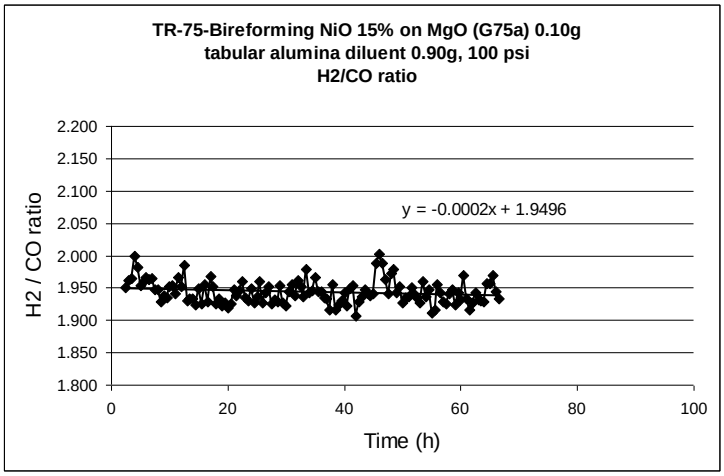

Figure 3.10

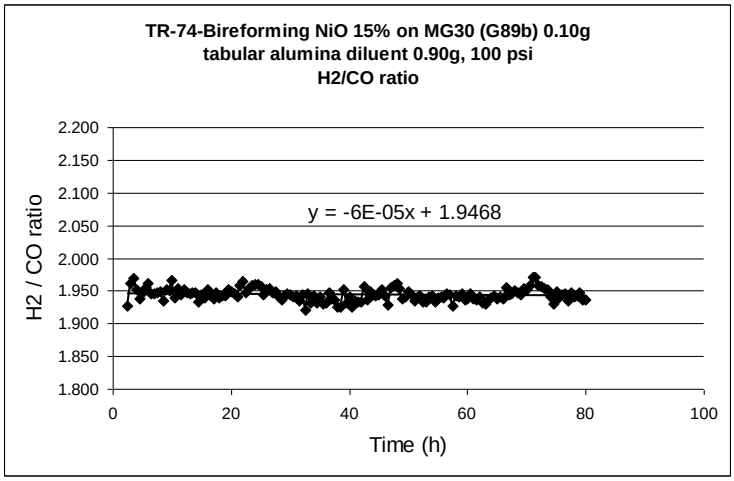

Figure 3.11

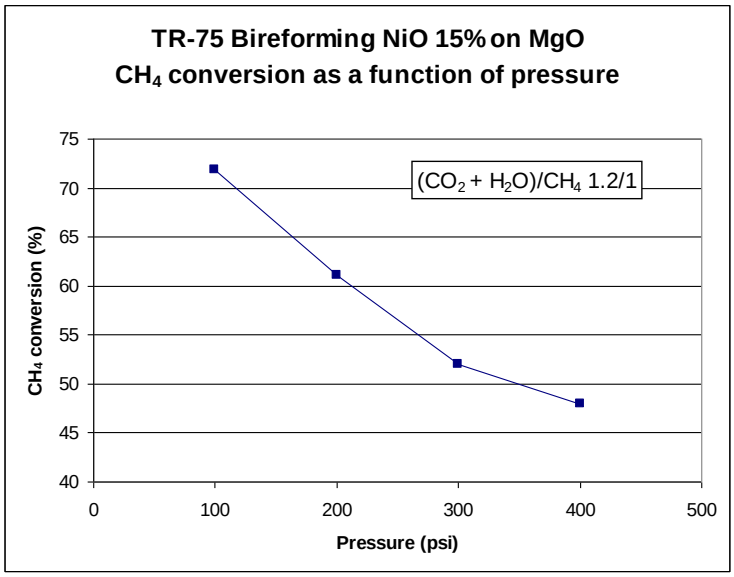

Figure 3.12

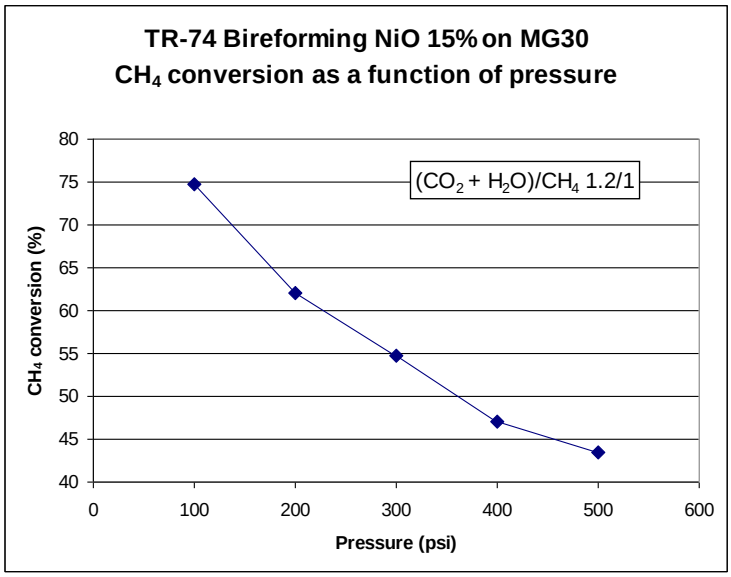

Figure 3.13

Even with a reaction duration of 320 h at 830 °C and 100 psi, NiO (15%) / MgO showed a stable activity for the bi-reforming, giving a constant CH_4 and CO_2 conversion of 71% and 62%, respectively (Figure 3.14). Due to the excess of CO_2 in the gas feed compared to the theoretical amount needed for bi-reforming (CH_4/CO_2 ratio of 3/1.2 instead of 3/1 theoretically), the CO_2 conversion was lower than the CH_4 conversion. However, when considering a theoretical maximum conversion based on the CH_4/CO_2 ratio of 3/1, the conversion of CO_2 was actually very close to the CH_4 conversion (Figure 3.15). The yields of CO and H_2 based on methane conversion were about 71% and remained constant for the duration of the experiment. The calculated selectivity for CO and H_2 were close to 100% as was the carbon balance (Figures 3.16 to 3.18).

The H_2/CO ratio was close to 2 and remained also stable over the reaction period (Figure 3.19). This means that the bi-reforming reaction was actually following the expected path, i.e. with a ratio of H_2O/CO_2 of 2/1 reacting with CH_4, a metgas mixture of H_2/CO with a ratio of 2 could be obtained. Under these conditions, the reaction with CH_4 did not seem to particularly favor dry over steam reforming or vice versa. This is in line with the general agreement that CO_2 reforming on nickel catalyst can be described by the same kinetics as steam reforming. When the temperature was increased from 830 °C to 910 °C, the conversion of both CH_4 and CO_2 increased (Figure 3.20). CH_4 conversion increased about 15% to reach 86% at 910 °C. CO_2 conversion on the other hand, increased about 17% to 79%. The H_2/CO decreased slightly from 1.99 to 1.97 (Figure 3.21). As observed in previous experiments and in the case of NiO (15%) / MG30 the conversion of methane decreased, from 71% at 100 psi to about 49% at 400 psi and 32% at 600 psi, as can be seen in Figure 3.22. Moreover, the H_2/CO ratio increased slightly from 1.99 to 2.03 when increasing the pressure from 100 psi to 600 psi (Figure 3.23). Doubling the amount of water and CO_2 ($CH_4/CO_2/H_2O/N_2$ with a molar ratio of 3/2.4/4.8/2.25) at 100 psi increased the CH_4 conversion from 71% to 84% (Figure 3.24).

In the case of NiO (15%)/alumina, doubling the amount of water and CO_2 at 100 psi increased the methane conversion from 71% to 88% (Figure 24).

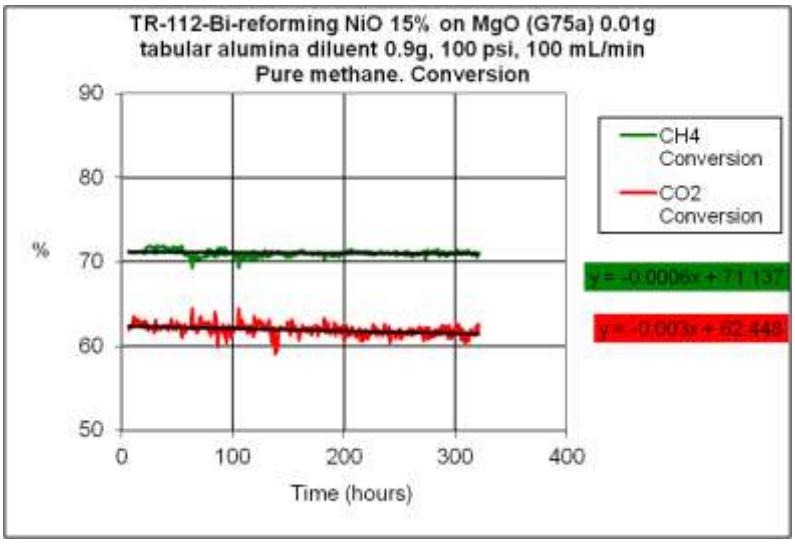

Figure 3.14

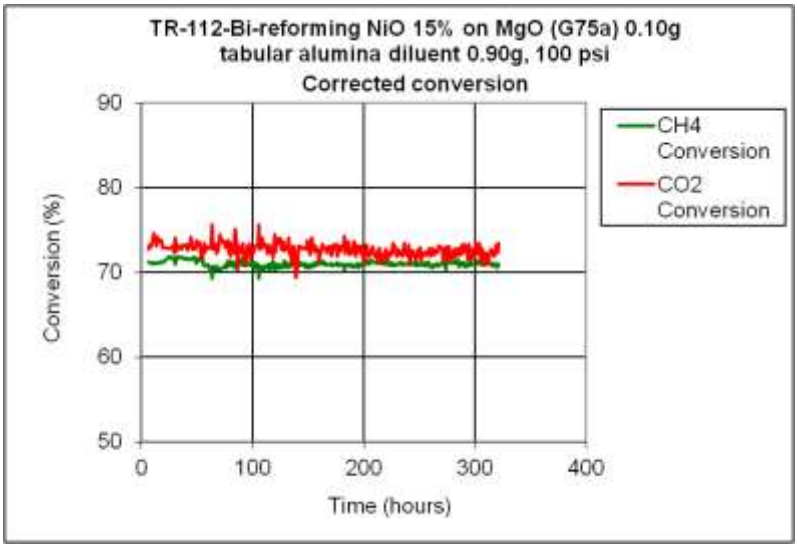

Figure 3.15

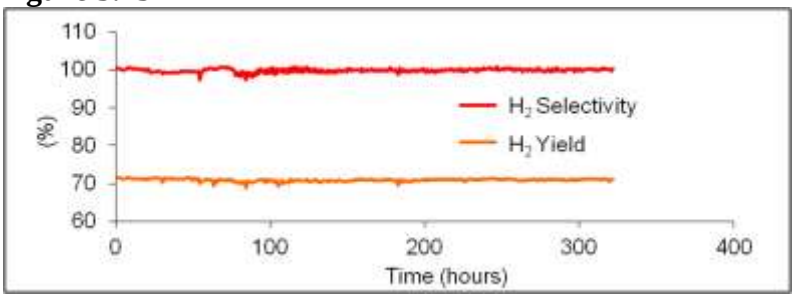

Figure 3.16 TR-112-Bireforming NiO 15% on MgO (G75a) 0.01g tabular alumina diluent 0.9g, 100 psi, hydrogen yield and selectivity

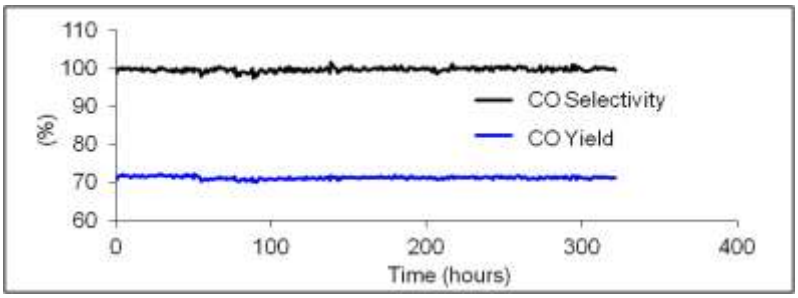

Figure 3.17 TR-112-Bireforming NiO 15% on MgO (G75a) 0.01g tabular alumina diluent 0.9g, 100 psi, CO yield and selectivity

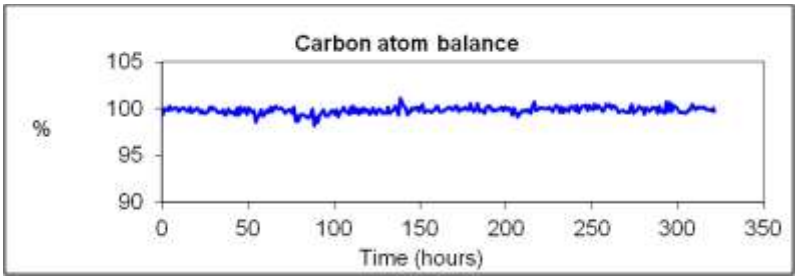

Figure 3.18 TR-112-Bireforming NiO 15% on MgO (G75a) 0.01g tabular alumina diluent 0.9g, 100 psi, Carbon atom balance with time

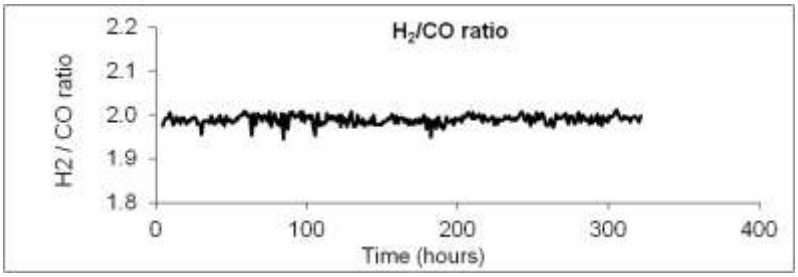

Figure 3.19 TR-112-Bireforming NiO 15% on MgO (G75a) 0.01g tabular alumina diluent 0.9g, 100 psi, H_2/CO ratio with time

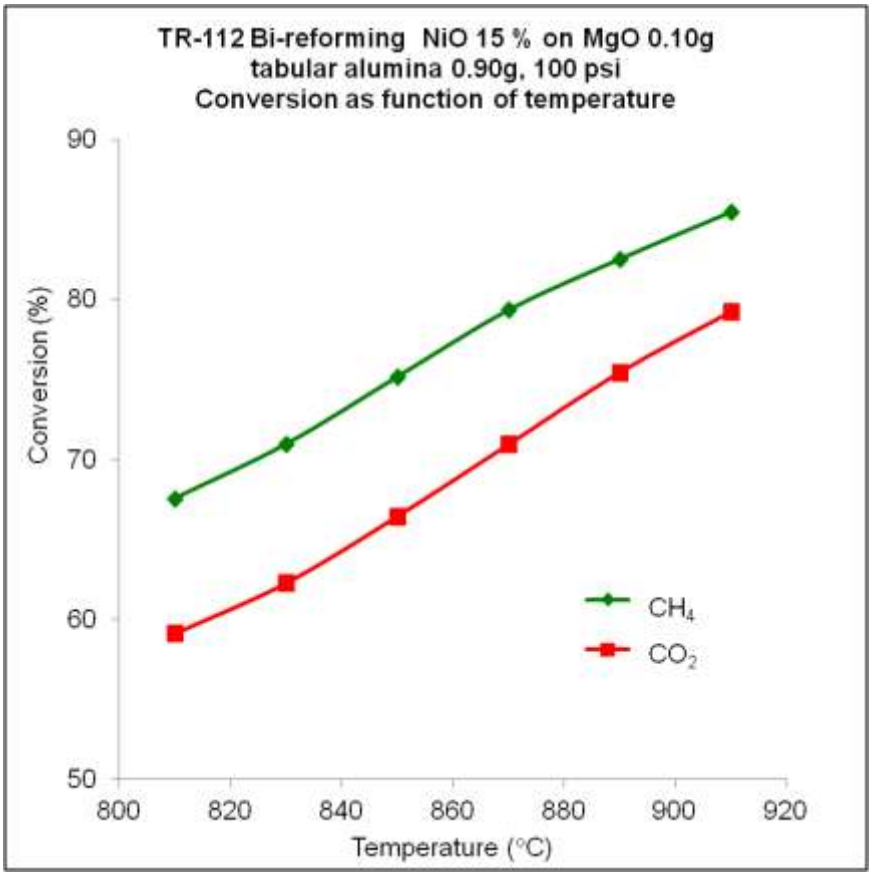

Figure 3.20

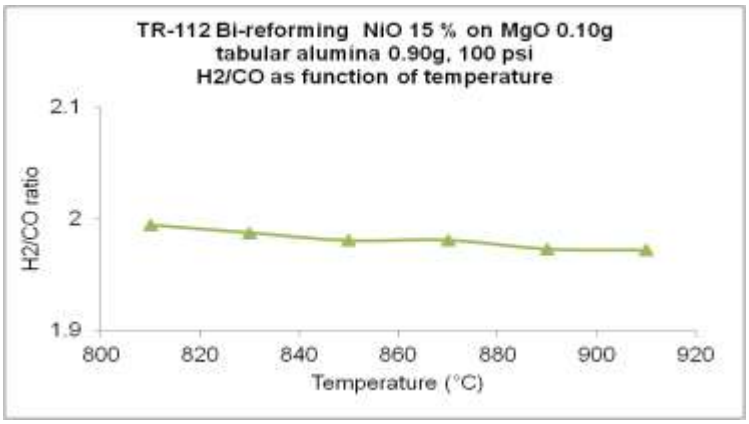

Figure 3.21

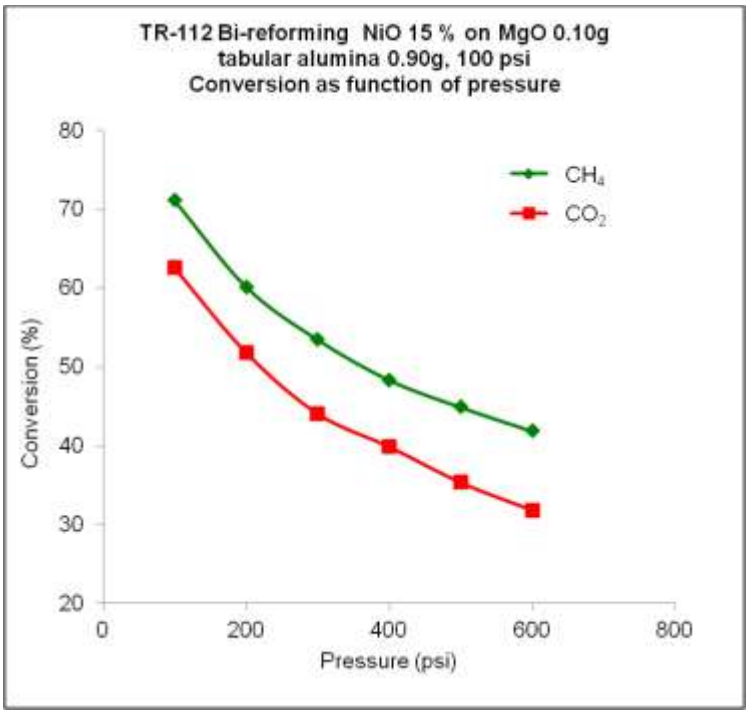

Figure 3.22

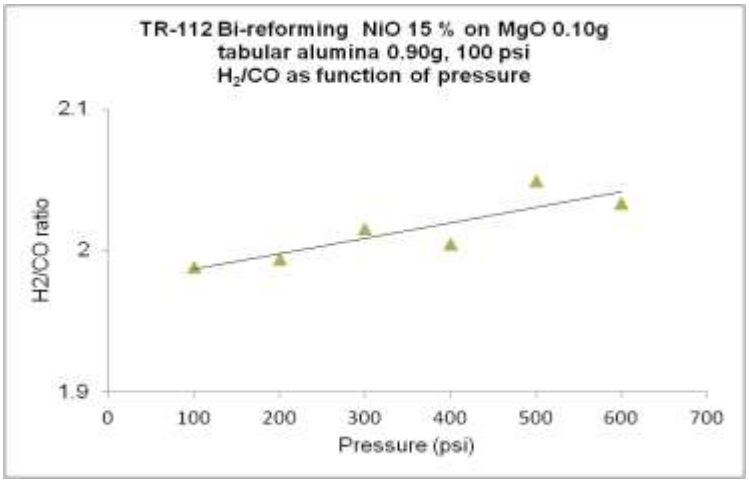

Figure 3.23

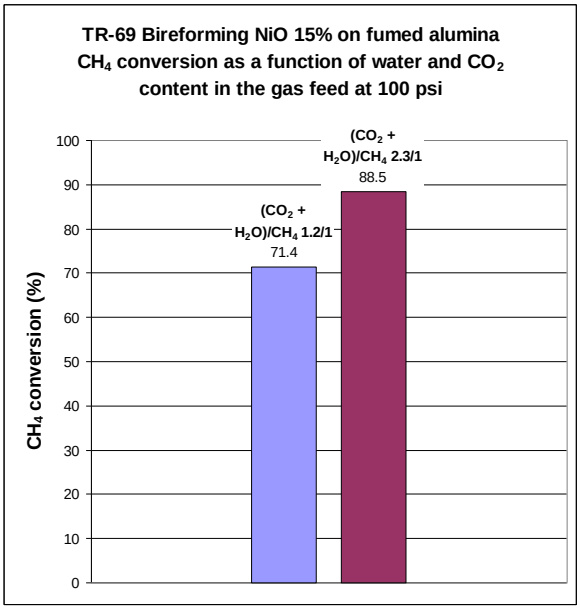

Figure 3.24

Influence of Gas Hourly Space Velocity (GHSV) on the bi-reforming reaction

As explained, *vide supra*, due to problems of metal dusting experienced during the dry reforming reaction of methane, all the internal parts of the reactor in contact with the reaction gases were replaced by alumina. As a consequence of these changes, the internal thermowell allowing the temperature measurement in the center of the tubular reactor was removed to avoid side reactions and possible failure of the material under dry reforming conditions. The disadvantage of removing the internal thermocouple is that the internal temperature close to the catalyst could not be determined. The deterioration or "dusting' of the reactor material under dry reforming conditions was due to the very high carbon activity of the gas mixture used. In the case of bi-reforming, the carbon activity is lower. In order to determine the effect of the endothermic reaction of bi-reforming on the temperature profile the thermowell was reinserted into the tubular reactor to measure the temperature. The catalyst used for this experiment was 0.1g of NiO (15%) on fumed alumina.

A GHSV (Gas hour space velocity) of 60000 $mL.h^{-1}.g^{-1}$ was used, typical for the experiments (100 mL gas feed over 0.1 g catalyst). The temperature in the two-zone furnace was set to 830 °C. The temperature profile of the reaction can be seen in Figure 3.25. In a blank experiment, that included every component except the catalyst, a relatively constant temperature at around 830 °C was observed along the reactor tube. In the presence of the catalyst a sharp decrease in temperature was noticed with a minimum of 802 °C measured close to the catalyst bed. The high endothermicity of the reaction is clearly apparent from these measurements.

At a higher GHSV, the effect was even more noticeable. Doubling the flow of the feed gas to 200 mL/min instead of 100 mL/min (keeping the same ratio between $CO_2/CH_4/H_2O/N_2$) decreased the temperature close to the catalyst to 784 °C; about 40 °C lower than above and under the catalyst. The high temperature gradient could in part be due to the lower heat

conductivity (compared to the metallic tubular reactor) of the alumina sleeve used to protect the reactor from the reaction gases.

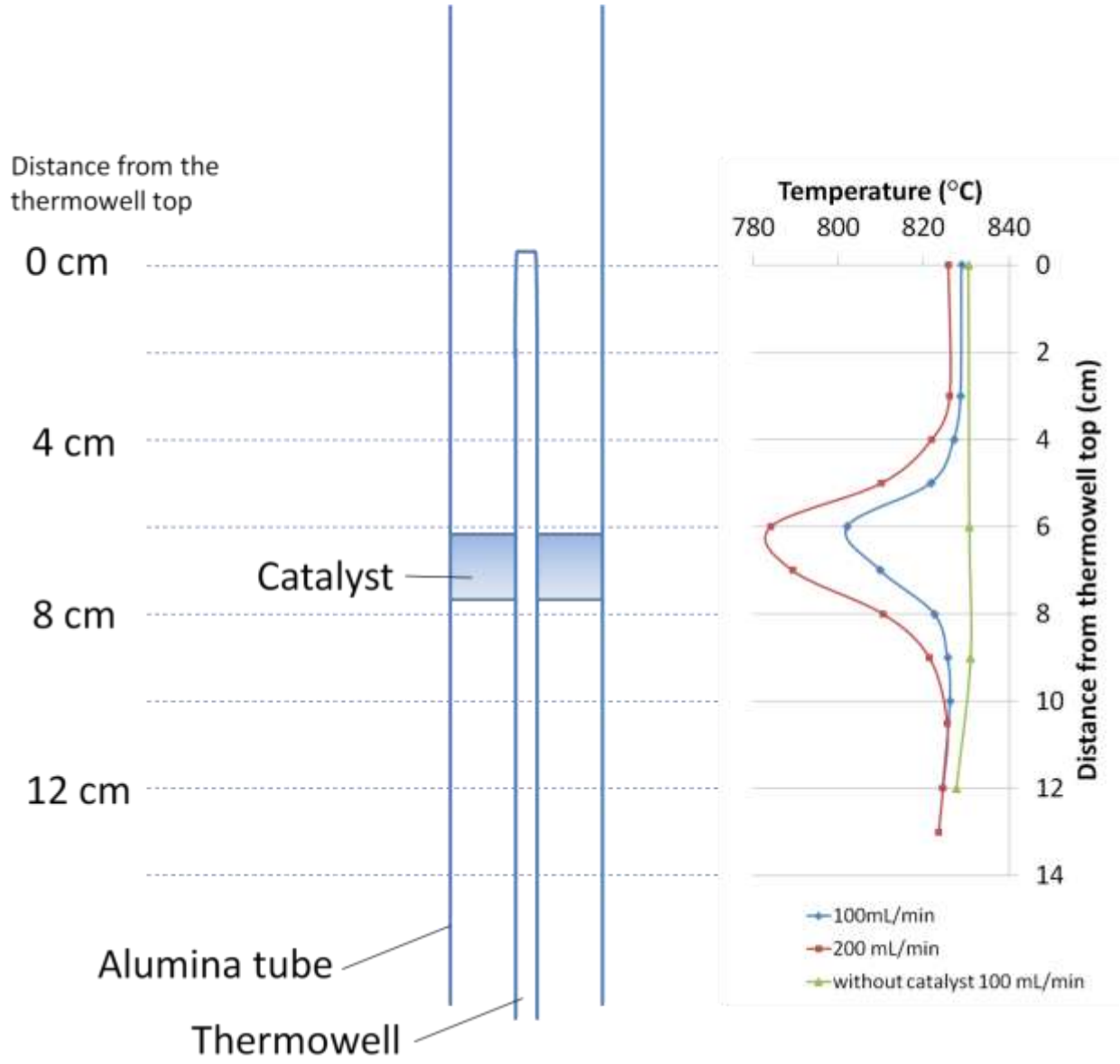

Figure 3.25 Temperature profile in the high pressure reactor depending on the flow rate

At a GHSV of 60000 $mL.h^{-1}.g^{-1}$, the conversion of methane was relatively stable over the duration of the experiment (Figure 3.26). The CH_4 conversion (around 70%) using this setup was comparable to the one observed in the setup with no thermowell in the center of the reactor. After decreasing at the beginning of the reaction, the CO_2 conversion was relatively stable and also comparable to the one obtained in the system without thermowell. The H_2/CO ratio was close to 2 (Figure 3.27).

At a higher GHSV of 120000 $mL.h^{-1}.g^{-1}$ obtained by doubling the flow rate to 200 mL/min, the relative CH_4 conversion decreased considerably to under 60% whereas the CO_2

conversion increased to about 68% (Figure 3.28). However, due to the higher flow rate, the absolute amount of methane and CO_2 converted actually increased explaining the sharper dip in the temperature profile of the reactor. The H_2/CO ratio, on the other hand, decreased to 1.78 (Figure 3.29). The higher GHSV which decreased the contact with the catalyst had thus a detrimental effect on both the CH_4 conversion and the H_2/CO ratio.

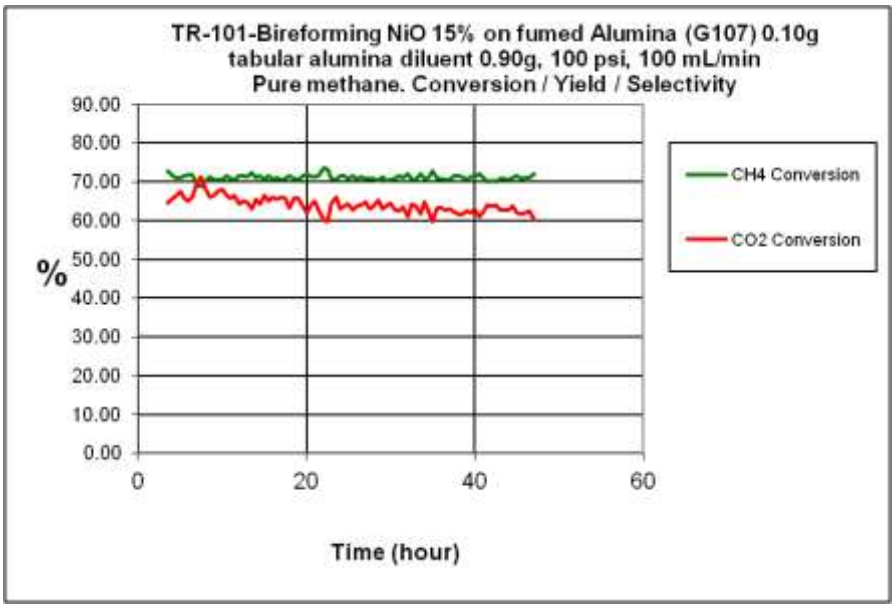

Figure 3.26

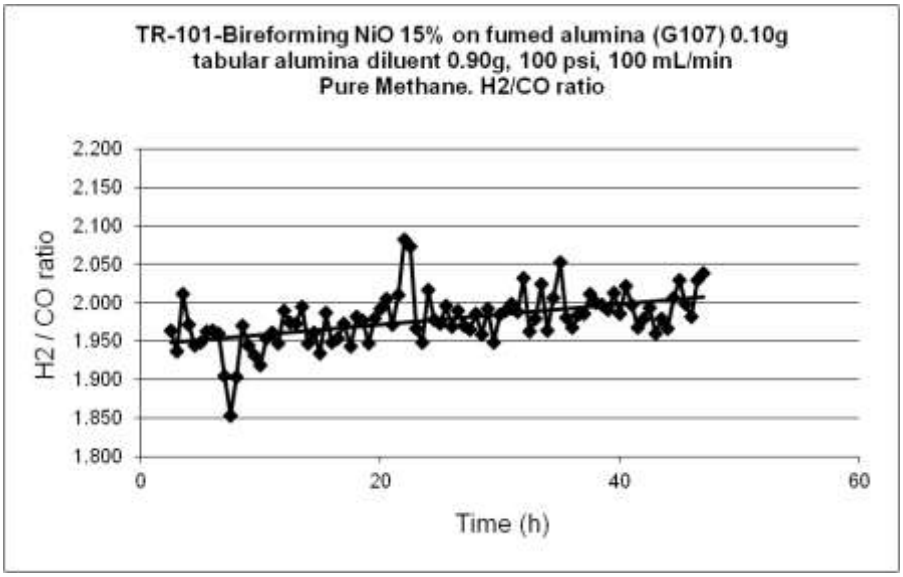

Figure 3.27

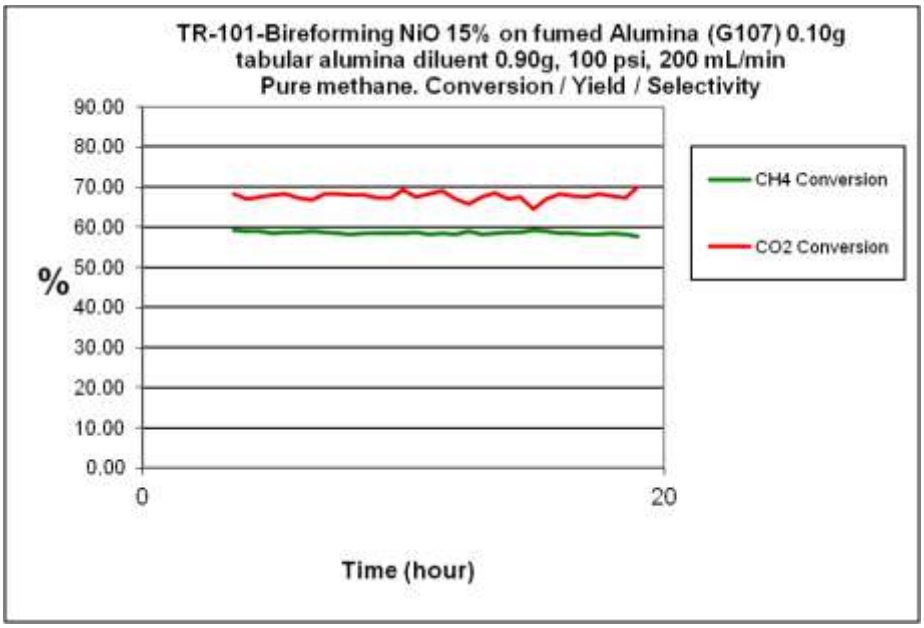

Figure 3.28

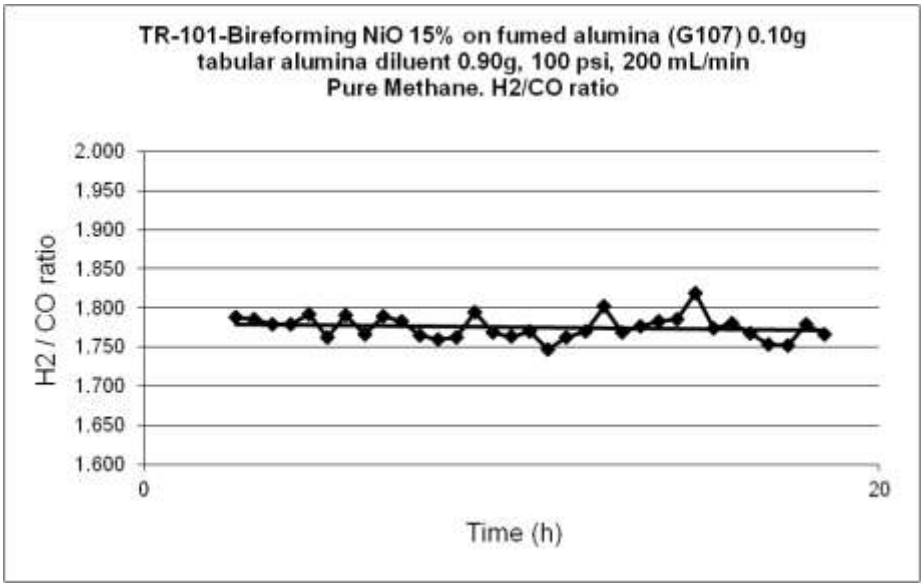

Figure 3.29

Another way to reduce the GHSV but without disturbing the temperature profile is to reduce the amount of catalyst. By using 10 times less catalyst (0.01g instead of 0.1g) and keeping the same flow rate (100mL/min), a GHSV of 600000 $mL.h^{-1}.g^{-1}$ was achieved. Under these conditions, methane conversion decreased only by about 2 percentage points and remained stable for more than 170 hours (Figure 3.30). CO_2 conversion increased slightly whereas the H_2/CO ratio decreased to about 1.95-1.97 (Figure 3.31).

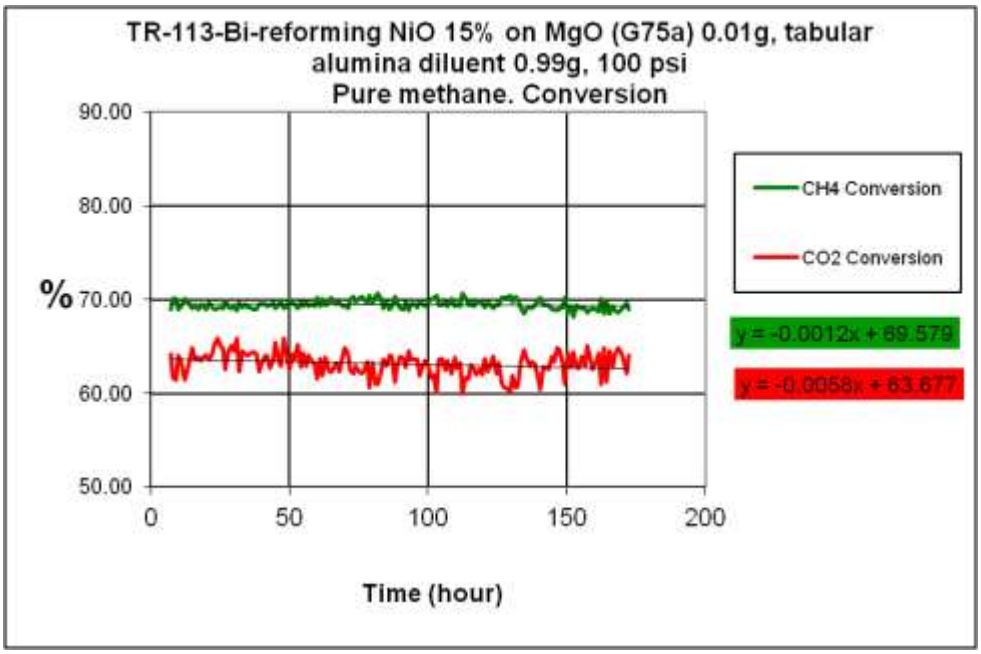

Figure 3.30

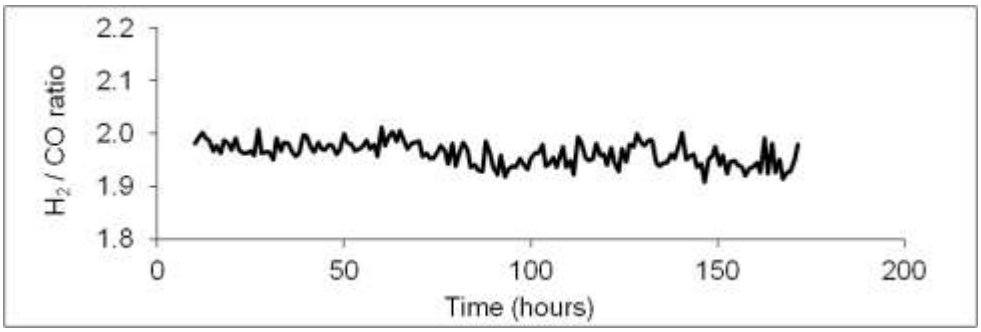

Figure 3.31 TR-113-Bireforming NiO 15% on MgO (G75a) 0.01g, tabular alumina diluent 0.99g, 100 psi Pure Methane, H_2/CO ratio with time

Cobalt based catalyst for the bi-reforming of methane

To test the influence of the catalyst metal on bi-reforming reaction, a cobalt based catalyst composed of 15% CoO supported on magnesium oxide was used. Using this catalyst the methane conversion remained stable and even increased slightly over 90 hour reaction (Figure 3.32). CO_2 conversion also increased (Figure 3.32) and was noticeably higher over CoO/MgO than on a similar catalyst based on nickel. This could be explained by a larger part of CO_2 undergoing reverse water gas shift reaction (RWGS) which converts part of the CO_2 with H_2 to water and CO. In fact, a lower H_2/CO ratio of about 1.94 was measured over CoO/MgO (Figure 3.33) compared to about 2.00 for NiO/MgO. This lower H_2/CO could be a sign that part of the H_2 is used up by reacting with CO_2 to form CO and water.

$$CO_2 + H_2 \rightleftharpoons CO + H_2O \qquad \Delta H_{298K} = 9.8 \text{ kcal.mol}^{-1} \qquad \text{Reverse water gas shift}$$

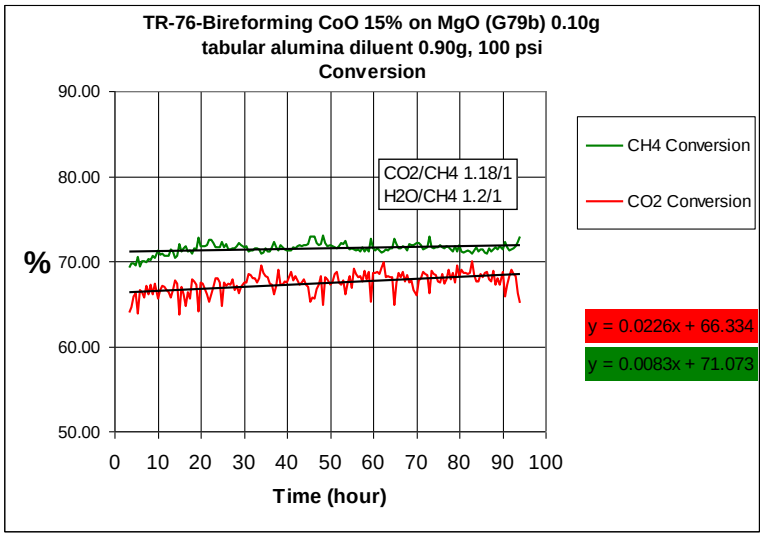

Figure 3.32

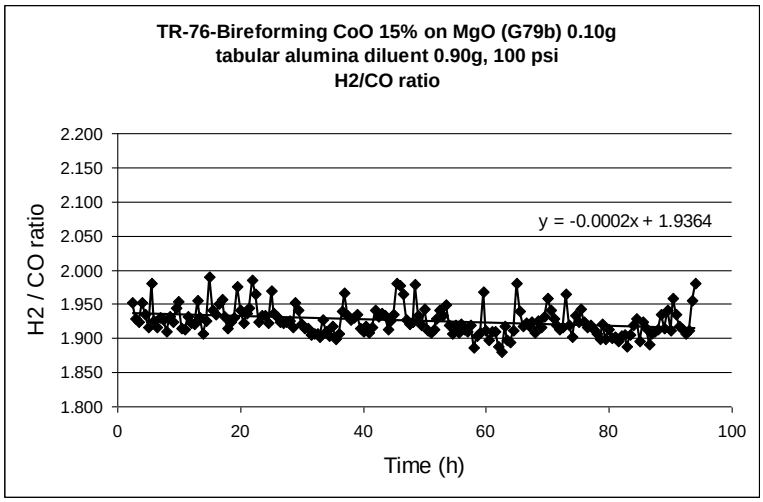

Figure 3.33

Effect of nickel loading in NiO/MgO on the bi-reforming of methane

Nickel loading going from 5% to 35% NiO on MgO had a minimal effect on the bi-reforming reaction at 100 psi (Figures 3.34 to 3.37). Methane conversion was stable in all cases. On the other hand, the CO_2 conversion increased slightly at a rate of about 1.4 points over a period of 100 hours on the catalyst containing 35% NiO. In experiments with lower NiO concentrations (5%, 15% and 25%) a slow decline in CO_2 conversion at a rate between 1 and 1.5 points over a period of 100 hours was observed. The catalyst with a 35% NiO content seems therefore to react somewhat differently with increasing time on stream. The higher CO_2 conversion might however not be welcome as it decreases the H_2/CO ratio, most probably through the reverse water gas shift reaction ($CO_2 + H_2 \rightarrow CO + H_2O$). Ideally both CH_4 and CO_2 conversion should remain stable over time. Alternatively, to keep the H_2/CO ratio constant, the composition of the feed gas could be slightly changed (i.e. adding more water) to counteract the slightly higher CO_2 conversion.

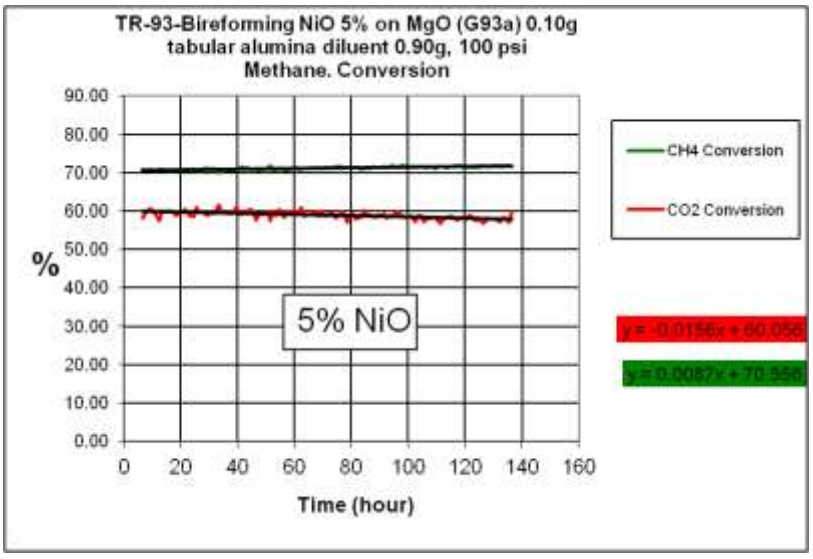

Figure 3.34

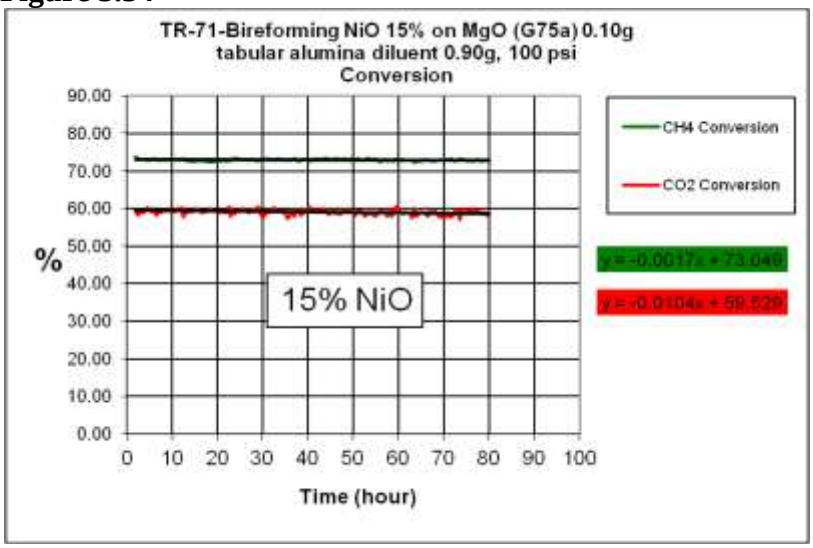

Figure 3.35

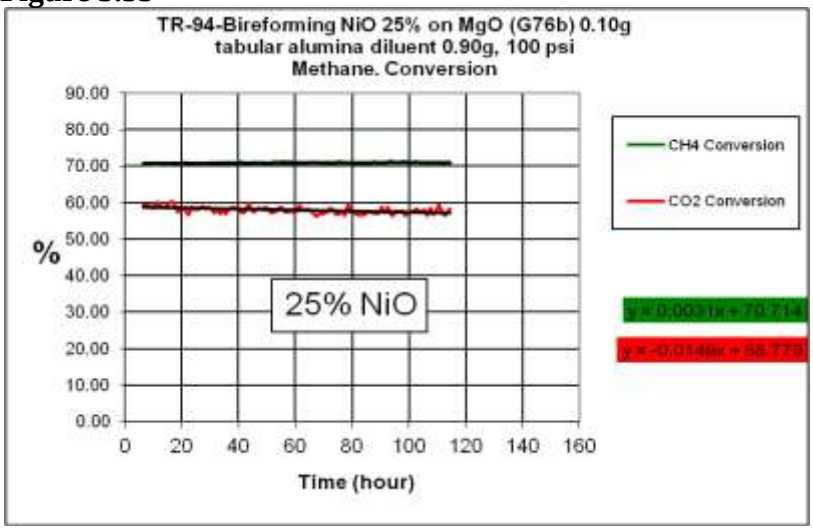

Figure 3.36

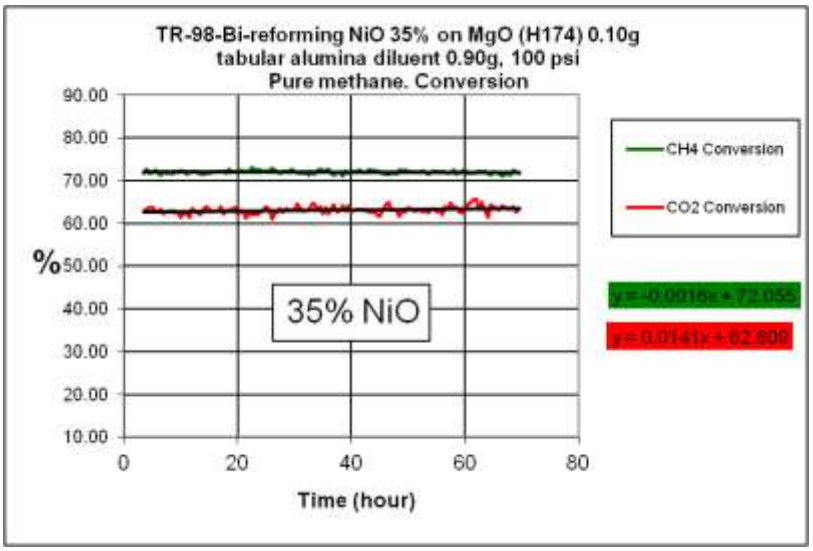

Figure 3.37

Bi-reforming of natural gas at high pressure

Nickel based catalysts

Bi-reforming to metgas is adaptable for reforming varied natural gas (containing hydrocarbon homologues) and CO_2 sources.

$$3\ C_nH_{(2n+2)} + (3n\text{-}1)H_2O + CO_2 \longrightarrow$$

$$(3n+1)CO + (6n+2)H_2 \longrightarrow (3n+1)CH_3OH \quad \text{Eq. 4}$$

In order to study conditions closer to an actual industrial reforming unit, the bi-reforming reaction was also conducted using natural gas containing a mixture of hydrocarbons. As it is the case for natural gas, the gas that was used was still mainly composed of methane. However, it also contained 2.6% ethane, about 0.9% propane as well as higher hydrocarbons such a butane, pentane, hexane, etc. (see Appendix 3.3). No hydrocarbons other than methane were detected in the products, indicating that all higher hydrocarbons had reacted. The higher hydrocarbons react on the metal surface to C_1 compounds, which can then desorb from the surface. Alternatively they can also form carbonaceous deposits.

The activity of NiO (15%) on fumed alumina was relatively stable for the duration of the reaction (100 h). The conversion of methane and carbon dioxide decreased only slightly over 100h (Figure 3.38). However, NiO (15%)/MgO showed a better stability than NiO/fumed alumina (Figures 3.39) for natural gas bi-reforming. The decrease in methane conversion was 1.2% per 100 hours for NiO/fumed alumina. Over the same period, NiO/MgO showed only a decline of 0.2%. On a catalyst containing 10% NiO on MgO, the stability was even higher with no noticeable decline of activity in CH_4 and CO_2 conversion over a period of 110 h. The conversion of CH_4 and CO_2 was however slightly lower (Figure 3.40).

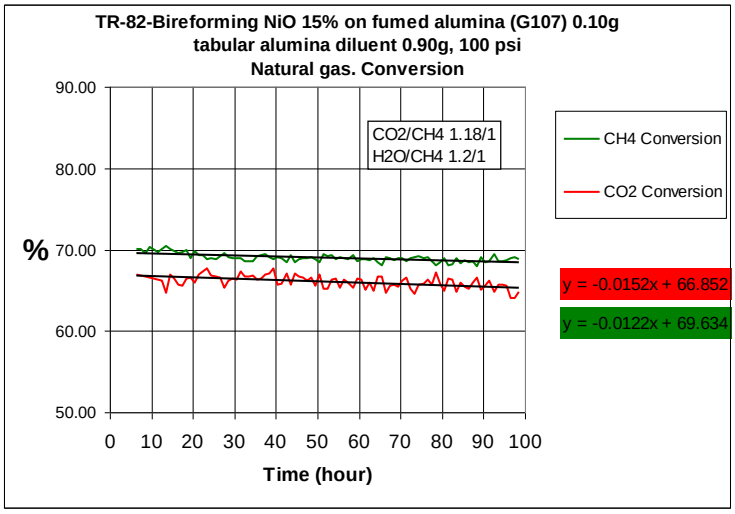

Figure 3.38

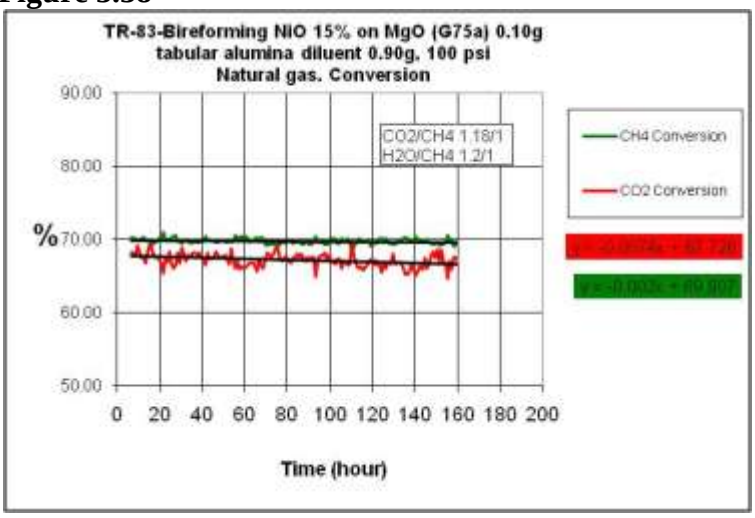

Figure 3.39

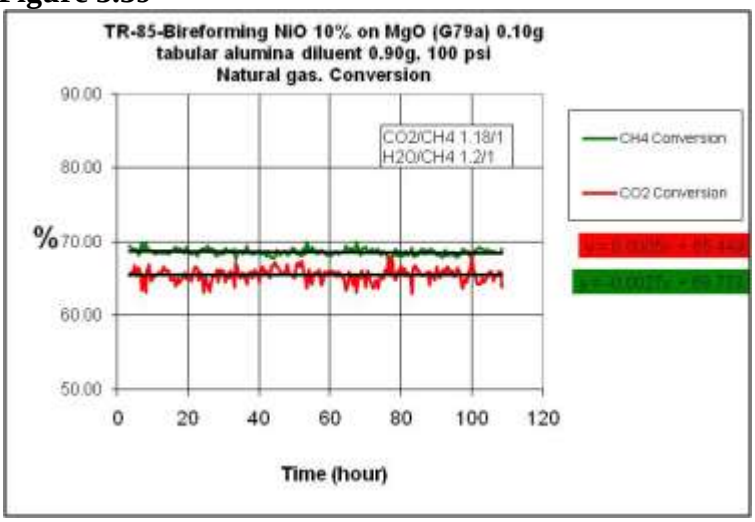

Figure 3.40

NiO (15%) / MgO was also tested for longer periods at various pressures. From Figure 3.41 it can be seen that at 100 psi a relatively stable CO_2 and natural gas conversion was observed for the duration of the experiment (160 h). Natural gas (mainly methane) conversion and CO_2 conversion were about 70% and 67%, respectively (Figure 3.42). The H_2/CO ratio remained stable at around 1.9 (Figure 3.43). This lower H_2/CO ratio compared to the reaction with pure methane is consistent with the presence of higher hydrocarbons having a lower H/C ratio. The H/C ratio will get closer to 2 as the alkane chain increases in size. Whereas methane has a H/C ratio of 4, ethane, propane and butane have a H/C ratio of 3, 2.7 and 2.5, respectively. Keeping the same ratio of water and CO_2 compared to the hydrocarbon feed leads to a lower H_2/CO ratio. However, when the amount of water in the gas feed was increased by 10% (from 0.021 $mL.min^{-1}$ to 0.023 $mL.min^{-1}$ of liquid water before vaporization), a H_2/CO ratio of 2 was obtained in accordance with eq. 4. Concomitantly, the observed conversion of CO_2 was lower. The H_2/CO ratio could therefore be easily modulated by simply adjusting the ratio of steam and CO_2 in the gas feed.

As observed in the case of pure methane, natural gas and carbon dioxide conversion decreased with increasing pressure (Figure 3.42). From 70% at 100 psi, natural gas conversion decreased to 61% at 200 psi, 55% at 300 psi and 51% at 400 psi. The CO_2 conversion decreased faster than the natural gas conversion with increasing pressure. From 100 psi to 400 psi, the CO_2 conversion decreased from 67% to 40% with a decline of 27% points compared to a decline of only 21% points for natural gas (from 70% to 51%). At each pressure, the catalyst showed, however, no noticeable decline in its activity over time.

On the other hand, the H_2/CO ratio did slightly increase with increasing pressure from about 1.90 at 100 psi to 1.92 at 200 psi, 1.96 at 300 psi and 2.01 at 400 psi (Figure 3.43) indicating that the increase in pressure seemed to actually have a positive effect on the H_2/CO ratio. A similar trend, although less pronounced, was also observed when using pure methane instead of natural gas (*vide supra*). This observation correlates with the lower relative conversion of CO_2 with increasing pressure and could indicate that at higher pressures the steam reforming reaction is somewhat favored compared to the dry reforming reaction. In the water gas shift (WGS) reaction the number of moles remains unchanged. Therefore the equilibrium composition should not be affected by the pressure. However, in the case of lower conversion, more water is present in the gas mixture, which could possibly favor the WGS reaction leading to higher hydrogen content in the products.

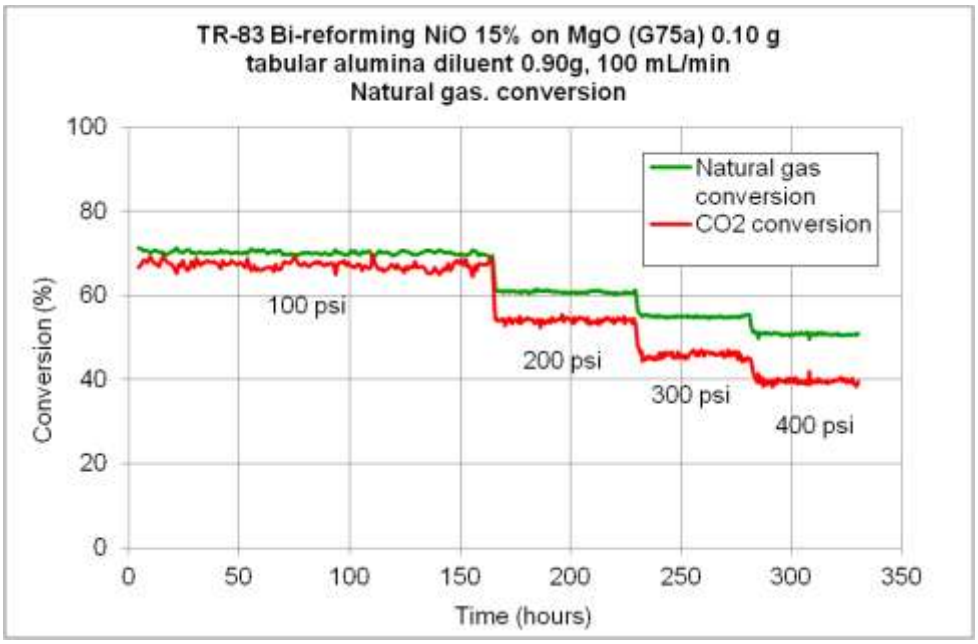

Figure 3.41

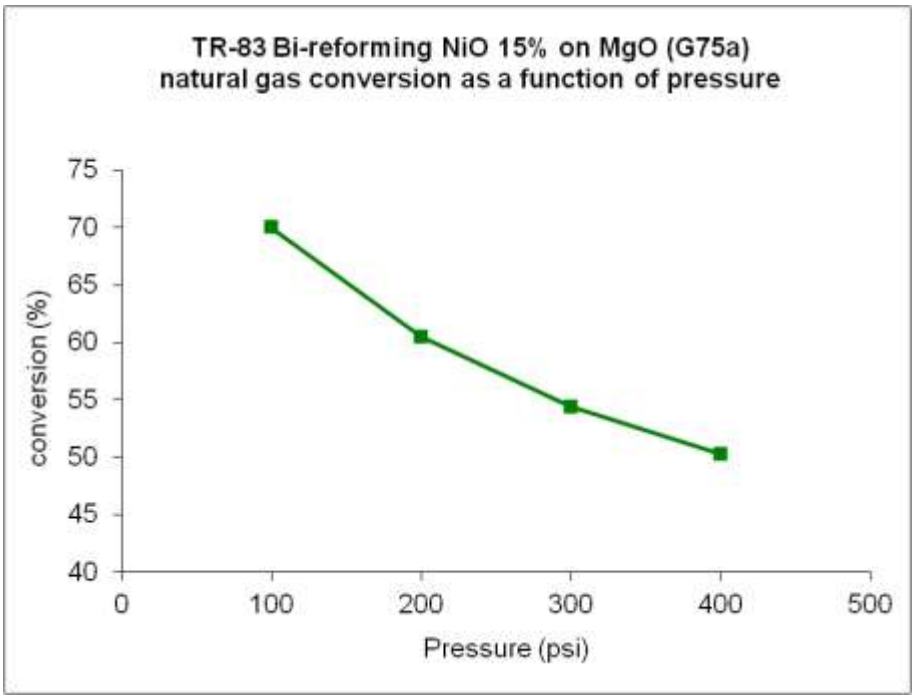

Figure 3.42

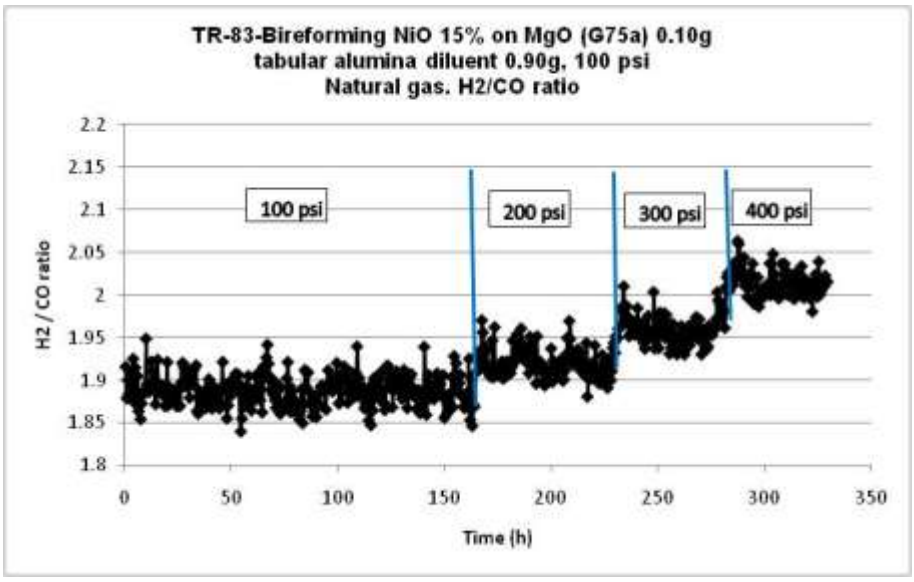

Figure 3.43

When NiO/MgO with a NiO content of 35% was tested for the bi-reforming of natural gas at 100 psi a stable activity was observed for more than 240 h. The natural gas conversion and the CO_2 conversion were almost constant at about 72% and 57%, respectively (Figure 3.44). Because of the slightly higher water flow rate of 0.023 mL/min the H_2/CO ratio remained relatively stable at around 2 for the duration of the experiment (Figure 3.45). Using the same catalyst, the conversion of natural gas was similar to the conversion of pure methane (see Figure 3.37). The H_2/CO ratio was also similar, although a lower flow rate of water was used (0.021 mL/min). The conversion of CO_2, however, was lower than in the case of methane with 57% compared to 63%. A lower conversion of CO_2 is to be expected from the reaction of CO_2 with natural gas, which contains beside methane also higher alkanes (see Appendix 3.3). Regardless of the alkane, only one mole of CO_2 for three moles of alkane is required to obtain a H_2/CO ratio of 2 as can be seen in the equation below. Only the amount of water has to be increased with increasing number of carbons in the alkane to achieve a H_2/CO ratio of 2.

$$3\ C_nH_{(2n+2)} + (3n\text{-}1)H_2O + CO_2 \longrightarrow (3n+1)CO + (6n+2)H_2 \longrightarrow 4nCH_3OH$$

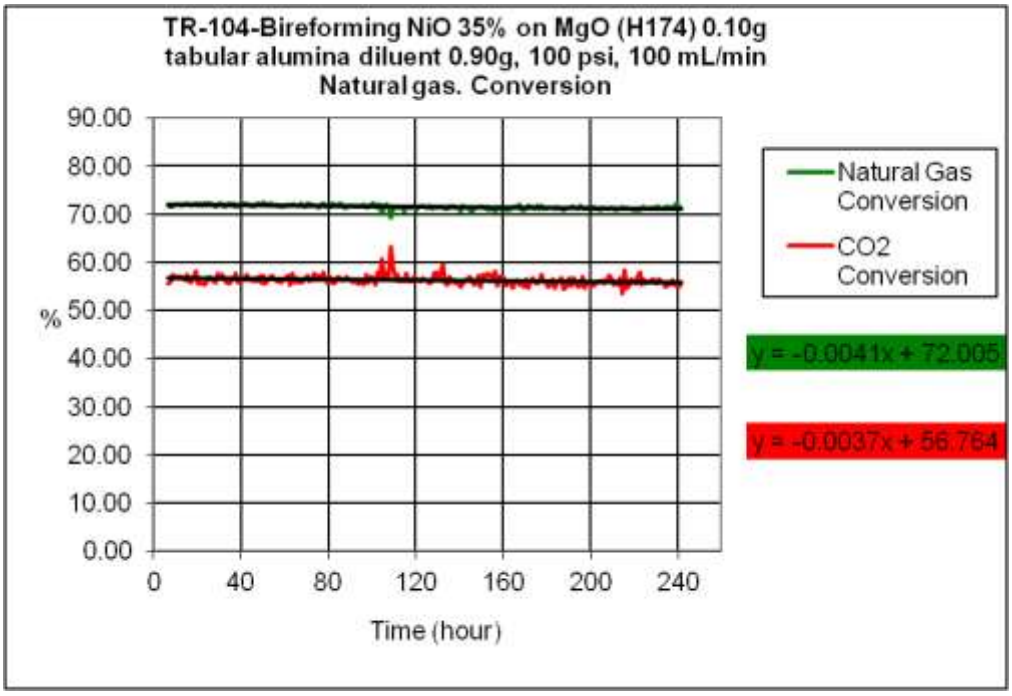

Figure 3.44

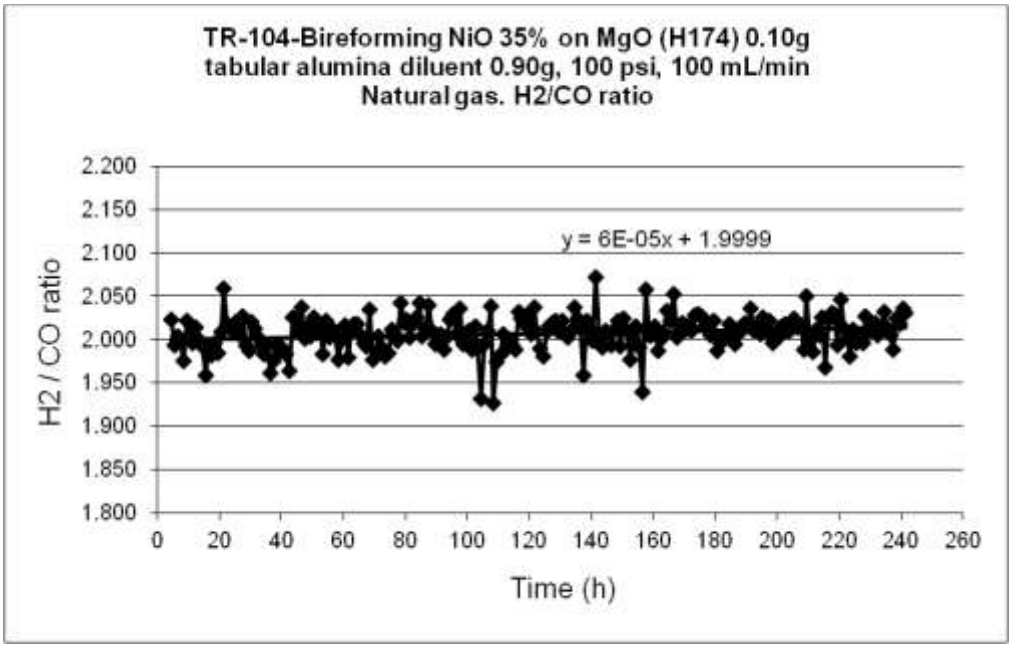

Figure 3.45

Effect of a higher GHSV on the bi-reforming of natural gas on NiO/MgO (35% NiO)

Generally in the performed experiments 100 mg of catalyst mixed with 900 mg of tabular alumina were used. Considering a ~100 mL gas feed, including water vapor, a GHSV of 60000 $mL.h^{-1}.g^{-1}$ was therefore a typical value for the testing of our catalysts. Keeping the same flow rate (100 mL/min) and ratio of $CO_2/CH_4/H_2O/N_2$ but decreasing the amount of catalyst (35% NiO on MgO) to 0.02g, the GHSV was effectively increased fivefold to 300000 $mL.h^{-1}.g^{-1}$. At this higher GHSV, the conversion of methane was relatively stable at about 70% over the duration of the experiment (Figure 3.46). The CH_4 conversion was slightly lower than the one observed at a higher catalyst loading. The CO_2 conversion also decreased slightly from 57% to 55% at a higher GHSV. On the other hand, the H_2/CO ratio increased somewhat to 2.03 from 2.00 with a lower GHSV(Figure 3.47).

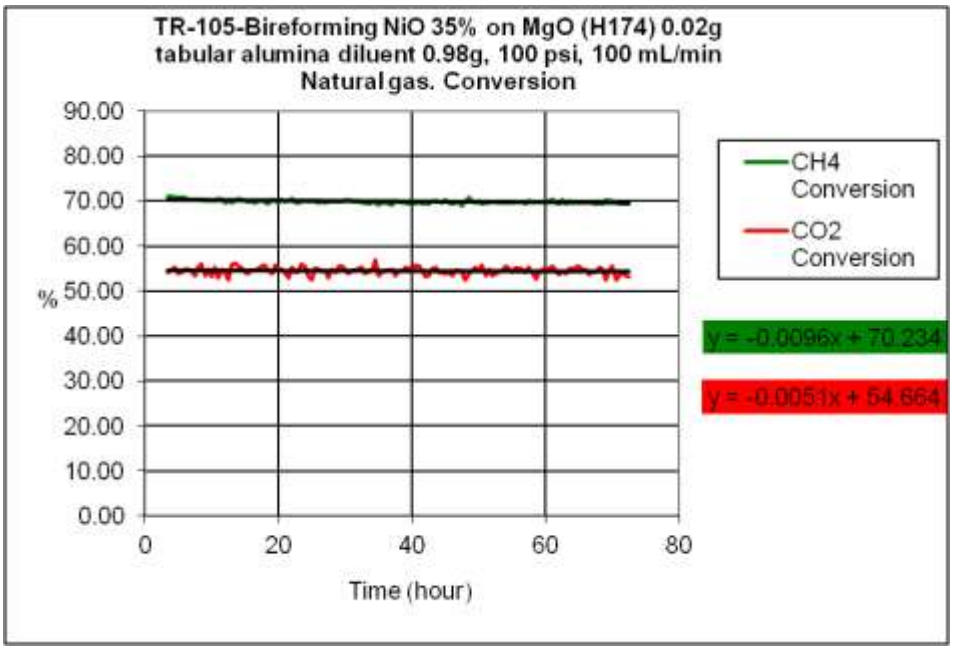

Figure 3.46

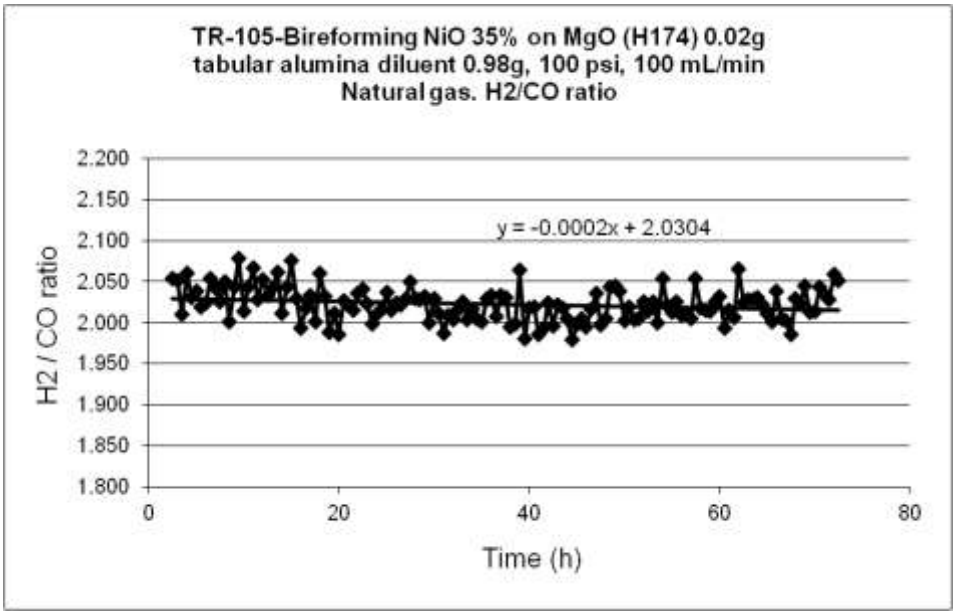

Figure 3.47

Cobalt based catalysts for the bi-reforming of natural gas

In this experiment, CoO/MgO with a CoO content of 15% was tested for the bi-reforming of natural gas at high pressure. It can be seen in Figure 48 that at 100 psi the conversion of CO_2 and natural gas decreased steadily over the duration of the experiment. Over 100 hours the conversion of CO_2 and natural gas decreased at a rate of about 3%. The H_2/CO ratio remained relatively stable at around 1.94 (Figure 3.49) when using a water flow of 0.021 mL/min. The H_2/CO ratio could be increased to 2 by increasing the amount of water from 0.021 mL/min to 0.023 mL/min. Utilizing the same catalyst, the conversion of natural gas was lower than the conversion of pure methane (see Figures 3.32 and 3.33 for comparison). In the case of pure methane, the activity also remained constant during the reaction.

With increasing reaction temperature the natural gas conversion increased as can be seen in Table 1. From about 64% at a furnace temperature of 830 °C to 82% at a furnace temperature of 890 °C. Increasing the temperature by 60 °C had therefore a very significant effect on the activity.

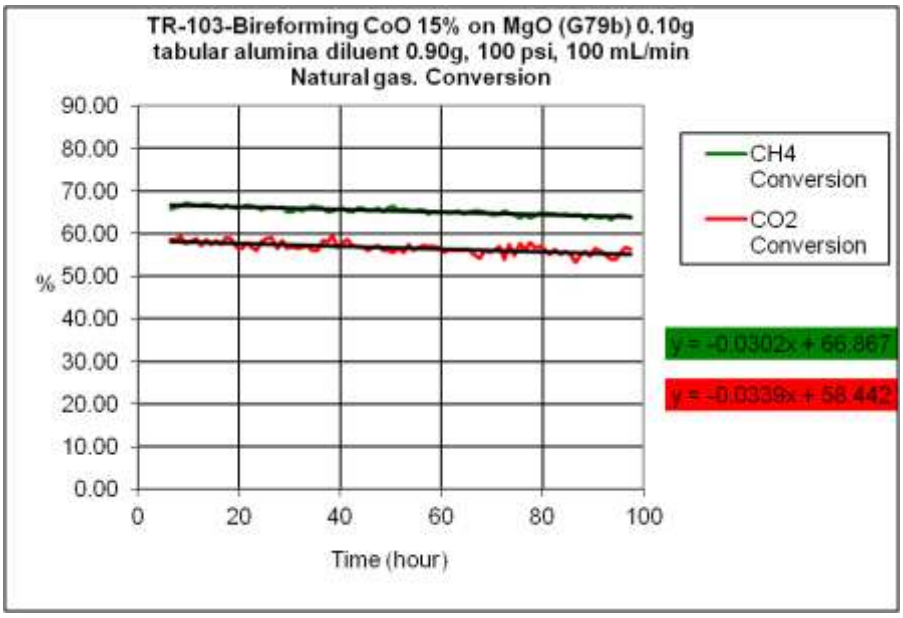

Figure 3.48

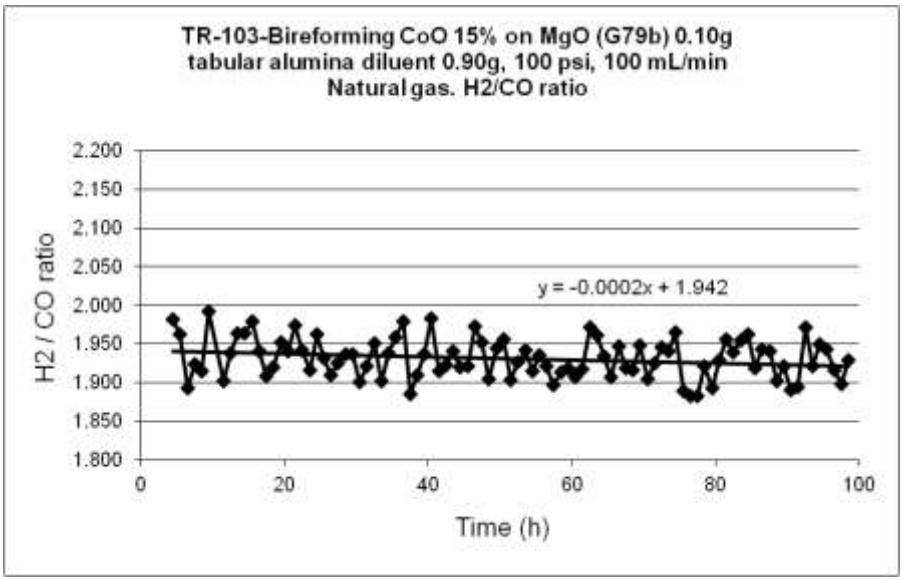

Figure 3.49

Table 3.1 Natural gas conversion as a function of temperature in the bi-reforming reaction over CoO/MgO (15% CoO)

Furnace temperature (°C)	Natural gas conversion (%)
830	64
850	71
870	77
890	82

General conclusions for Task 3: Methane bi-reforming at high pressures

Over the duration of the project, a flow reactor system was designed, built and adapted to the study of dry- and bi-reforming of methane and natural gas at high pressures and high temperatures. Some of the highlights of the research over this period are given below:

- At the beginning of the work, technical issues experienced included coking and degradation of the reactor material (metal dusting) due mainly to the high carbon activity of the gas mixtures used. These technical problems were successfully solved by the implementation of reactor modifications. The utilization of an alumina sleeve and alumina filling material in particular proved to be an essential step, enabling reliable operation, catalyst testing and data collection.
- A number of catalysts based on nickel and cobalt deposited on various supports were tested. Among them, NiO/fumed alumina, NiO/MgO, NiO/PURAL MG30 as well as CoO/MgO were found to have a stable activity for the bi-reforming reaction of methane under pressure. Reactions at pressures up to 500 psi (35 atm) were performed. In accordance with the thermodynamics of the reaction, the CH_4 and CO_2 conversion decreased with increasing pressure. This effect could be in part countered by increasing the amount of steam and CO_2 in the gas feed.
- NiO/fumed alumina and NiO/MgO with NiO content from 10% to 35% were successfully tested for the bi-reforming of natural gas for up to 250 hours on stream. The activity remained stable over the duration of the experiment for pressures up to 400 psi (28 atm). A desired H_2/CO ratio of 2 could be obtained by varying the amount of water added in the gas feed.

Task 4: Efficient Ways to Capture CO_2 and Its Electrochemical Conversion

Subtask 4.1: Adsorbents for CO_2 Capture

Introduction

The ever-increasing consumption of fossil fuels by humankind resulted in an accumulation of carbon dioxide in the atmosphere, from a concentration of 270 ppm before the industrial revolution to more than 400 ppm today. It is now widely accepted that anthropogenic CO_2, due to its role as a greenhouse gas is the largest contributor to climate change. Other environmental implications of these emissions, such as ocean acidification, are also becoming increasingly apparent and worrisome. Thus, CO_2 management is one of the most challenging problems of the current century. CO_2 capture and sequestration (CCS) underground has been proposed but none of the existing technologies has been proven on the enormous scale needed. One needs to make sure that if billions of tonnes of CO_2 are pumped underground much will remain there not leak out overtime, making the process pointless. While fossil fuels will be used for as long as they can be easily and economically produced, it should also be clear that their amounts are finite and that they will be increasingly depleted. Post-fossil fuel alternative sources of carbon have therefore to be found to fulfill the needs for fuels, hydrocarbons, polymers and other products presently derived mostly from petroleum oil and natural gas. Instead of considering CO_2 as a problematic and unwanted combustion byproduct, it should be seen as a valuable feedstock for the production of fuels and materials.[1,2] While the required CO_2 can be presently captured from concentrated industrial sources, eventually it will have to be obtained directly from the atmosphere. The total cost associated with the capture of CO_2 employing existing technologies is relatively high. It is therefore highly desirable to improve on current technologies to reduce the cost for CO_2 capture and reuse it to produce new fuels and synthetic hydrocarbons and derived materials.

Background

The removal and capture of CO_2 from gas streams can be achieved by a range of separation techniques depending on CO_2 concentration, pressure, temperature, etc. They are based on different physical and chemical processes including absorption into a liquid solution, adsorption onto a solid, cryogenic separation and permeation through membranes (Figure 4.1).[3] Cryogenic distillation is very energy intensive and generally considered impractical for large scale CO_2 separation. Membranes are more suited for relatively high concentrations of CO_2 such as those encountered in some natural gas deposits or for pre-combustion separation.

Among the different CO_2 separation techniques, amine based solution CO_2 absorption/desorption systems are one of the presently most suitable technologies for high volume flue gas streams. The commonly used solvents are aqueous solutions of alkanolamines such as monoethanolamine (MEA), diethanolamine (DEA), diisopropanolamine (DIPA) and methyldiethanolamine (MDEA). In addition, certain sterically hindered amines (e.g. 2-amino-2-methyl-1-propanol (AMP)) also offer suitable properties as absorbents due to their high CO_2 loading capacities.[4]

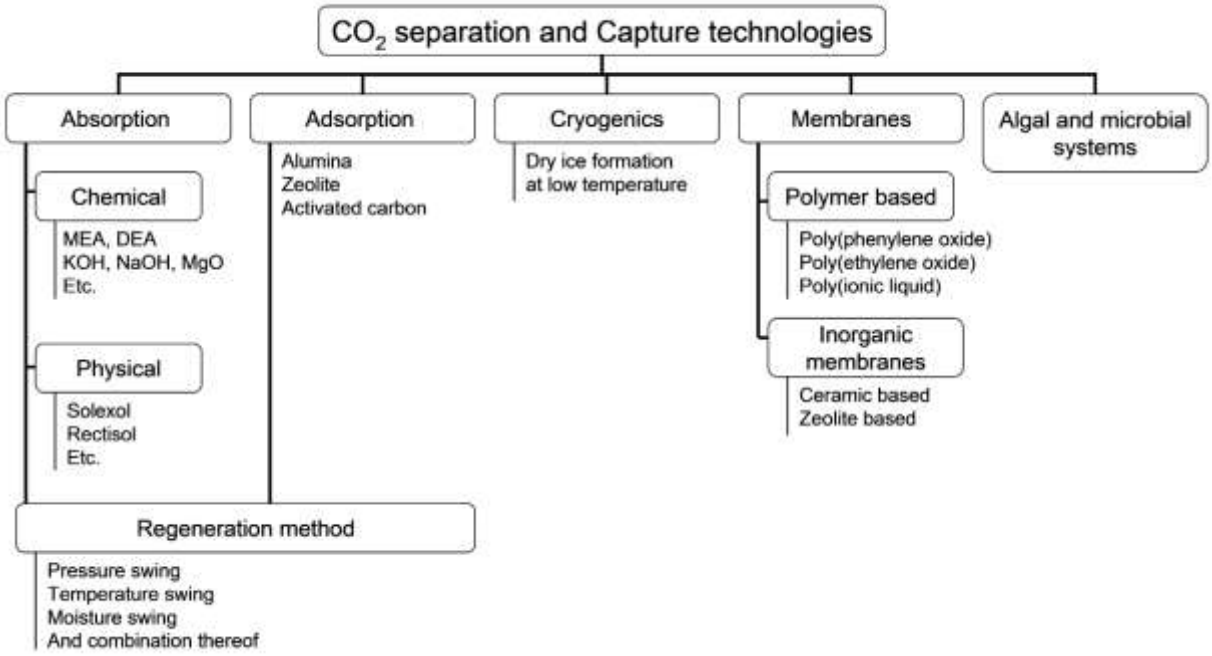

Figure 4.1 CO_2 adsorption and adsorption technologies available

Among the mentioned amines, MEA is the most widely used because it has a fast CO_2 absorption rate that allows the use of shorter absorption columns. MEA based systems were developed some 60 years ago as a general, non selective absorbent to remove acidic impurities (e.g. H_2S, CO_2) from natural gas streams. The MEA based process was later adapted to treat flue gases for CO_2 capture. Fluor Daniel Inc. Dow Chemicals Co., Kerr McGee Chemical Corp., ABB Lummus Crest Inc. and UOP are some of the developers of such technology.

Sterically unhindered primary alkanolamines such as MEA react with CO_2 to form carbamates. Two moles of amine are necessary to capture one mole of CO_2.

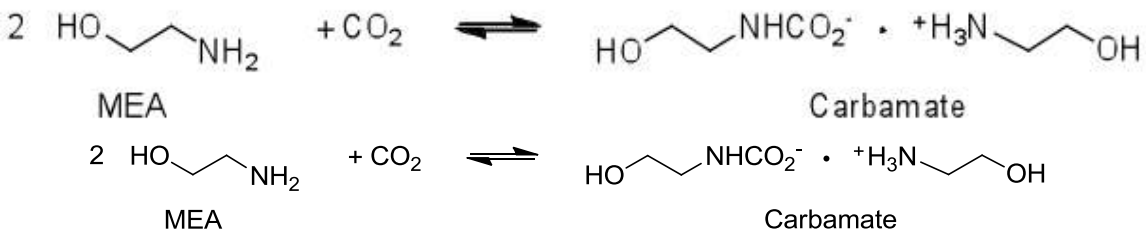

The heat of absorption for this reaction (458 kcal/kg CO_2[4]) is considered high. The major drawback of the MEA system is therefore the large amount of heat required to regenerate the amine and free the captured CO_2. There are also operational problems due to corrosion and chemical degradation of the amine. In order to prevent excessive corrosion, aqueous solutions containing only 10-30 wt % MEA are used. During the endothermic regeneration step however, the high water content (70-90%), which is not involved for CO_2 capture, has also to be heated, increasing the amounts of energy needed.

Secondary and hindered amines (DEA, DIPA, AMP) have more moderate CO_2 absorption abilities but also lead to corrosion problems and are prone to chemical degradation. MDEA always absorbs CO_2 at a slow rate.

In the case of unhindered secondary amines such as DEA, CO_2 reacts to form a carbamate which may also further react to a bicarbonate product in the presence of water and high CO_2 concentrations. In this case, only 1 mole of amine is necessary to capture 1 mole of CO_2. The heat of reaction for the absorption of 389 kcal/kg CO_2[4] is still high but lower than with MEA.

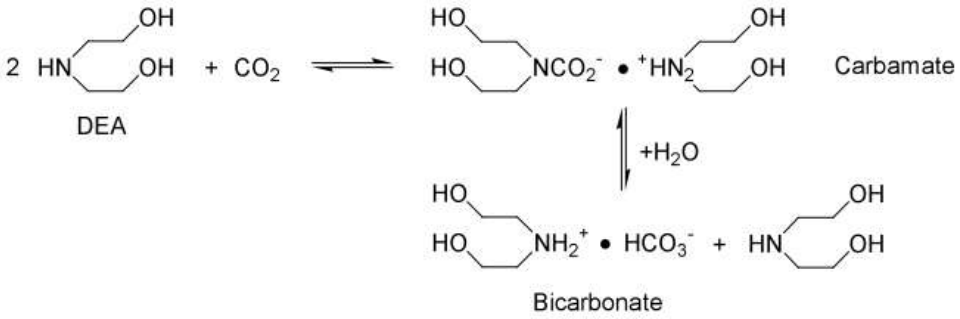

Tertiary alkanolamines such as TEA do not react directly with CO_2 to form a carbamate because of the lack of protons of these amines. In aqueous media however, the tertiary alkanolamine acts as a base, which catalyzes the hydration of CO_2 leading to the formation of bicarbonate. This reaction with CO_2 is slow but TEA is easier to regenerate due to the lower heat of absorption (236 kcal/kg CO_2) compared to MEA or DEA. The addition of activators such as MEA, DEA or piperazine, the absorption and desorption rates can be enhanced.

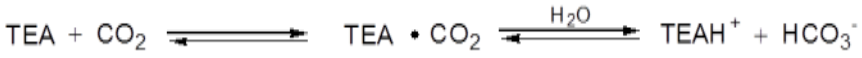

With an activator:

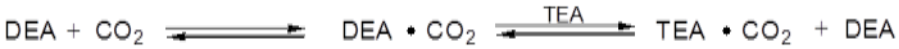

Formulations combining several alkanolamines are also of interest because they can take advantage of the favorable characteristics while partially suppressing unfavorable ones. A number of blended alkanolamines have been developed *inter alia* by UOP and Dow Chemicals Co.[4] The most common blends are MDEA based solutions containing MEA or DEA.

CO_2 absorption using liquid amines is a well-known and widely used technology, which is highly selective for the separation of CO_2 from gas mixtures. However, it is far from being an optimal system. High-energy requirements for the CO_2 regeneration step, limited loadings in amines due to corrosion problems and amine degradation are major drawbacks. Other technologies have also high-energy requirements limiting their applicability (Table 4.1). The development of more efficient, regenerable CO_2 sorbents is therefore warranted.

Table 4.1 Estimated energy required to remove and recover CO_2 from coal-fired power plant using various technologies[5]

Process	CO_2 removal efficiency (%)	kWh(e)/lb CO_2 recovered
Improved amine absorption/stripping integrated plant	90	0.11
Oxygen/coal-fired power plant	100	0.15
Amine (MEA) absorption/stripping nonintegrated plant	90	0.27
Potassium carbonate absorption/stripping	90	0.32
Molecular sieves adsorption/stripping	90	0.40
Refrigeration	90	0.40
seawater absorption	90	0.80
Membrane separation	90	0.36

A possible way to get around the difficulties encountered by liquid systems is to use solid CO_2 absorption systems, which are either chemical or physical adsorbents. Solid chemical adsorbents include CaO, MgO and hydrotalcites. They are attractive because of their low cost and wide availability from precursors such as limestone and dolomite. However, an acceptable adsorption rate can only be achieved at relatively high temperatures (200 to 500 °C). On the other hand, the desorption step requires even higher temperatures. Stability over repeated absorption/desorption cycles is also an issue.[6]

Physical CO_2 adsorption on solids is based on the ability of porous solids to reversibly adsorb certain components in mixtures. Solids such as silica gel, alumina and activated carbon can have a large pore size distribution. Others, like zeolites have a defined pore size controlled by their crystal structure. At room temperature, zeolite based adsorbents have shown high adsorption capacities for CO_2 (zeolite 13X: 160 mg CO_2/g and zeolite 4A 135 mg CO_2/g at 25°C in pure CO_2).[7] The problem with these adsorbents is the fast decline in adsorption capacities with increasing temperature. The presence of water also decreases drastically their ability to adsorb CO_2. Moreover, as the gases are only physically adsorbed on these adsorbents, the separation factors between different gases (such as CO_2/N_2 mixtures) are low, which makes capture from sources containing low CO_2 concentrations impractical.

For practical applications, sorbents with high selectivity for CO_2, high capacity and easy regeneration are desired. Recently, metal-organic frameworks (MOF) with high CO_2 storage capacity have been reported. MOF are a class of highly porous materials with high surface area. MOF 177 composed of zinc clusters joined by 3,5-benzenetribenzoate units, for example, has a surface area of 4500 m^2/g and a CO_2 storage capacity of about 1.47 g CO_2 per g of MOF at a pressure of 30 atm.[8,9] These MOFs remain, however, costly to produce and a lot of them are also sensitive to moisture.

To achieve a higher selectivity to CO_2 in solid adsorbents, chemical adsorption applied to the solid is also one of the possible pathways. For this, different approaches can be envisioned including: (i) use of solid amines or polyamine directly as adsorbent,[10] (ii) amines or polyamines

chemically bonded to the surface of a solid,[11-15] (iii) amines or polyamines deposited (physical adsorption) on a solid support such as silica or alumina. The latter third option has been to a certain extent studied by several research groups. MEA, widely used in solution systems has been deposited on various supports in an effort to create a solid adsorbent for the removal of CO_2. However, due to the low boiling point (170°C) and associated high volatility of MEA, these solid adsorbents were found to be unstable, releasing considerable amounts of MEA during the regeneration step.[16,17]

The same was observed for DEA deposited on mesoporous silica supports including MCM-41. Despite a reported high CO_2 adsorption capacity (up to 130 mg CO_2 per g sorbent), due to the volatility of DEA under the desorption condition, the effectiveness of this adsorbent was gradually lowered in consequent CO_2 adsorption / desorption cycles (-16.8% after only 5 cycles at a moderate regeneration temperature of 60°C).[18]

To obtain a stable and regenerable solid CO_2 adsorbent, it is therefore important to choose an amine with a sufficiently low volatility to avoid contamination of the gas stream and excessive loss of adsorption capacity over time.

Using polyethylenimine (PEI), a polymeric amine bearing such characteristics, Satyapal et al.[19] described the development of a sorbent based on PEI and polyethyleneglycol (PEG) impregnated on a high surface area poly(methylmethacrylate) polymeric support (code name HSC^+). No details are given about the method of preparation or the exact composition of this adsorbent. This solid is used in the space shuttles to remove CO_2 from the cabin atmosphere and release it into space in a Pressure Swing Adsorption mode (PSA). The reported capacity is approximately 40 mg CO_2/g adsorbent at 50°C and 0.02 atm. of CO_2. Details of such a material and modifications thereof are covered by several U.S. Patents.[20-22] The preferred supports are of polymeric nature, acrylic ester resins such as AMBERLITE® having particularly suitable characteristics.

Xu et al.[23] described the preparation and performances of a solid adsorbent consisting of PEI deposited on the mesoporous MCM-41 characterized as a "molecular basket" adsorbent. CO_2 adsorption capacities for MCM-41-PEI with different loadings in PEI were measured with pure CO_2. The best result was achieved with MCM-41-PEI containing 75 wt. % of PEI with 133 mg CO_2/g sorbent at 75°C. With MCM-41-PEI containing 50 wt. % PEI, the optimal value was obtained at 75°C with 112 mg CO_2/g sorbent. In a subsequent publication, using more solvent during the sorbent preparation step, Xu et al.[24] improved the adsorption to 126 mg CO_2/g with the MCM-41 sorbent containing 50% PEI. At the same temperature, silica gel-PEI containing 50 wt. % PEI adsorbed only 78 mg CO_2/g adsorbent despite the high surface area (550 m^2/g) of the employed silica gel.

In the current DOE-NETL sponsored program it was found that the use of mesoporous material such as MCM-41 and SBA-15 was not necessary to obtain good CO_2 adsorption. Better results were achieved using easy to obtain and widely available fumed or precipitated silica as supports.[25] For effective CO_2 adsorption, the size of the silica particles constituting the support as well as its morphology was found to be of greater importance than the surface area of the support. Furthermore, mesoporous silica is presently not commercially available in large

quantities and first has to be synthesized. Ironically, one of the starting materials used by Xu et al. for the synthesis of MCM-41 is fumed silica. The direct use of fumed or precipitated silica therefore also avoids an additional preparation step.

CO_2 capture with amines impregnated on solid supports

Preparation of silica based sorbents using various amines.

A number of amines, polyamines and polymeric amines were deposited on precipitated silica to assess their suitability to form solid sorbents to capture CO_2. The results are presented in Table 4.2. To avoid excessive release of amine from the sorbent, amines with a relatively high boiling point, in general higher than 200°C, were selected. Molecular structures and boiling points of the considered amines are shown in Figure 4.2.

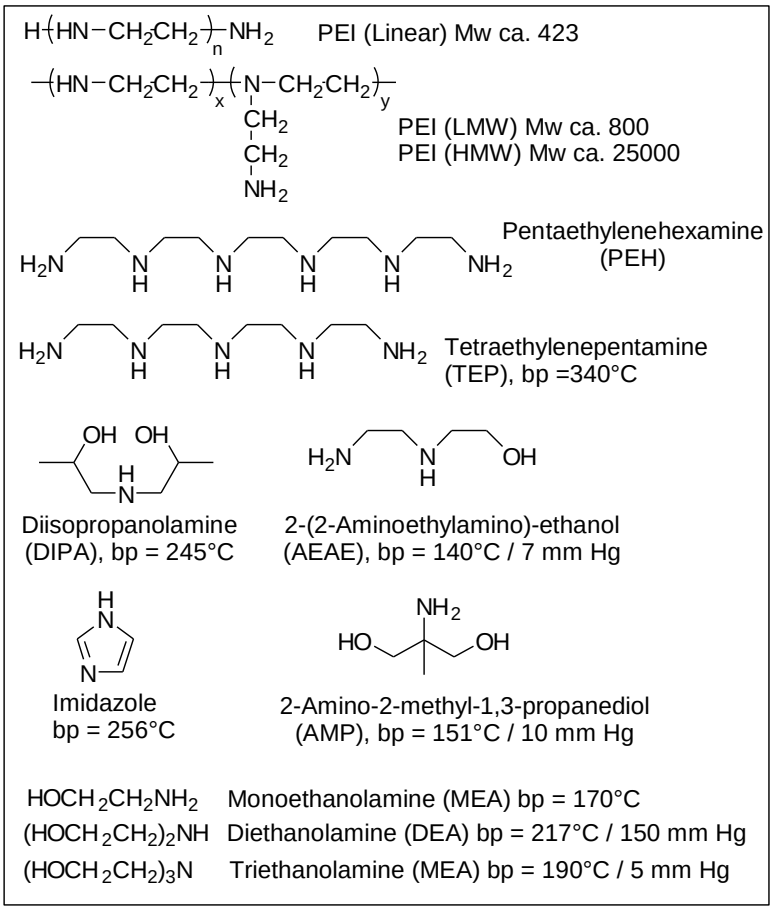

Figure 4.2 Structure of amines deposited on solid supports for CO_2 adsorption.

The data in Table 4.2 indicate that precipitated silica forms powdery products with all the amine selected in sorbents containing 50% amine (1/1 ratio amine/support). With PEI (LMW), PEI (HMW), DEA, TEA, DIPA and AEAE, precipitated silica formed also a powder with an amine/support ratio of 2/1 (the sorbent contains 67% amine). At the same PEI loading, PEI (linear) gave, however, an unsuitable, partly sticky powder. At higher amine concentration,

precipitated silica led only to the formation of sticky solids, for example with the sorbents containing 75% PEI (LMW) and DEA respectively.

Considering the theoretical maximum adsorbable amount of CO_2 (assuming that two amino groups are needed to bind one CO_2 molecule to form a carbamate), for a same amount of amine used, adsorbents containing TEP and PEH should be the ones with the highest CO_2 adsorption capacity with values of 291 and 284 mg CO_2/g for an adsorbent containing 50% amine. They are closely followed by polymeric amines PEI (HMW), PEI (LMW) and PEI (linear) with 256 mg CO_2/g. This is due to the high proportion of amino groups compared to the molecular weight of the amine. Nitrogen represents for example 37% of the molecular mass in TEP, 36% in PEH and about 33% in PEI. Amines with a lower nitrogen content compared to the total molecular weight should have a lower CO_2 adsorption capacity. The lowest CO_2 adsorption should therefore be observed with DEA, DIPA and AMP based adsorbents for which the theoretical maximum CO_2 adsorption capacity is around 100 mg CO_2/ g for an adsorbent containing 50% amine. To determine the actual CO_2 adsorption capacity of these solids, CO_2 adsorption measurements were carried out.

Table 4.2 Comparison of various amines for the preparation of solid adsorbents supported on precipitated silica (HI-SIL T-600)

Amine	Ratio amine / support (by wt.)	mmol amino groups / g solid (calculated)	maximum theoretical adsorbeable amount of CO_2 in mg / g solid adsorbent[a]	Characteristics
PEI (HMW)	1	11.6	256	White powder
PEI (HMW)	2	15.5	341	White powder
PEI (LMW)	1	11.6	256	White powder
PEI (LMW)	2	15.5	341	White powder
PEI (LMW)	3	17.4	384	Yellow, waxy solid
PEI (Linear)	1	11.6	256	White powder
PEI (Linear)	2	15.5	341	White powder
PEH	1	12.9	284	White powder
TEP	1	13.2	291	White powder
MEA	1	8.2	180	White powder
DEA	1	4.8	105	White powder
DEA	2	6.3	139	White powder
DEA	3	7.1	157	Yellow, sticky
TEA	2	4.5	98	White powder
DIPA	2	5.0	110	White powder
AEAE	1	9.6	211	White powder
AEAE	2	12.8	282	White powder
AMP	1	4.8	105	White powder
Imidazole	1	7.4	162	White powder

[a] Based on each CO_2 reacting with 2 amino groups in the amine, polyamine and PEI to form a carbamate under dry conditions.

CO_2 adsorption capacity of solid adsorbents

The prepared solid adsorbents were successfully used for efficient and regenerable CO_2 adsorption. Table 4.3 presents the adsorption capacity in mg CO_2 per g adsorbent of these amines when impregnated in a 1 to 1 ratio on precipitated silica.

Table 4.3 Adsorption of CO_2 on various amine / precipitated silica (1/1) sorbents

Entry	Amine	Adsorption capacity (mg CO_2 / g adsorbent) at 70°C	Stability of the sorbents
1	PEI (HMW)	130	no amine leaching
2	PEI (LMW)	147	minimal amine leaching
3	PEI (Linear)	173	some leaching of the amine
4	PEH	192	some leaching of the amine
5	TEP	200	some leaching of the amine
6	MEA	----[a]	extensive leaching of the amine
7	DEA	113	leaching of the amine
8	TEA	3	no amine leaching
9	DIPA	71	leaching of the amine
10	AEAE	183	leaching of the amine
11	AEAE [b]	230	leaching of the amine
12	AMP	91	sublimes
13	Imidazole [c]	8	sublimes
14	Povidone / PEI (LMW)	61	no amine leaching

[a] No meaningful measurement due to extensive amine leaching. [b] Sorbent having a ratio AEAE / precipitated silica of 2/1. [c] Measured at room temperature.

Shorter chain oligomers of ethyleneimine, tetraethylenepentamine (TEP) and pentaethylenehexamine (PEH) had higher CO_2 adsorption capacities than PEI (linear). Desorption, however, was more difficult and considerable leaching of the amine was also a major drawback for the use of these amines.

Simple amines, DEA, MEA, TEA, AEAE, DIPA, imidazole and AMP even when they formed solid adsorbents when supported on solids, were not suitable because of excessive leaching problems and/or poor CO_2 adsorption.

Adsorbents based on PEI (linear, Mw ca. 423) had high adsorption capacities, but suffered from some leaching problems. PEI (LMW, Mw ca. 800) had a better adsorption capacity than PEI (HMW, Mw ca. 25000). Precipitated silica / PEI (LMW, Mw ca. 800) containing 67% PEI adsorbed up to 200 mg CO_2/g adsorbent. The adsorption capacity increased gradually with

increasing adsorption temperature as can be seen in Figure 4.3. Lower loadings of PEI (LMW) reduced the amount of CO_2 that could be captured, but at the same time increased the efficiency of PEI utilization (Figures 4.4 and 4.5). At lower PEI concentrations, adsorptions in excess of 350 mg CO_2/g PEI were obtained. PEI (LMW) adsorbents had, however, some minimal leaching problems at higher temperature, which did not occur in the case of PEI (HMW). Despite their lower adsorption capacity, solid adsorbents containing PEI (HMW) might therefore be a better choice for CO_2 capture.

Figure 4.6 shows the density of precipitated silica based adsorbents as a function of the concentration in PEI. With increasing PEI content, the density of the adsorbent increases dramatically, from under 0.2 at lower PEI loadings to 0.57 for the sorbent containing 67% PEI. The density of liquid PEI (LMW) itself is 1.05 g/mL. This translates into a higher increase in CO_2 adsorption per mL of adsorbent that would be otherwise expected from the increase in PEI concentration alone (Figure 4.7). The adsorbent containing 67% PEI adsorbs more than three times as much CO_2 per mL than the adsorbent composed of only 33% PEI. Density is of some importance in applications such as in a space vehicle in which the space allocated to the adsorbent is limited. A higher density is also of advantage in most cases as the volume, and thus the size and cost of the CO_2 capture system will be reduced. Due to the enormous volumes of adsorbents that would be necessary for the treatment of flue gases from a large fossil fuel burning power plant, any increase in the density of the adsorbent will be beneficial to reduce infrastructure costs and size.

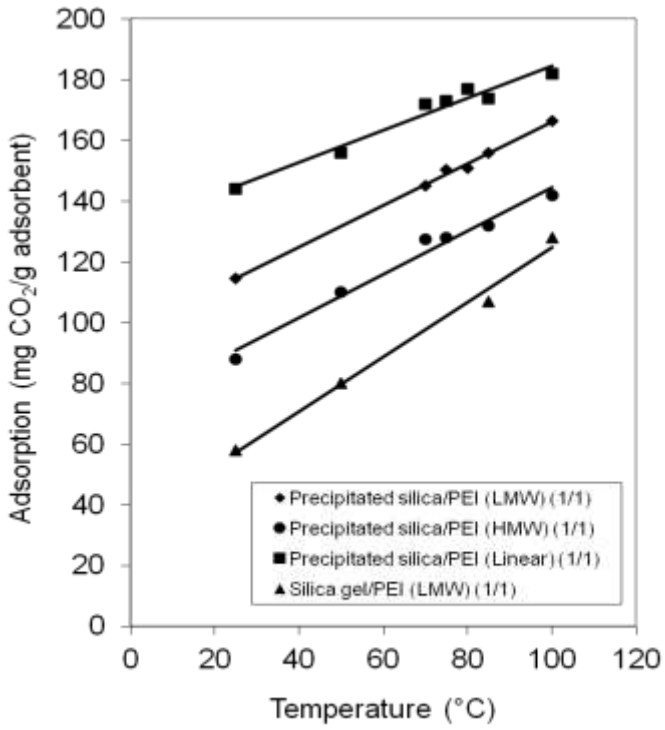

Figure 4.3 CO_2 adsorption in PEI based adsorbents as a function of the temperature.

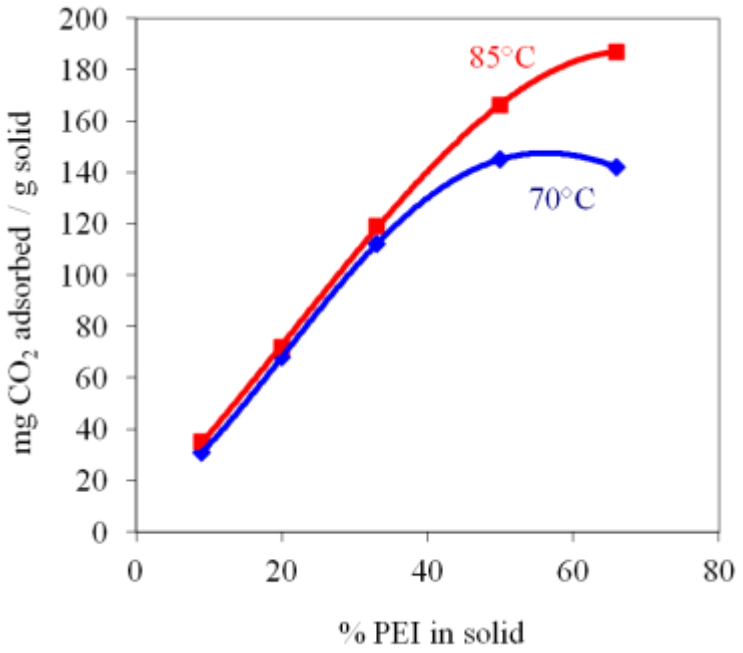

Figure 4.4 Adsorbed CO_2 / g solid as a function of PEI concentration in SiO_2 (HI-SIL T-600) / PEI (LMW) at 70°C and 85°C.

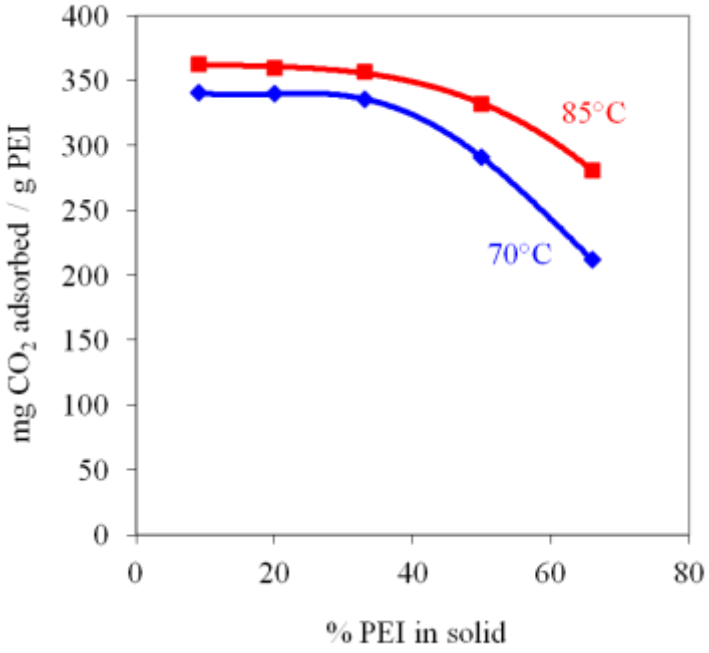

Figure 4.5 Adsorbed CO_2 / g PEI as a function of PEI concentration in SiO_2 (HI-SIL T-600) / PEI (LMW) at 70°C and 85°C.

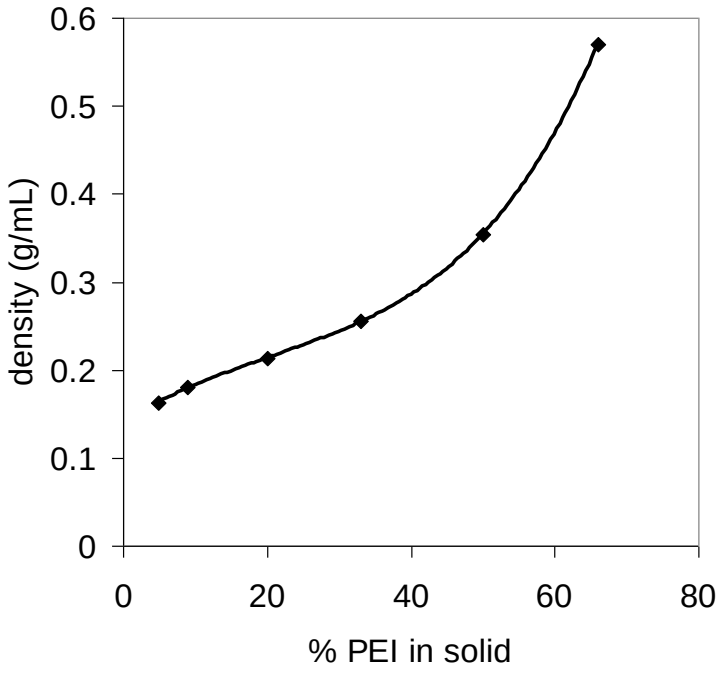

Figure 4.6 Density of SiO_2 (HI-SIL T-600) / PEI (LMW) as a function of PEI concentration.

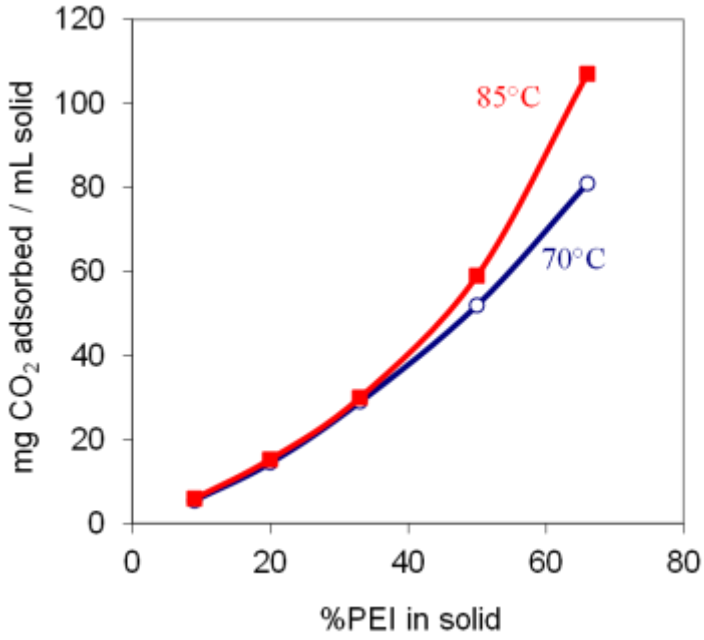

Figure 4.7 Adsorbed CO_2 / mL solid as a function of PEI concentration in SiO_2 (HI-SIL T-600) / PEI (LMW) at 70°C and 85°C.

Effect of the specific surface area of the support

To determine the influence of the surface area and particle size of the support on CO_2 adsorption and desorption characteristics, PEI (LMW) was deposited on different silica supports. The results, presented in Table 4.4, are an average of five consecutive measurements.

Table 4.4 Support/PEI (LMW) (1/1) adsorbents. Influence of the surface area of the support on the adsorption and desorption of CO_2

Adsorbent support	Adsorption capacity at 85°C (mg CO_2/g adsorbent) [a]	Desorption capacity, 1h under vacuum at 85°C (%) [a]	Specific surface area (m^2/g)[b]	Pore volume (cm^3/g)[c]
Fumed SiO_2 (Aldrich)	156	82	344	0.961
Fumed SiO_2 (Aerosil 300)	165	80	276	0.714
Fumed SiO_2 (Aerosil 150)	159	75	145	0.426
Precipitated SiO_2 (Hi-Sil T-600)	160	72	125	0.704
Silica gel	109	61	283	1.094

[a] Average of five consecutive measurements. [b] Measured using the BET method. [c] Determined from the N_2 adsorption isotherm.

It was observed that all the adsorbents based on precipitated silica and fumed silica (Aldrich, Aerosil 150 and Aerosil 300) gave a comparable adsorption around 160 mg CO_2/g. The surface area of these supports, ranging from 125 m^2/g to 344 m^2/g had no observable influence on the adsorption capacity. On the other hand, silica gel, despite having one of the highest surface area and largest measured pore volume, had a much lower adsorption capacity (109 mg CO_2/g). Fumed and precipitated silica have primary particle sizes between ca. 5 and 20 nm. These primary particles can subsequently aggregate to form larger particles. Fumed silica is produced by the vapor-phase hydrolysis of silicon chlorides in a hydrogen-oxygen flame (Figure 4.8). The combustion process creates silicon dioxide molecules that condense to form primary particles. The particles collide, attach and sinter together. The result of these processes is a three-dimensional branched-chain aggregate with sizes between approximately 100 and 400 nm. Once the aggregates cool down, further collisions result in mechanical entanglement of the chains resulting in so-called agglomerates in the µm range. In the case of precipitated silica Hi-Sil T-600, the median particle size of these larger particles is 2 µm. This is much lower than the 74 to 250 µm (60-200 mesh) particle size of silica gel. As mentioned earlier, the particle size of the silica based supports seems to have a greater influence on CO_2 adsorption than its surface area. The mesoporous support MCM-41 used by Xu et al. had also a very high surface area of 1480 m^2/g with a particle size of 5 to 10 µm.[26] The high surface area was the result of the presence of numerous pores with an average pore diameter of 2.75 nm. When loaded with PEI, the PEI was mainly dispersed into these pores and not on the outer surface of the support's particles. The average pore diameter decreased to about 0.4 nm on an adsorbent containing equal amounts of MCM-41 and PEI. CO_2 access to PEI packed into the pores was most probably made more difficult than if PEI was simply dispersed on the surface, explaining the CO_2 adsorption capacity

of only 112 mg / g adsorbent, despite the exceptionally high surface area of the support. The use of mesoporous supports seems therefore to have a rather limited if not negative effect on the CO_2 adsorption capacity, by limiting access to a portion of the PEI. Dispersion of PEI on the more accessible outer surface of the support's particles as obtained on fumed and precipitated silica allows seemingly a more efficient use of PEI. In the case of amines grafted on solid supports such as MCM-41, MCM-48, SBA-15 and others, the morphology of the support was also shown to have a more significant importance than the surface area for CO_2 adsorption properties.[14,15]

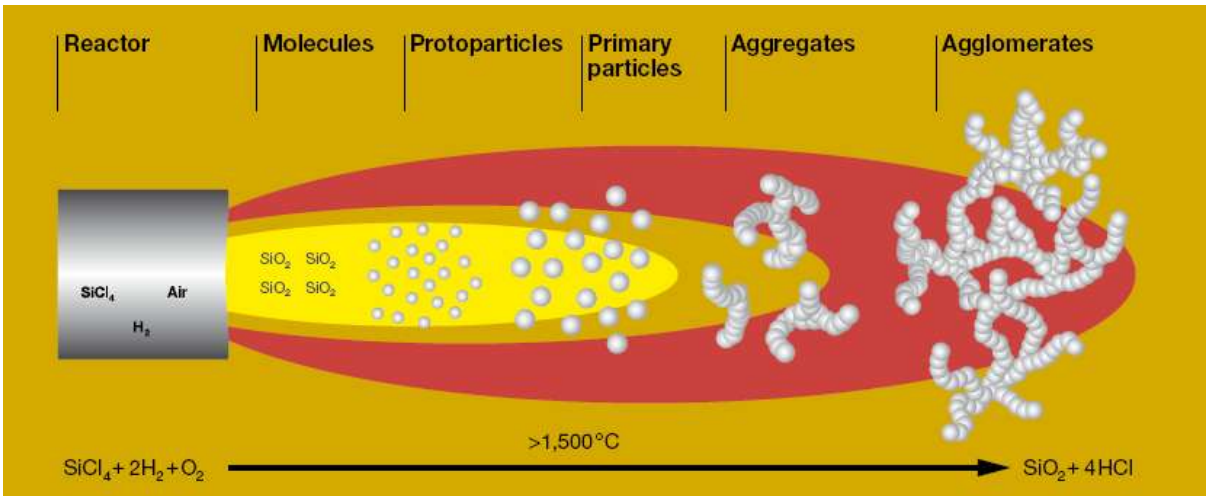

Figure 4.8 Fumed silica synthesis

Fumed silicas used in the present work all exhibited a pseudo type 2 adsorption isotherm (Figures 4.9 and 4.10).[27] In type 2 isotherms, the adsorption and desorption branches are following the same path and there is no plateau in the high P/P_0 region. They are typically obtained in the case of non-porous or macroporous adsorbents.[28] In the case of fumed silica as well as precipitated silica, we have a slight adsorption hysteresis, which is mostly confined to the high P/P_0 region. Silica gel, in contrast, follows a type 4 adsorption isotherm characteristic of mesopores (20 to 500 Å) within the solid. This can be clearly seen in the pore size distribution measured following the BHJ method (Figure 4.11). In the case of silica gel, a relatively well-defined pore size distribution is observed with a maximum at a pore diameter around 125 Å. The cumulative pore volume reaches a plateau after 175 Å, meaning that most of the volume of silica is the result of pores of 175 Å or less (Figure 4.12). Fumed silicas and precipitated silica on the other hand did not show such a clear pore size distribution (Figure 4.11) in the mesopore region. Precipitated silica and Aerosil 150 exhibited a weak maximum at a pore diameter around 175 Å and 120 Å respectively. Aerosil 300 and fumed silica from Aldrich, however showed only a decreasing tendency when moving to higher pore diameters, as reported in the literature.[29] Whereas silica gel reached a plateau, the cumulative volume of fumed silicas and precipitated silica still increased and in most cases more than doubled compared to the volume at a pore diameter of 175 Å. It has also to be noted that the pore volumes measured by the present method for precipitated silica and fumed silicas (from 0.426 to 0.961 cm^3/g, see Table 4.4) is much lower than the real "bulk" volume of these solids. According to the manufacturer (Evonik), fumed silicas have a bulk volume of about 20 cm^3/g (0.05 g/cm^3), meaning that a lot of empty space is present in the solid, most probably in the form of large macropores resulting from the random and loose arrangement of silica aggregates and agglomerates. The measured tapped density of

silica gel was 2.55 cm^3/g. Considering a total pore volume of 1.094 cm^3/g and the density of pure silica of about 2.1 g/cm^3 (0.48 cm^3/g), the space between particles is limited to less than 1 g/cm^3, much lower than in the case of fumed silicas. The presence of large volumes in big mesopores and macropores to which PEI can easily access but still allows facile CO_2 diffusion could in part explain the superior characteristics of fumed silicas as well as precipitated silica as supports for amines.

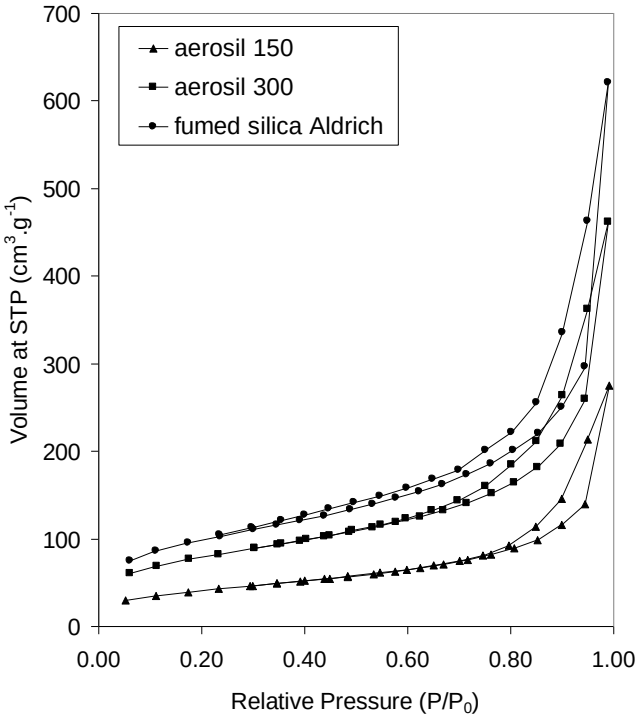

Figure 4.9 N_2 adsorption/desorption isotherm for fumed silicas.

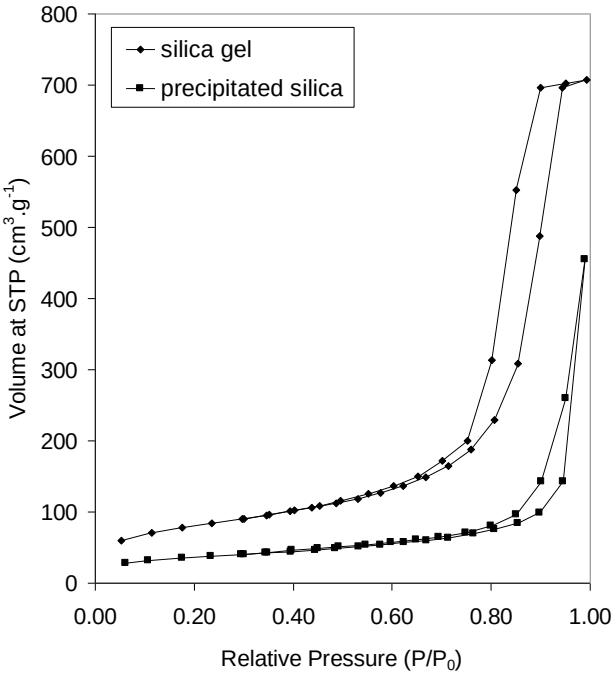

Figure 4.10 N_2 adsorption/desorption isotherm for silica gel and precipitated silica.

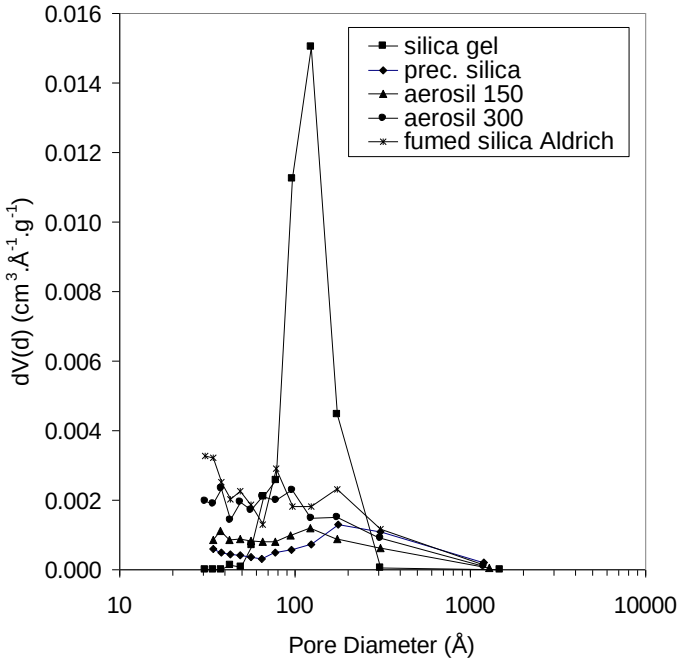

Figure 4.11 Pore size distribution of silica gel, precipitated silica and fumed silicas.

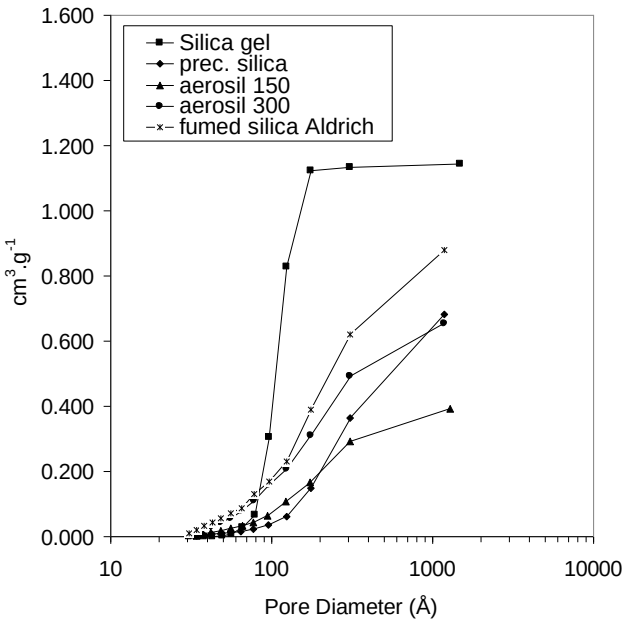

Figure 4.12 Cumulative pore volume as a function of pore diameter of silica gel, precipitated silica and fumed silicas.

After impregnation with PEI (HMW), the pore diameter profile of the fumed alumina based adsorbents was very different. Adsorbents prepared with fumed silica (Aerosil 380) displayed a clear peak at around 350 Å as can be seen in Figure 4.13. Higher loadings in PEI (HMW) in the adsorbent decreased the surface area and pore volume but the pore distribution remained remarkably similar.

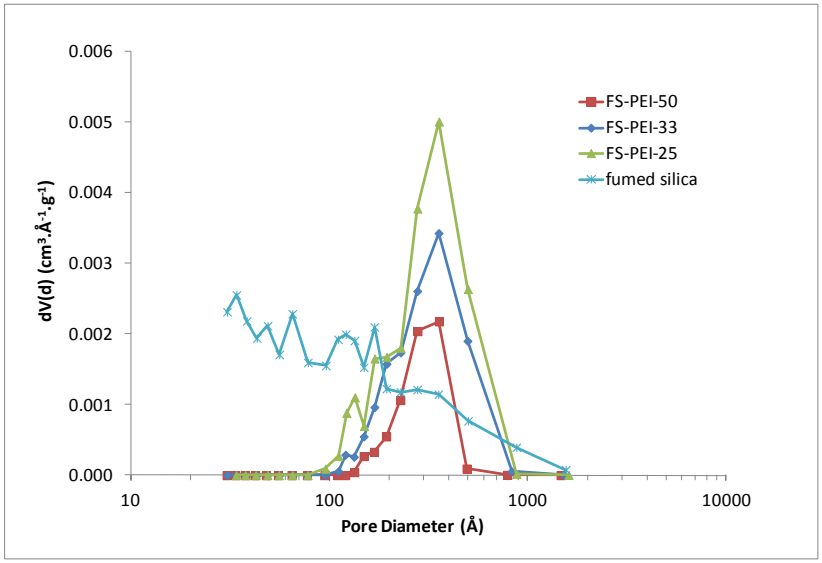

Figure 4.13 Pore size distribution in fumed silica/PEI (HMW) adsorbents with various PEI loadings

The desorption capacity between adsorbents was compared by keeping the sample under vacuum (<1 mm Hg) during one hour at 85°C (Table 4.4). With a longer desorption time, the desorption would have been complete for most samples and relative comparisons would be difficult. Considering CO_2 desorption characteristics, the best supports were found to be the fumed silicas with the highest surface area (Aldrich and Aerosil 300). In one hour, they desorbed around 80% of the adsorbed CO_2. They were followed closely by Aerosil 150 and precipitated silica, which had surface areas of 145 m^2/g and 125 m^2/g, respectively. While higher surface area fumed silica had no effect on CO_2 adsorption, it had, however, a positive influence on CO_2 desorption capacity. The use of fumed silica with high surface area for faster CO_2 desorption could therefore be an advantage compared to the fumed and precipitated silica having a lower surface area. Overall, however, as it was the case for adsorption, the particle size of the support matters more than the actual surface area. This can be verified by silica gel having a very high surface area but composed of larger particle sizes. Silica gel, which had already the worst adsorption capacity studied, showed also the poorest desorption characteristics, with only 61% of the CO_2 desorbed after 1h at 85°C.

Effect of multiple adsorption/desorption cycles

The stability of the adsorbent PEI(HMW)/fumed silica 1/1 was tested over more than 110 adsorption/desorption cycles using the TGA instrument. The test was conducted isothermally at 75°C with an adsorption time of 10 min in a gas mixture containing 85% CO_2 (53 mL/min CO_2 and 10 mL/min N_2) and a desorption time of 15 min under pure nitrogen. At this temperature the adsorbent adsorbed about 125 mg CO_2/g in only 10 minutes. This adsorption capacity remained stable for the duration of the experiment, i.e. 110 cycles (Figure 4.14).

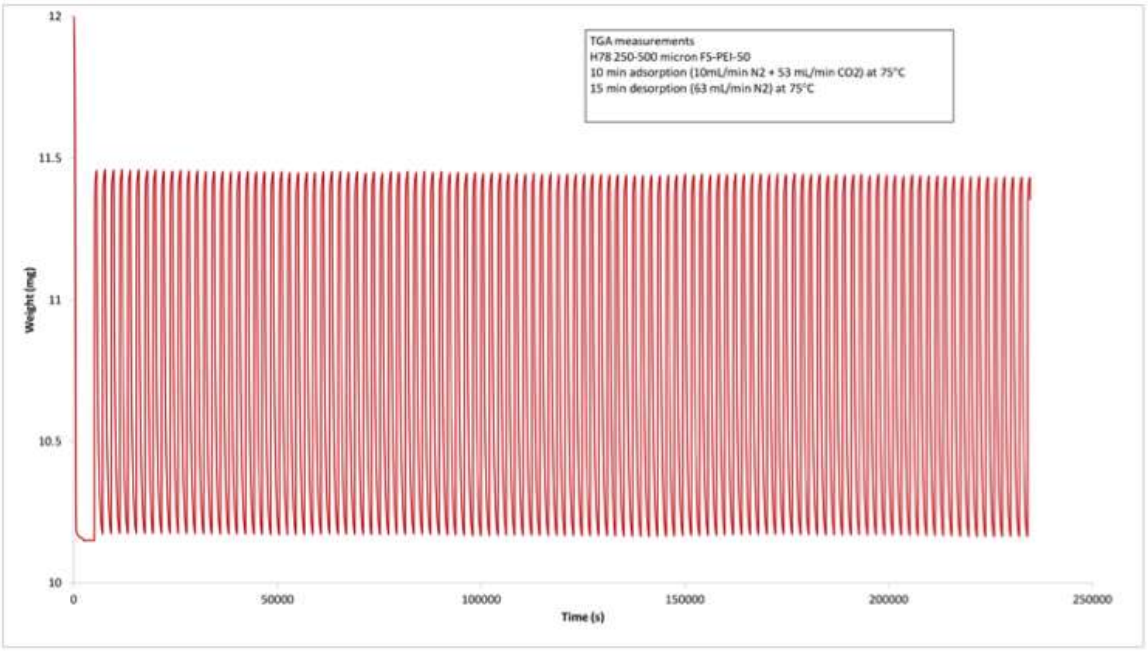

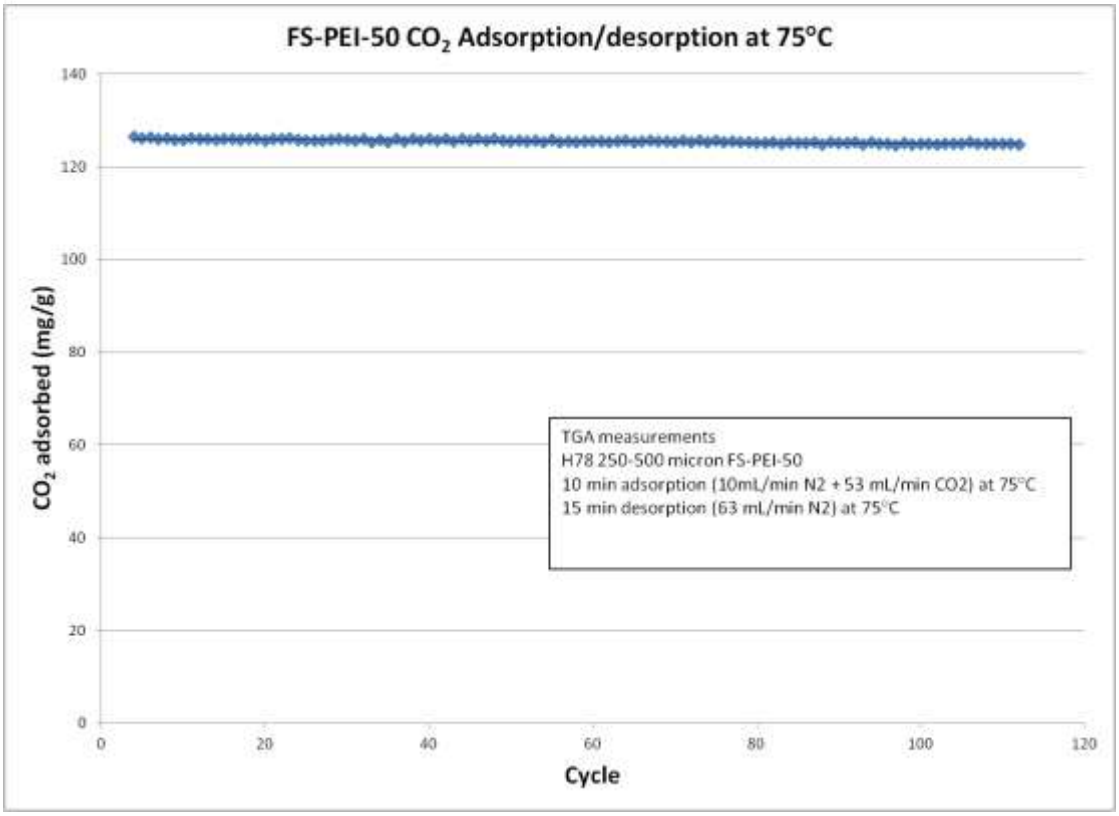

Figure 4.14 CO_2 adsorption/desorption cycles on PEI (HMW)/fumed silica 1/1 at 75 °C

Effect of the addition of PEG on the adsorption and desorption capacity

The addition of PEG (LMW) was found to improve substantially the desorption properties of PEI (LMW) based adsorbents (Table 4.5). The precipitated silica /PEI (LMW) adsorbents containing PEG (HMW) or PEO (entry 5 and 6) led to a comparable adsorption capacity of just under 140 mg CO_2/g and a desorption capacity under 80%. As a comparison, the desorption capacities of these two adsorbents were only slightly higher than the one for precipitated silica / PEI (LMW). On fumed silica / PEI (LMW), it was found that for a same loading in PEG, the sample containing low molecular weight PEG had a slightly higher adsorption than the one containing high molecular weight PEG (entry 2 and 3). The addition of PEG (HMW) did not affect the desorption characteristics of the adsorbent, compared to a sample containing no PEG. Addition of PEG (LMW), however, improved significantly the desorption capacity of the PEI based adsorbent and after one hour under vacuum at 85°C, 98% of CO_2 had been desorbed compared to only 78% with PEG (HMW). The better adsorption and especially desorption characteristics of adsorbents containing low molecular PEG is believed to be the result of the lower viscosity of PEG (LMW) compared to PEG (HMW), which allows CO_2 to access and also detach itself from the active amino groups more easily. It has also been suggested that the presence of hydroxyl groups in PEG could change to some extent the adsorption mechanism by forming bicarbonates.[24]

Table 4.5 Influence of PEG and PEO on the adsorption and desorption of CO_2 on silica/PEI adsorbents

Entry	Adsorbent	Adsorption capacity at 85°C (mg CO_2/g adsorbent)	Desorption capacity, 1h under vacuum at 85°C (%)
1	Fumed SiO_2 / PEI (LMW) (1/1)	156	82
2	Fumed SiO_2 / PEI(LMW) / PEG(LMW) (1/1/0.5)	119	98
3	Fumed SiO_2 / PEI(LMW) / PEG(HMW) (1/1/0.5)	113	78
4	Prec. SiO_2 / PEI(LMW) (1/1)	160	72
5	Prec. SiO_2 / PEI(LMW) / PEG(HMW) (1/1/0.3)	139	79
6	Prec. SiO_2 / PEI(LMW) / PEO (1/1/0.3)	137	77

Influence of the concentration of PEG on the adsorption properties

In a first series of experiments, the compositions using fumed silica were checked with a fixed PEI (HMW) concentration of 45 % and a variable concentration of PEG to determine the best concentration of PEG (Figure 4.15). The highest adsorption was observed at a PEG concentration of 10%. Considering these results, adsorbents with a fixed concentration of PEG of 10% but varying concentrations of PEI (HMW) were tested for their adsorption characteristics (see Figure 4.16). The results led to the conclusion that at room temperature the best composition for optimal CO_2 adsorption is 47.5 % fumed silica, PEI (HMW) 42.5 % and PEG 10 %. Visually, this material was a fluid powder with no tendency for agglomeration and a CO_2 adsorption capacity of about 150 mg/g at room temperature. We called this exact composition "OPAM". Furthermore, the Adsorption Efficiency, i.e. the percentage of total amount of the amine groups utilized in the reaction (see experimental section), was the best at this composition, at about 68 %

(Figures 4.17 and 4.18). As expected, nitrogen, argon, oxygen and/or methane were not adsorbed at all on this material.

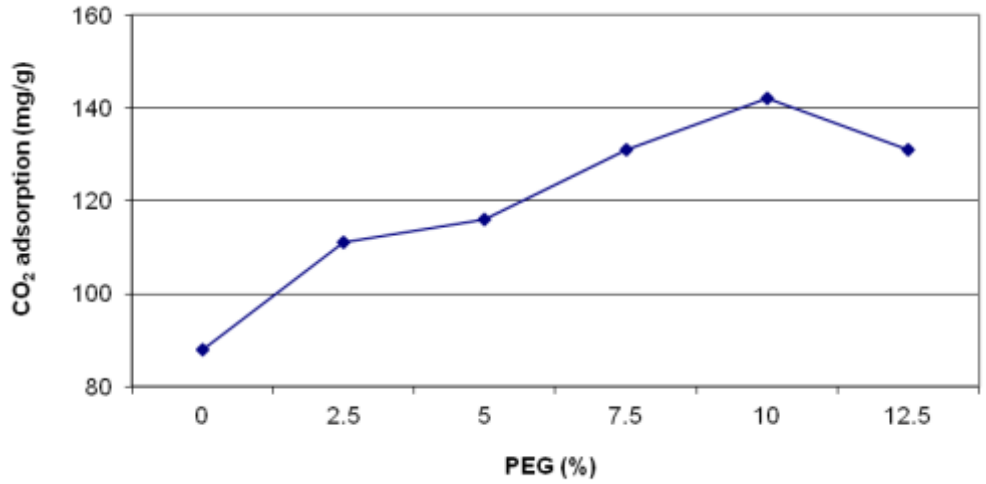

Figure 4.15 CO_2 adsorption as a function of PEG concentration for a material composed of fumed silica, PEI (HMW) (45 % - fixed concentration) and PEG. The tests were carried out using the static procedure at room temperature.

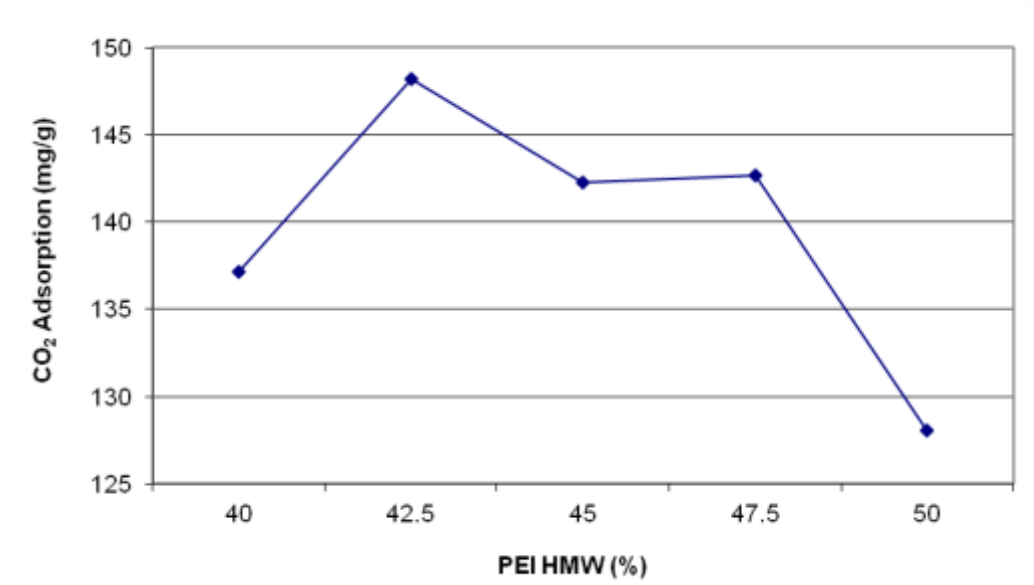

Figure 4.16 CO_2 Adsorption as a function of PEI HMW concentration for a material composed of fumed silica, PEI HMW and PEG (10 % - fixed concentration). The tests were carried out using the static procedure at room temperature.

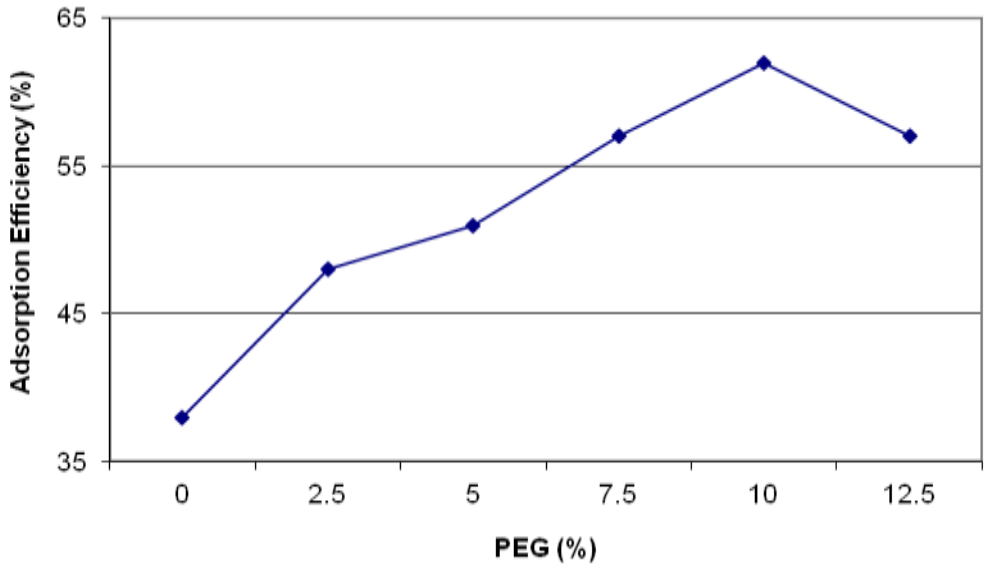

Figure 4.17 Adsorption efficiency as a function of PEG concentration for a material composed of fumed silica, PEI HMW (45 % - fixed concentration) and PEG. The tests were carried out using the static procedure at room temperature.

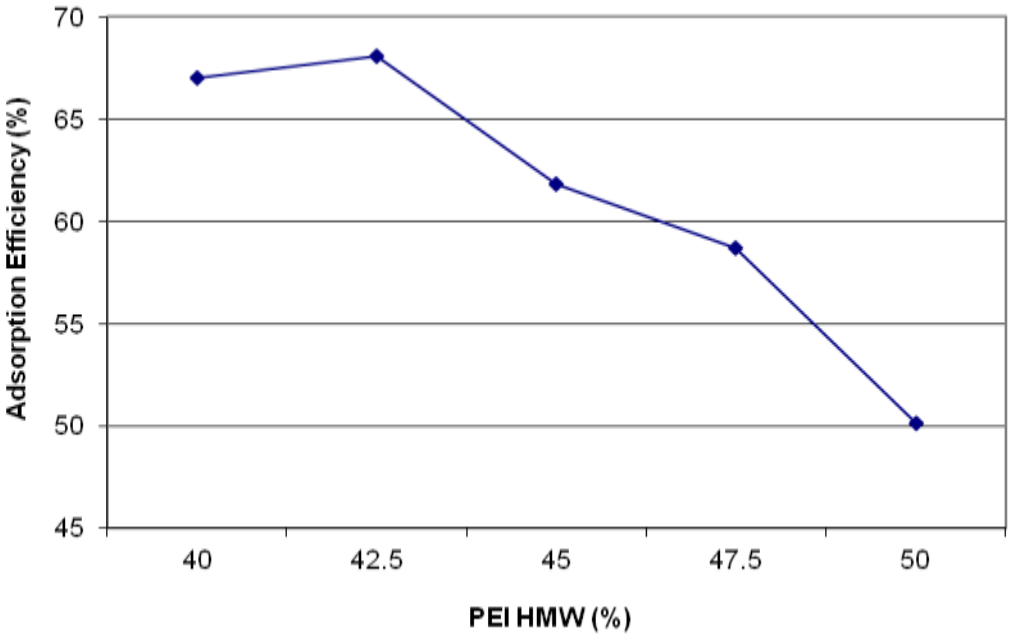

Figure 4.18 Adsorption efficiency as function of PEI HMW concentration for a material composed of fumed silica, PEI HMW and PEG (10 % - fixed concentration). The tests were done using the static procedure at room temperature

When the OPAM composition was checked with precipitated silica, the material obtained was also a dry powder (no apparent stickiness) but with apparently less fluid properties than the

material obtained based on fumed silica. The CO_2 adsorption (room temperature – static test) was also much lower (87 mg/g) than on the similar material prepared with the fumed silica. Since the mechanical properties were also better with fumed silica, the focus was put on the OPAM – fumed silica adsorbent. It is worthwhile to note that better results can be obtained using precipitated silica at different concentrations of PEI and PEG[30] but with slightly inferior fluid properties compared to OPAM – fumed silica.

The material (OPAM – fumed silica) was tested in gas flow conditions consistent with a fluidized bed. About 100 g of OPAM were used in this experiment. It was observed that the adsorbent performed well as a free-flowing solid powder under fluidized bed conditions on a laboratory scale. Initially only N_2 was passed over the adsorbent. When CO_2 was mixed in, it was possible to feel the heat released by the adsorption reaction on the walls of the reactor. There was no agglomeration or other visible negative effects. Through a desorption measurement by TGA it was possible to determine that the maximum amount of CO_2 adsorbed in this way was 134 mg/g, practically the same as in the static test.

The influence of temperature on the adsorption can be seen in the Figures 4.19-4.21. The experiments were carried out using the TGA procedure and CO_2 at a concentration of 10% in nitrogen. With a gas mixture containing 10% CO_2 in nitrogen, OPAM had its highest total adsorption at 50°C with 97 mg CO_2/g (Figure 4.19). Fumed silica: PEI (HMW) in a ratio of 1:1 (FS/PEI) on the other hand showed its highest total adsorption at 80°C with 99 mg CO_2/g (Figure 4.20). This observation is reasonable, since the addition of PEG seems to lower the viscosity of PEI making it more "fluid" and possibly allowing an easier access to the active adsorption sites at lower temperature. This could explain why the highest CO_2 adsorption took place at a lower temperature on the adsorbent to which PEG was added compared to the one containing PEI only. It is also possible to see the effect of the temperature on the adsorption properties. On OPAM, the adsorption peaked at 50°C followed by a decrease due to the equilibrium between adsorption and desorption shifting progressively in favor of the desorption process.

The adsorption rate in the initial period was also determined at different temperatures for both OPAM and FS/PEI. The highest adsorption rate of 7.8 $mg.g^{-1}.min^{-1}$ was obtained with the OPAM material at 50°C (Figure 4.21). This was significantly higher than the maximum rate observed for FS/PEI at 80 °C (4.5 $mg.g^{-1}.min^{-1}$). Higher CO_2 adsorption rates are generally preferable, allowing a faster and more efficient CO_2 capture and possibly enabling to run more adsorption/desorption cycles in a given timeframe. Thus, PEG had a considerable positive effect not only on lowering the temperature for the maximum CO_2 adsorption but also on the adsorption rate. In the case of a rapid adsorption rate, efficient heat management could however become an issue that has to be addressed.

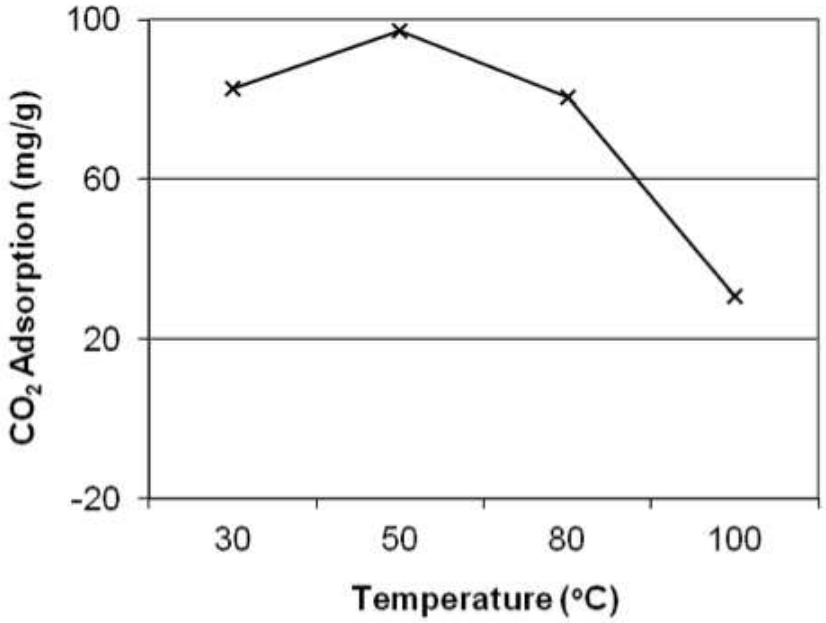

Figure 4.19 Adsorption of CO_2 as function of temperature for OPAM – fumed silica. The tests were carried out using TGA procedure and a stream of nitrogen containing 10 % of CO_2.

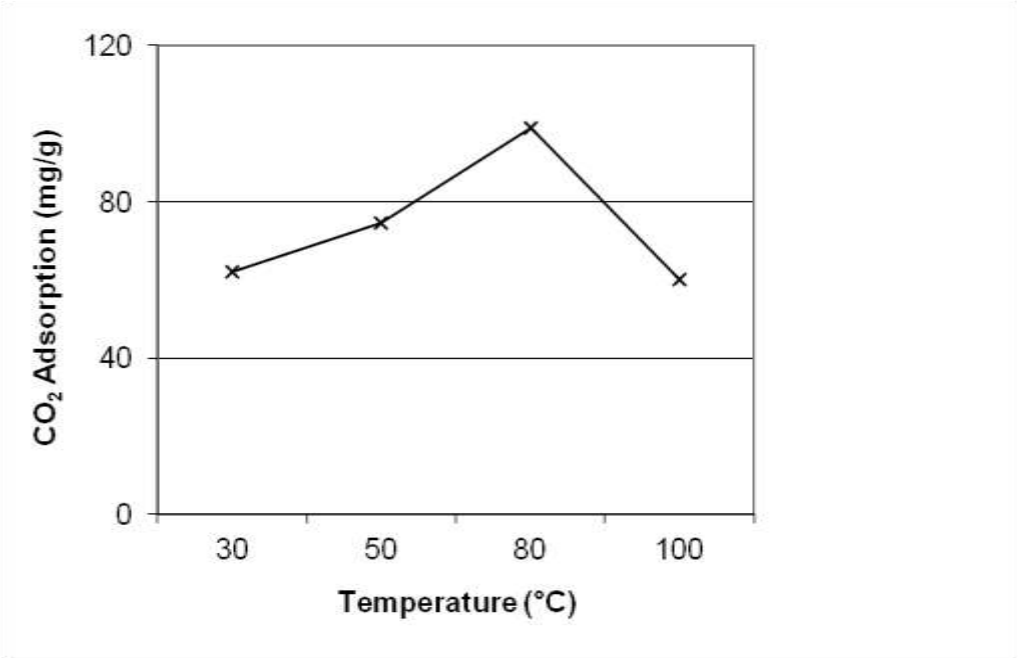

Figure 4.20 Adsorption of CO_2 as function of temperature for fumed silica + PEI HMW (1:1). The tests were carried out using TGA procedure and a stream of nitrogen containing 10 % of CO_2.

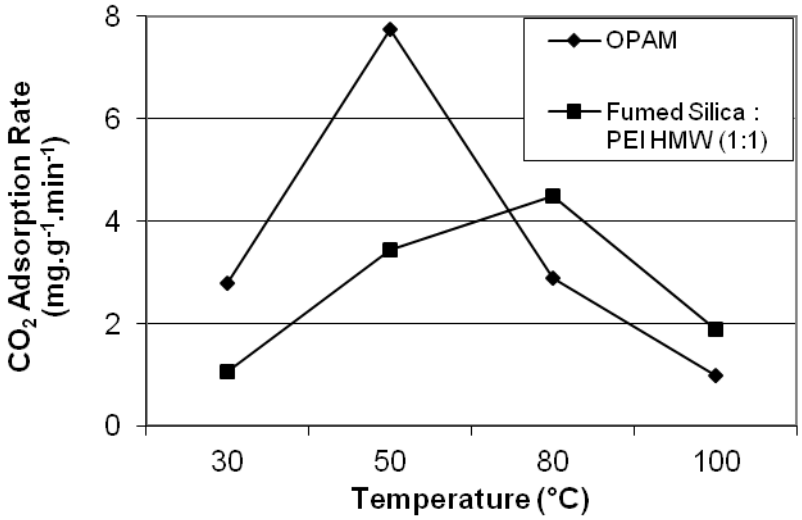

Figure 4.21 CO_2 Adsorption rate as a function of temperature. The tests were carried out using TGA procedure and a stream of nitrogen containing 10 % of CO_2.

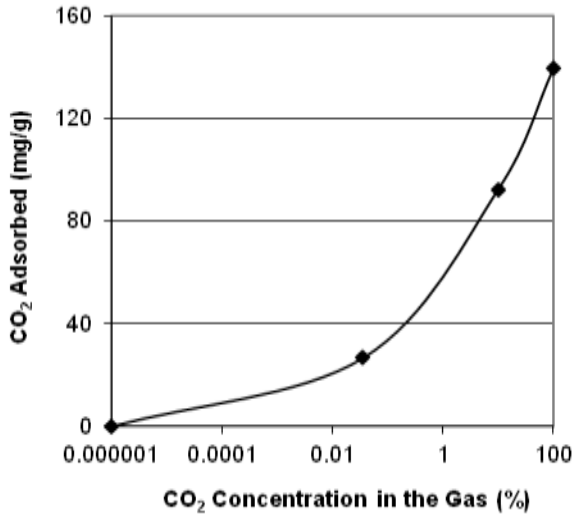

Figure 4.22 CO_2 Adsorbed on OPAM (fumed silica) as a function of the CO_2 concentration in the gas stream (nitrogen) at 50°C. The tests were carried out by TGA.

The effect of the CO_2 concentration on the adsorption capacity was also determined. Gas mixtures with varying concentrations of CO_2 were streamed over OPAM in the TGA apparatus and the weight gain of the adsorbent recorded over time. Figure 4.22 shows the total CO_2 adsorption capacity obtained for these experiments at 50°C. It can be observed that the higher the concentration of CO_2 in the gas, the higher the amount of CO_2 adsorbed. This is logical, since the figure is reflecting the fact of an equilibrium situation between adsorption and desorption. The higher the nitrogen content in the gas mixture, the more the desorption should be favored. It is however important to note that even for a concentration as low as 360 ppm (0.0360% in the figure), close to the one present in the air, the adsorbent could still extract about 30 mg CO_2 per

gram adsorbent from the gas mixture. The adsorption capacity decreased only by a factor of 3.1, when the CO_2 concentration decreased by a factor of 280 from 10% to 360 ppm. This is consistent with results obtained by other research groups under similar conditions.[13,31,32] Thus, one gram of this material could theoretically adsorb the CO_2 contained in about 40 L of air which has presently a CO_2 concentration of about 390 ppm.

In order to ascertain the chemical stability of the material, OPAM was submitted to multiples fast adsorption / desorption measurements cycles using the static procedure. Each cycle included a 10 minutes desorption phase at 110°C under vacuum followed by a 3 minutes adsorption phase at room temperature with pure carbon dioxide. The CO_2 adsorption capacity was determined by the difference in weight between the desorbed and adsorbed states in each cycle. Under these conditions, the CO_2 adsorption capacity of the adsorbent remained almost unchanged between 105 mg/g and 118 mg/g over ten adsorption/desorption cycles and even increased somewhat (Figure 4.23). The CO_2 adsorption rate determined from these values was around 35 to 40 mg $(CO_2).g^{-1}.min^{-1}$.

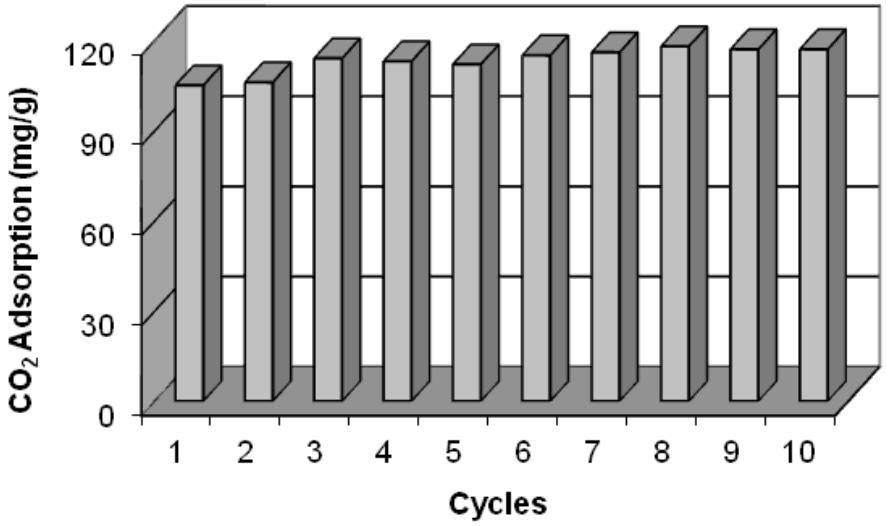

Figure 4.23 OPAM submitted to multiple CO_2 adsorption / desorption cycles using the static procedure (10 minutes for desorption at 110°C and 3 minutes for adsorption at room temperature with pure carbon dioxide).

The effect of the temperature on the desorption kinetics was measured using the static procedure by placing the sample tube in an oil bath under vacuum and waiting for the pressure to drop and stabilize at around 0.30 mmHg. The time to reach this pressure as well as the weight decrease were recorded and used to determine the desorption rate in mg CO_2 per gram sample per minute (mg $(CO_2).g^{-1}.min^{-1}$). As expected, the desorption rate was higher at higher temperatures with 8.16 mg $(CO_2).g^{-1}.min^{-1}$ at 110°C compared to only 5.16 mg $(CO_2).g^{-1}.min^{-1}$ at 80°C.

Pictures taken by SEM (Figure 4.24) show perfectly the differences between the types of silica and the effect of aggregation due to the organic polymers adsorbed on the surface of the nanoparticles. The silica gel appears as a solid material without the particulate nature shown by

the nanosilica. Together with the adsorption results, this is another evidence supporting the findings discussed in our previous paper;[30] namely that for the preparation of PEI impregnated adsorbents the morphology of the support seems to play a more important role than its porosity and surface area. This is reflected in the surface area data (determined by the BET method) reported in Table 4.6, which shows that the surface area of silica gel is practically the same as for fumed silica although the latter was a poor support for PEI. The surface area of fumed silica decreased with successive impregnations with PEG and PEI, probably due to the fact that this adsorbed organic material promotes aggregation between the particles. Since the outside surface area in silica gel is smaller, this aggregation is expressed macroscopically as "gummy" and "sticky" solid. The addition of 10% PEG to fumed silica decreased the surface area by about one third to 194 m^2/g. With the further addition of PEI to obtain the OPAM composition, the surface area decreased dramatically to about 20 m^2/g. The same adsorbent prepared with precipitated silica had a similar surface area (22.7 m^2/g). Interestingly, the adsorption of CO_2 further decreased the surface area of the fumed silica based OPAM adsorbent by about 5 m^2/g.

Pictures taken by TEM with a much higher magnification (see Figure 4.25) confirmed the results obtained by SEM and it was even possible to distinguish the difference in size and in aggregation properties between fumed and precipitated silica (photo B and C, respectively). Precipitated silica had somewhat larger particles than fumed silica as expected from the manufacturing process and supplier information. The aggregation effect of the organic impregnation in fumed silica could also be seen in photo D. Silica gel on the other hand is clearly a more aggregated and compact solid material with a rough surface.

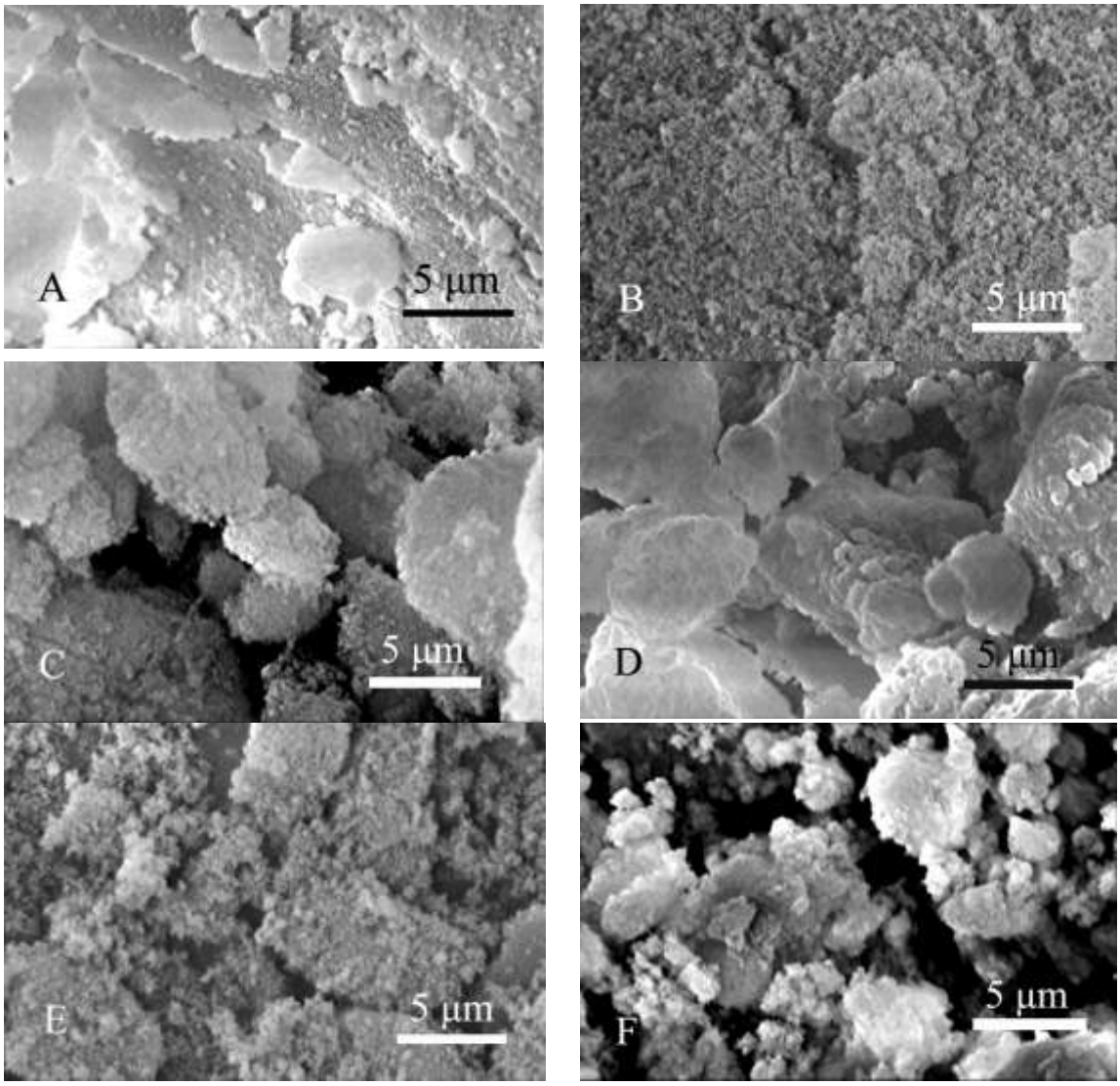

Figure 4.24 SEM (Scanning Electronic Microscopy) of : A – Silica Gel; B – Fumed Silica; C – Fumed Silica + PEG; D – OPAM (Fumed Silica / PEG LMW / PEI HMW); E – Precipitated Silica; F – OPAM Composition using Precipitated Silica as support. All pictures were taken with 5,000x magnification.

Table 4.6 Surface areas of the materials in this study measured by BET.

Material	Surface Area (m^2/g) – BET measurement
Silica Gel	296
Fumed Silica	344
Fumed Silica + PEG (10%)	194
OPAM (fumed silica) before CO_2 adsorption	20.0
OPAM (fumed silica) after CO_2 adsorption	15.4
Precipitated silica	124
OPAM (precipitated silica) before CO_2 adsorption	22.7

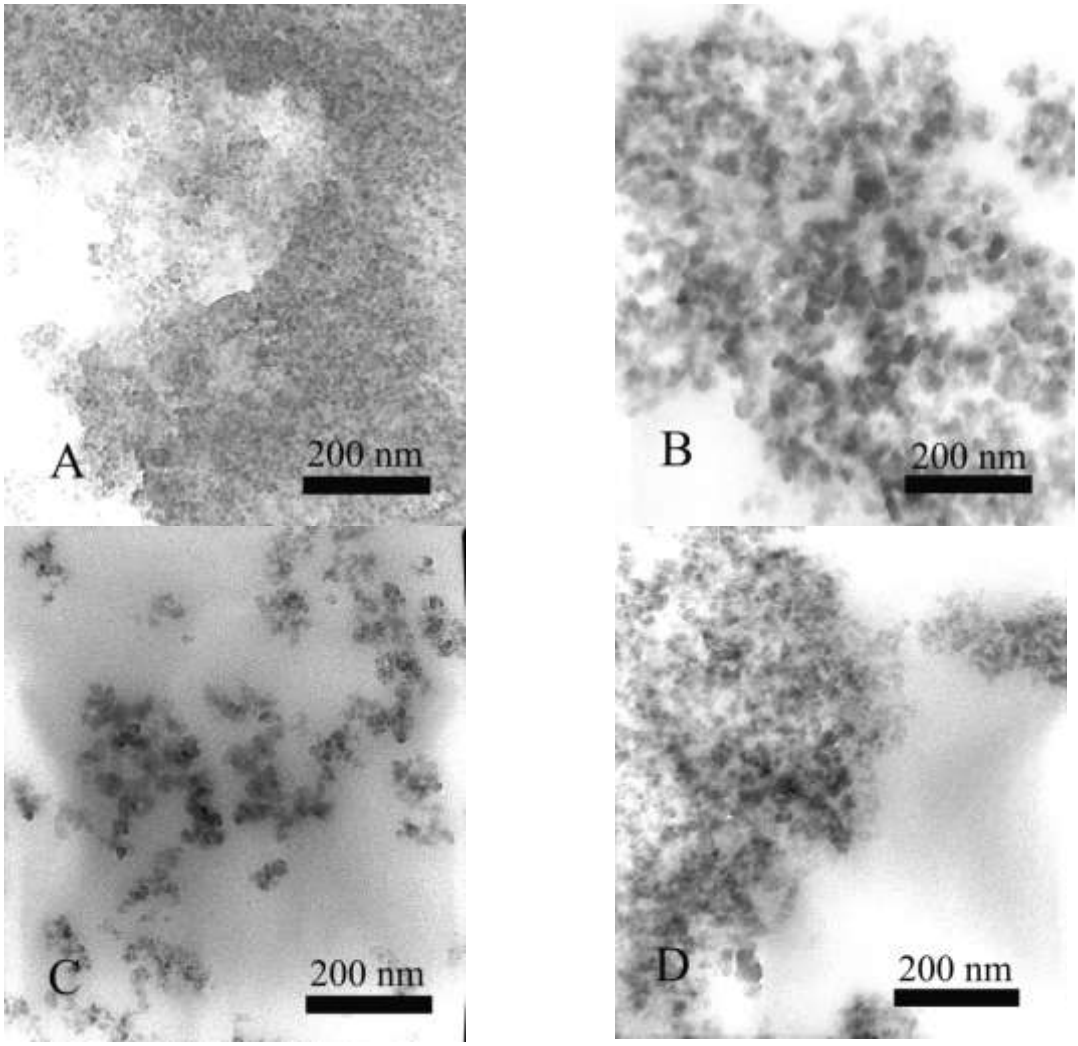

Figure 4.25 TEM (Transmission Electronic Microscopy) of: A – Silica Gel; B – Precipitated Silica; C – Fumed Silica; D – OPAM (Fumed Silica / PEG LMW / PEI HMW. All pictures were taken with 105,000x magnification.

CO_2 capture from the air

The capture of CO_2 from concentrated industrial streams such as exhaust gases of coal burning power plants, cement or aluminum factories and fermentation plants has gained a lot of attention and has been well described in recent publications.[33-37] While about half of the anthropogenic CO_2 emissions are the result of large industrial sources such as power plants and cement factories, the other half originate from small distributed sources such as cars, home heating and cooking.[38] For those, CO_2 capture at the emission source is not practical and/or economical. A possible pathway to deal with these emissions is to capture CO_2 directly from the air. One of the advantages of CO_2 capture from the atmosphere is that the needed infrastructure can be placed anywhere, preferably where it has the least impact on the environment and human activities or close to CO_2 recycling centers. CO_2 capture from the air and recycling into fuels and products constitutes an anthropogenic version of nature's photosynthetic cycle.[39] It offers a long term, post-fossil fuel solution to fulfill humankind's needs for fuels, hydrocarbons, polymers and other products presently derived mostly from petroleum oil and natural gas. CO_2 is not an unwanted combustion byproduct but should be considered as a valuable feedstock for the production of fuels and materials.[40-42]

CO_2 capture from the air has not been studied extensively and data on this subject is still limited. Practical applications have been developed for the essential removal of CO_2 from submarines and spacecrafts.[19,43] However, the separation and recovery of CO_2 from ambient air on a larger scale is still in its infancy and has only relatively recently attracted increased interest.[44] Adsorbents based on $Ca(OH)_2$,[45] NaOH,[46-50] and combination thereof have been suggested but their regeneration is generally energy intensive. Amine and polyamine based sorbents either chemically bound[14,15,51-54] or physically adsorbed[23,24,26,55-57] on a supports such as silica, mesoporous solids (MCM-41, MCM-48, SBA-15) and carbon fibers have also been proposed and in some cases tested for CO_2 capture from the air.[13,32,58] More recently hyperbranched aminosilicas (HAS) prepared by in-situ aziridine polymerization on porous solids have been reported as adsorbents for CO_2 capture from the air.[31,59]

Polymeric amines and polyethylenimines (PEI) have attracted much attention. Following our study on PEI impregnated on fumed silica and precipitated silica,[60] we present herein our work on the properties of a silica-organic hybrid adsorbents for CO_2 capture from the air.

Measurement of CO_2 adsorption and desorption capacity

Data were obtained using an all-glass grease free flow system built especially for the study of CO_2 adsorption from the air, using parts, instruments and materials available in our laboratory (see Figure 4.26). The adsorbent was placed in a U-tube between two glass wool plugs and air passed through it at a given flow rate and temperature.

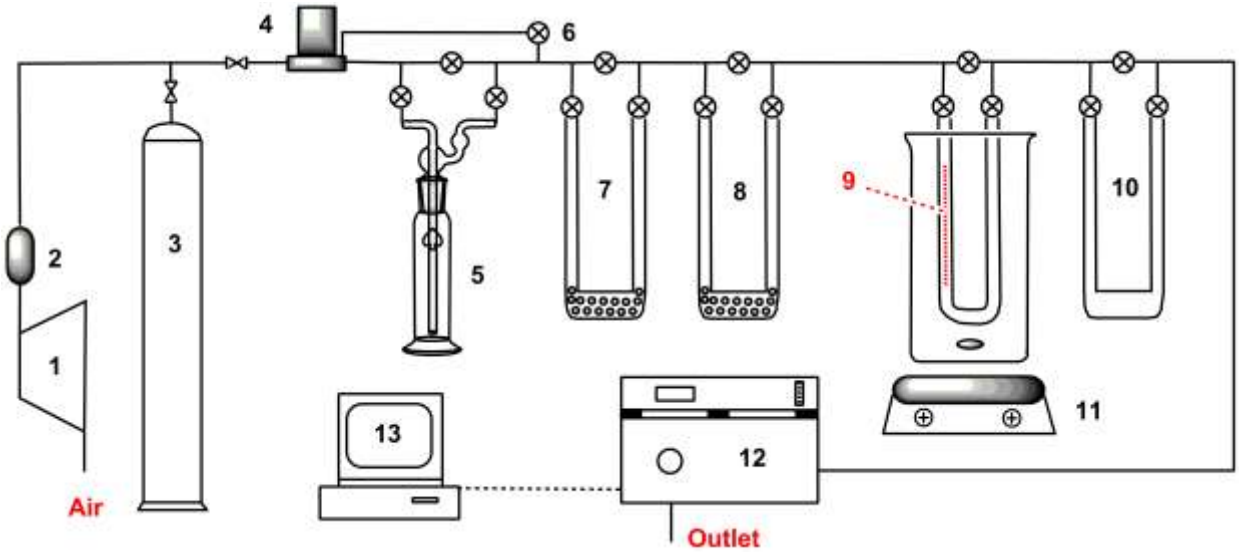

1. Compressor
2. Air dryer (silica gel)
3.Reservoir
4.Mass flow controller
5.Humidifier
6.Dry air inlet
7.Water droplet separator I.
8. Water droplet separator II
9. Adsorbent
10. Particle separator
11. Stirrer and oil bath
12. Horiba CO_2 analyzer
13. Computer

Figure 4.26 Schematic diagram of the bench-top test system for CO_2 adsorption studies

For the initial experiments, branched PEI with a high molecular weight (M_w=25000) was selected as adsorbent material in large part because of its very low volatility. Samples with PEI loadings of 33 wt% and 50 wt% were prepared and labeled as FS-PEI-33 and FS-PEI-50, respectively.

Figure 4.27 represents the results obtained for the CO_2 adsorption at 25 ºC on FS-PEI-50. The first segment of the curve shows the CO_2 concentration of the air when the adsorbent was bypassed (420 ppm). After opening of the flow to the adsorbent, complete adsorption of CO_2 was observed with CO_2 concentration close to 0 ppm. After this initial adsorption period the adsorbent started to get saturated and a slow increase in CO_2 concentration in the outlet gas was observed until complete saturation. From 0.6 h to 7.1 h, when the outlet gas was practically CO_2 free, 2.39 mmol CO_2 were removed from the air. An additional 2.25 mmol of CO_2 were adsorbed during the partial CO_2 removal period until complete saturation. A total of 4.64 mmol CO_2 were thus adsorbed from ambient air by 2.72 g of adsorbent, representing 1.71 mmol CO_2 per g or 75 mg CO_2 per g of adsorbent.

To test the regenerability of the FS-PEI-50 adsorbent previously used for CO_2 adsorption from air was heated under vacuum at 85 ºC for 3 hours combining pressure and temperature swings. The adsorbent was then used again for CO_2 adsorption from the air. These adsorption/desorption cycles were repeated four times with no appreciable decrease in adsorption

capacity. The total CO_2 adsorption capacity varied from 73 to 75 mg CO_2/g adsorbent (1.65 to 1.71 mmol/g). At the same time, between 34.7 and 38.6 mg CO_2/g were adsorbed during the initial period, where complete CO_2 adsorption from the air was observed.

On FS-PEI-33, the adsorption under dry condition was expectedly lower at 52 mg/g (see Table 7 and Figure 4.28). Humidity had a substantial promoting effect on the CO_2 adsorption on FS-PEI-33. Using this adsorbent, an adsorption of 78 mg CO_2/g could be achieved at a relative humidity of 67%. This represents 1.74 mmol CO_2/g. Interestingly, under humid conditions, FS-PEI-50 which contained more PEI adsorbed less CO_2 (62 mg CO_2/g).

The adsorption of CO_2 from air using FS-PEI-50 at various temperatures showed that an optimal CO_2 adsorption capacity was achieved below 45°C (Figure 4.29). At higher temperature, the adsorption capacity decreased rapidly until reaching almost zero at 85°C.

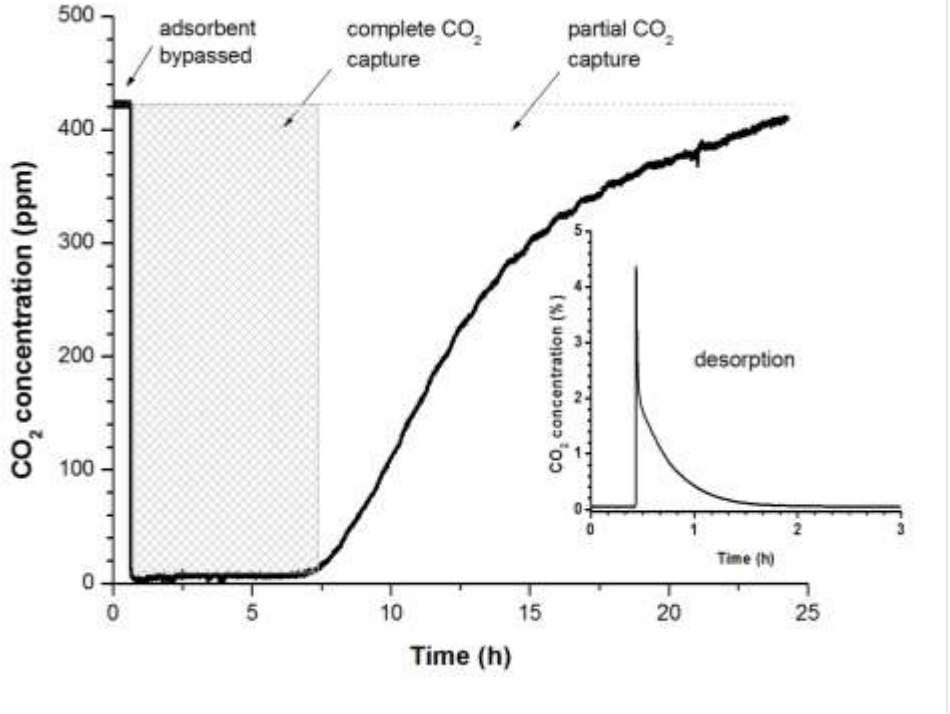

Figure 4.27 Adsorption of CO_2 from the air at 25 °C on FS-PEI-50. Inset: Desorption at 85 °C

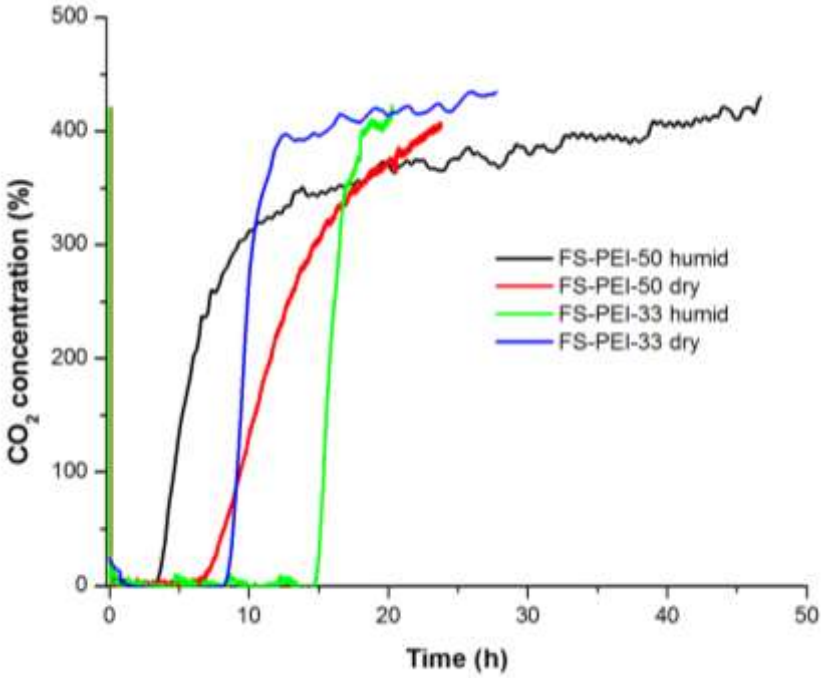

Figure 4.28 Adsorption of CO_2 from the air at 25 °C on FS-PEI-50 and FS-PEI-33 under dry and humid conditions.

Table 4.7 Properties of PEI (HMW)/fumed silica based adsorbents

PEI content in FS-PEI (%)	Surface area (m^2/g)	Volume of pores (cm^3/g)	CO_2 Adsorption from air (mg/g)	
			Dry condition	Humid condition
0	344	0.961	---[a]	---[a]
33	79.9	1.057	52	78
50	27.2	0.401	75	62

[a] Negligible

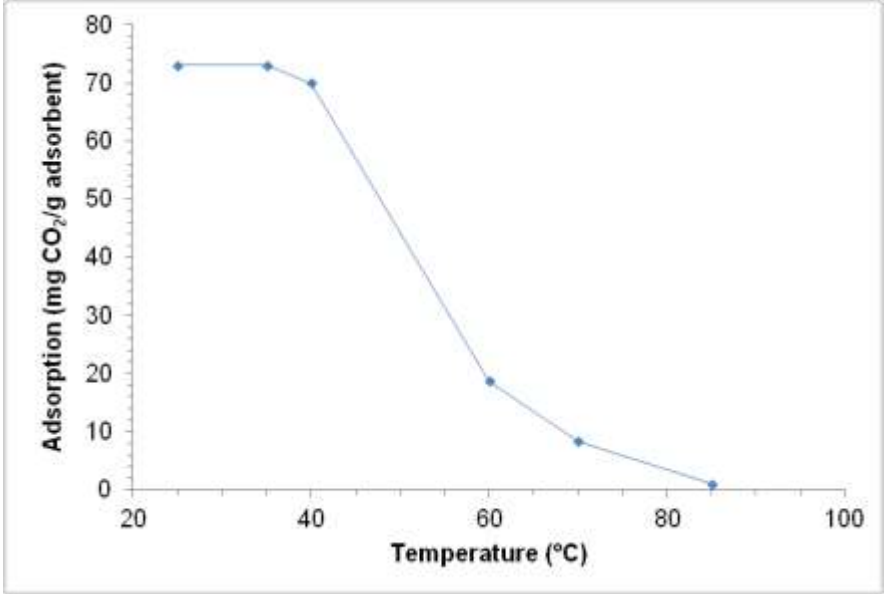

Figure 4.29 Adsorption as a function of temperature on FS-PEI-50 (250-500 micrometer, H78, particle size mix) (Air mix from the atmosphere)

Effect of the molecular weight of PEI on the adsorption

PEI with molecular weights from 423 to 25000 impregnated on fumed silica were tested for their capacity to adsorb CO_2 from the air. Adsorbents with PEI loadings of 33 and 50% were investigated. In all the cases, adsorbents with a size of 0.25-0.50 mm were used. All the PEIs in this study were branched except for PEI(423) which was linear. The results are presented in Figure 4.30 and Table 4.8. The adsorption characteristics of PEI(423) and PEI(800) were very similar at a PEI loading of 33%. Their adsorption capacities (72-75 mg CO_2/g) were, however, significantly higher than the adsorbents containing PEI(1800) and PEI(25000) with 50 and 56 mg CO_2/g, respectively. The initial adsorption capacity before breakthrough followed the same order as the PEI M_w, i.e. increasing from PEI(800) to PEI (25000). At a higher PEI loading of 50%, the highest adsorption capacity was also obtained with PEI (800) at 107 mg CO_2/g (2.4 mmol CO_2/g). FS-PEI(423)-50 with a lower M_w PEI had a slightly lower adsorption capacity but was still noticeably higher than on the adsorbents with higher M_w PEI of 1800 and 25000 which had a very similar total CO_2 adsorption capacity (~74 mg CO_2/g). At a PEI loading of 50%, the initial adsorption capacity before breakthrough did not follow a clear trend. The initial adsorption capacity of FS-PEI(800)-50 with about 76 mg CO_2/g was significantly higher than the one for FS-PEI(25000)-50 and FS-PEI(1800)-50. As a general trend, the use of PEI with lower molecular weight offers advantages in terms of both total adsorption capacity and initial adsorption capacity. However, as already pointed out, *vide supra*, lower molecular weight PEI can be more prone to leaching leading to a loss of capacity overtime, negating the initial positive effect gained by using them in adsorbent formulations.

Compared to other solid adsorbents based on PEI and different supports reported in the literature, FS-PEI adsorbents exhibited some of the highest CO_2 adsorption capacities from air. With PEI 800, the most commonly used PEI for these studies, the highest adsorption capacity, 107.3 mg CO_2 per g of adsorbent, was obtained with adsorbent based on fumed silica. The fact

that fumed silica is also easily available in large quantities from a variety of suppliers for a relatively low cost and that the preparation of the adsorbent is extremely easy and straightforward is also an added advantage.

Table 4.8 Effect of PEI molecular weight on the adsorption of CO_2 from the air.

Adsorbent	*total CO_2 adsorption from air (mg/g)*	*CO_2 adsorption from air under 10 ppm(mg/g)*
FS-PEI(423)-33	71.9	59.8
FS-PEI(800)-33	74.7	62.7
FS-PEI(1800)-33	56.0	48.0
FS-PEI(25000)-33	50.0	40.8
FS-PEI(423)-50	103.0	64.1
FS-PEI(800)-50	107.3	75.9
FS-PEI(1800)-50	74.6	42.5
FS-PEI(25000)-50	73.7	51.8

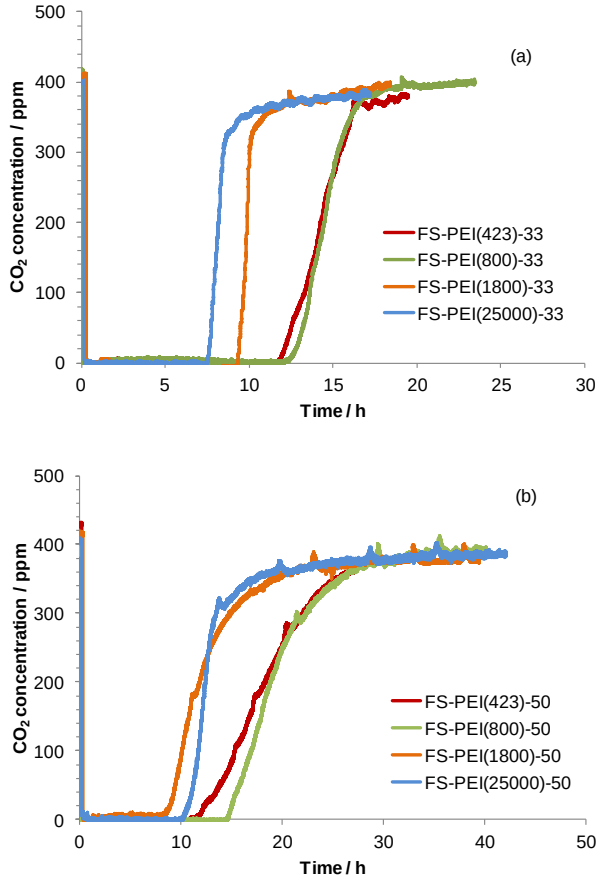

Figure 4.30 Effect of PEI molecular weight on CO_2 adsorption from the air. (a) On FS-PEI(x)-33 (0.25-0.50 mm). (b) On FS-PEI(x)-50 (0.25-0.50 mm).

Heat (reaction enthalpy) of adsorption and desorption of CO_2 on PEI/Nanosilica

The heat of adsorption and desorption of CO_2 on PEI based adsorbents were measured using Differential Scanning Calorimetry (DSC). The instrument used was a Perkin Elmer DSC 7. Figure 4.31 shows a typical heat of adsorption graph obtained for the adsorption of CO_2 at 85°C. After the adsorption was completed, heat of the desorption of the same sample was measured by heating the sample from 0°C to 140°C under nitrogen.

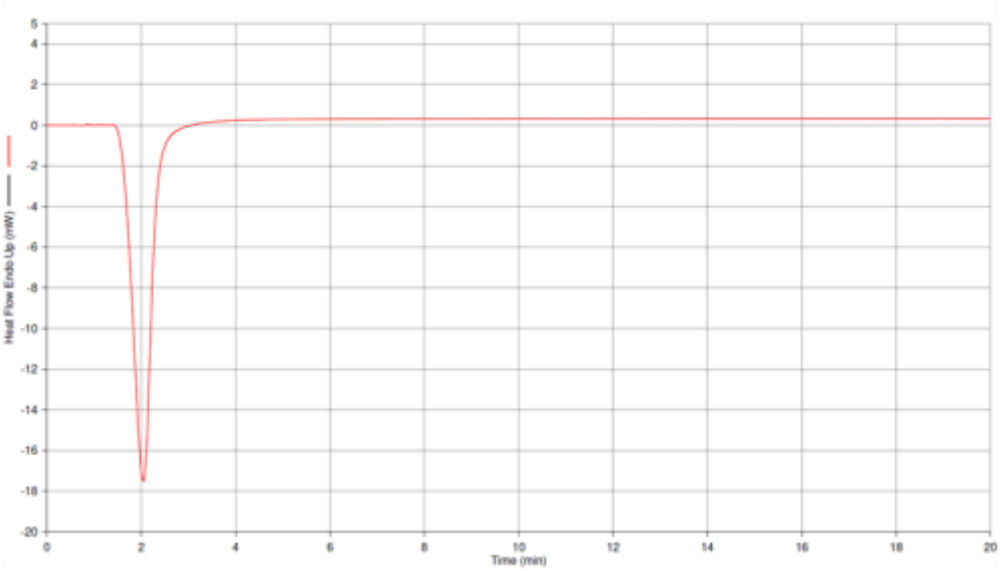

Figure 4.31 Typical heat of adsorption graph obtained on the Perkin Elmer DSC 7

According to these measurements, the heat (enthalpy) of adsorption for FS-PEI-50 was determined to be -83 kJ/mol CO_2, whereas the enthalpy for desorption was 82 kJ/mol CO_2. These values are an average of 5 measurements. The enthalpy of adsorption and desorption on FS-PEI-33 were -85 and 87 kJ/mol CO_2, respectively. For both adsorbents the results obtained for the adsorption are in good correlation with the ones obtained for the desorption and are within the experimental error. These values are consistent with the reaction of an amine with CO_2. Monoethanolamine (MEA) has a heat of adsorption around -85 kJ/mol, diethanolamine (DEA) about -72 kJ/mol. Tertiary amine, triethanolamine, which forms much weaker bonds with CO_2 has a heat of adsorption of -48 kJ/mol. These values are also close to the ones obtained by Satyapal et al. on a PEI bonded on a high-surface-area solid polymethyl metacrylate polymeric support. The measurements of the heat of adsorption of CO_2 on this adsorbent was -94 kJ/mol; about 10 kJ/mol higher than the values that were obtained.

In the desorption of CO_2 from aqueous solutions of alkanolamines, it is necessary to heat the MEA solution as a whole to around 110°C. This requires a desorption heat of about 1800 cal / g CO_2 (330 kJ/mol CO_2), considering an aqueous solution of 20 % MEA and an adsorption of 0.4 mol of CO_2 for 1 mol of MEA. This value has been estimated using thermodynamic data from the literature. The nanosilica supported material needs less energy for the desorption step because it is composed of organics and SiO_2, which have a lower heat capacity when compared to water at about 0.5 – 0.6 $cal.g^{-1}.°C^{-1}$ for the organics and 0.23 $cal.g^{-1}.°C^{-1}$ for silica compared to 1 $cal.g^{-1}.°C^{-1}$ for water. Consequently, to heat FS-PEI-50 from 25°C to 110°C, about 34.5 cal/g

are needed. If an adsorption rate of 100 mg CO_2/g adsorbent is assumed, 10g of adsorbent would be needed to capture 1 g of CO_2. About 460 cal/g (85 kJ/mol) are needed to desorb 1 g of CO_2. This means that about 34.5 x 10 + 460 = 805 cal are required to heat the adsorbent to 110°C and desorb 1g of CO_2. According to these calculations, this is only about half what is needed for aqueous MEA based systems.

The heat of adsorption of adsorbents based on PEI with lower molecular weights were not measured. However, the results are not expected to be significantly different from the ones obtained with PEI (HMW) as the basic structure of these polyamines is the same.

CO_2 adsorption isotherms

The adsorption of CO_2 as a function of the CO_2 partial pressure in the gas phase was determined for FS-PEI-50 and FS-PEI-33. For these experiments, gases with CO_2 concentrations varying between 400 ppm and 100% were used. The results obtained for FS-PEI-50 and FS-PEI-33 at 25°C are presented in Figure 4.32. It can be seen that despite the higher PEI concentration of FS-PEI-50, the CO_2 adsorption over the entire range was only slightly higher than on FS-PEI-33. On FS-PEI-33, the CO_2 adsorption increased from about 52 mg/g at 400 ppm to 95 mg/g at 100% CO_2, i.e. a less than two-fold increase. This difference in adsorption capacity between 400 ppm and 100% CO_2 was surprisingly small considering the 2500 fold increase in CO_2 concentration in the gas feed. A similar effect was observed on FS-PEI-50.

While it was shown that the adsorption of pure CO_2 is increasing with increasing temperatures (up to 100°C, see Figure 4.3), the adsorption at very low CO_2 concentrations is expected to decrease. The difference in adsorption between 400 ppm and 100% CO_2 is therefore expected to be larger with increasing temperature. Figure 4.33 shows the CO_2 adsorption at 50 °C obtained on an adsorbent containing 42.5% PEI (HMW) and 10% PEG on fumed silica. From a CO_2 adsorption of 140 mg/g at 100% CO_2 the adsorption decreased to about 30 mg/g at 370 ppm, a decrease of almost 80%. Individual measurements of CO_2 adsorption from the air as a function of the temperature on FS-PEI-50 also confirm this trend. From 75 mg/g at 25°C the CO_2 adsorption decreased to 70, 19, 8, and 1 mg/g at 40, 60, 70 and 85°C, respectively (Figure 4.29).

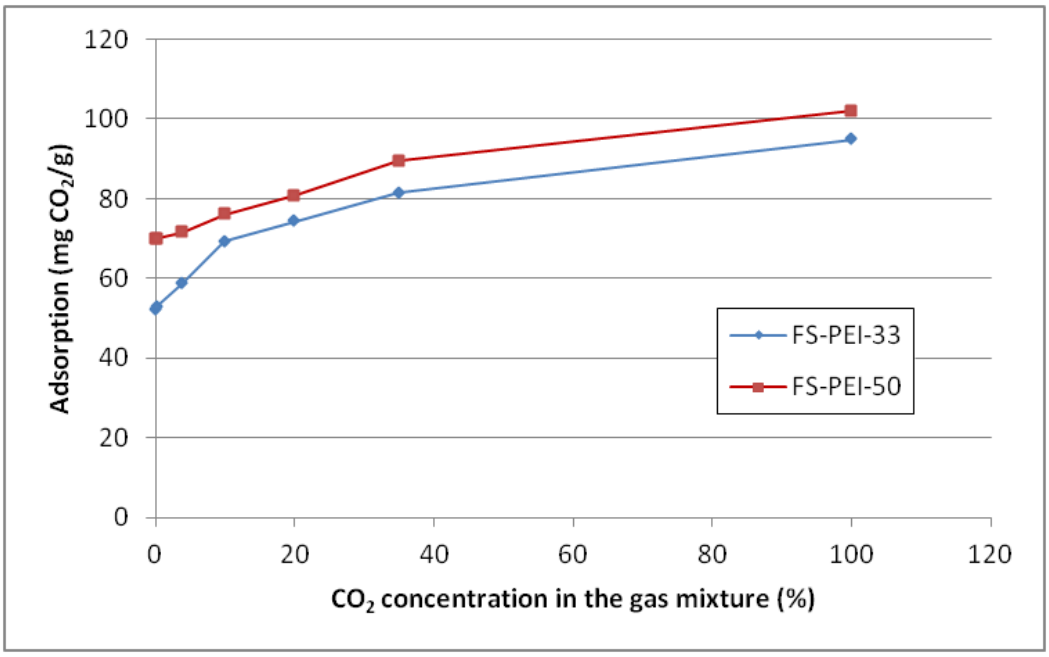

Figure 4.32 CO_2 adsorption on FS-PEI-33 and FS-PEI-50 as a function of CO_2 partial pressure at 25°C

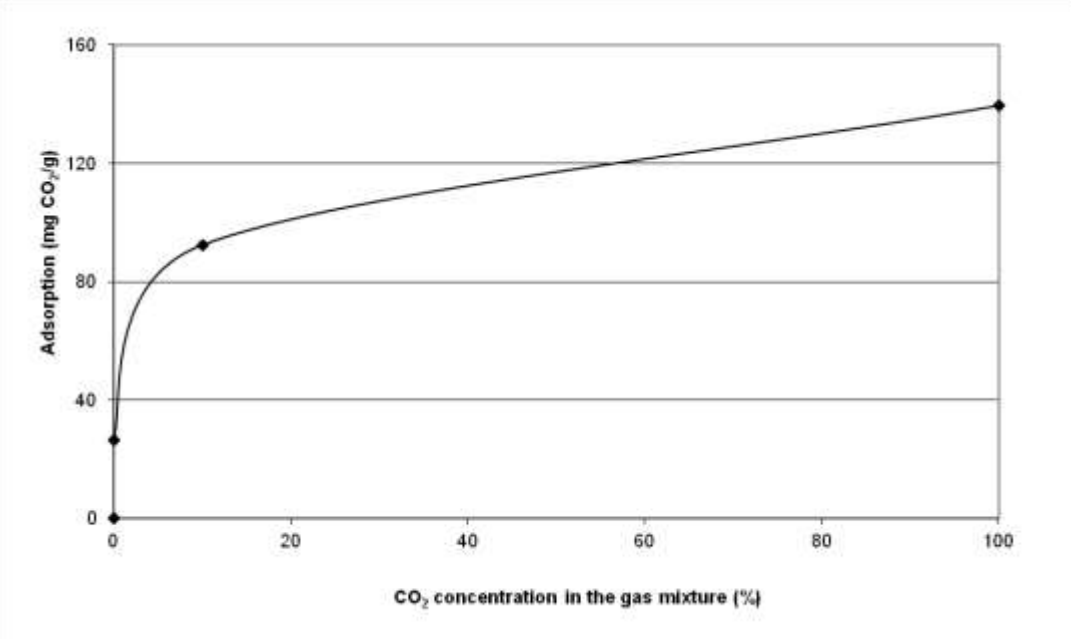

Figure 4.33 CO_2 adsorption on PEI(HMW)/PEG/fumed silica as a function of the CO_2 concentration in the gas stream (nitrogen) at 50°C.

CO_2 capture with amines grafted on solid supports

Although the adsorbents prepared by impregnation of amines on nano-silicas showed high adsorption capacity, the lack of chemical bonds between the amines and the silica may result in loss of organic content after repeated adsorption-desorption cycles due to elevated temperature and vacuum applied during the desorption process.

In order to overcome these issues, a chemical bond between the organic phase and the silica surface is necessary, in other words to chemically graft active adsorbents to the surface. The reaction of end-functionalized oligo- or polyamines with surface OH groups results in immobilized adsorbents on the silica support.

Preparation and characterization of adsorbent materials

Alkylamine-fumed silica hybrid materials were easily prepared from commercially available and relatively inexpensive starting materials. Primary and secondary trialkoxysilylalkylamines such as 3-aminopropyl-trimethoxysilane (**N1**), 3-(2-aminoethylamino)propyltrimethoxysilane (**N2**), 3-[2-(2-aminoethylamino)ethylamino]propyl-trimethoxysilane (**N3**), and trimethoxysilylpropyl-polyethyleneimine (**PEI**) were immobilized onto Aerosil-380 by the reaction of alkoxysilyl anchoring groups and surface silanol groups of the support giving siloxane linkages (Scheme 4.1).

The obtained suspension was separated by centrifugation and the adsorbent particles were washed repeatedly with toluene and methanol and dried under reduced pressure (65 mTorr) at 85 °C. Hybrid materials were characterized by thermogravimetric analysis (TGA) and diffuse reflectance infrared Fourier transform spectroscopy (DRIFT). The surface area was determined by the Brunauer-Emmett-Teller method (BET).

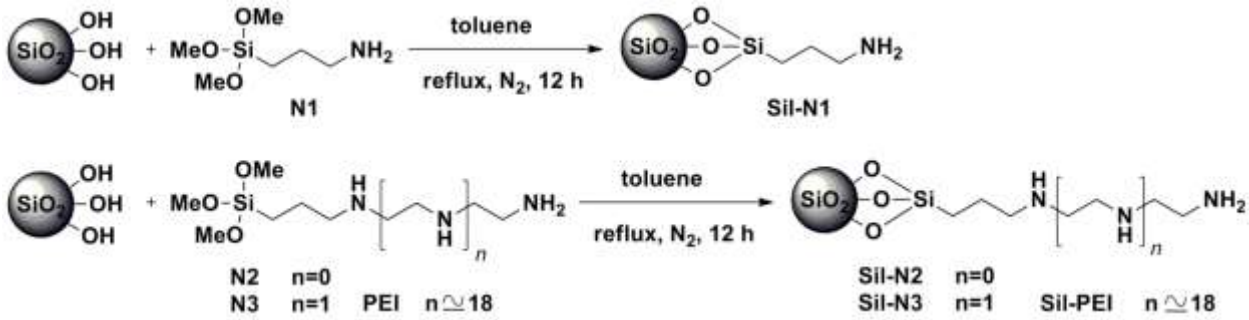

Scheme 4.1 Immobilization of **N1**, **N2**, **N3** and **PEI** onto Aerosil-380.

Graft density and nitrogen content of adsorbent-grafted silica particles were calculated on the basis of weight losses indicated by the thermograms. Representative thermograms of bare Aerosil-380 (a), **Sil-N3** (b), **Sil-N3-CO_2** (c), **Sil-PEI** (d) (heating rate 10 °C min^{-1}, 30 mL min^{-1} air) are shown in Figure 4.34.Weight losses (WL) were recorded in the temperature range from 25 to 800 °C and nitrogen contents (NC) are summarized in Table 4.9.

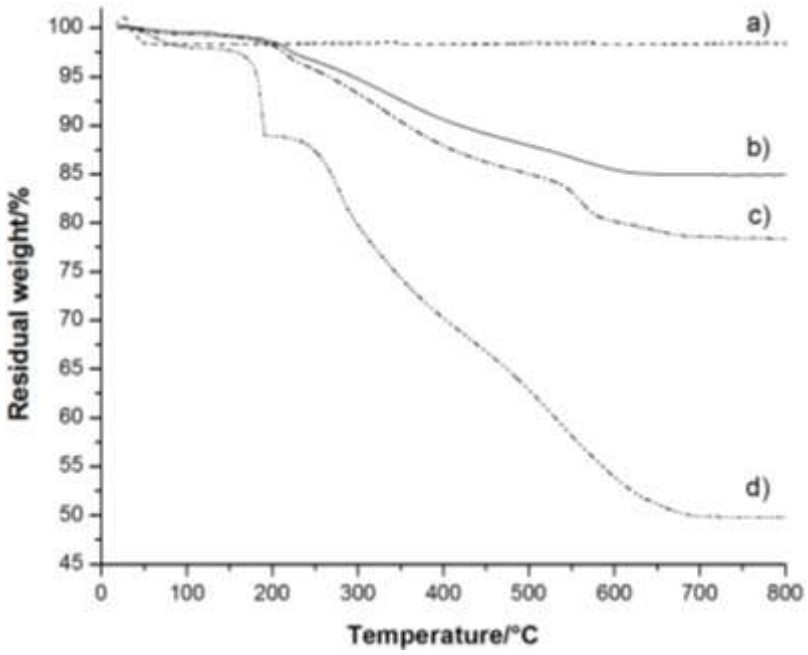

Figure 4.34 TGA curves of bare Aerosil-380 (a), **Sil-N3** (b), **Sil-N3-CO_2** (c), **Sil-PEI** (d).

Table 4.9 Weight loss (WL), nitrogen content (NC), surface area (A_{BET}) and pure CO_2 adsorption capacity of silica-organic hybrids.

Hybrid	WL (%)	NC[a] (mmolN g^{-1})	Adsorption Capacity[b] (mg g^{-1})			Ads. CO_2 per N at 25 °C	A_{BET} (m^2 g^{-1})	Total pore volume (mL·g^{-1})
			25 °C	55 °C	85 °C			
Sil-N1	9.9	1.89	32.4	26.2	19.7	0.43	159	1.66
Sil-N2	14.7	3.42	35.6	27.2	18.3	0.28	148	1.61
Sil-N3	14.6	3.56	41.3	33.2	24.6	0.31	157	1.63
Sil-N1-CO_2	11.8	2.29	37.4	31.5	24.5	0.42	149	1.75
Sil-N2-CO_2	18.6	4.51	47.3	39.3	30.1	0.29	132	1.47
Sil-N3-CO_2	21.0	5.52	49.8	42.9	33.7	0.26	127	1.26
Sil-PEI	47.0	20.6	24.0	50.2	68.0	0.05	43.0	0.76
Sil-PEI-CO_2	46.3	20.0	30.1	58.8	69.7	0.06	19.6	0.31

[a]Millimoles of NH_2 and NH groups per gram silica support, [b]milligrams of adsorbed CO_2 per gram adsorbent.

Grafting of **N1** onto Aerosil-380 resulted in **Sil-N1** adsorbent, which contained 1.89 mmol N atom g^{-1} silica while immobilization of **N2** containing two nitrogen atom per molecule resulted in an almost double amine loading (3.42 mmol N atom g^{-1} silica). Immobilization of **N3** did not follow the same trend and resulted only in slightly higher amine content (3.56 mmol N atom g^{-1} silica) compared with **Sil-N2**.

Not surprisingly, covalent immobilization of alkylaminotrimethoxysilanes onto Aerosil-380 resulted in significant decrease in surface area compared to the bare support. While Aerosil-380 had a surface area of 329 m^2 g^{-1}, **Sil-N1**, **Sil-N2** and **Sil-N3** were found to have 159, 148 and 157 m^2 g^{-1}, respectively, indicating a 54-57 % drop in surface area. It can also be observed that the surface area of the grafted silica particles are very similar regardless of the silane coupling agent applied. Diffuse reflectance infrared Fourier transform spectroscopy is a very powerful method to gain structural information about the molecules immobilized on the surface of inorganic materials. Successful grafting of the silane coupling agents **N1-3** is indicated by the antisymmetric ($\upsilon_{as}NH_2$) and symmetric stretching vibrations ($\upsilon_{s}NH_2$) of hydrogen bonded NH_2 groups (3366 and 3302 cm^{-1})[61,62], respectively, and the corresponding vibrations of CH_2 groups ($\upsilon_{as}CH_2$ at 2928 and $\upsilon_{s}CH_2$ at 2856 cm^{-1}) [63] (Figure 4.35).

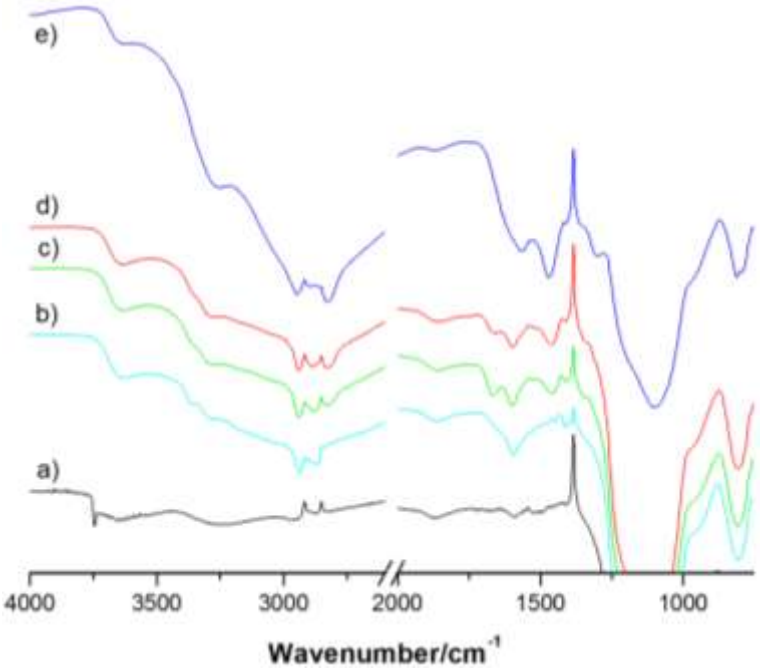

Figure 4.35 DRIFT spectra of bare Aerosil-380 (a), **Sil-N1** (b), **Sil-N2** (c), **Sil-N3** (d), **Sil-PEI** (e).

Deformation vibration of amino groups (δNH_2) could also be detected at 1595 cm^{-1} in **Sil-N1-3** while CH_2 deformations were observed at 1475 and 1449 cm^{-1}[63] in **Sil-N1**. These peaks are overlapped in **Sil-N2-3** giving a relatively broad band at 1458 cm^{-1}. The disappearance of the signal in the DRIFT spectrum of Aerosil-380 at 3745 cm^{-1} attributed to surface OH groups [64] further confirmed the surface modification of surface OH groups using methoxysilanes.

Measurement of adsorption capacities

Adsorption capacities of the silica-alkylamine hybrids were measured with a Shimadzu TGA-50 thermogravimetric analyzer at room temperature, 55 °C and 85 °C using instrument grade CO_2 under flow conditions. Adsorbents were heated at 110 °C for 30 minutes under N_2 atmosphere prior to the measurements. The weight increases were determined after an exposure to CO_2 (3 hours) at each temperature. The adsorption and desorption cycles were repeated ten

times at 85 °C showing insignificant changes in the adsorption capacities (Figures 4.36 and 4.37).

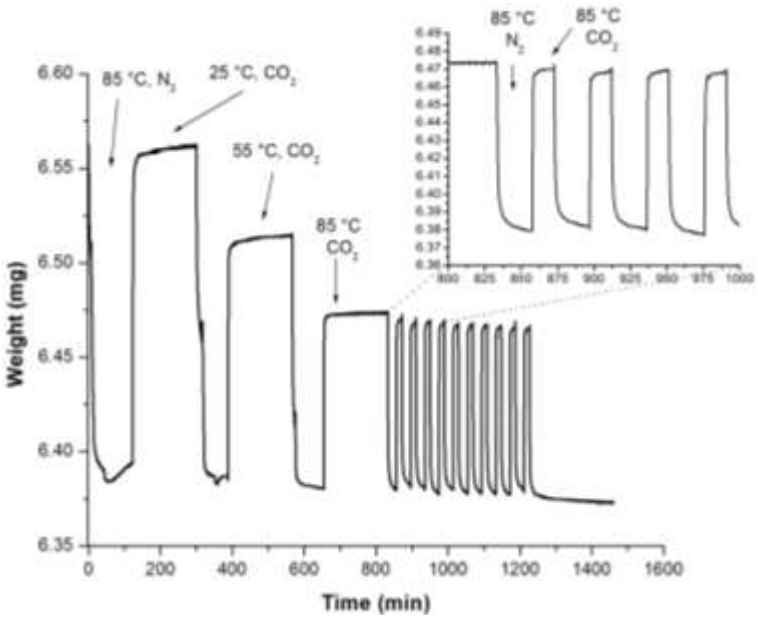

Figure 4.36 A typical thermogram of adsorption/desorption measurements for **Sil-N1**.

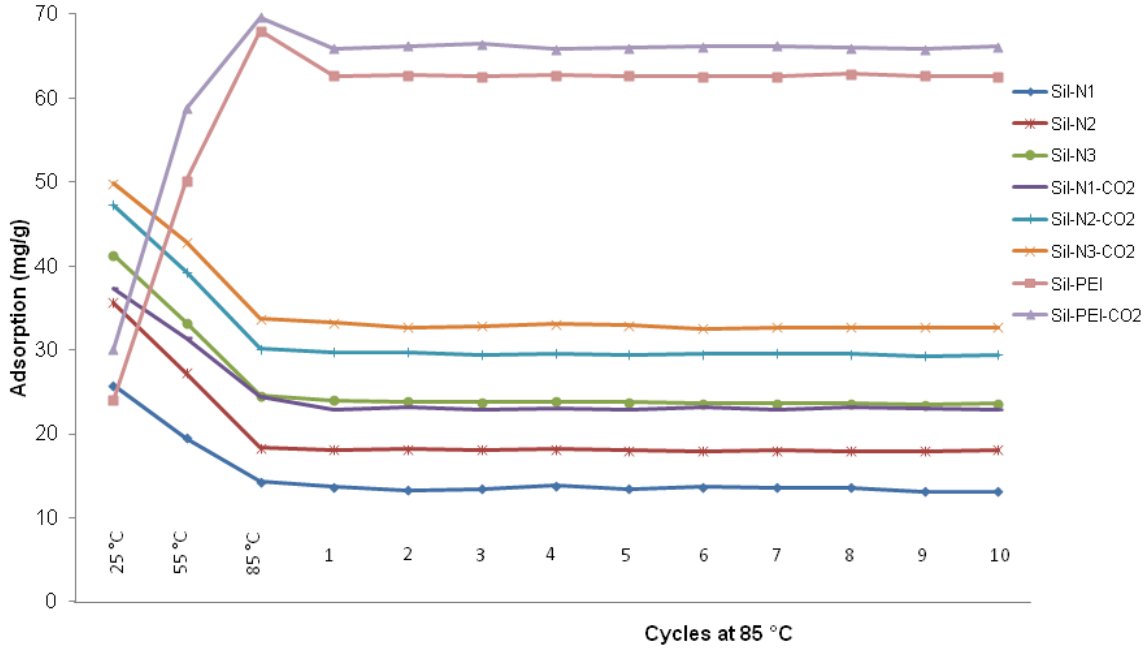

Figure 4.37 Adsorption capacities of functionalized silica particles at 25/55/85 °C followed by 10 cycles of adsorption/desorption at 85 °C.

For two selected adsorbents (**Sil-N1** and **Sil-PEI**) the adsorption/desorption cycles were repeated 100 times at the same temperature confirming the good stability of the hybrid adsorbents (Figure 4.38). It should be noted here that slightly lower adsorption capacities were

measured in the course of 100 cycles due to shorter adsorption (10 min) and desorption (15 min) times.

The monoamino derivative (**Sil-N1**) showed moderate CO_2 uptake at room temperature (32.4 mg CO_2 g^{-1} adsorbent), but as expected the adsorbents with higher nitrogen content (3.42 for **Sil-N2** and 3.56 mmol N g^{-1} for **Sil-N3**) exhibited a higher CO_2 adsorption capacities at 35.6 and 41.3 mg CO_2 g^{-1} adsorbent, respectively. CO_2 adsorption was also measured at 55 and 85 °C showing decreasing adsorption capacity, 26.2 and 19.7 mg g^{-1} for **Sil-N1** respectively, as the temperature increased. A trend could be observed for the diamine and triamine functionalized silica giving lower adsorption capacities, 27.2/18.3 mg $g^{-1}$and 33.2/24.6 mg g^{-1}at 55 and 85 °C, respectively.

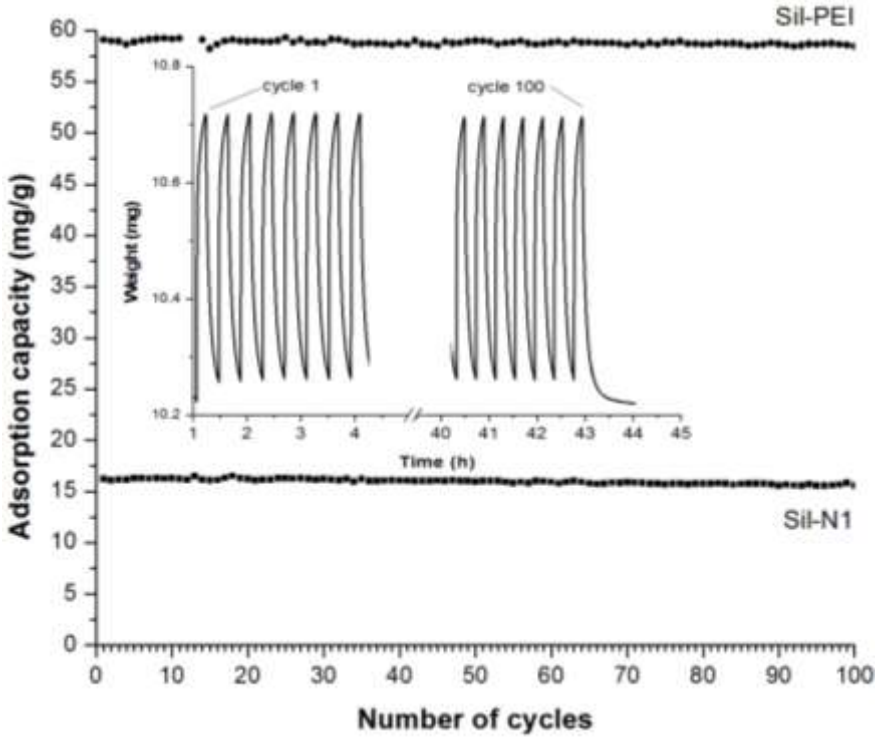

Figure 4.38 Adsorption capacity of **Sil-N1** and **Sil-PEI** in repeated adsorption and desorption cycles at 85 °C. Inset: Adsorbent weight versus time diagram for **Sil-PEI**.

In order to further increase the adsorption capacities of the hybrid materials, higher graft densities were attempted by following a different grafting procedure. It was shown that H-bonded aminopropylsilanes are less reactive and only a small portion of alkoxysilane groups participates in Si–O–Si bond formation.[61]

Effect of the presence of CO_2 during the synthesis

It was also suggested that the saturation of alkylaminotrimethoxysilane solutions with CO_2 prior to introducing the solid support facilitates covalent immobilization preventing the interaction of amine nitrogens of silane coupling agents with surface silanols through hydrogen bonding.[65] Following these leads, toluene solutions of **N1-3** were evacuated and then exposed to

CO_2 for 15 minutes before silica particles were added. The suspension was then slowly heated to 60 °C and the temperature was maintained for 30 minutes. After that, the reaction mixture was heated and kept at 110 °C for 12 hours. In accordance with the results of Knowles and co-workers [65], we obtained alkylamino-grafted silica with higher graft densities (**Sil-N1-CO_2**: 2.29; **Sil-N2-CO_2**: 4.51; **Sil-N3-CO_2**: 5.52 mmol N atom/g silica) which corresponds to a 21, 32 and 55 % increase compared to the adsorbents prepared in the absence of CO_2. Interestingly the increase in graft density is higher when the silane coupling agent contains more nitrogen which seems to confirm that the reaction of amino groups with CO_2 makes the formation of hydrogen bond with surface silanol groups less favourable. The higher graft densities resulted in higher CO_2 adsorption capacities of 37.4, 47.3 and 49.8 mg CO_2 g^{-1} adsorbent at 25 °C, respectively, and similar trend could be observed at 55 and 85 °C as well (Table 4.9).

Similar to the adsorbents prepared from practically CO_2 free silane coupling agents and silica suspension these hybrid materials also showed lower adsorption capacity at higher temperature (Table 4.9). Immobilization of **N1, N2** and **N3** using solutions saturated with CO_2 resulted in slightly lower surface areas (149, 132 and 127 m^2 g^{-1}) than those obtained for **Sil-N1, Sil-N2** and **Sil-N3** but significantly lower than that of bare Aerosil-380.

As the increasing number of secondary amino groups in the grafted layer resulted in better CO_2 adsorption capacity per g adsorbent, we attempted to immobilize polyethyleneimine bearing trimethoxysilyl (**PEI**) anchoring groups. (The average number of ethyleneimine groups in the PEI chain was 18 based on ^{1}H NMR measurements).[§] The high organic content of the hybrid materials was reflected by the significant weight losses in TGA experiments. **Sil-PEI** showed a weight loss of 47.0 % (20.6 mmolN g^{-1}) between 200 and 800 °C.

DRIFT study of PEI-grafted silica revealed stretching vibration of NH groups at 3255 cm^{-1} and a group of signals from 2947 to 2825 cm^{-1} due to antisymmetric and symmetric CH_2 stretching vibrations. Moreover the CH_2 deformation bands overlapped showing an intense band.

Impregnation or covalent grafting of polymers onto supports usually causes dramatic decrease of the surface area as it was observed in the case of **Sil-PEI**. Surface area of **Sil-PEI** (43 m^2 g^{-1}) showed a 87 % decrease compared to that of Aerosil-380. Regardless, the low surface area PEI-grafted silica exhibited remarkable adsorption capacities of 68.0 mg CO_2 g^{-1} at 85 °C compared with mono-, di- and triamine functionalized silica.

Attempts were made to obtain a higher graft density of amine adsorbents on silica by saturating the toluene solution of silane coupling agents with CO_2 prior to the addition of Aerosil-380 using **PEI**. Although the saturation of the silane coupling agent with CO_2 resulted in higher graft density for the mono-, di- and triamine derivatives it did not increase the graft density for **PEI**. (N content of 20.0 mmolN g^{-1}) compared to what we obtained under a nitrogen atmosphere (20.6 mmolN g^{-1}). Furthermore, while all the mono-, di- and triamine-functionalized silica showed lower adsorption capacity at higher temperature a reverse trend could be observed in the adsorption capacity in the case of **Sil-PEI** and **Sil-PEI-CO_2**. Although the graft density of **Sil-PEI-CO_2** was somewhat lower than for **Sil-PEI**, its CO_2 adsorption was however slightly higher. This hybrid material exhibited an adsorption capacity of 24.0/50.2/68.0 mg g^{-1} and 30.1/58.8/69.7 mg g^{-1} at 25, 55 and 85 °C, respectively.

Preparation of amine-functionalized polysiloxanes

Condensation of aminoalkylsilanols derived from different trimethoxysilyl-aminoalkanes and tris(3-trimethoxysilylpropyl)isocyanurate was applied as the third approach to prepare organic-silica hybrids for CO_2 adsorption. The reaction between tris(3-trimethoxysilylpropyl)isocyanurate and 3-aminopropyl-trimethoxysilane resulted in an adsorbent material showing 129.8 mg/g CO_2 adsorption at 85 ºC) while the condensation product from where N-(2-aminoethyl)-3-aminopropylmethyl-dimethoxysilane and N-methylaminopropyltrimethoxysilane showed adsorption capacities of 103.3 and 36.9 mg/g, respectively (measured with the static method).

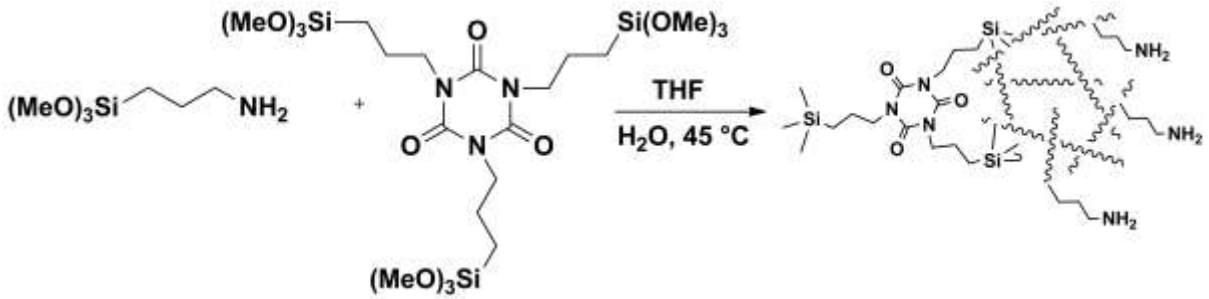

Figure 4.39 Condensation of aminoalkyl methoxysilanes with tris (3-trimethoxysilylpropyl) isocyanurate.

Table 4.10 Graft density and CO2 adsorption capacity of hybrid adsorbents obtained by condensation of methoxysilanes.

Entry	Co-monomer	Graft density (%)	CO_2 adsorption (mg/g)	
			RT	85 ºC
1	3-aminopropyl-trimethoxysilane	50.33	54.7	129.8
2	N-methylaminopropyltrimethoxysilane	48.67	22.6	36.9
3	N-(2-aminoethyl)-3-aminopropyl-methyl-dimethoxysilane	57.64	68.4	103.3

Conclusions

Nano structured precipitated and fumed silica (nano-silica) were found to be superior supports for the immobilization of varied organo-amines. The easily prepared solids were found to be regenerable and effective CO_2 adsorbents at moderate temperatures from room temperature up to 100°C. PEI based adsorbents were able to adsorb efficiently and repeatedly CO_2 even at concentration as low as 400 ppm CO_2. Supported polyethylenimines (PEIs), especially branched low molecular weight (LMW, Mw ca. 800) and high molecular weight (HMW, Mw ca. 25000) PEIs were particularly suitable as CO_2 adsorbents. Amines with lower molecular weights and lower boiling points such as pentaethylenehexamine (PEH), tetraethylenepentamine (TEP), monoethanolamine (MEA) and diethanolamine (DEA) showed sorbent leaching from the solid adsorbents. The addition of polyethylene glycol was found to significantly enhance the subsequently needed desorption of CO_2 from PEI based solid adsorbents. In the preparation of

CO_2 adsorbents, the particle size of the nano-silica was found to be of advantage compared to other solid supports having similar or higher surface area but larger particle size.

As solids, the novel nano-silica / PEI adsorbents circumvent many of the difficulties and inconveniencies encountered in the currently used technology employing liquid amines. While further studies are necessary, they are promising candidates for the capture of CO_2 from flue gases of fossil fuel burning power plants, cement factories and other industrial sources, eventually even from the atmosphere itself. Amines and polyamines grafted on solid supports can solve some of the leaching problems of low molecular weight amines associated with adsorbents prepared by simple impregnation method.

Clearly, adsorbents based on supported amines are promising materials for the capture of CO_2 from the atmosphere and warrants further studies.

The present work in the field of CO_2 capture has already resulted in the publication of 3 papers,[55,66,67] and a review.[68]

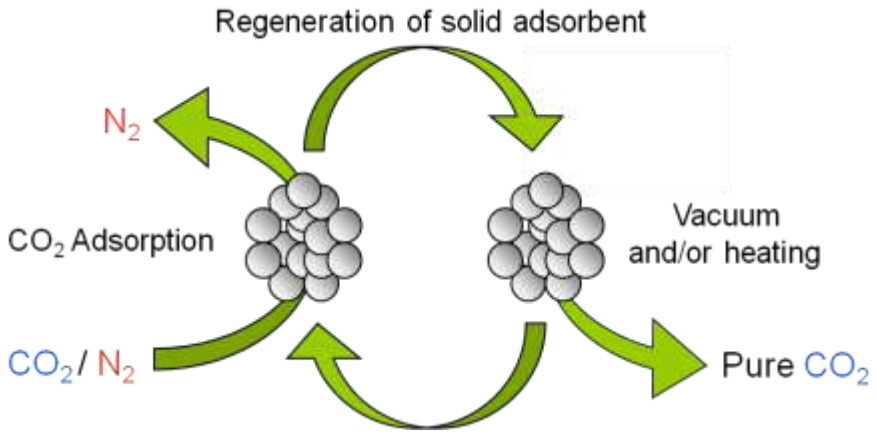

References

(1) *Carbon Dioxide Recovery and Utilization*; Kluwer Academic Publishers: Dordrecht, The Netherlands, 2003.

(2) Olah, G. A.; Goeppert, A.; Prakash, G. K. S. *J. Org. Chem.* **2009**, *74*, 487.

(3) Allam, R. J.; Bredesen, R.; Drioli, E. *Carbon Dioxide Separation Technologies*; Kluwer Academic Publishers: Dordrecht, The Netherlands, 2003.

(4) Kohl, A.; Nielsen, R. *Gas Purification*; 5th ed.; Gulf Publishing Company: Houston, Texas, 1997.

(5) Halmann, M. M.; Steinberg, M. *Greenhouse Gas Carbon Dioxide Mitigation: Science and Technology*; CRC Press, 1999.

(6) Choi, S.; Drese, J. H.; Jones, C. W. *ChemSusChem* **2009**, *2*, 796.

(7) Siriwardane, R. V.; Shen, M.-S.; Fisher, E. P.; Poston, J. A. *Energy & Fuels* **2001**, *15*, 279.

(8) Banerjee, R.; Phan, A.; Wang, B.; Knobler, C.; Furukawa, H.; O'Keeffe, M.; Yaghi, O. M. *Science* **2008**, *319*, 939.

(9) Millward, A. R.; Yaghi, O. M. *J. Am. Chem. Soc.* **2005**, *127*, 17998.

(10) Beckman, E. J., *Polymers Capable of Reversibly Complexing Acid Gases and Foamed Polymers Produced Therefrom, US Patent 5,886,061*, 5 886 061, **1999**.

(11) Knowles, G.; Graham, J. V.; Delaney, S. W.; Chaffee, A. L. *Fuel Process. Technol.* **2005**, *86*, 1435.

(12) Hiyoshi, N.; Yogo, K.; Yashima, T. *J. Jpn. Pet. Inst.* **2005**, *48*, 29.

(13) Belmabkhout, Y.; Serna-Guerrero, R.; Sayari, A. *Ind. Eng. Chem. Res.* **2010**, *49*, 359.

(14) Serna-Guerrero, R.; Da'na, E.; Sayari, A. *Ind. Eng. Chem. Res.* **2008**, *47*, 9406.

(15) Harlick, P. J. E.; Sayari, A. *Ind. Eng. Chem. Res.* **2007**, *46*, 446.

(16) Zinnen, H. A.; Oroskar, R.; Chang, C.-H., *Carbon Dioxide Removal Using Aminated Carbon Molecular Sieves , US Patent 4,810,266*, 4 810 266, **1989**.

(17) Stoneburner, G. R., *Reactivation of Monoethanolamine Impregnated Activated Carbon, US Patent 3,491,031*, 3 491 031, **1970**.

(18) Sayari, A., *Amine Modified Adsorbent, Its Preparation and Use for Dry Scrubbing of Acid Gases, WO Patent Application 2004/054708 A2,* **2004**.

(19) Satyapal, S.; Filburn, T.; Trela, J.; Strange, J. *Energy & Fuels* **2001**, *15*, 250.

(20) Birbara, P. J.; Nalette, T. A., *Regenerable Supported Amine-Polyol Sorbent, US Patents 5,376,614 and 5,492,683*, 5 376 614 and 5 492 683, **1996**.

(21) Birbara, P. J.; Filburn, T. P.; Nalette, T. A., *Regenerable Solid Amine Sorbent, US Patent 5,876,488*, 5 876 488, **1999**.

(22) Birbara, P. J.; Filburn, T. P.; Michels, H.; Nalette, T. A., *Sorbent System and Method for Absorbing Carbon Dioxide (CO_2) From the Atmosphere of a Closed Habitable Environment, US Patent 6,364,938 B1*, 6 364 938, **2002**.

(23) Xu, X.; Song, C.; Andresen, J. M.; Miller, B. G.; Scaroni, A. W. *Energy and Fuels* **2002**, *16*, 1463.

(24) Xu, X.; Song, C.; Andresen, J. M.; Miller, B. G.; Scaroni, A. W. *Microporous Mesoporous Mater.* **2003**, *62*, 29.

(25) Olah, G. A.; Goeppert, A.; Meth, S.; Prakash, G. K. S. *US Patent 7,795,175* **2008**.

(26) Xu, X.; Song, C.; Miller, B. G.; Scaroni, A. W. *Fuel Process. Technol.* **2005**, *86*, 1457.

(27) Sing, K. S. W. *J. Porous. Mater.* **1995**, *2*, 5.

(28) Lowell, S.; Shields, J. E.; Thomas, M. A.; Thommes, M. *Characterization of Porous Solids and Powders: Surface Area, Pore Size and Density*; Springer: Dordrecht, The Netherlands, 2004.
(29) Gun'ko, V. M.; Leboda, R.; Zarko, V. I.; Skubiszewska-Zieba, J.; Grzegorczyk, W.; Pakhlov, E. M.; Voronin, E. F.; Seledets, O.; Chibowski, E. *Colloids Surf. A* **2003**, *218*, 103.
(30) Goeppert, A.; Meth, S.; Prakash, G. K. S.; Olah, G. A. *Energy Environ. Sci.* **2010**, *3*, 1949.
(31) Choi, S.; Drese, J. H.; Chance, R. R.; Eisenberger, P. M.; Jones, C. W. US Pat. Appl. 2011/0179948A1, 2011.
(32) Belmabkhout, Y.; Serna-Guerrero, R.; Sayari, A. *Chem. Eng. Sci.* **2010**, *65*, 3695.
(33) Choi, S.; Drese, J. H.; Jones, C. W. *ChemSusChem* **2009**, *2*, 796.
(34) Macdowell, N.; Florin, N.; Buchard, A.; Hallett, J.; Galindo, A.; Jackson, G.; Adjiman, C. S.; Williams, C. K.; Shah, N.; Fennell, P. *Energy Environ. Sci.* **2010**, *3*, 1645.
(35) *DOE/NETL Carbon Dioxide Capture and Storage RD&D Roadmap*, National Energy Technology Laboratory, 2010.
(36) Wang, Q.; Luo, J.; Zhong, Z.; Borgna, A. *Energy Environ. Sci.* **2011**, *4*, 42.
(37) D'Alessandro, D. M.; Smit, B.; Long, J. R. *Angew. Chem. Int. Ed.* **2010**, *49*, 6058.
(38) *IPCC Fourth Assessment Report: Climate Change 2007*; Cambridge University Press: Cambridge, U.K., 2007.
(39) Olah, G. A.; Prakash, G. K. S.; Goeppert, A. *J. Am. Chem. Soc.* **2011**, *133*, 12881.
(40) Xiaoding, X.; Moulijn, J. A. *Energy & Fuels* **1996**, *10*, 305.
(41) Olah, G. A.; Goeppert, A.; Prakash, G. K. S. *Beyond Oil and Gas: The Methanol Economy, 2nd edition*; Wiley-VCH: Weinheim, 2009.
(42) Graves, C.; Ebbesen, S. D.; Mogensen, M.; Lackner, K. S. *Renew. Sust. Energy Rev.* **2011**, *15*, 1.
(43) Huang, Z.; Chen, Z. B.; Ren, N. Q.; Hu, D. X.; Zheng, D. H.; Zhang, Z. P. *J. Zhejiang Univ.-Sci. A* **2009**, *10*, 1642.
(44) Jones, C. W. *Annu. Rev. Chem. Biomol. Eng* **2010**, *2*, 31.
(45) Lackner, K. S.; Ziock, H.-J.; Grimes, P. *SourceBook* **1999**, *57*, 6.
(46) Zeman, F. S.; Lackner, K. S. *World Res. Rev.* **2004**, *16*, 157.
(47) Keith, D.; Ha-Duong, M.; Stolaroff, J. *Climatic Change* **2006**, *74*, 17.
(48) Stolaroff, J. K.; Keith, D. W.; Lowry, G. V. *Environ. Sci. Technol.* **2008**, *42*, 2728.
(49) Zeman, F. S. *Environ. Sci. Technol.* **2007**, *41*, 7558.
(50) Mahmoudkhani, M.; Keith, D. *Int. J. Greenhouse Gas Control* **2009**, *3*, 376.
(51) Harlick, P. J. E.; Sayari, A. *Ind. Eng. Chem. Res.* **2006**, *45*, 3248.
(52) Serna-Guerrero, R.; Belmabkhout, Y.; Sayari, A. *Adsorption* **2010**, *16*.
(53) Huang, H. Y.; Yang, R. T.; Chinn, D.; Munson, C. L. *Ind. Eng. Chem. Res.* **2003**, *42*, 2427.
(54) Chang, A. C. C.; Chuang, S. S. C.; Gray, M.; Soong, Y. *Energy & Fuels* **2003**, *17*, 468.
(55) Goeppert, A.; Meth, S.; Prakash, G. K. S.; Olah, G. A. *Energy Environ. Sci.* **2010** *3*, 1949.
(56) Franchi, R. S.; Harlick, P. J. E.; Sayari, A. *Ind. Eng. Chem. Res.* **2005**, *44*, 8007.
(57) Yue, M. B.; B., S. L.; Cao, Y.; Wang, Y.; Wang, Z. J.; Zhu, J. H. *Chem. Eur. J.* **2008**, *14*, 3442.
(58) Gebald, C.; Wurzbacher, J. A.; Steinfeld, A. Eur. Pat. Appl. EP2266680A1, 2010.

(59) Choi, S.; Drese, J. H.; Eisenberger, P. M.; Jones, C. W. *Environ. Sci. Technol.* **2011**, *45*, 2420.
(60) Olah, G. A.; Goeppert, A.; Meth, S.; Prakash, G. K. S. *Energy Environ. Sci.* **2010**, *3*, 1949.
(61) White, L. D.; Tripp, C. P. *J. Colloid Interf. Sci.* **2000**, *232*, 400.
(62) Vrancken, K. C.; Vandervoort, P.; Gillisdhamers, I.; Vansant, E. F.; Grobet, P. *J. Chem. Soc. Faraday Trans.* **1992**, *88*, 3197.
(63) Hiyoshi, N.; Yogo, K.; Yashima, T. *Micropor. Mesopor. Mat.* **2005**, *84*, 357.
(64) Takei, T.; Kato, K.; Meguro, A.; Chikazawa, M. *Colloid Surface A* **1999**, *150*, 77.
(65) Knowles, G. P.; Beyton, V.; Chaffee, A. L. *Prepr. Symp.-Am. Chem. Soc., Div. Fuel Chem.* **2006**, *51*, 102.
(66) Goeppert, A.; Czaun, M.; May, R. B.; Prakash, G. K. S.; Olah, G. A.; Narayanan, S. R. *J. Am. Chem. Soc.* **2011**, *133*, 20164.
(67) Meth, S.; Goeppert, A.; Prakash, G. K. S.; Olah, G. A. *Energy & Fuels* **2012**, *26*, 3082.
(68) Goeppert, A.; Czaun, M.; Prakash, G. K. S.; Olah, G. A. *Energy Environ. Sci.* **2012**, *5*, 7833.

Subtask 4.2 Electrochemical Reduction of CO_2 to Formic Acid and Syngas

Introduction

As the world's demand for cheap energy steadily increases, one is forced to deal with the reality that increasing CO_2 emissions that began with the dawn of the industrial revolution have changed the earth's atmosphere by significantly increasing the concentration of CO_2, which is currently hovering around 400 ppm. Although the exact effects of this increase are not fully understood yet, it is clear that technologies that mitigate CO_2 emissions are critical to the environment as humankind moves forward. Currently, carbon capture and sequestration (CCS) is the most prominently used method to divert CO_2 from the atmosphere, but it has many shortfalls. The goal of this particular part of the methanol economy project was to develop technologies that have the potential to change the state of this field by converting CO_2 into useful products. Not only does this have the potential to decrease the levels of atmospheric CO_2, but it also sets up the possibility of a man-made carbon cycle not unlike the natural carbon cycle (photosynthesis), which we benefit from currently.

Electrochemical CO_2 reduction offers significant promise for a number of reasons, among them one can typically selectively reduce CO_2 to one product, rather than a mix of products based on careful selection of catalyst and conditions. Table 4.11 lists the reduction potentials for CO_2 to various products of interest vs. the standard hydrogen electrode (SHE) at standard conditions.

Table 4.11 CO_2 Reduction to Various Products vs. SHE

Entry	Half-Cell Reaction	E^0 vs. SHE
1	$CO_2 + 2H^+ + 2e^- \rightarrow HCOOH$	-0.11
2	$CO_2 + 2H^+ + 2e^- \rightarrow CO + H_2O$	-0.10
3	$CO_2 + 4H^+ + 4e^- \rightarrow CH_2O + H_2O$	-0.028
4	$CO_2 + 6H^+ + 6e^- \rightarrow CH_3OH + H_2O$	+0.031
5	$CO_2 + 8H^+ + 8e^- \rightarrow CH_4 + H_2O$	+0.17

Electrochemical CO_2 reduction can occur efficiently and rapidly to either formate or CO, both of which were studied as potential products of interest. For CO_2 reduction to CO, the aim was to develop and operate a high pressure flow electrolyzer capable of operating at a fivefold higher current density than what was observed for atmospheric pressure reduction under static conditions. Because the catalysts that typically evolve CO also evolve H_2 from H_2O to some extent, the focus was not to exclusively reduce CO_2 to CO, but rather to simultaneously reduce CO_2 and H_2O to a combination of CO and H_2 in a favorable ratio. Low temperature (<100 °C) CO_2 reduction to CO and H_2 has yet to be fully developed, and is one of the parameters of this investigation. Any combination of CO and H_2 has widely been called syngas, and we have termed the specific ratio of 2:1 H_2:CO metgas, due to its equivalent stoichiometry to produce from it methanol.

For CO_2 reduction to formate, the goal was to demonstrate a high pressure flow electrolysis process capable of reducing CO_2 to formate at a high current density and with high efficiency (95%) towards formate. Electrodes that reduce CO_2 to formate are typically reported

to achieve it quite efficiently and therefore a high pressure flow system was designed that could speed up this process while demonstrating its scalability.

Atmospheric Pressure CO_2 Reduction to Formate

Initial testing for this project began with atmospheric pressure systems using standard electrochemical 3-electrode cells in 0.5 M $NaHCO_3$. Figure 4.40 gives an early cyclic voltammogram (CV) from one of these tests using a tin powder electrode with a Nafion binder on toray carbon paper. The current detected after -1.4 V is primarily due to CO_2 reduction, however this is also the region where the hydrogen evolution reaction (HER) takes place. Tests like these served to verify that CO_2 reduction takes place on tin and lead electrodes at -1.6 V vs. Ag/AgCl.

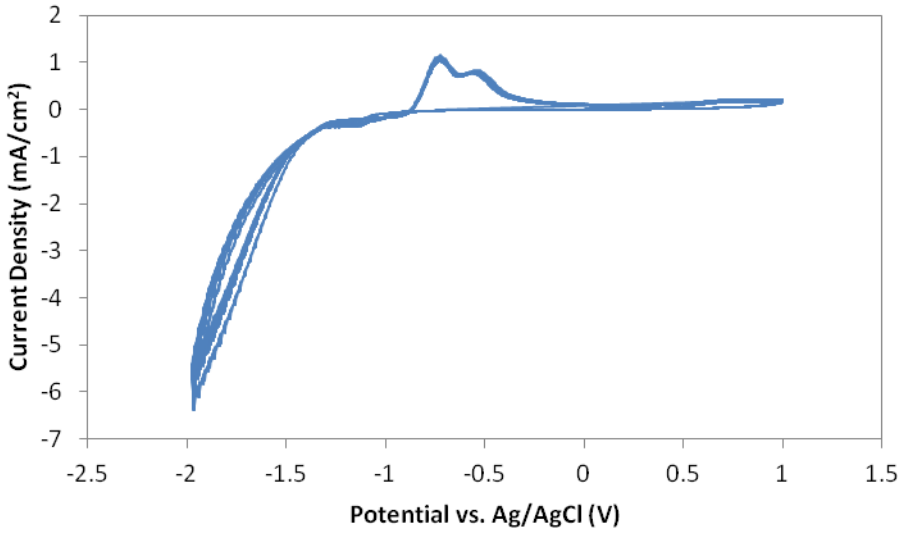

Figure 4.40 Cyclic Voltammetry of CO_2 Reduction on a Tin Powder Electrode

After determining the approximate potential for CO_2 reduction, a potentiostatic experiment was carried out, where the potential was heald steady at -1.6 V vs. Ag/AgCl for 1.5 hours, as shown in Figure 4.41.

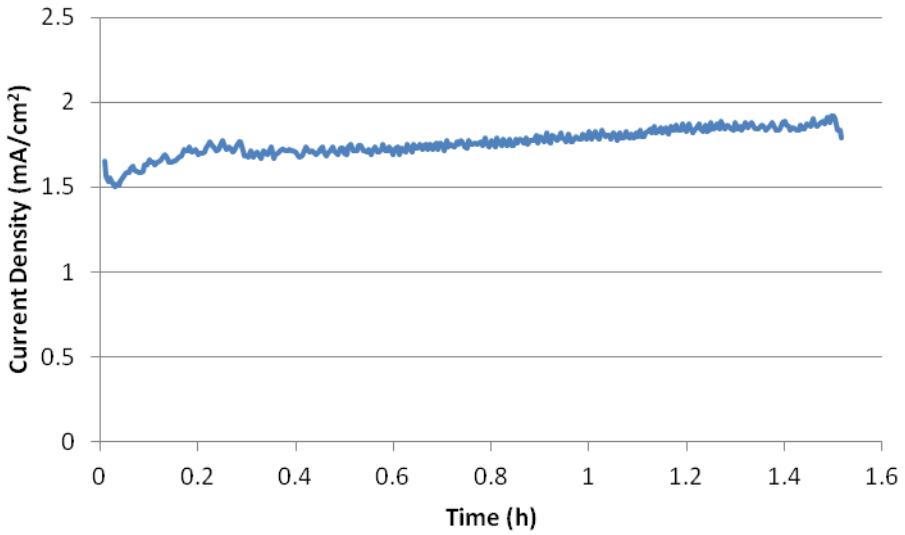

Figure 4.41 Chronoamperometry of CO_2 Reduction on Tin Powder at -1.6 V vs. Ag/AgCl

Average current density over the full time period was 1.76 mA/cm^2, with faradaic efficiency towards formate of 52.6%. These results are not significantly different from those found in the literature since the cell was not operated under CO_2 pressure or at high potentials. Given results such as this, attention was turned to more sophisticated experimental setups to determine the limits that could be reached on lead and tin electrodes.

Atmospheric Pressure CO_2 Reduction to Syngas

The investigation of CO_2 reduction to syngas began with experiments on gold foil electrodes at atmospheric pressure of CO_2 in a conventional 3-electrode cell. Figure 4.42 demonstrates some of this early data, in which a very strong relationship between the potential of the gold electrode and the molar ratio of H_2:CO was determined. The desired ratio of 2:1 was achieved at -3.2 V vs. Ag/AgCl. These data were collected using 0.1 M $KHCO_3$ as the supporting electrolyte with CO_2 bubbled into the solution.

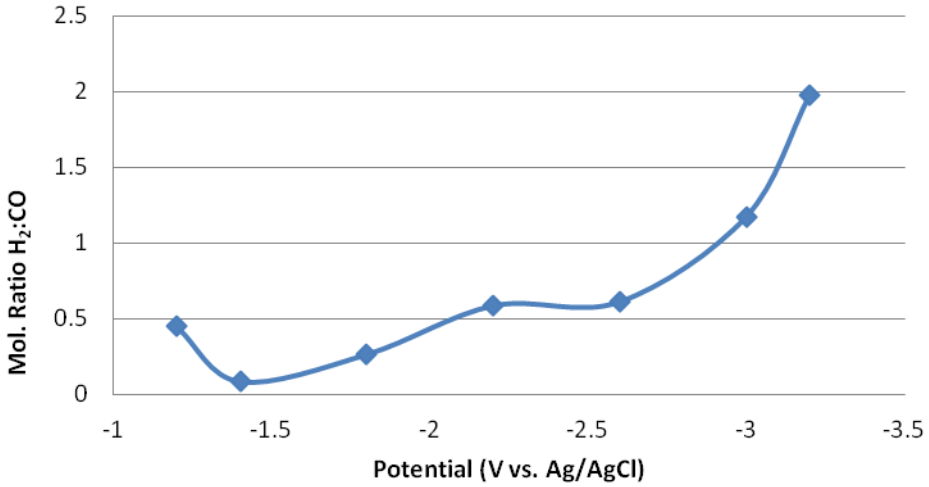

Figure 4.42 CO_2 Reduction on Gold Foil at Atmospheric Pressure

Given the results from Figure 4.42, work moved on to developing electrodes that would be more suitable for high pressure flow systems, which was intended to be used for demonstration of a viable process. The next set of experiments centered on electrodes prepared on carbon paper used in gas diffusion electrodes (GDEs). Three loadings were prepared, 4, 8, and 16 mg/cm^2 of 5 μm gold spherical particles painted on standard toray carbon paper using Nafion as a binder. Figures 4.43, 4.44 and 4.45 give some results from these experiments, which were carried out under the same conditions as described above for the gold foil case.

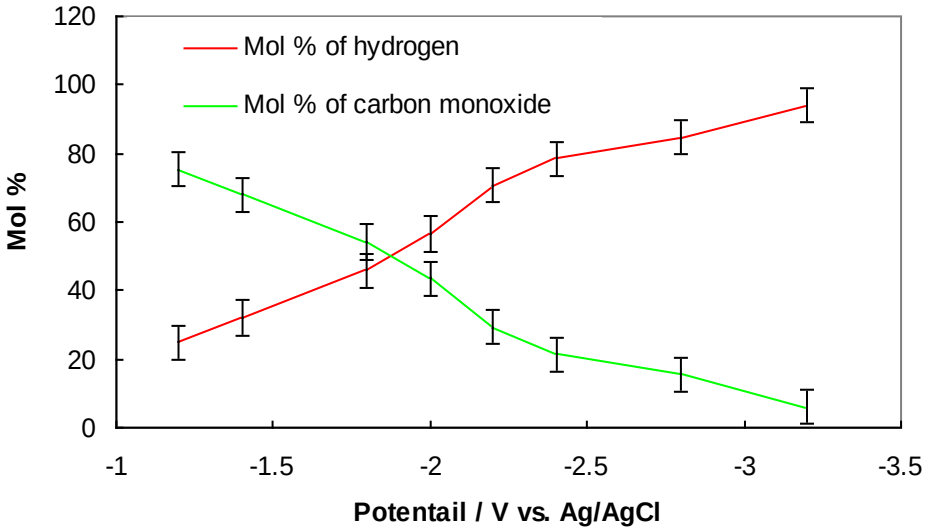

Figure 4.43 4 mg/cm^2 Gold on Graphite

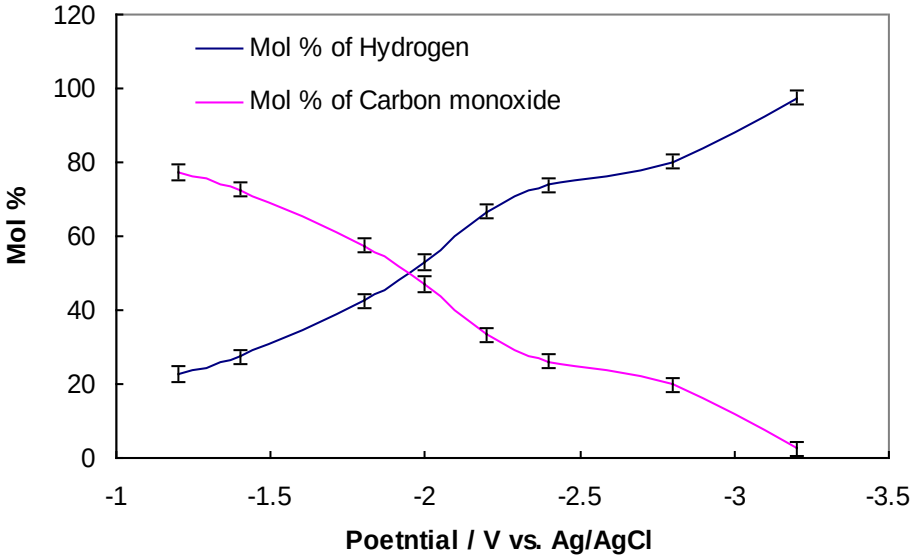

Figure 4.44 8 mg/cm^2 Gold on Graphite

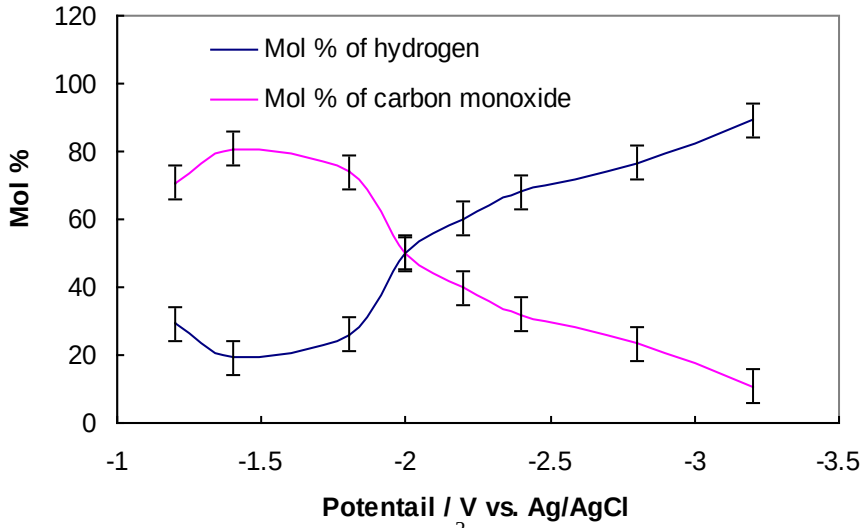

Figure 4.45 16 mg/cm^2 Gold on Graphite

All three of these figures provide essentially the same information, that there is an optimal potential for each electrode if the goal is to obtain a particular ratio of H_2:CO. Increasing loading did not significantly impact the observed geometric current density at any particular potential (all three gave ~3 mA/cm^2 at -2 V vs. Ag/AgCl), indicating that the reduction was not significantly limited by surface area at this point.

Elevated Pressure Flow CO_2 Reduction Reactor Design

In addition to reports in the literature that high pressure CO_2 could significantly improve the rate and selectivity of CO_2 reduction on tin and lead, the possibility of moving to a flow system that would be more relevant for practical industrial purposes was also considered. This is especially true for electrochemical CO_2 reduction to syngas, where downstream processing would likely also be conducted at elevated pressure, so pumps to achieve higher pressure would

not necessarily be required. Attention therefore turned towards designing and testing a high pressure flow system. The design of the electrolyzer was based on the design of the graphite plates that were used for fuel cell testing in the laboratory. Figure 4.46 gives the basic schematic of the design and operation of the high pressure flow electrolyzer.

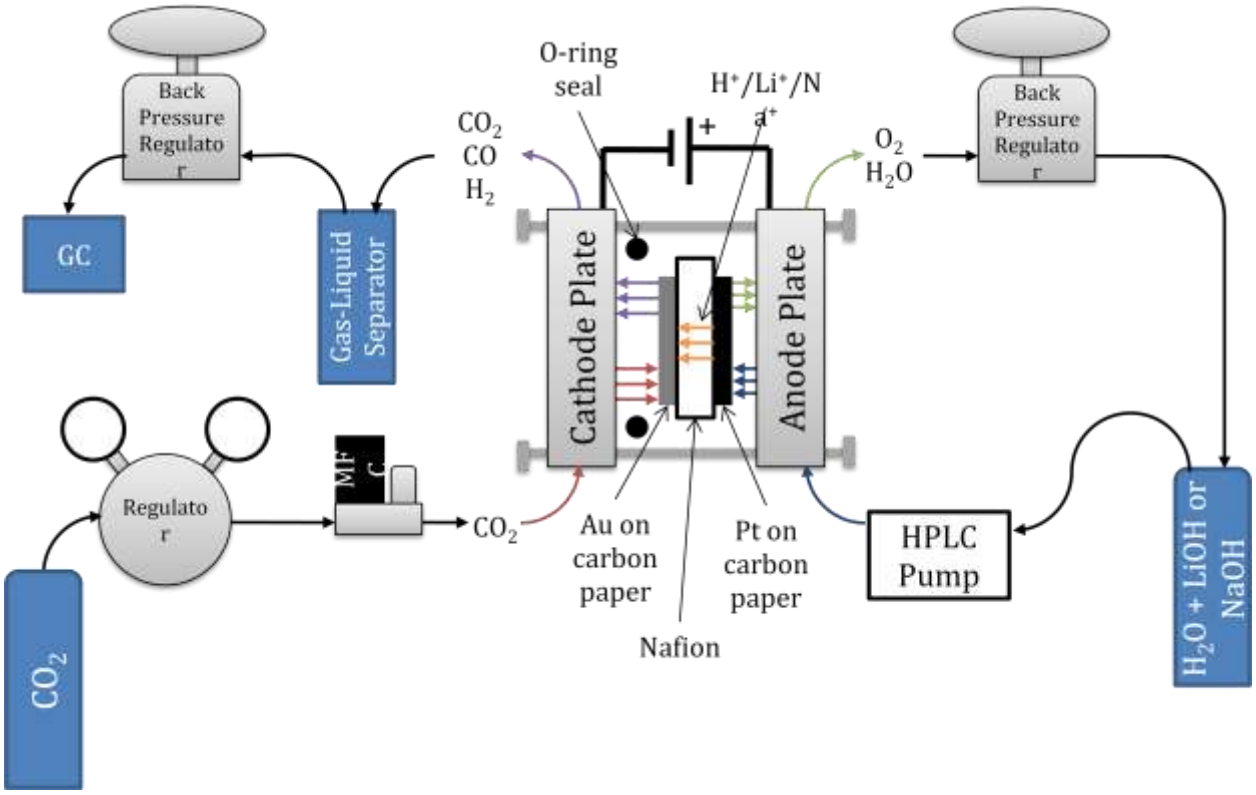

Figure 4.46 High Pressure Flow Electrolyzer Schematic

Obviously, graphite plates could not be used in a high pressure application, so 316 stainless steel was considered, which was readily available and easily machined in the machine shop at USC. The plates were designed to sustain a pressure of up to 1500 psig, which is almost twice the pressure of liquid CO_2 at room temperature, or the highest pressure achievable without a supercritical CO_2 pump.

While the plates themselves could withstand very high pressures, the membrane electrode assembly (MEA that was comprised of two graphite backed electrodes and a Nafion membrane, could not withstand such high pressures. To combat this, pressurized water was used on the anode compartment of the reactor system to balance the system and provide equal pressure on both sides of the MEA. This system required a computer based PID controller running LabVIEW to precisely control the back pressure regulator, which regulates the pressure of the flow system. Analysis of the gaseous products was achieved by an in-line GC/TCD, while the liquid products were analyzed by NMR. Prior calibration of the GC made it possible to determine real-time H_2 and CO flow rates while running the system. The liquid collected in the gas liquid separator was analyzed after each run for formate by comparison to an internal standard of dimethylformamide (DMF).

Despite the great pains that were taken to develop a high pressure flow system for CO_2 reduction, the initial experimental results showed a few flaws in the system. First of all, the graphite electrodes disintegrated under the stress imparted by the stainless steel plates required to effectively seal the system for high pressure operation. Secondly, even 316 stainless steel was oxidized on the anode, and iron was detected on the cathode side of the reactor, plating out at high potentials. This caused system instability as well as an abundance of H_2 evolution, as iron is a reasonably good H_2 evolution cathode.

Both of these problems were solved or at least mitigated by developing the floating flow field, as depicted in Figure 4.47. To solve the problem of instability of steel at high potentials, a graphite flow field was used instead of a steel one. The high pressure rating was maintained by making the flow field a separate part of the assembly rather than integral to the entire unit. The problem of crushing the fragile graphite electrodes was solved by using a wave disc spring between the graphite flow field and the stainless steel plate. This allowed to put as much torque as necessary on the bolts that hold the anode and cathode plates together without impacting the force on the electrodes. As the wave disc spring compresses, the force on the electrode does change slightly, but far less than with a static design. Another advantage to this design has to do with one of the intrinsic properties of Nafion. Making an MEA involves hot pressing at 140 °C, which drives out most of the water from the membrane and, as a result, the Nafion shrinks. When the membrane rehydrates inside the cell, it swells again. This swelling force is more than enough to crush the graphite electrodes, but can easily be mitigated by using a spring underneath the flow field.

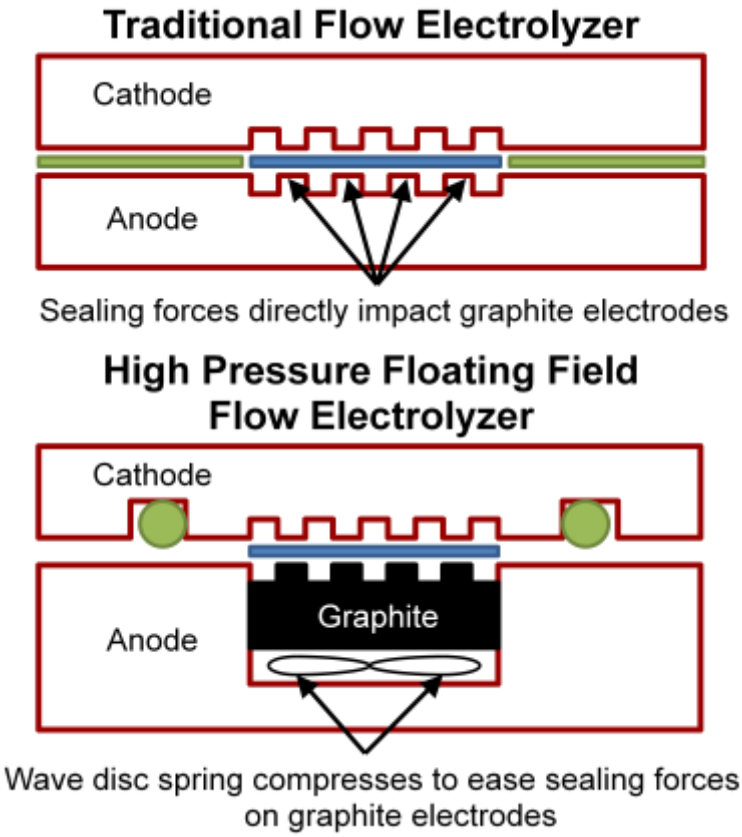

Figure 4.47 Traditional vs. Floating Field Electrolyzer

With a reliable system in hand, experiments were performed at elevated pressure. The first task was to determine appropriate conditions because the high pressure flow system was dramatically different from the traditional 3-electrode electrochemical cells which were previously used. Probably the biggest difference was that the electrolyte was now Nafion instead of aqueous $NaHCO_3$ or $KHCO_3$. Although the use of pure water on the anode side and pure CO_2 on the cathode side was envisioned, it was quickly realized that this led to almost exclusively H_2 evolution. To mitigate this problem, either LiOH or NaOH was added to the water pumped through the anode compartment to basify the Nafion membrane. Although Nafion is traditionally used in fuel cell applications in the protic form Nafion-H, it was actually developed as a general cation exchange membrane, and can easily transport alkali metal ions. By substituting 0.1 M LiOH for pure water, appreciable amounts of formate were observed from electrolyzing CO_2 on lead and tin electrodes. Sodium hydroxide also works, however it was determined that suppression of H_2 was higher with lithium hydroxide.

High Pressure Flow Electrolysis of CO_2 to Formate

The first few experiments centered on determining how much of an effect the pressure of the system had on the CO_2 reduction. Figure 4.48 shows the results from two experiments on the same MEA, one at 0 psig and one at 300 psig. All other factors were controlled to be as close as possible. The effect of pressure is clearly present in current density, however it is less pronounced than one had initially hoped it would be. The average current density for the

atmospheric pressure experiment worked out to be 7.7 mA/cm^2, while the experiment at 300 psig worked out to be 13.3 mA/cm^2, for a 1.7 fold improvement after a 20 fold increase in CO_2 concentration, improving the overall selectivity.

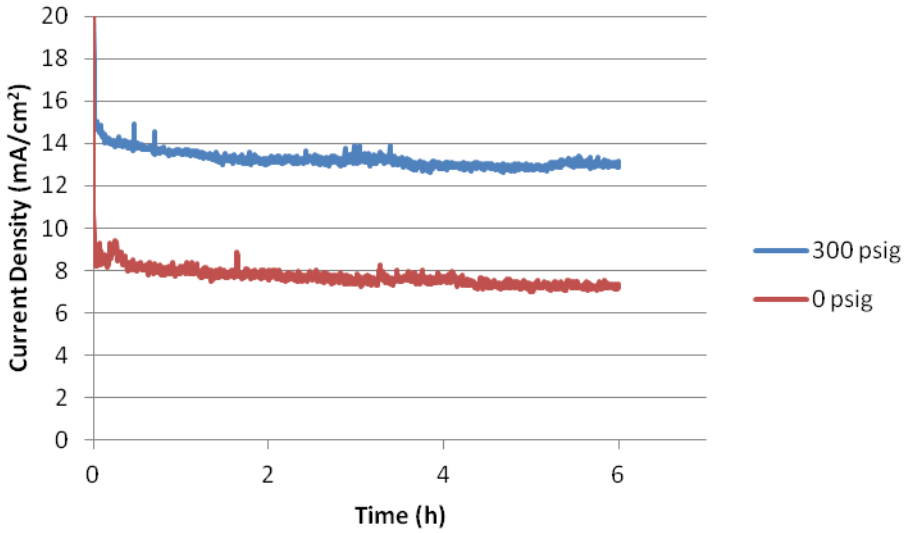

Figure 4.48 Effect of Pressure on Flow System on a Lead Electrode at 3.3 V

HER was detected to account for 56% of the current density at 0 psig, while it only accounted for 23% at 300 psig. Although a substantial boost in performance was achieved by moving to a high pressure flow system, the monumental improvement that had been reported in the literature was not reached. If one compares the results at 0 psig in the present flow system to those in the three electrode cell reported earlier, however, the current density did improve by a factor of ~4.4, however these conditions are drastically different. Overall, then, the improvement from moving from a 3-electrode glass cell to a high pressure flow reactor was ~7.6 based on current density alone on this particular experiment. These data suggest that, while there is some performance to be gained by increasing the concentration of CO_2 at the electrode, conditions where the reduction is no longer limited by CO_2 concentration were reached.

One of the first things that was noticed with CO_2 reduction on tin was significant CO evolution depending on the conditions. Most reports in the literature give exclusively formate, with some measuring very small levels of CO and higher reduction products. While higher reduction products (such as formaldehyde, for example) were not observed, very large fractions of CO were produced in experiments conducted on tin, with many experiments giving as much or more CO as formate. The general consensus about the electrochemical reduction of CO_2 on lead and tin is that it proceeds through an indirect pathway, i.e. that CO_2 does not come into close contact with the electrode surface. Using this reasoning, it seems likely that lead and tin should not exhibit much selectivity for either of these $2e^-$ reduction products. Despite this seemingly natural extension, most reports in the literature demonstrate very high selectivities for formate while using lead or tin. Given that the only significant difference between the current results and their results has to do with the Nafion-based MEA that was utilized in the present study, it could be that the electrolyte has more to do with CO_2 reduction than what has been previously understood.

With the improvement in performance more limited than initially hoped, other controllable factors were probed, which could improve the performance of CO_2 reduction to formate on lead and tin while retaining the scalable high pressure flow design. Table 4.12 lists 31 experiments in which catalyst, catalyst particle size, membrane composition, catholyte composition, anolyte composition, cell potential, pressure, temperature, and flow rate were modified to determine the best set of conditions for reaction of CO_2 to formate. Some reaction conditions were excluded from the table for the sake of readability. Exceptional experiments have been highlighted in red for high current density, high formate faradaic efficiency, high CO faradaic efficiency, or high hydrogen evolution faradaic efficiency. Due to the drastically different methods used to measure effluent composition (GC and NMR), the total faradaic efficiency does not always add up to 100%, but it generally comes close.

Table 4.12 CO_2 Reduction on Tin and Lead at Elevated Pressure

	Electrode	Membrane	Catholyte	Anolyte	Cell Potential (V)	Cathode Pressure (psig)	Current Density (mA/cm^2)	Formate (%)	CO (%)	H_2 (%)	Total (%)
1	100 mesh Sn	Nafion-H	CO_2	0.1 M LiOH	3.3	300	23.7	27%	36%	29%	92%
2	100 mesh Sn	Nafion-H	CO_2	0.1 M LiOH	3.3	300	17.8	34%	54%	10%	98%
3	100 mesh Sn	Nafion-H	CO_2	0.1 M LiOH	3.3	300	13.8	29%	57%	11%	97%
4	100 mesh Sn	Nafion-H	CO_2	0.1 M LiOH	3.6	300	24.2	39%	51%	10%	100%
5	300 mesh Pb	Nafion-H	CO_2	0.1 M LiOH	3.3	300	13.4	48%	0%	19%	68%
6	300 mesh Pb	Nafion-H	CO_2	0.1 M LiOH	3.3	300	7.9	29%	0%	23%	51%
7	300 mesh Pb	Nafion-H	CO_2	0.1 M LiOH	3.3	300	13.3	37%	26%	23%	86%
8	300 mesh Pb	Nafion-H	CO_2	0.1 M LiOH	3.6	300	14.6	39%	29%	21%	89%
9	Sn plated on Pb	Nafion-H	CO_2	0.1 M LiOH	3.3	300	12.3	28%	34%	27%	89%
10	Sn plated on Pb	Nafion-H	CO_2	0.1 M LiOH	3.3	300	11.0	28%	46%	19%	94%
11	Sn plated on Pb	Nafion-H	CO_2	0.1 M LiOH	3.3	300	11.2	26%	0%	0%	26%
12	100 mesh Sn	Nafion-H	CO_2	0.1 M LiOH	3.3	300	14.2	32%	49%	14%	95%
13	100 mesh Sn	Nafion-H	$CO_2 + H_2O$	0.1 M LiOH	3.3	300	12.3	35%	48%	9%	92%
14	100 mesh Sn	Nafion-H	$CO_2 + H_2O$	0.1 M LiOH	3.3	300	19.9	30%	43%	15%	88%
15	100 mesh Sn	Nafion-H	$CO_2 + H_2O$	0.1 M LiOH	3.3	300	10.7	31%	51%	12%	95%
16	100 mesh Sn	Nafion-H	$CO_2 + H_2O$	0.1 M LiOH	3.3	300	9.4	28%	88%	21%	137%
17	100 mesh Sn	Nafion-Li	CO_2	0.1 M LiOH	3.3	300	76.8	7%	9%	84%	100%
18	100 mesh Sn	Nafion-Li	CO_2	0.1 M LiOH	3.3	300	67.0	7%	13%	69%	90%
19	100 mesh Sn	Nafion-Li	CO_2	0.1 M LiOH	3.3	300	30.6	25%	50%	13%	88%
20	100 mesh Sn	Nafion-Na	CO_2	0.1 M NaOH	3.3	300	79.9	13%	16%	68%	97%
21	100 mesh Sn	Nafion-Na	CO_2	0.1 M NaOH	3.3	300	53.8	19%	27%	46%	91%
22	100 mesh Sn	Nafion-Na	CO_2	0.1 M NaOH	3.6	300	132.4	12%	11%	78%	101%
23	100 mesh Sn	Nafion-Na	CO_2	0.1 M NaOH	3.3	450	79.2	15%	18%	49%	82%
24	100 mesh Sn	Nafion-Na	$CO_2 + H_2O$	0.1 M NaOH	3.3	300	53.2	18%	27%	50%	95%
25	100 mesh Sn	Nafion-Na	CO_2	H_2O	3.3	300	55.5	1%	7%	85%	92%
26	<150 nm Sn	Nafion-H	CO_2	0.1 M LiOH	3.3	300	97.2	10%	13%	72%	95%
27	<150 nm Sn	Nafion-H	CO_2	0.1 M LiOH	3.3	300	71.2	8%	11%	73%	92%
28	<150 nm Sn	Nafion-H	CO_2	0.1 M LiOH	3.3	450	78.3	11%	12%	54%	77%
29	<150 nm Sn	Nafion-H	CO_2	0.1 M LiOH	3.6	300	121.3	6%	5%	86%	96%
30	<150 nm Sn	Nafion-H	CO_2	0.1 M LiOH	3.0	300	26.2	17%	28%	31%	77%
31	<150 nm Sn	Nafion-H	CO_2	0.1 M LiOH	3.6	450	68.0	11%	13%	77%	101%

The electrocatalyst has quite a significant effect on the reaction, with tin generally giving higher current density at equivalent conditions, while lead generally gave higher formate efficiency with lower current density. Smaller particle size (going from 100 mesh tin particles to <150 nm tin particles) gave higher current density, but at the expense of formate efficiency.

While higher current density was expected given the higher absolute surface area, lower formate efficiency was not expected because particle size should not impact selectivity. The idea of tin plating a lead powder electrode was also probed in entries 9 through 11. There do not appear to be any synergistic effects from the combination of tin and lead, at least in the way that they were combined them through first painting lead on toray carbon paper, followed by electroplating tin.

Membrane composition was a factor that produced very interesting results. Nafion is typically sold in the sodium ion form, which is then typically treated with a sequence of sulfuric acid and hydrogen peroxide steps to produce the proton form. This process was reversed in several experiments by boiling the membrane in 1 M NaOH or LiOH before pressing the MEA. Since the experiments being conducted had already switched to using either 0.1 M NaOH or 0.1 M LiOH as an anolyte, much change was not expected by using this pre-treatment method. Surprisingly, it was found that significantly increased current density was the result of either Nafion-Li or Nafion-Na pre-treated membranes. Unfortunately, this was also coupled with significantly higher hydrogen evolution, therefore the formate efficiency plunged. Despite this, the amount of formate being produced on a geometric basis actually increased compared to some of the previous experiments with much higher formate efficiencies. For example, in entry 4, 39% formate efficiency and 24.2 mA/cm^2 current density were observed, for 9.4 mA/cm^2 formate current density. In entry 22, 12% formate efficiency and 132.4 mA/cm^2 were observed, for 15.9 mA/cm^2 formate current density. Both of these experiments were conducted using the same electrocatalyst with otherwise almost identical conditions, except for the pre-treatment of the membrane with boiling 1 M NaOH for entry 22. Similar experiments for LiOH produced similar results, however the current densities were higher with NaOH-treated membranes.

For some time, there was a concern that not enough water was present on the cathode side of the MEA because dry CO_2 was used under standard conditions. While water is the source of hydrogen evolution and undesirable for that reason, it is essential to CO_2 reduction because formate cannot be produced without the proton from water. Two ways to mitigate this potential issue were developed; the first is to use an overpressure on the anode side of 5-15 psi to "push" water through the membrane. This approach yielded mixed results, however a 5 psi overpressure was uilized as our standard condition for the reactions described in Table 4.12. The next idea was to use a second HPLC pump to introduce water with the pressurized CO_2 stream on the cathode side at a very low flow rate. A flow of 0.05-0.15 mL/min water on the cathode was tried, but variable results were observed. Experiments 12-16 demonstrate some of the results, where lower current densities were observed after adding water, as well as variable amounts of CO and H_2. Interestingly, virtually no change whatsoever was observed for the formate efficiency.

The composition of the fluid on the anode side of the reactor was also varied to observe the effects, mostly using 0.1 M LiOH. One example of pure water is given, entry 25, where 85% hydrogen was detected and only 1% formate. This further reinforced ther earlier conviction that acidic Nafion does not facilitate efficient CO_2 reduction.

Cell potential was not investigated as thoroughly as with the syngas system, however experiments with 3.6 and 3.0 V cell potential instead of our standard 3.3 V were performed. One can expect the system to give higher current density with increased cell potential, however higher formate efficiency in some cases (entry 4, for example) was observed when increasing the

potential. This effect could not be replicated with different electrodes, however, so it appears to be specific to the electrocatalyst.

Increasing pressure much above 300 psig did not significantly affect the results, although in some cases modest increases in either formate efficiency or current density were observed, but not both. The explanation for this is likely that the experiments are not limited by CO_2 concentration at the electrode at 300 psi, and that there is some other factor that is limiting our CO_2 reduction current density. Increasing flow rate, the other way to increase CO_2 availability, gave mixed results and is not shown in Table 4.12. Experiments doubling the flow rate from 30 mL/min to 60 mL/min were performed, but did not give significant benefits. Slowing down the flow to 15 mL/min slightly decreased the formate efficiency, however.

CO_2 Reduction on Tin Over a Wide Current Density Range

In an attempt to better understand CO_2 reduction on a tin electrode in the present system, a broad range of current densities, from 3 mA/cm^2 to 500 mA/cm^2, was investigated. By controlling the current instead of the voltage, variability due to resistance was minimized. The experiments were run in a random order to ensure that temporal effects would not present themselves. Based on the new knowledge of the dependence of CO_2 reduction efficiency on flow rate, flow was increased to 60 mL/min to minimize this effect. Figure 4.49 plots the results from this series of experiments.

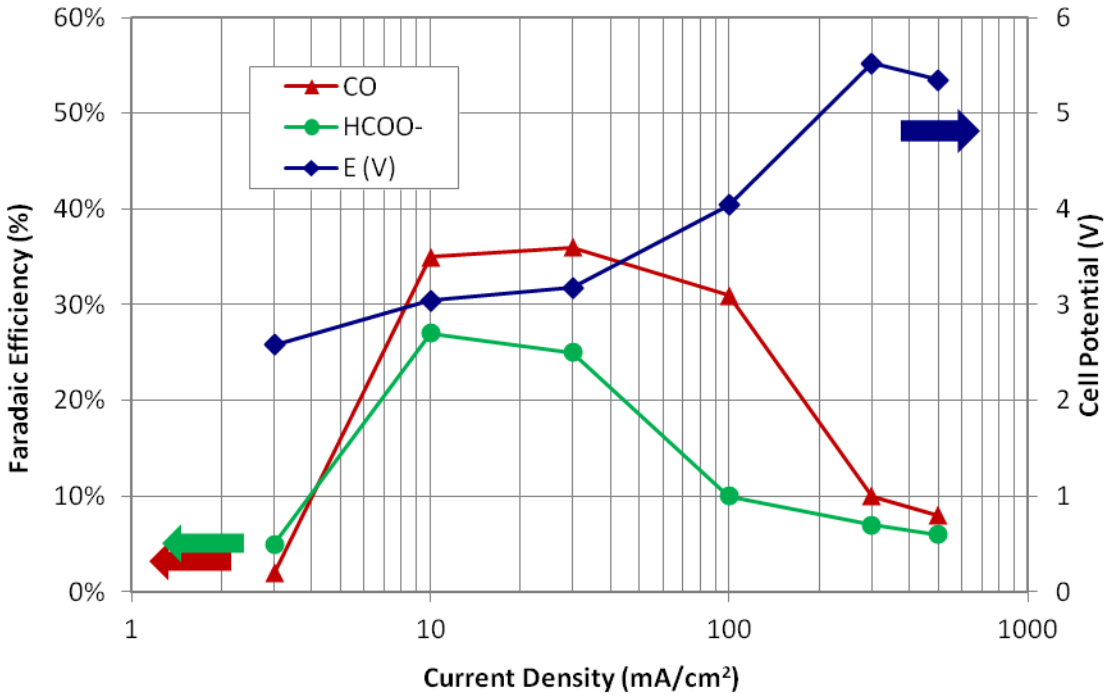

Figure 4.49 Galvanostatic Study on Tin

Conditions: All experiments carried out galvanostatically for 2 hours, <150 μm Sn on 10% Teflonized Toray paper cathode, Pt on non-Teflonized Toray paper anode, Nafion 117 membrane, 450 psig cell pressure, 60 mL/min CO_2 flow rate across the cathode, 2 mL/min 0.1 M NaOH flow rate across the anode, 40 °C.

As expected, the average voltage increases nearly linearly with logarithmic current density increase. Faradaic efficiency for formate peaks at 10 mA/cm^2, while faradaic efficiency for CO peaks at 30 mA/cm^2. Interestingly, CO is always the favored CO_2 reduction product, except at the lowest current density, where the results are not very reliable due to detection limits. The shape of the CO and formate curves are similar, however CO appears to be favored over a broader range of current densities than formate. Another interesting point is the 100 mA/cm^2 data point, where 30% faradaic efficiency for CO at 4.0 V was observed. This is the first time that reasonable potential and current density were simultaneously observed in the system. This particular experiment also produces CO at a higher rate than what was observed on a gold electrode. Typically on gold, potentials this high would lead to much higher H_2 formation.

High Pressure Flow Electrolysis of CO_2 to CO

The investigation began by studying the potential dependence of CO_2 reduction on gold, as was done previously at atmospheric pressure. Chronoamperometric experiments were carried out at various potentials, as depicted in Figure 4.50. One important point to take note of is that a reference electrode is not present in the high pressure flow system, so the full cell potentials are reported, rather than potentials of just the gold electrode. A rough assumption that oxygen evolution on our platinum anode takes place at ~+1.5 V can be made, so subtracting 1.5 V from

the values reported here will give values that have some meaning compared to those reported at atmospheric pressure vs. Ag/AgCl. These experiments were carried out with a gold cathode at 18 mg/cm^2 on 10 % teflonized toray carbon paper with a platinum black on non-teflonized toray carbon paper anode using Nafion-117 at 300 psig with 15 mL/min CO_2 flow across the cathode, 2 mL/min 0.1 M LiOH flow across the anode at 50 °C.

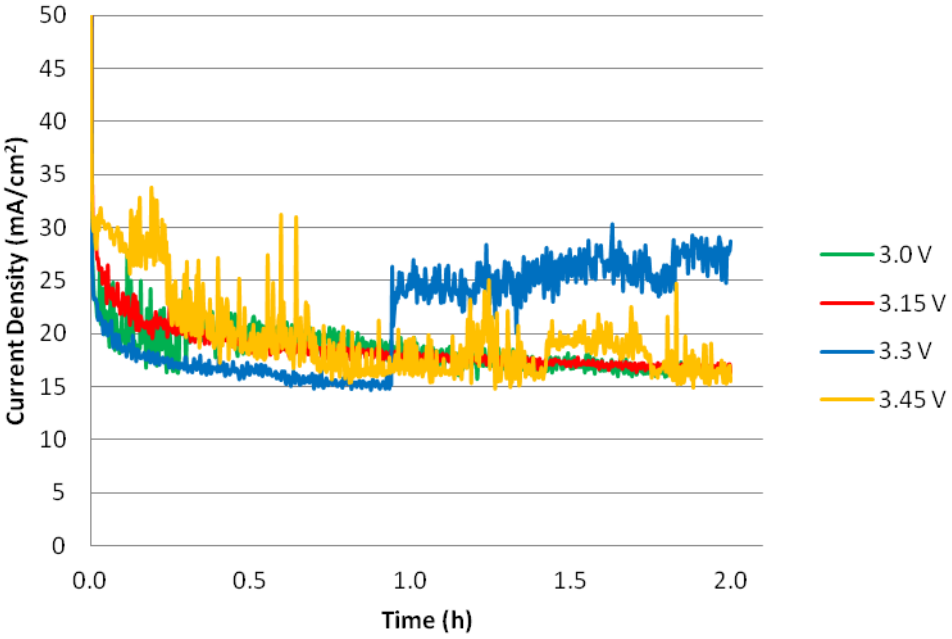

Figure 4.50 Chronoamperometry for Syngas Production on Gold at Various Potentials

Initially, these data were encouraging, as the current densities were quite a bit higher than previously observed for comparable electrodes at ambient conditions. The amount of "noise" in the current traces was a concern, however, especially since it appeared to increase with increasing potential. Also, the step change in the 3.3 V experiment at ~1 hour was not a good sign of a stable system. Despite this, enough information about the CO and H_2 formation was obtained from the GC, which is presented in Figure 4.51.

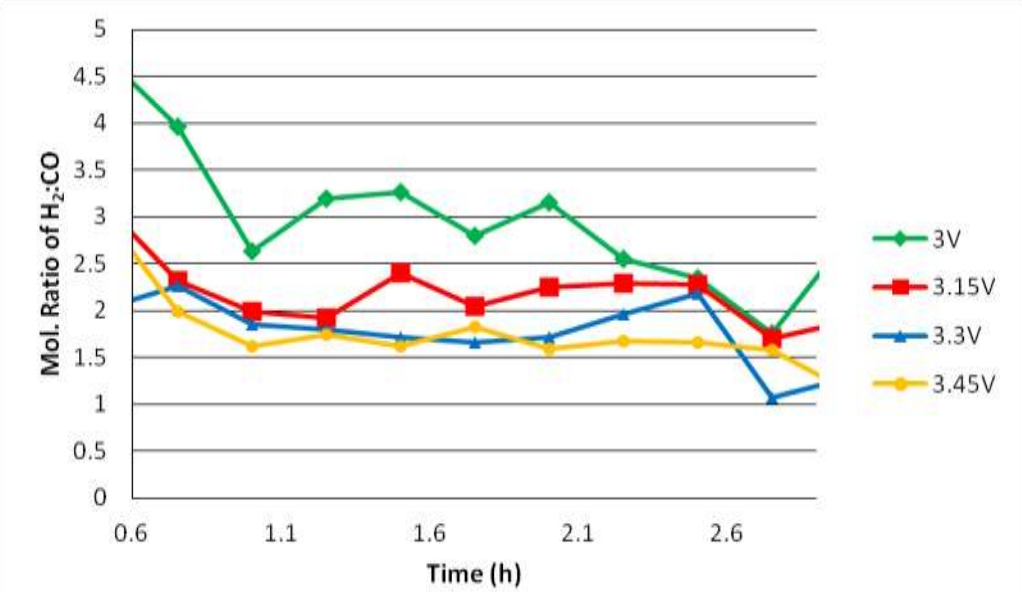

Figure 4.51 Ratio of H_2:CO as a Function of Time at Various Potentials on Gold

One very encouraging result from these experiments is that the ratio of H_2:CO at 3.15 V, 3.3 V, and 3.45 V are all very close to 2:1. Although high current densities (>5 fold improvement over the results at atmospheric pressure) and approximately the desired ratio of 2:1 H_2:CO were achieved, the overall process was not stable from an electrochemical standpoint at least. This stability was addressed by a series of small improvements to the system. First, both sides of the stainless steel plates were coated with polyethylene to ensure that no steel was in contact with Nafion. Second, the pressure on the anode side of the reactor was increased by 5 psi to increase the availability of water on the cathode side. Third, a denser grade of graphite was used for the floating flow field called isomolded graphite. Fourth, the flow rate of the CO_2 was increased to 30 mL/min to quickly sweep bubbles off the surface of the electrode and thus keep the surface area relatively constant. Lastly, the temperature was lowered slightly to 40 °C since this appeared to increase the stability of the system and limit H_2 evolution without significantly harming current density. Figure 4.52 demonstrates the effects of these combined changes.

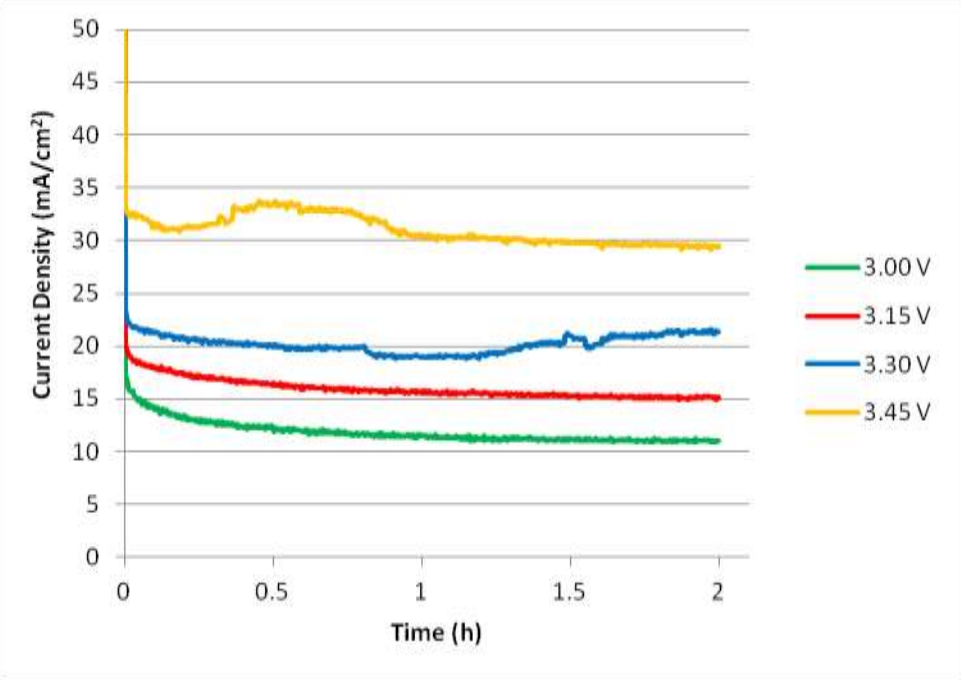

Figure 4.52 Chronoamperometry for Syngas Production with Improved Conditions

More reliable data for H_2 and CO evolution was generated by integrating the amounts detected during the experiment, giving the data presented in Figure 4.53.

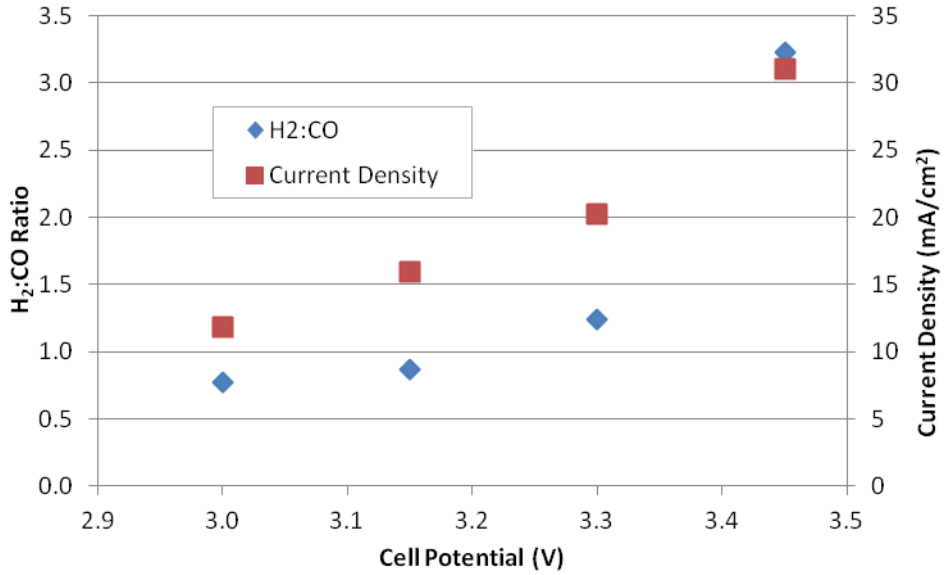

Figure 4.53 Syngas Ratio and Current Density as Functions of Cell Potential

Although the cell was not operated at a ratio of exactly 2:1 H_2:CO, the very close relationship between electrode potential and H_2:CO ratio on a gold electrode was once again demonstrated. More than 20 mA/cm^2 current density was also demonstrated when operating at the desired ratio, indicating that current density increased from the atmospheric pressure results by a factor of >5 while simultaneously increasing energy efficiency significantly.

Flow Rate at High Pressure:

In this series of experiments (each using a newly fabricated membrane electrode assembly), the exact effect of pressure was probed by holding all other factors constant and increasing only pressure in 150 psi steps. As one might expect, increased CO_2 pressure (and thus CO_2 concentration) increases the percentage of CO in the product gas, however the increase did not continue past 300 psig. Since the flow reactor has a fixed pillar design, the amount of mixing in the cell is directly proportional to the volumetric flow rate inside the cell. Flow rates on the cathode have been reported in mL/min CO_2, however this is measured at atmospheric pressure, not at high pressure. Therefore, during the cell operation at 300 psig (21 atm), the volumetric flow inside the cell is ~1.43 mL/min as opposed to 30 mL/min at atmospheric pressure. At 600 psig the volumetric flow rate is only 0.71 mL/min, which is less than half of the volumetric flow on the anode side. Figure 4.54 shows the faradaic efficiency for CO production as a function of pressure with all other conditions being identical. The CO faradaic efficiency increases dramatically to 56% when the flow was increased to 90 mL/min, which is the highest observed on a gold electrode.

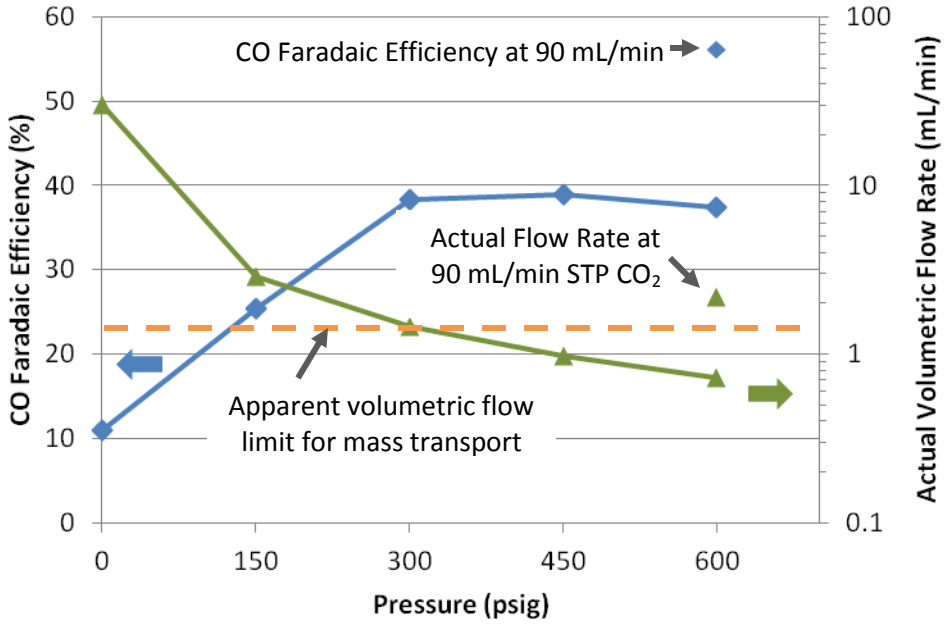

Figure 4.54 CO_2 Reduction on Gold
Conditions: All experiments carried out galvanostatically at 30 mA/cm^2 for 1 hour, 0.5-0.8 μm Au on 10% Teflonized Toray paper cathode, Pt on non-Teflonized Toray paper anode, Nafion 117 membrane, indicated cell pressure, 30 mL/min CO2 flow rate across the cathode except where indicated, 2 mL/min 0.1 M NaOH flow rate across the anode, 40 °C.

Increasing flow to 90 mL/min at 600 psi is equivalent to ~2.2 mL/min volumetric flow rate at standard conditions. For comparison, the standard conditions of 30 mL/min at 600 psig is equivalent to ~0.73 mL/min at standard conditions. Typically, results such as these would indicate that, at the lower flow rate, a region of mass transport limitation has been reached.

Although more experiments would be needed to be certain of this effect and to explain it more precisely, the qualitative arguments put forth regarding volumetric flow appear to be valid.

Stability of Gold Electrodes:

Based on several reports in the literature,[1] the stability of the performance of CO_2 reduction on gold was probed by running a sequence of 1 hour CO_2 reductions. After the 4th experiment, the anolyte (0.1 M NaOH) was changed for a fresh solution. The two sets of data presented in Figure 4.55 are the ratio of H_2:CO and the cell potential. The cell potential can be influenced by both the gold and the platinum electrodes, however the H_2:CO ratio can only be affected by the gold electrode. After four hours of operation at 30 mA/cm^2, the system had consumed 17.9 mmol of electrons, which would have decreased the concentration of NaOH in the 2.8 L reservoir from 0.1 M to 0.094 M. Because a drop of this magnitude does not appear significant, the possibility that the change in molarity of the base in the anolyte would have a significant effect on the performance had not been considered previously. Although the possibility cannot be ruled out that other factors contributed to the increase in CO_2 reduction efficiency on the addition of fresh 0.1 M NaOH on the anode, it is interesting that some of the CO_2 reduction efficiency was retrieved after switching to fresh electrolyte for the 5th experiment.

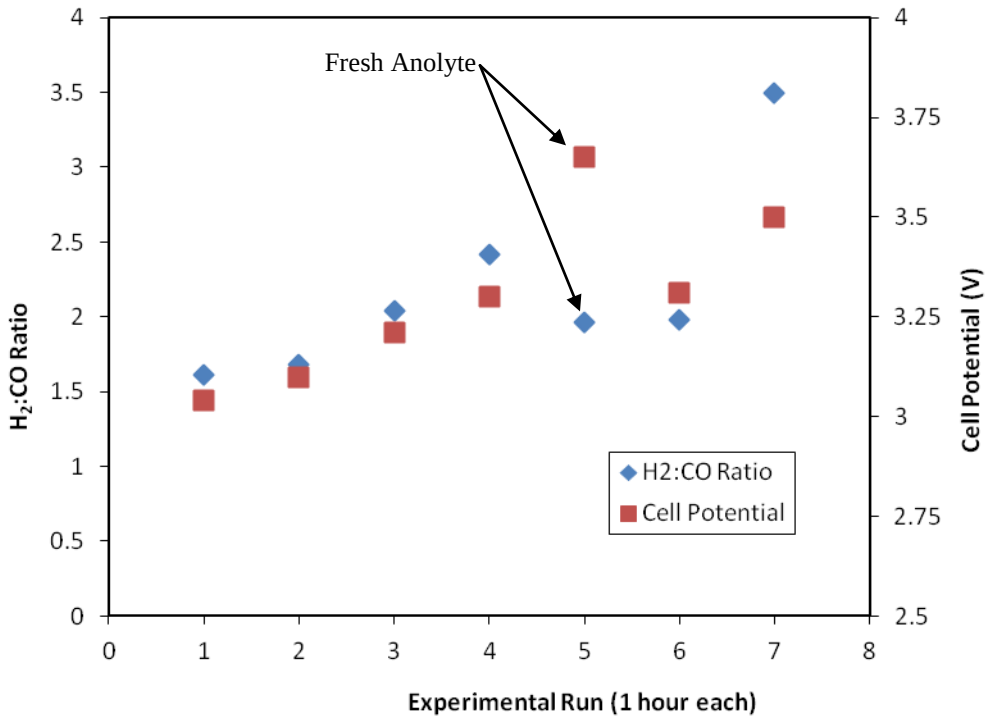

Figure 4.55 Stability of Gold for CO_2 Reduction
Conditions: All experiments carried out galvanostatically at 30 mA/cm^2 for 1 hour, 0.5-0.8 μm Au on 10% Teflonized Toray paper cathode, Pt on non-Teflonized Toray paper anode, Nafion

[1]A good discussion of the poisoning effects of CO_2 reduction on Au and Ag electrodes can be found here: C. Delacourt, P. L. Ridgway, J. B. Kerr, and J. Newman, *J. Electrochem. Soc.*, **155**, B42 (2008).

117 membrane, 300 psig cell pressure, 30 mL/min CO_2 flow rate across the cathode, 2 mL/min 0.1 M NaOH flow rate across the anode, 40 °C.

Despite the initial increase in CO_2 reduction efficiency on the 5^{th} cycle, the cell potential increased significantly and became erratic in subsequent experiments. By the 7^{th} cycle, it was clear that the MEA was beginning to show significant signs of degradation, and no further experiments were pursued.

Electrochemical CO_2 Reduction with a Tokuyama Hydroxide Conducting Membrane:

Given that the focus was entirely on CO_2 reduction in basic media, it seemed prudent that the reaction be tested using a hydroxide conducing membrane instead of a cation conducting membrane like Nafion. Since negative ions flow though the membrane instead of positive ions, one issue with this setup is that the flow of ions is opposite to the usual case with Nafion. Hydroxide ions will be formed on the cathode as a by-product of CO_2 reduction, and these ions must then flow through the membrane to be oxidized to O_2 at the anode. To provide the necessary water molecules to the cathode of the reactor, a second HPLC pump was connected that delivered 0.15 mL/min of 0.1 M NaOH to the cathode in addition to 30 mL/min CO_2.

Although current flow was observed when a tin electrode in a Tokuyama MEA was tested, only trace formate was detected in the gas-liquid separator. Despite this, <50% of the current could be accounted for by analyzing the effluent gasses (for H_2 and CO) by GC. Thinking about this further, it was surmised that the formate ions are most likely migrating into the Tokuyama membrane instead of making their way to the gas-liquid separator. In the case of a Nafion membrane, anionic species like formate are rejected from the membrane because they carry the same charge as the sulfonic acid groups on the surface. With the Tokuyama membrane, the positively charged alkyl ammonium groups attract the formate ions that are produced on a tin electrode during CO_2 reduction.

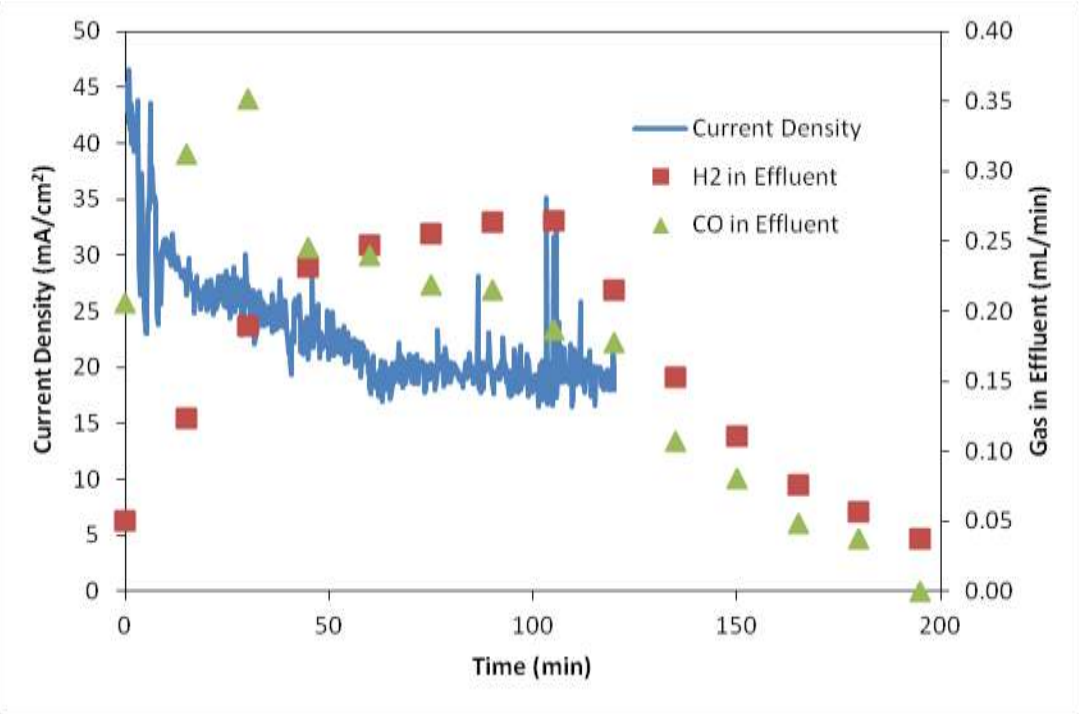

Figure 4.56 CO_2 Reduction using the Tokuyama Membrane
Conditions: Carried out potentiostatically at 3.3 V for 2 hours, 0.5-1.0 μm Ag on 10% Teflonized Toray paper cathode, Pt on non-Teflonized Toray paper anode, Nafion 117 membrane, 300 psig cell pressure, 30 mL/min CO_2, 0.15 mL/min 0.1 M NaOH flow rate across the cathode, 2 mL/min H_2O flow rate across the anode, 50 °C.

Since no formate formation was observed while reducing CO_2 in a Tokuyama membrane, attention was turned to reducing CO_2 on silver to generate CO instead of formate. Presumably, CO would not be trapped by the membrane as was the case with formate. Figure 4.56 gives the results of one experiment, showing the current density, H_2 and CO flow in the effluent. An average of 23.0 mA/cm^2 over 2 hours was observed, with 47.5% CO faradaic efficiency and 44.9% H_2 faradaic efficiency. These figures fall fairly well in line with other experiments previously performed under similar conditions using Nafion instead of the Tokuyama membrane. Unfortunately, it appears that CO production starts off as the major product of the reaction, but drops of significantly after 45 minutes and falls gradually until the end of the reaction. The current density also falls considerably from the initial state, where it appeared to start close to 45 mA/cm^2. This decreasing performance could be partially due to catalyst deactivation, as has been suggested for gold electrodes evolving CO.

Conclusions

A high pressure flow electrolyzer was successfully built from the ground up to study the effects of flow and pressure on CO_2 electrolysis to formate and CO. The studies managed to improve the current density of CO_2 reduction to formate from the initial conditions at 1.76 mA/cm^2 to 24.2 mA/cm^2 for similar electrodes, a 13.8 fold improvement. Based on extensive system development and testing, certain suggestions can be made on achieving either high efficiency CO_2 reduction (Nafion-H membrane) or high rate electrolysis (Nafion-Na) coupled

with CO_2 reduction to either formate or CO. The high efficiency conditions gave 89% CO_2 reduction efficiency, however this was essentially split evenly between formate and CO. The high rate electrolysis gave 132.4 mA/cm^2 current density, however the CO_2 reduction efficiency dropped to 23%. Increased pressure will likely not give results much better than this, and most of the engineering-related improvement possibilities can be ruled out for increasing selectivity or rate. Success in this project will likely require significant development either towards improving the catalysts so that they are more selective at high rates, or changing the electrolyte, which the results suggest strongly influences CO_2 reduction.

The high pressure flow electrolyzer is capable of operating at significantly higher current density than a batch reactor at atmospheric pressure using a gold electrode. While ~3 mA/cm^2 at -2.0 V vs. Ag/AgCl to achieve 2:1 H_2:CO under atmospheric pressure was observed, ~20 mA/cm^2 at -3.3 V cell voltage at 300 psig was observed. Thus, the improvement was ~6.7 fold increase in current density while maintaining the desired syngas composition. Higher pressures may lead to higher faradaic efficiency towards CO, however only when coupled with higher flow rates, as was demonstrated in Figure 4.54. Gold was also determined to have some significant durability issues, however, whereby selectivity for CO_2 reduction drops off considerably after an electrolysis period of as little as 30 minutes.

An unexpected set of conditions to generate CO at a high rate were discovered using a tin electrode operating at 450 psig at 100 mA/cm^2, where ~2:1 H_2:CO is generated at 90% faradaic efficiency and 4 V. Although this cell potential is significantly higher than what was achieved for a similar product composition using gold (3.3 V), syngas is produced 5 times faster. In addition to this, although exhaustive testing of the durability of tin catalysts has not been performed, they do not appear to exhibit the severe degradation characteristics of gold over such a short period of time. If this new set of conditions is taken into account and compared to the original values for gold at atmospheric pressure, the current density has increased 33 fold.

The Tokuyama hydroxide conducting membrane was also tested for use in a CO_2 electrolyzer, and it performed similarly to a basic Nafion membrane, although it exhibited slightly less system stability. This may be related to the suboptimal experimental setup for this type of membrane, however, since the ionic flow is reversed for a hydroxide conducting membrane. Further experimentation would definitely be required to determine whether or not there are significant advantages to using hydroxide conducting membranes.

Task 5: Utilization of Formic Acid as a Feed-stock and Fuel in Fuel Cells

Background

Research activities on the development of alternative procedures to synthesize FA are not only fuelled by the demand on FA as an industrial intermediate but also by the potential application of FA as a hydrogen/energy storage material and as a fuel that can be used in direct and indirect formic acid fuel cells.

The purpose of this sub-project was to develop highly active and selective catalysts for the decomposition of FA to hydrogen and carbon dioxide, which can be directly used in hydrogen/air fuel cells to produce electricity.

The decomposition of formic acid may take place via two main pathways (a) decarboxylation giving carbon dioxide and hydrogen and (b) dehydration providing carbon monoxide and water (Figure 5.1). The latter reaction must be suppressed because carbon monoxide may poison the noble metal catalysts of fuel cells.

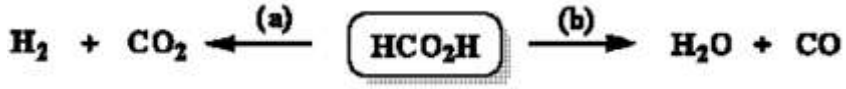

Figure 5.1 Decarboxylation (a) and decarbonylation of FA (b).

Development of homogeneous catalysts with high activity for the selective decarboxylation of FA while at the same time suppressing the decarbonylation has received increasing attention. A ruthenium catalyst developed by Beller *et al*. which is formed *in situ* from $RuX_3 \cdot xH_2O$ (X=Cl, Br) in the presence of triethylamine (TEA) and PPh_3, exhibited one of the highest activities reported for FA decomposition (TOF=3630 h^{-1} after 20 minutes at 40 ºC).[1] Another outstanding example was reported by Laurenczy *et. al* in 2009 using $[Ru(H_2O)_6](tos)_2]$, $[Ru(H_2O)_6](tos)_3]$ or $RuCl_3$ in an aqueous solution of FA/Na-formate (9:1) (TOF=460 h^{-1}) and *meta*-trisulfonated triphenylphosphine (TPPTS) as catalyst precursors.[2] Although these systems showed excellent performance, their large-scale application may bring up feasibility concerns due to the relatively high cost of both the Ru complexes and ligands. In addition to this, volatile amine additives (e.g. Et_3N) may contaminate the gaseous products, necessitating gas purification before their utilization in a fuel cell.

For the wide practical application of continuous hydrogen generation from FA, the development of more cost effective systems would be essential for example (I) by using less expensive ligands that can be produced on a large scale or (II) development of active catalysts using non-precious metals.

Decomposition of FA in the presence of $RuCl_3$ in aqueous solutions

An aqueous formic acid-sodium formate (9:1) mixture was heated in a high pressure autoclave in the presence of ruthenium trichloride (3.0 mM) at 109 ºC. The pressure increase due to the formation of gaseous products, which was monitored over time (Figure 5.2) and the

reaction rate was determined (22.882×10^{-5} M·s^{-1} at 109ºC). Gaseous products were subjected to GC analysis giving 51.3 % H_2 48.5 % CO_2, 0.21 % CO.

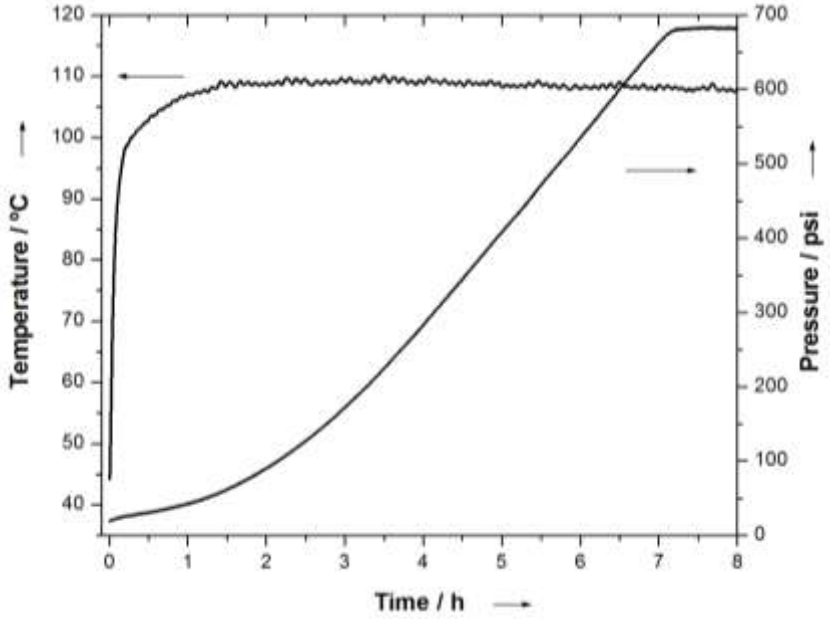

Figure 5.2 Pressure and temperature *versus* time diagram for decomposition of formic acid (FA) in aqueous solution. $[HCO_2H]_0$=3.5 M, $[HCO_2Na]_0$=0.4 M, $[RuCl_3]_0$=3.0 mM.

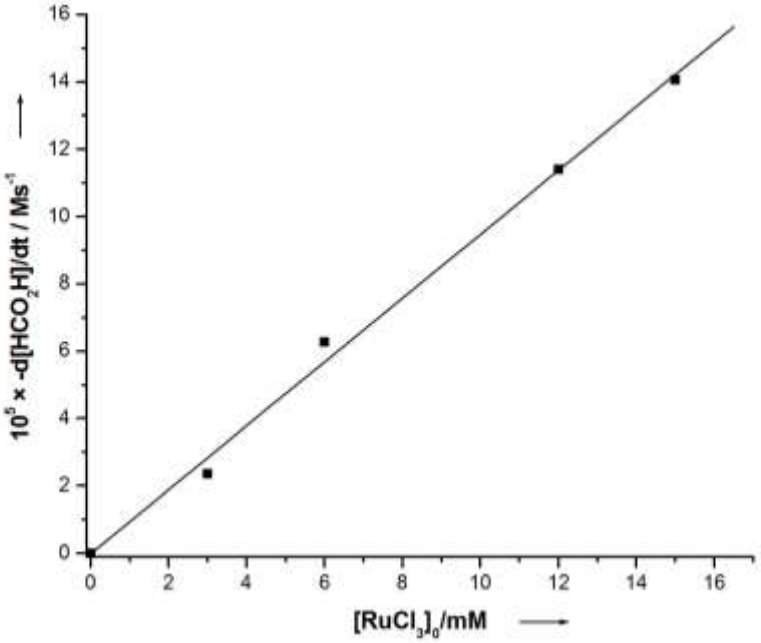

Figure 5.3 Reaction rate of FA decomposition as a function of $[RuCl_3]_0$. $[HCO_2H]_0$=3.5 M, $[HCO_2Na]_0$=0.4 M.

The decomposition of FA was carried out in the presence of different amounts of $RuCl_3$ and it was found that the reaction rate is of first order with respect to $RuCl_3$ concentration (Figure 5.3). The brown catalyst mixture could be recycled and seemed to be active after the addition of neat FA. The second cycle resulted in a yellow reaction mixture from which a yellow crystalline solid was isolated in 67 % yield. A typical five-band absorption at 2080.6, 2065.9, 2029.7, 2023.9 and 2007.8 cm^{-1} has been observed in the IR spectrum (Figure 5.4a) in cyclohexane solution of the complex and assigned to terminal carbonyl ligands. The ^{1}H NMR spectrum in $CDCl_3$ showed an intensive peak at -17.80 ppm (Figure 5.4b) characteristic of metal hydride clusters while a carbonyl peak was observed in the ^{13}C NMR spectrum at 188.97 ppm (Figure 4c).

In accordance with NMR and FTIR results, x-ray diffraction analysis of single crystals grown from CH_2Cl_2-pentane revealed a tetranuclear ruthenium complex $[Ru_4(CO)_{12}H_4]$ (12) consisting of a distorted tetrahedral core (Ru_4) as shown in Figure 4.5.

The distorted geometry reflects in the unequal adjacent Ru-Ru distances exhibiting four long and two short distances. The longer metal-metal distances correspond to Ru-H-Ru bonds, where the hydride is in edge-bridging position while short distances correspond to Ru-Ru bonds.

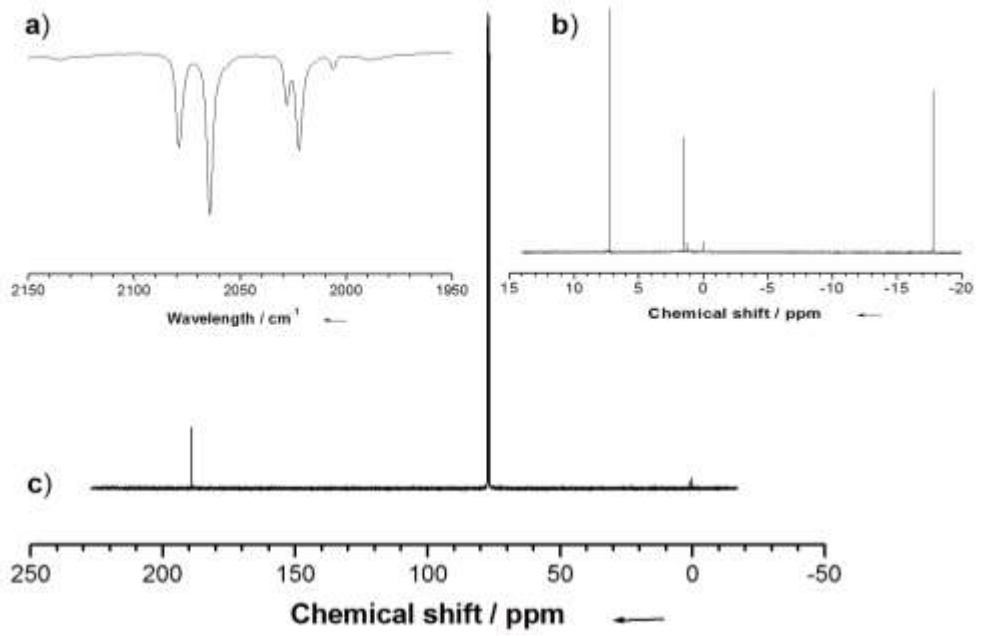

Figure 5.4 Spectroscopic identification of isolated catalyst ($[Ru_4(CO)_{12}H_4]$), a) FTIR spectrum in cyclohexane solution, b) ^{1}H NMR and c) ^{13}C NMR spectra in $CDCl_3$.

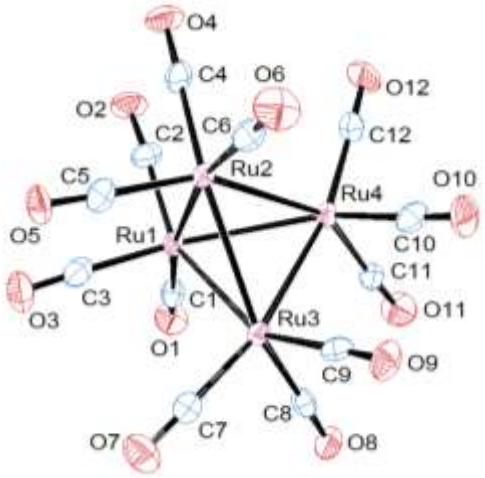

Figure 5.5 Crystal structure of $[Ru_4(CO)_{12}H_4]$. Hydrogen atoms are omitted for clarity.

It was found that $[Ru_4(CO)_{12}H_4]$ *in situ* forms from $RuCl_3$ in the presence of FA and sodium formate. Question arises if $[Ru_4(CO)_{12}H_4]$ is an active catalyst, a direct precursor of the active catalyst or a "dead end" in the catalytic cycle.

For more extensive study of the catalytic activity of $[Ru_4(CO)_{12}H_4]$ for FA decomposition, the complex was prepared in a two step synthesis namely (a) the carbonylation of $RuCl_3$ giving $Ru_3(CO)_{12}$ intermediate and (b) the hydrogenation of $Ru_3(CO)_{12}$ according to a literature procedure (Figure 5.6).

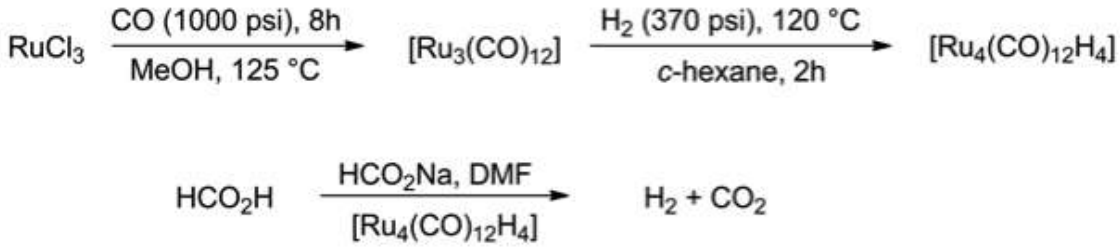

Figure 5.6 Synthesis of $[Ru_4(CO)_{12}H_4]$ from $RuCl_3$.

The decomposition of FA was carried out in DMF in the presence of sodium formate and the synthesized $[Ru_4(CO)_{12}H_4]$ in a high pressure autoclave resulting in a gas mixture of 50.38 % H_2 and 49.62 % CO_2. As indicated in Figure 5.7, FA could be reproducibly decomposed in the presence of $[Ru_4(CO)_{12}H_4]$ at different temperatures (curve a-c) giving the reaction rates of 1.226×10^{-3} M s^{-1}, 2.182×10^{-3} M s^{-1}, 2.098×10^{-4} M s^{-1}, at 106, 79 and 85 ºC respectively.

Figure 5.7 shows the pressure of the gases produced as a function of time. Even though the formation of CO_2 and H_2 results in elevated pressures, the maximum pressures in the first and second run (430 and 1250 psi) are lower than those observed using $RuCl_3$ catalyst under similar experimental conditions (685 and 2225 psi).

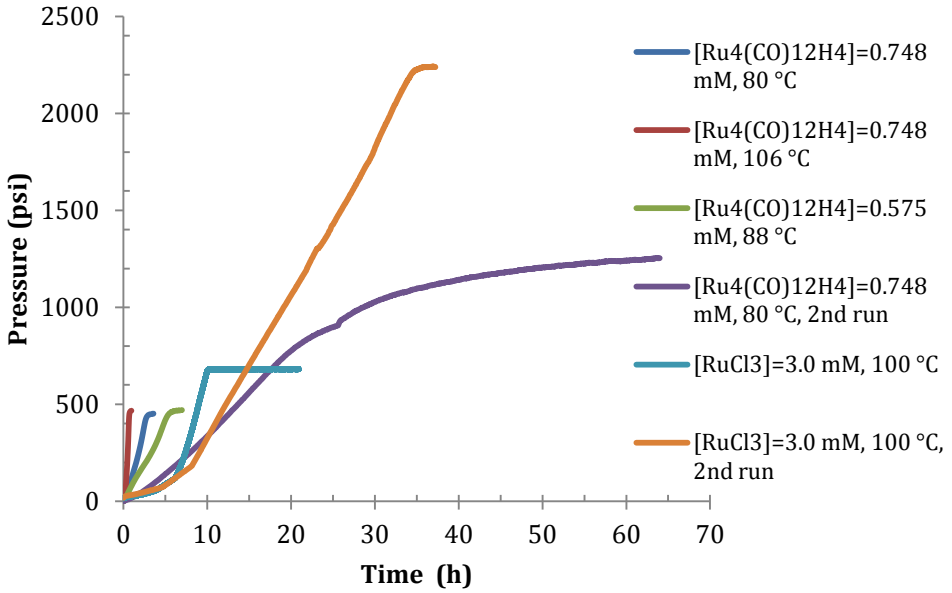

Figure 5.7 Pressure of H_2-CO_2 mixture as a function of time. $[FA]_0$= 3.6 M, $[HCO_2Na]$= 0.4 M, DMF (21.6 mL).

Table 5.1 Decomposition rates and chemical composition of product gas mixture.

Entry	$[Ru_4(CO)_{12}H_4]$ (mM)	Temp. (°C)	Reaction rate ($M\ s^{-1}$)	Gas composition (%) H_2, CO_2, CO
MC-217	0.575	88	9.548×10^{-4}	52.91, 47.09, 0[a]
MC-199 (first run)	0.748	80	2.098×10^{-4}	56.45, 43.48, 0.075
MC-199-2 (second run)	0.748	80	5.448×10^{-5}	61.22, 37.47, 1.31
MC-197	0.748	106	1.226×10^{-3}	64.57, 35.34, 0.084
MC-160	3.0 [$RuCl_3$]	100	3.671×10^{-5}	51.40, 48,37, 0.23

[a]CO level was under the detection limit of TCD.

Rate of FA decomposition was determined at different catalyst concentrations (0.575-3.008 mM) giving a 'bell-shaped' curve as shown in Figure 5.8.

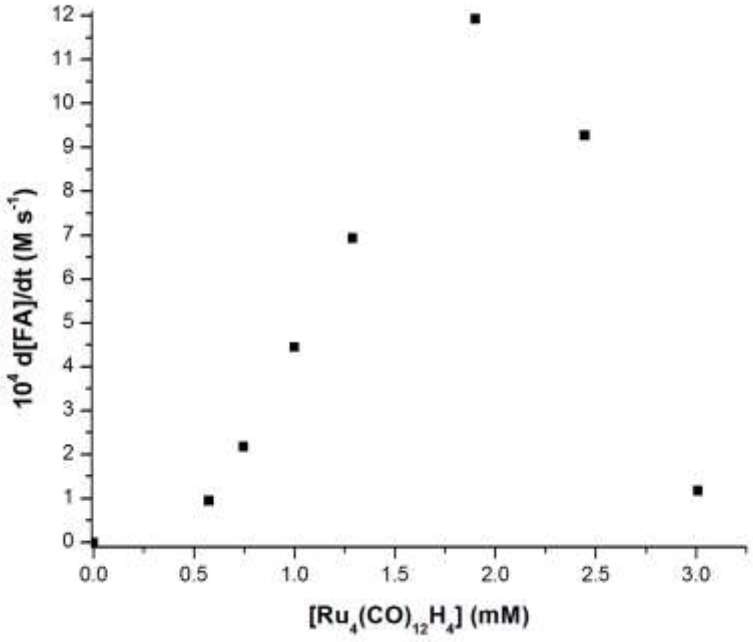

Figure 5.8 Rate of decomposition as a function of catalyst concentration. $[FA]_0$ = 3.6 M, $[HCO_2Na]$ = 0.4 M, DMF (21.6 mL).

Decomposition of FA under atmospheric conditions in the presence of $[Ru_4(CO)_{12}H_4]$ catalyst

Since the utilization of hydrogen in PEM type fuel cells does not require elevated pressures, reaction rate of FA decomposition was also investigated in the presence of $[Ru_4(CO)_{12}H_4]$ under atmospheric conditions.

In a typical experiment, a solution of 0.68 g Na-formate in 4.28 g of FA (97 %) was added to a solution of $[Ru_4(CO)_{12}H_4]$ catalyst in 21 mL DMF giving a total volume of 25 mL. The reaction mixture was transferred to a jacketed glass reactor connected to a jacketed gas burette, which was maintained at a constant temperature using a circulator bath. The custom designed gas volumetric apparatus (Figure 5.9) was used to monitor the change in volume as a function of time in the temperature range, 35 to 50 °C, followed by a repeat measurement at 35 °C to find out whether the catalyst undergoes activation.

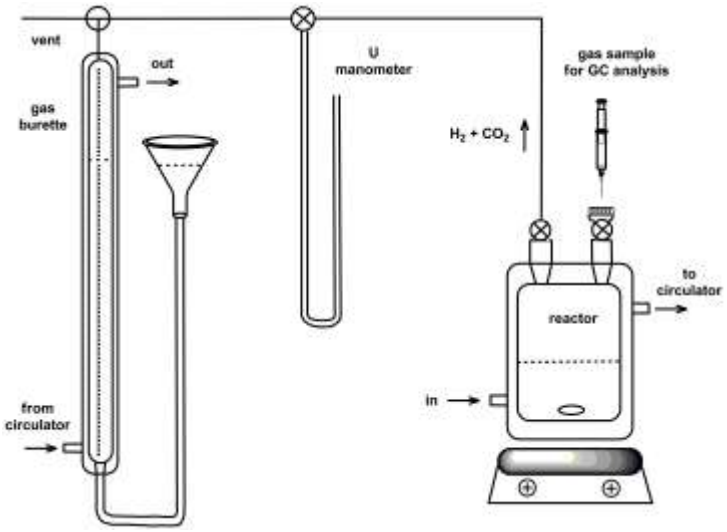

Figure 5.9 Gas volumetric apparatus.

The volume of the H_2-CO_2 mixture at different temperatures is shown in Figure 5.10. One can see that higher reaction rate (5.441×10^{-6} M·s^{-1}) could be measured at 35 °C in the second run than in the first one (2.001×10^{-6} M·s^{-1}) indicating an activation step for the catalyst. The Eyring equation describes the correlation between reaction rate and temperature. Measuring the temperature dependence of the reaction rate permits the determination of the activation parameters and gain a deeper insight into the reaction mechanism. Based on the Arrhenius and Eyring diagrams (Figure 5.11), the activation parameters of the decomposition reaction in the presence of $[Ru_4(CO)_{12}H_4]$ were calculated as follows: $\Delta H^{\ddagger}$ = 28.3 kcal mol^{-1}, $\Delta S^{\ddagger}$ = 30.2 cal mol^{-1} K^{-1}, $\Delta G^{\ddagger}$ = 21.3 kcal mol^{-1} (30 ºC) and E_a=31.3 kcal mol^{-1}. Positive entropy of activation indicates a dissociative rate determining step in which the activated compex is at higher entropy level than the reactants.

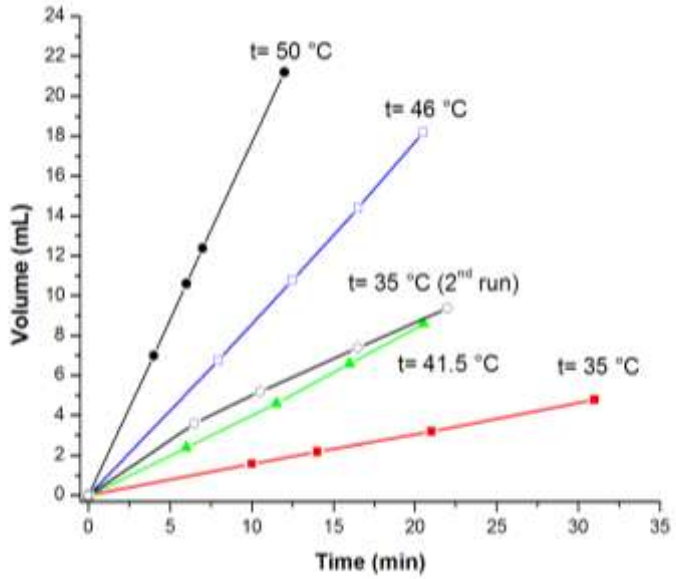

Figure 5.10 Volume of H_2-CO_2 mixture as a function of time at different temperatures. $[Ru_4(CO)_{12}H_4]$ = 0.34 mM, $[FA]_0$= 3.6 M, $[HCO_2Na]$ = 0.4 M, DMF (21.6 mL).

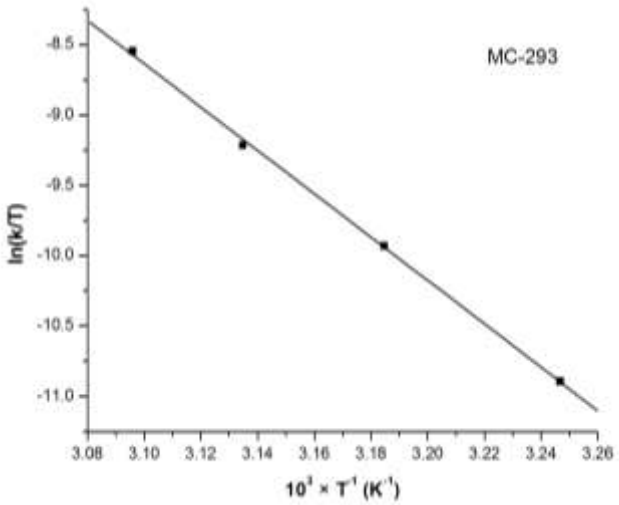

Figure 5.11 Eyring diagram for the decomposition of FA in the presence of $[Ru_4(CO)_{12}H_4]$. $[Ru_4(CO)_{12}H_4]$ = 0.34 mM, $[FA]_0$= 3.6 M, $[HCO_2Na]$ = 0.4 M, DMF (21.6 mL).

In order to design an apparatus for practical use, which can enable feeding hydrogen to a hydrogen fuel cell continuously by decomposition of FA, the catalyst concentration must be carefully selected. Reaction rates were measured in the presence of different $[Ru_4(CO)_{12}H_4]$ concentrations (0.263-1.316 mM) giving an unusual correlation (Figure 5.12) that resembles the one we observed for the decomposition reactions under pressure. The 'bell-shaped' curve indicates that there is an optimal catalyst concentration at each temperature (e.g. 0.850 mM at 41 °C) and that higher catalyst concentration would result in a less effective system.

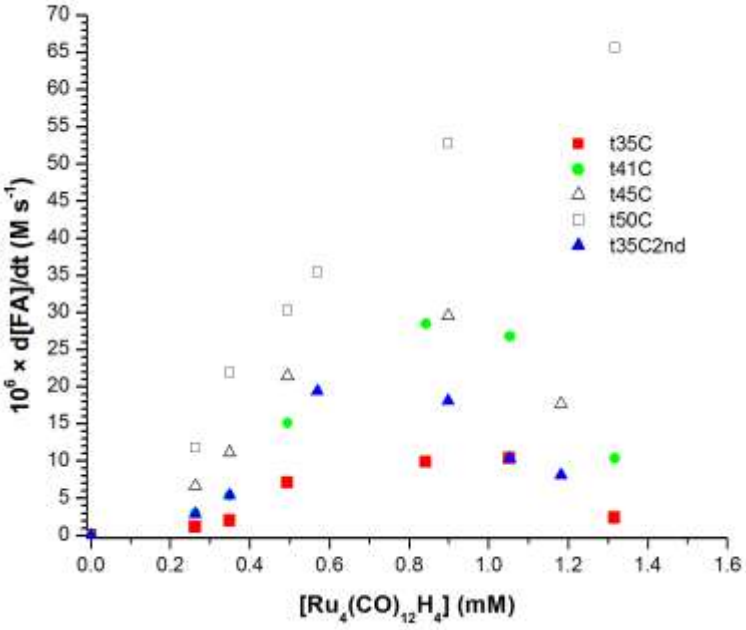

Figure 5.12 Reaction rates of FA decomposition as a function of $[Ru_4(CO)_{12}H_4]$ at different temperatures. $[FA]_0$ = 3.6 M, $[HCO_2Na]$ = 0.4 M, DMF (21.6 mL).

Summary

1) $[Ru_4(CO)_{12}H_4]$ was found to be an active and selective catalyst for FA decomposition under atmospheric conditions.

2) Kinetic measurements proved that there is an optimum $[Ru_4(CO)_{12}H_4]$ concentration for FA decomposition under both high pressure and atmospheric conditions in DMF.

Decomposition of FA in the presence of $RuCl_3$ and PPh_3 derivatives in emulsion

Triphenylphosphine (PPh_3) is a commonly used P-donor ligand in organometallic chemistry. However, its poor solubility in water disfavors its application in aqueous reaction mixtures. On the other hand, transition metal salts like $RuCl_3$ as well as FA and sodium formate are mainly soluble in water. The miscibility of aqueous and organic phases can be enhanced by the addition of surfactants to form emulsions. Even though these emulsions may not be stable over the entire reaction time period due to the dramatic changes in the composition of the reaction mixture, the initial presence of an emulsion can provide the proper medium for the *in situ* formation of active catalytic species.

The aqueous solution of FA, sodium formate and $RuCl_3$ was added dropwise to the vigorously stirred mixture of toluene, PPh_3 and sodium dodecyl sulfate (SDS) followed by sonication of the formed emulsion for 15 minutes at room temperature. The light brown emulsion was then transferred to a high pressure Monel autoclave and heated to temperatures of 90 to 117 °C. The internal temperature of the reactor and the pressure of the gaseous product were recorded using Lab View and the rate of decomposition was calculated on the basis of the pressure *versus* time profiles (Figure 5.13) at various temperatures (e.g. 1.692×10^{-5} $M \cdot s^{-1}$ at 90 °C, Table 5.2). In order to determine the selectivity of the decomposition, the chemical composition of the gas mixture was analyzed by gas chromatography using a thermal conductivity detector (TCD) and in some cases by Fourier transform infrared spectroscopy (FTIR) as well.

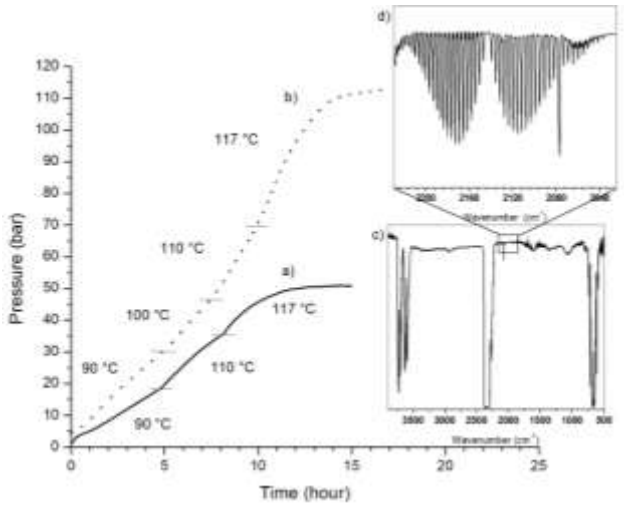

Figure 5.13 Pressure vs. time diagram for the FA decomposition in the presence of $RuCl_3$-PPh_3-SDS; a) first run, b) second run. FTIR spectra of gaseous products (c and d).

Table 5.2 Reaction rates of FA decomposition in the presence of various phosphine ligands and composition of gaseous products.

	Phosphine[a]	t (°C)	10^6 × React. rate ($M \cdot s^{-1}$)	Gas composition (%)[b]		
				H_2	CO_2	CO
1[c]	PPh_3	90	16.920	54.20	45.80	nd
2[d]	PPh_3	90	20.010	56.19	43.56	0.25
3[c]	$P(C_6H_4\text{-}CH_3)_3$	90	13.990	54.71	45.29	nd
4[d]	$P(C_6H_4\text{-}CH_3)_3$	90	7.314	55.70	44.10	0.20
5[c]	$PPh_3 \cdot HBr$	90	30.172	53.46	46.54	nd
6[d]	$PPh_3 \cdot HBr$	90	61.243	51.31	48.69	nd
7[c]	$P(C_6H_4\text{-}Cl)_3$	90	16.288	53.60	46.40	nd
8[c]	$O=PPh_3$ [e]	90	4.428	54.17	45.83	nd
9[d]	$O=PPh_3$ [e]	90	1.096	54.01	45.99	nd
10[c]	$P(C_6H_4\text{-}F)_3$	90	0.579	48.67	47.57	3.76
11[c]	$P(C_6H_4\text{-}F)_3$	110	0.997			
12	no catalyst[f]	117	0.377	39.39	50.58	10.1

[a]$[RuCl_3]$= 2.43 mM, [Phosphine]=5.0 mM, [FA]=3.6 M, $[HCO_2Na]$= 0.4 M, [SDS]= 19.65 mM, 25 mL aqueous solution, 5 mL toluene, [b]determined by gas chromatography using TCD, nd: no CO could be detected. [c]first run, [d]second run. [e]no SDS was added, [f][FA] = 9 × $[HCO_2Na]$=3.6 M, 25 mL aqueous solution, no catalyst.

In another experiment, the emulsion was separated by centrifugation directly after the first run and the aqueous phase was extracted with toluene. In order to understand the nature of the organometallic species formed *in situ* that may contribute to the catalytic activity, the identification of Ru-complexes was carried out directly from the crude reaction mixture. The ^1H NMR spectra of the crude extract showed the presence of unreacted FA and Na-formate, ruthenium coordinated formate, the mixture of PPh_3 and $O=PPh_3$. ^{13}C NMR studies (Figure 5.14) revealed the presence of $[Ru(HCO_2)_2(CO)_2(PPh_3)_2]$ (196.7 (t, 11.2 Hz, CO), 167.5 (s, HCO_2^-)), $[Ru(CO)_3(PPh_3)_2]$ (208.0 ppm (t, 16.1 Hz, CO)) and $[Ru_2(HCO_2)_2(CO)_4(PPh_3)_2]$ complex (204.7 ppm, (t, 4.1 Hz, CO), 176.3 (t, 8.2 Hz, HCO_2^-)).

^{31}P NMR measurements (Figure 5.14d) also confirmed the presence of complex $[Ru_2(HCO_2)_2(CO)_4(PPh_3)_2]$, $[Ru(HCO_2)_2(CO)_2(PPh_3)_2]$, and $[Ru(CO)_3(PPh_3)_2]$ at 12.6, 31.2 and 55.6 ppm, respectively.

The isolated crude catalyst mixture was washed with hexane and recrystallized from chloroform by pentane diffusion. The obtained yellow prisms were characterized by various spectroscopic methods and subjected to X-ray crystal structure analysis.

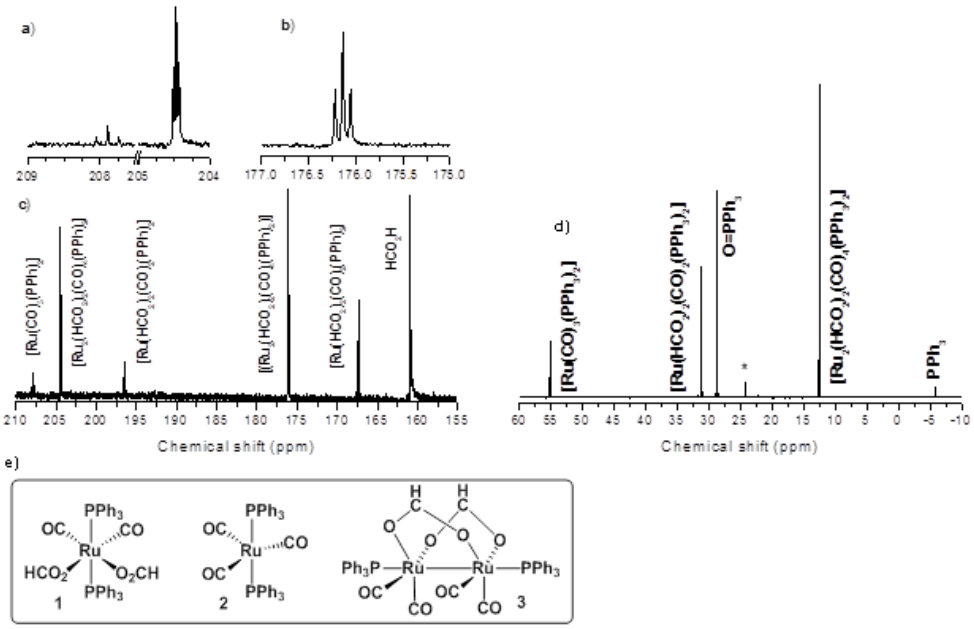

Figure 5.14 ^{13}C NMR (a-c) and ^{31}P NMR spectra (d) of crude catalyst mixture and the structure of the Ru complexes formed *in situ* (e). (*unidentified species).

The ^{1}H, ^{13}C and ^{31}P NMR measurements revealed that these prisms were complex $[Ru(HCO_2)_2(CO)_2(PPh_3)_2]$. The FTIR spectrum of the yellow prisms collected in carbon tetrachloride exhibits intense bands at 2052.8, 1991.1, 1957.0 cm^{-1} due to the stretching vibration of coordinated CO ligands. Furthermore, the bands at 1606.6 and 1300.6 cm^{-1} can be attributed to the asymmetric and symmetric carbonyl stretching vibration of unidentate formate ligand, respectively.

The X-ray crystal structure of the obtained yellow-colored prisms revealed that the mononuclear hexacoordinated Ru(II) compound $[Ru(HCO_2)_2(CO)_2(PPh_3)_2]$ crystallizes together with two molecules of chloroform solvent in the triclinic space group *P*-1 with two symmetry related units in the unit cell (*Z*=2).

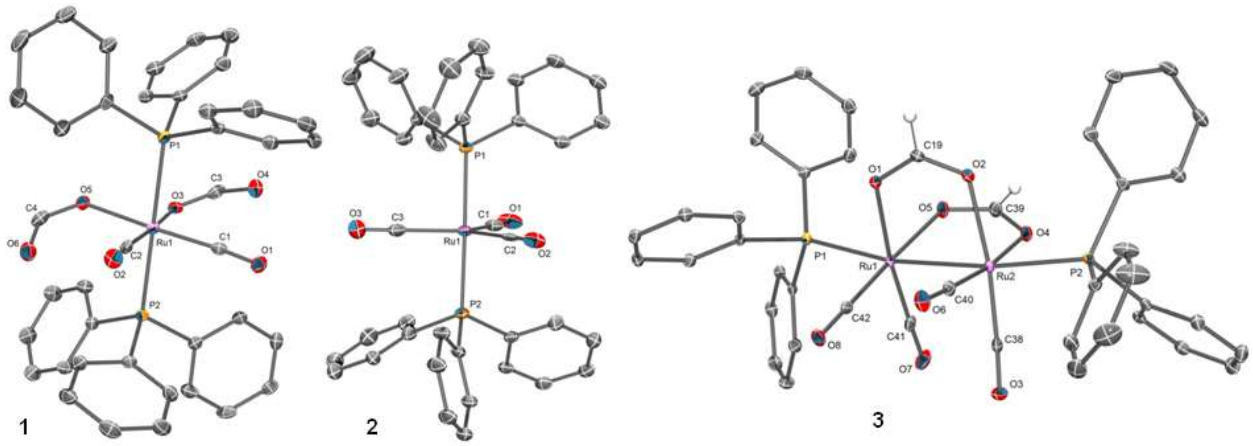

Figure 5.15 Crystal structure of complexes $[Ru(HCO_2)_2(CO)_2(PPh_3)_2]$ (**1**), $[Ru(CO)_3(PPh_3)_2]$ (**2**) and $[Ru_2(HCO_2)_2(CO)_4(PPh_3)_2]$ (**3**). Hydrogen atoms and the solvent molecules have been omitted for clarity. Thermal ellipsoids are drawn at the 50% probability level.

Table 5.3 Crystallographic parameters for $[Ru(HCO_2)_2(CO)_2(PPh_3)_2]\cdot 2CHCl_3$, $[Ru(CO)_3(PPh_3)_2]\cdot$toluene and $[Ru_{12}C_{30}H_{14}Na_2O_{50}\cdot 6(C_{18}H_{15}OP)\cdot 2(C_7H_8)\cdot 4(H_2O)]$ (**4**).

	1 • 2CHCl$_3$	**2 • toluene**	**4**
formula	$C_{42}H_{34}Cl_6O_6P_2Ru$	$C_{42.20}H_{34}Cl_{0.30}O_{2.71}P_2Ru$	$C_{76}H_{66}NaO_{30}P_3Ru_6$
MW	1010.40 g/mol	757.84	2181.61
space group	P-1	$P2_1/c$	P-1
a (Å)	9.915(2)	17.7301(6)	16.3958(9)
b (Å)	11.919(2)	12.3659(4)	17.5531(9)
c (Å)	20.194(4)	18.3431(6)	17.6055(9)
α (°)	97.563(3)	90	101.4600(10)
β (°)	91.490(3)	102.9990(10)	113.7560(10)
γ (°)	112.378(3)	90	107.5850(10)
V (Å^3)	2180.0(8)	3918.6(2)	4111.9(4)
Z	2	4	2
T (K)	133(2)	100(2)	100.(2)
λ (Å)	0.71073	0.71073	0.71073
D_{calcd} (g/cm^3)	1.539	1.285	1.762
μ (mm^{-1})	0.847	0.554	1.220
Crystal size (mm)	0.15 × 0.15 × 0.15	0.32 × 0.24 × 0.15	0.570 × 0.080 × 0.080
Reflections collected	13889	94892	99952
Independent reflections	9554 [R(int) = 0.0344]	13990 [R(int) = 0.0365]	24604 [R(int) = 0.0275
Goodness-of-fit on F^2	1.047	1.132	1.088
Final R indices [I>2sigma(I)]	R1 = 0.0447, wR2 = 0.0802	R1 = 0.0566, wR2 = 0.1579	R1 = 0.0279, wR2 = 0.0602
R indices (all data)	R1 = 0.0720, wR2 = 0.1004	R1 = 0.0739, wR2 = 0.1704	R1 = 0.0391, wR2 = 0.0648

After isolating $[Ru(HCO_2)_2(CO)_2(PPh_3)_2]$ from the chloroform solution by pentane diffusion, the supernatant was evaporated and re-dissolved in toluene. Hexane was diffused into the toluene solution and stored at 0 °C for a week giving two different types of crystals: yellow plates and yellow blocks. The yellow plates were found suitable for single crystal X-ray

diffraction and the structure determination revealed the binuclear complex $[Ru_2(HCO_2)_2(CO)_4(PPh_3)_2]$ with two bridging formato ligands (Figure 5.15, Table 5.3).

The yellow block-like crystals were identified by single crystal X-ray diffraction as $[Ru(CO)_3(PPh_3)_2]$ (**2**), which crystallizes with one molecule of toluene solvent in the asymmetric unit. The crystal structure of the compound is depicted in Figure 5.15.

In order to explore the robustness of the $RuCl_3$-phosphine system in an emulsion, triphenylphosphine oxide ($O=PPh_3$) was used as a ligand to model practical conditions (e.g. PPh_3 is contaminated with $O=PPh_3$ impurity and/or the FA feed contains dissolved oxygen). Although the reaction rate in the presence of $O=PPh_3$ was relatively low (4.43×10^{-6} M s^{-1}) at 90 °C the selectivity of the reaction was high, giving a mixture of H_2 and CO_2 (Table 5.2) with no traces of CO.

Based on ^{31}P NMR results, the presence of any phosphine ligands in the orange-red compound was ruled out (except for $O=PPh_3$) while signals at 181.4 and 162.3 ppm in the ^{13}C NMR spectrum can be assigned to carbonyl and carbonate ligands, respectively. IR measurements showed five adsorption bands in the region from 2051 to 1922 cm^{-1} (carbonyl ligands) and also a broad adsorption at 1540 cm^{-1} (carbonato).

The orange-red blocks were subject to single crystal X-ray diffraction, which showed the presence of a large unexpected Ru carbonato cluster incorporating twelve ruthenium atoms ($[Ru_{12}C_{30}H_{14}Na_2O_{50}\cdot 6(C_{18}H_{15}OP)\cdot 2(C_7H_8)\cdot 4(H_2O)]$ (**4**), unit cell volume = 4111.9(4) $Å^3$). Crystallographic parameters of the complex are summarized in Table 5.3. The structure is quite unique because it consist of two identical cluster units $[Ru_6(CO_3)_3(CO)_{12}(OH)(H_2O)_2]$ that are bridged by a $[Na_2(H_2O)_2]$ unit (Figure 5.16).

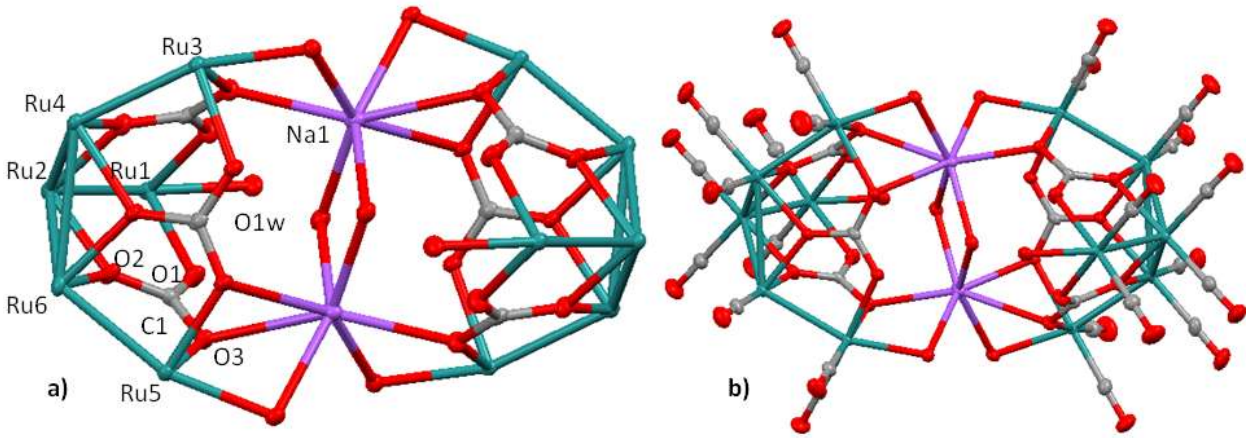

Figure 5.16 The core structure of the Ru cluster in the crystal structure of $[Ru_{12}C_{30}H_{14}Na_2O_{50}\cdot 6(C_{18}H_{15}OP)\cdot 2(C_7H_8)\cdot 4(H_2O)]$ (**4**). a) Hydrogen atoms, water, toluene, triphenylphosphine oxide and carbon monoxide molecules have been omitted for clarity, b) hydrogen atoms, water, toluene, triphenylphosphine oxide have been omitted for clarity.

In the Ru_3 triangle, the bond angles range between 59.380(6)° and 60.442(7)° resulting in an equilateral triangular geometry. In all cases two Ru atoms of the triangle are bridged by one

oxygen atom of a carbonato groups. In addition, each of the Ru atoms of the triangle is coordinated by two terminal CO ligands and another Ru atom that is not involved in the Ru_3 triangle.

Study of the effect of surfactants on the reaction rate and on the formation of Ru species

A series of control experiments were carried out to investigate the effect of surfactants on the reaction rate and the formation of Ru species. Although, the lack of toluene and surfactant did not result in complete inhibition, a significantly lower reaction rate (0.990×10^{-5} $M\cdot s^{-1}$ at 100 °C, Table 5.4) and selectivity (CO: 0.3 %) could be observed. Experiments were also carried out in the absence of surfactant in a water-toluene biphasic system giving a slightly higher reaction rate (1.409×10^{-5} $M\cdot s^{-1}$ at 100 °C) than the one observed in the aqueous phase. The selectivity of the decomposition reaction also increased with only 0.15 % CO present in the gaseous phase.

The utilization of an alkylammonium salts such as tetrabutylammonium bromide (TBAB) as a detergent, instead of SDS was also investigated. The reaction rate of the decomposition in the presence TBAB was 2.622×10^{-5} $M\cdot s^{-1}$ (rr=6.914×10^{-5} $M\cdot s^{-1}$ at 100 °C using SDS). Based on the ^{31}P NMR spectrum, $[Ru_2(HCO_2)_2(CO)_4(PPh_3)_2]$ was formed in high yield in addition to some $[Ru(HCO_2)_2(CO)_2(PPh_3)_2]$ and negligible amounts of $[Ru(CO)_3(PPh_3)_2]$.

Using *myristyl trimethylammonium bromide* (MiTMAB) resulted in a slightly lower reaction rate (0.958×10^{-5} $M\cdot s^{-1}$ at 100 °C) than the one measured in the absence of surfactant and toluene (0.990×10^{-5} $M\cdot s^{-1}$). Although ^{31}P NMR investigation of the freshly prepared sample revealed the initial presence of $[Ru(CO)_3(PPh_3)_2]$, one day later $[Ru_2(HCO_2)_2(CO)_4(PPh_3)_2]$ was the only Ru-phosphine species present in significant concentration.

Comparison of reaction rates and CO contents led us conclude that the addition of surfactants, particularly SDS, significantly increased the activity and the selectivity of the FA decarboxylation and also affected the *in situ* formation of Ru-carbonyl complexes.

Table 5.4 Comparison of reaction rates and selectivity using $RuCl_3/PPh_3$ in the presence of different surfactants.

	Surfactant	t (°C)	$10^6\times$ React. rate ($M\cdot s^{-1}$)	Gas composition (%)[b]		
				H_2	CO_2	CO
1[a]	SDS	100	69.14	54.20	45.80	nd
2[a]	TBAB	100	26.22	54.49	45.44	0.07
3[a]	MiTMAB	100	9.58	55.80	43.98	0.22
4[c]	-	100	9.90	52.23	47.47	0.30
5[d]	-	100	14.09	54.91	44.95	0.15

[a]$[RuCl_3]$= 2.43 mM, [Phosphine]=5.0 mM, [FA]=3.6 M, $[HCO_2Na]$= 0.4 M, [surfactant]= 19.65 mM, 25 mL aqueous solution, 5 mL toluene, [b]determined by gas chromatography using TCD, nd: no CO could be detected, [c]no toluene and surfactant was added, [d]no surfactant was added

Study of FA decomposition in the presence of complexes 1, 2 and 3

Questions arise whether the isolated Ru complexes **(**$[Ru(HCO_2)_2(CO)_2(PPh_3)_2]$ (**1**), $[Ru(CO)_3(PPh_3)_2]$ (**2**) and $[Ru_2(HCO_2)_2(CO)_4(PPh_3)_2]$ (**3**) are active catalysts for FA decomposition or the resting states of the active species or simply inactive complexes representing "dead ends" in the catalytic cycle? In order to answer these questions, authentic complexes **1-3** were synthesized and used as catalyst for the decarboxylation of FA (Table 5.5).

Authentic $[Ru(CO)_3(PPh_3)_2]$ (**2**) was synthesized according to a literature method,[3] recrystallized from the mixture of THF and heptanes (1:1) and used as a catalyst for FA decomposition in emulsion (see experimental section). Analysis of the product gases (H_2%= 55.31, CO_2%= 42.95, CO%= 1.74) and the observed reaction rate (2.060×10^{-6} M/s at 115 °C) suggested that complex **2** contributes to the catalytic activity to a certain degree but does not give high selectivity. In addition, the ^{31}P NMR study of the crude reaction mixture revealed the transformation of **2** into $[Ru(HCO_2)_2(CO)_2(PPh_3)_2]$ (**1**) and $[Ru_2(HCO_2)_2(CO)_4(PPh_3)_2]$ (**3**).

$[Ru_2(HCO_2)_2(CO)_4(PPh_3)_2]$ (**3**) was synthesized from $RuCl_3$ in the presence of FA and Na-formate in water/toluene biphasic system in the absence of detergent and the crude material was recrystallized from $CHCl_3$ by hexane diffusion as it was described earlier. It is very unlikely that complex **3** is an active species (or its direct precursor) in the FA decomposition as reflected by the low catalytic activity and poor selectivity (7.027×10^{-7} M/s at 115 °C, H_2%= 54.23, CO_2%= 37.12, CO%= 8.66) which we observed using **3** as a catalyst in emulsion. The low catalytic activity is in accordance with the similar finding of Wills et al.[4] Intact complex **3** could be recovered from the toluene phase after the decomposition reaction, demonstrating the high stability (and most likely low activity) of the complex. $[Ru(HCO_2)_2(CO)_2(PPh_3)_2]$ (**1**) was synthesized from $[Ru(CO)_3(PPh_3)_2]$ (**2**) by treating FA under reflux following a literature method.[5] Utilization of **1** as a catalyst resulted in moderate activity (1.210×10^{-6} M/s at 115 °C) and selectivity H_2%=46.54, CO_2%=50.74, CO%=2.72).

One can conclude that isolated and structurally characterized Ru complexes (**1-3**) formed *in situ* from $RuCl_3$ and PPh_3 in the presence of FA do not contribute significantly to the overall catalytic activity. Regardless of their low catalytic activity, the one pot preparation of **1-4** from FA without using explosive and/or toxic gases such as H_2 and CO provides a very attractive approach to the synthesis of Ru carbonyls.

Table 5.5 Comparison of reaction rates and selectivity using catalyst 1-3.

	Catalyst [a]	t (°C)	$10^6 \times$ React. rate ($M \cdot s^{-1}$)	Gas composition (%)		
				H_2	CO_2	CO
1	**1**	115	1.210	46.54	50.74	2.72
2	**2**	115	2.060	55.31	42.95	1.74
3	**3**	115	0.703	54.23	37.12	8.66

[a] [Catalyst]= 0.424 mM, [FA]=3.6 M, [HCO_2Na]= 0.4 M, [SDS]= 19.65 mM, 25 mL aqueous solution, 5 mL toluene.

Decomposition of FA in the presence of $IrCl_3$ and N-donor ligands

During the studies, the results on screening the catalytic activity of $IrCl_3$ in the presence of *N*-donor ligands including the monodentate pyridine (py), the bidentate bipyridine (bpy), phenanthroline (phen) and tetramethylethylenediamine (TMEDA), tridentate pentamethyldiethylenetriamine (PMDETA) and 1,3-bis(2'-pyridyl-imino)-isoindoline (IndH), and the multidentate 1,4-di(2-pyridyl)-aminophthalazine ($PAPH_2$) and porphine derivative (POR) were reported. The structure of the applied *N*-donor ligands in shown in Figure 5.17.

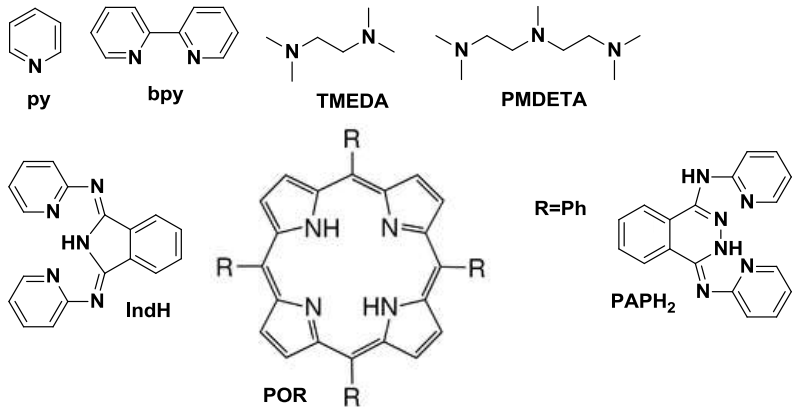

Figure 5.17 The structure of *N*-donor ligands.

An aqueous solution of FA and HCO_2Na was mixed with $IrCl_3$, and the *N*-donor ligand was charged to a Monel autoclave and the reactor was closed under air. The reaction mixture was heated to 90 °C gradually. The pressure and the internal temperature of the reactor was monitored with LabView and the reaction rates were calculated from the pressure *versus* time diagrams (Figures 5.18 and 5.19).

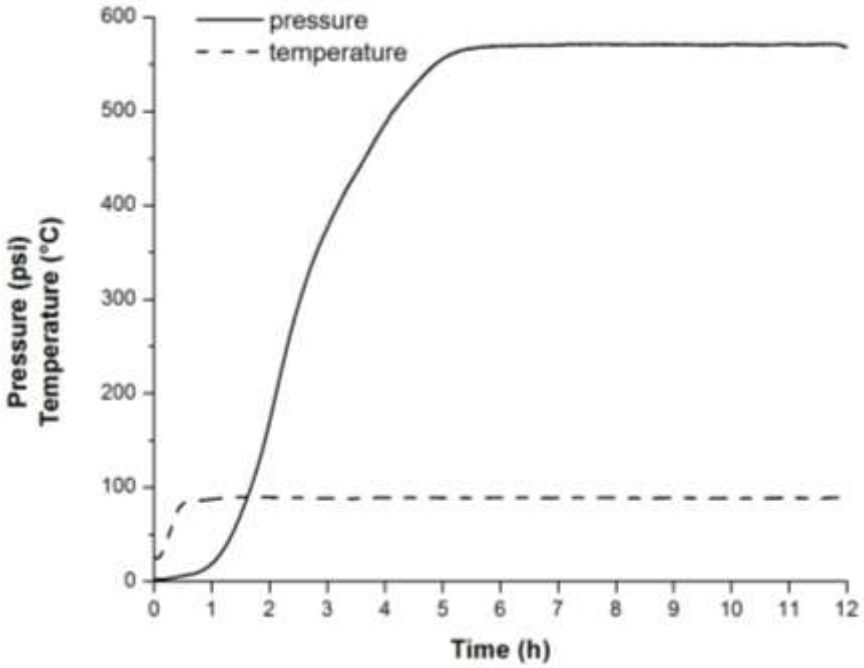

Figure 5.18 Pressure/temperature *versus* time diagram for the decomposition of FA in the presence of $IrCl_3$ and bipyridine.

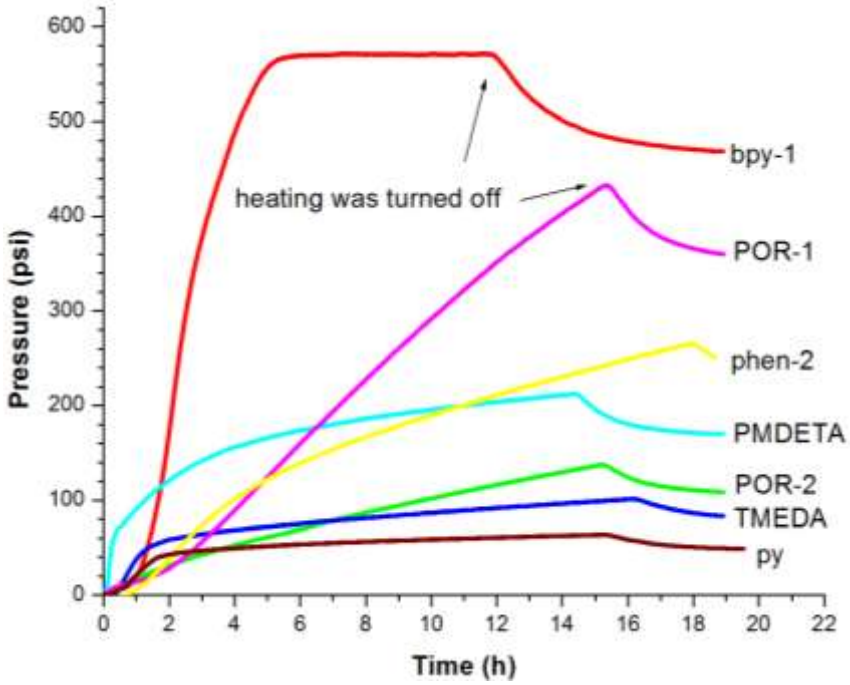

Figure 5.19 Pressure *versus* time diagram for the decomposition of FA in the presence of $IrCl_3$ and various *N*-donor ligands.

After 10-12 hours of reaction time the gaseous product was vented into a plastic bag and samples were taken for gas chromatographic analysis. Gas composition data and reaction rates are shown in Table 5.6.

Table 5.6 Reaction rates and the chemical composition of gaseous products

Ligand	Run	H_2%	CO_2%	CO%	10^6 × Rate 1 (M/s)	10^6 × Rate 2 (M/s)
Bipyridine	first	54.18	45.82	nd	350.6	-
Bipyridine	second	52.64	47.24	0.12	526.1	-
Phenanthroline	first	43.67	56.30	0.03	58.3	20.14
Phenanthroline	second	51.02	48.58	0.41	48.4	16.2
PMDETA	first	56.29	43.66	0.05	48.6	5.7
TMEDA	first	54.31	45.52	0.17	3.7	-
Pyridine	first	54.68	44.89	0.44	1.39	-
Porphine	first	54.74	45.26	nd	46.4	-
Porphine	second	58.26	40.20	1.54	9.80	-
IndH	second	49.9	50.11	nd	34.92	-

The bidentate, flexible backbone bipyridine (bpy) in the presence of iridium chloride showed relatively high activity (3.51×10^{-4} M/s) even in the first run and the pressure *versus* time diagram did not show deactivation of the catalyst. The high selectivity of the catalyst was reflected by the lack of carbon monoxide in the gas mixture (TCD detection). After the addition of 15 g FA (97 %) the decomposition reaction was monitored again showing an even higher activity in the second run (5.26×10^{-4} M/s). However, the selectivity of the catalyst decreased (CO concentration=0.12 %).

The other bidentate ligand, phenanthroline (phen) with a non-flexible backbone gave one order of magnitude lower activity (4.98×10^{-5} M/s) than the one observed using bipyridine as ligand. Very similar activity (4.84×10^{-5} M/s) was observed in the second run after the addition of 15 g FA indicating that the gradual deactivation (reaction rate=1.32×10^{-5} M/s) in the last segment of the first run was reversible. A similar degree of deactivation was observed in the second run (reaction rate=1.62×10^{-5} M/s). This catalyst precursor showed lower selectivity in both the first and the second run giving 0.03 and 0.41 % CO content respectively.

Although the decomposition in the presence of the tridentate *N,N,N′,N′,N″*-pentamethyldiethylenetriamine (PMDETA) and $IrCl_3$ catalyst precursors took place at similar reaction rate (4.86×10^{-5} M/s) than those observed in the presence of phenanthroline, the deactivation (reaction rate=5.70×10^{-6} M/s) in the last segment seemed to be irreversible. The selectivity of the catalyst formed *in situ* was very similar to that which we observed using phenanthroline in the first run giving a CO content of 0.05 %.

The relatively flexible bidentate ligand, tetramethylethylenediamine (TMEDA) in combination with $IrCl_3$ showed a very low decomposition rate (3.70×10^{-6} M/s) and poor selectivity (CO%=0.17). Due to the low reaction rate the activity of the catalyst, a second run was not carried out.

The tetradentate cyclic ligand, 5,10,15,20-tetraphenyl-21*H*,23*H*-porphine (POR) showed good activity and selectivity (4.6×10^{-5} M/s) in the presence of $IrCl_3$. However, moderate

reaction rate (9.80 x 10^{-6} M/s) and lower selectivity (1.54 % CO content) was observed in the second run. The lowest decomposition rate (1.39 x 10^{-6} M/s) and low selectivity was observed in the presence of $IrCl_3$ and the monodentate pyridine (py) ligand.

In order to increase the probability of the formation of binuclear complex (in that one of the bridging ligand is formate) a multidentate *N*-donor ligand, 1,4-di-(2-pyridyl)aminophthalazine ($PAPH_2$) was utilized. In the phthalazine ring of the $PAPH_2$ ligand there are two N atoms in close proximity which may bring the metal centers close enough to favor the formation of a binuclear complex. 1,4-di-(2-pyridyl)aminophthalazine ($PAPH_2$) was synthesized in a heterocyclic ring-expansion step in the reaction between IndH and hydrazine (Figure 5.20).

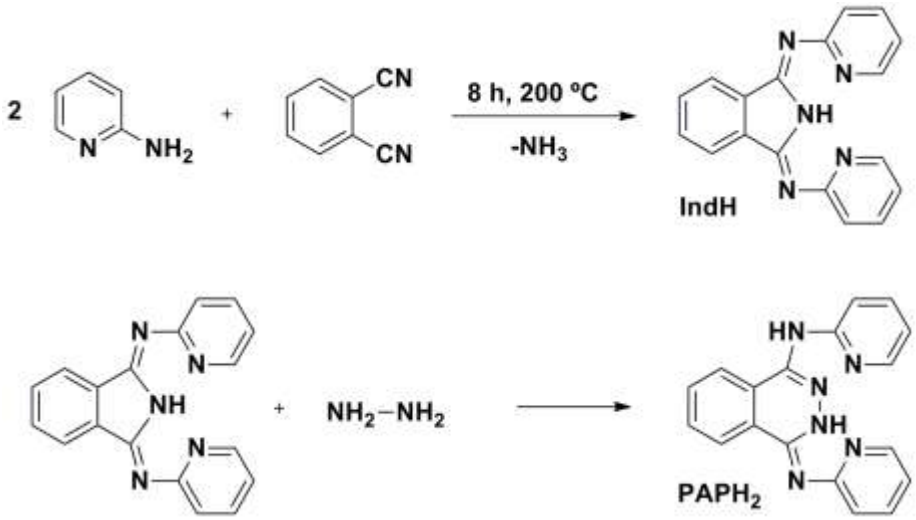

Figure 5.20 Synthetic procedure for $PAPH_2$.

The catalytic activity of $IrCl_3/PAPH_2$ was also tested under conditions similar to the ones previously reported for $IrCl_3$ and IndH. 0.0277 g of $IrCl_3$ was mixed with 0.0472 g of $PAPH_2$ and the aqueous solution of FA and Na-formate (9:1) was added. The reaction mixture was heated in a Parr reactor to 100 °C and the pressure was monitored. It was found that the reaction rate of the decomposition reaction was 8.559×10^{-5} M/s in the first run. This was one order of magnitude lower than we observed for the $IrCl_3$-IndH system (6.210×10^{-4} M/s, *vide infra*). After addition of 15 g FA (97%) the reaction rate was measured (1.886×10^{-4} M/s) giving a similar reaction rate (3.392×10^{-4} M/s) to the corresponding $IrCl_3$-IndH system (Table 5.7).

0.0156 g $RuCl_3$ was mixed with 0.0472 g $PAPH_2$ in FA/Na-formic acid aqueous solution and transferred into a Parr reactor and heated to 100 °C. The good selectivity of the reaction was reflected by the low CO content of the gas phase. After opening the reactor, the yellow solid was filtered and washed with distilled water. The FTIR spectrum of the isolated Ru complex revealed the presence of carbonyl ligands (2022.3 and 1934.7 cm^{-1}) and a formato ligand at 1631.6 cm^{-1}. The dry material was dissolved in $CHCl_3$ and recrystallized at -20 °C. The obtained yellow blocks were suitable for X-ray diffraction. Structural analysis revealed a binuclear structure involving two Ru atoms bridged by a N-N backbone in the phthalazine moiety and by the

formato ligand (Figure 5.21). The octahedral geometry of the Ru atoms is completed by four carbonyl ligands and by two N-atoms from the pyridyl moieties of PAPH ligand. As it was suggested, application of $PAPH_2$ (a typical binucleating ligand) resulted in the formation of the binuclear $[Ru_2(HCO_2)(CO)_4(PAPH)]$ complex.

$[Ru_2(HCO_2)(CO)_4(PAPH)]$ is a new compound and its direct synthesis from $RuCl_3$ in a one pot reaction is an additional example of the promising utilization of FA as both reducing agent and the source of carbonyl ligands. This synthesis further emphasizes the importance of FA for organometallic synthesis as was already shown for $[Ru_4(CO)_{12}H_4]$, $[Ru_2(HCO_2)_2(CO)_4(PPh_3)_2]$, $[Ru(HCO_2)_2(CO)_2(PPh_3)_2]$, $[Ru_{12}C_{30}H_{16}Na_2O_{50}\cdot 6(C_{18}H_{15}OP)\cdot 2(C_7H_8)\cdot 4(H_2O)]$ in this report.

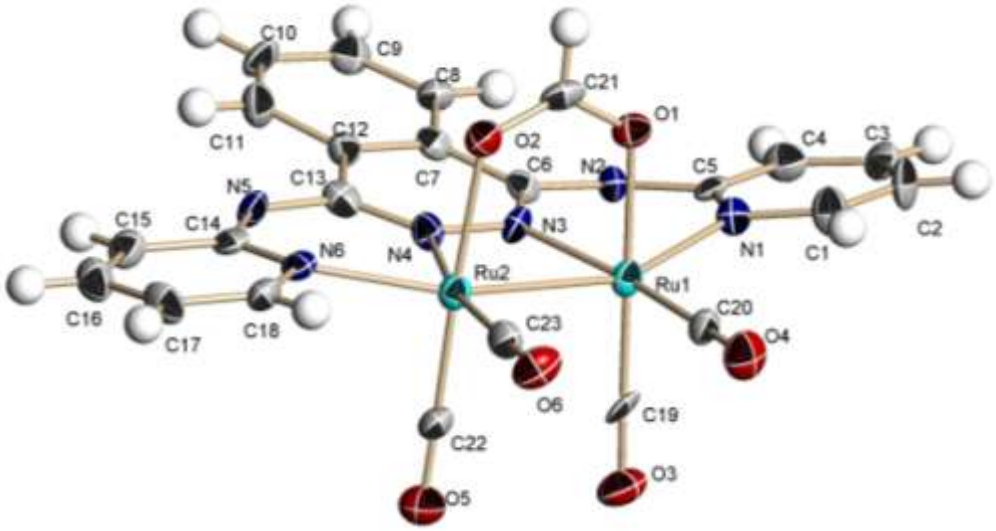

Figure 5.21 Structure of $[Ru_2(HCO_2)(CO)_4(PAPH)]$.

Table 5.7 Composition of gaseous products and reaction rates for the decomposition of FA in the presence of $IrCl_3$, $RuCl_3$, IndH, $PAPH_2$.

Entry	Metal	Ligand	T (°C)	H_2%	CO_2%	CO%	Reaction rate (M/s)
MC-134-1	$IrCl_3$	2 $PAPH_2$	100	48.18	51.82	nd	8.559×10^{-5}
MC-134-2	$IrCl_3$	2 $PAPH_2$	100	49.63	50.37	nd	1.886×10^{-4}
MC-135-1	$RuCl_3$	2 $PAPH_2$	100	50.37	48.65	0.98	4.884×10^{-6}
MC-135-2	$RuCl_3$	2 $PAPH_2$	100	50.38	48.67	0.95	2.667×10^{-6}
MC-124-1	$IrCl_3$	IndH	100	53.07	46.93	nd	6.210×10^{-4}
MC-124-2	$IrCl_3$	IndH	100	49.89	50.11	nd	3.392×10^{-4}
MC-122-1	$RuCl_3$	2 IndH	100	51.80	48.20	nd	8.064×10^{-5}
MC-122-1	$RuCl_3$	2 IndH	100	51.94	48.05	nd	3.495×10^{-5}
MC-273-1	$RuCl_3$	IndH	100	52.01	47.85	0.06	3.999×10^{-4}
MC-273-2	$RuCl_3$	IndH	107	51.02	48.73	0.27	6.738×10^{-5}

Notes: MC-XXX-1 stands for first run while MC-XXX-2 stands for second run.

Decomposition of formic acid in the presence of iridium chloride and 1,3-bis(2'-pyridyl-imino)-isoindoline ligand (under low pressure conditions)

A glass pressure tube was connected to a gas volumetric apparatus through a modified gauge block assembly including a pressure relief valve (Figure 5.22). The pressure relief valve was set to 65 psi.

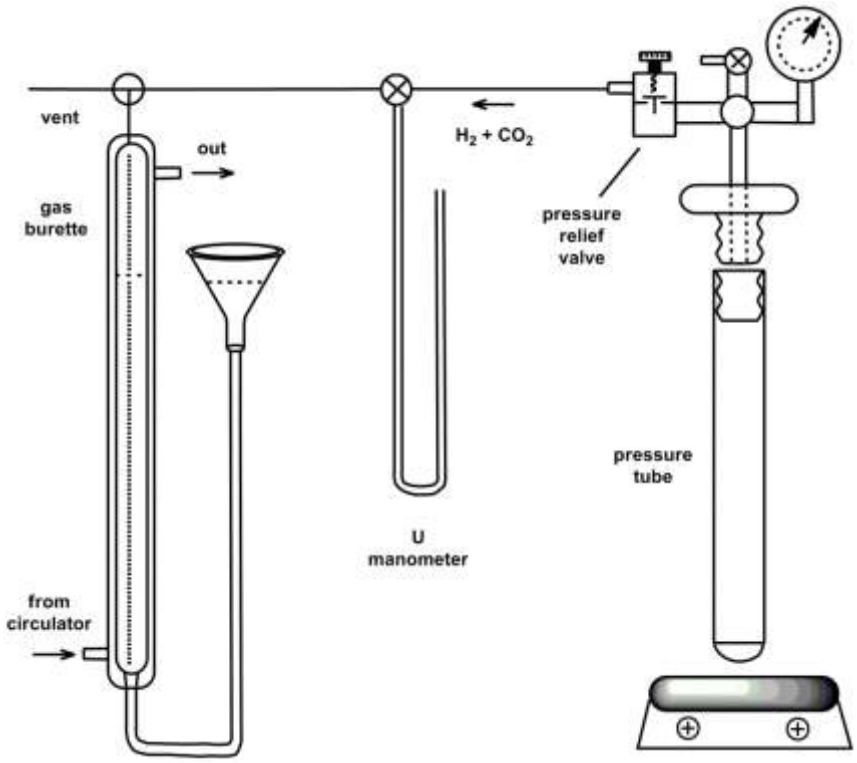

Figure 5. 22 Gas volumetric apparatus connected to a pressure tube reactor.

An aqueous suspension of $IrCl_3$, IndH, HCO_2Na was charged to the pressure tube and the reactor was closed under air. The reaction mixture was heated to 90 °C gradually. When the temperature reached 80 °C gas evolution started and as the decomposition was proceeding the formation of fine black particles was observed. Once the internal pressure exceeded 65 psi the valve vented the gas mixture to the gas burette and the volume of the gaseous products was monitored as a function of time (Figure 5.23). Reaction rate was calculated from the slope of volume *vs.* time diagram (rate = 2.431×10^{-4} M/s at 90 °C) and is summarized in Table 5.8.

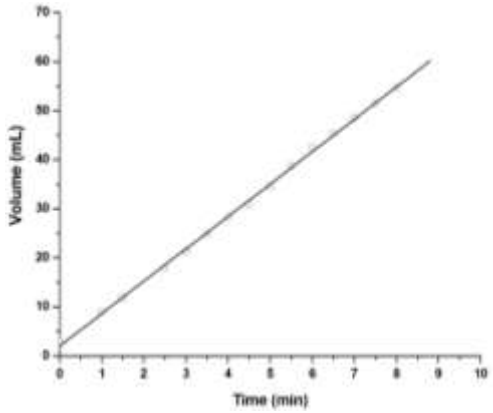

Figure 5.23 Volume *versus* time diagram for FA decomposition in the presence of different catalyst precursors.

Table 5.8 Decomposition rates at different temperatures.

Catalyst precursors	**10^{-5} × d[FA]/dt [M s^{-1}]**				
	70˚C	75˚C	80˚C	85˚C	90˚C
$IrCl_3$ IndH (MC-435) [a]	2.949	4.976	7.327	13.019	24.313

[a] $[IrCl_3]_0$= 9.987 mM, [IndH]= 9.987 mM, $[FA]_o$=3.50 M, $[HCO_2Na]$=0.40 M

The composition of gaseous products was determined by gas chromatography. Since the concentration of CO was under the detection limit of thermal conductivity detector the gas mixture was subjected to FTIR analysis, a more sensitive technique to detect trace amount of CO.

The precipitated black particles were separated from the reaction mixture, washed with distilled water and dried. The presence of carbonyl ligands in the black material was reflected by a very intense and broad signal from 2093 to 1946 cm^{-1} indicating the formation of Ir carbonyls in the presence of FA (Figure 5.24). This measurement was carried out after the induction period. $[IrCl_3]_0$= 9.987 mM, [IndH]= 9.987 mM, $[FA]_0$=3.50 M, $[HCO_2Na]$=0.40 M, 7.5 mL HCO_2H/HCO_2Na aqueous solution.

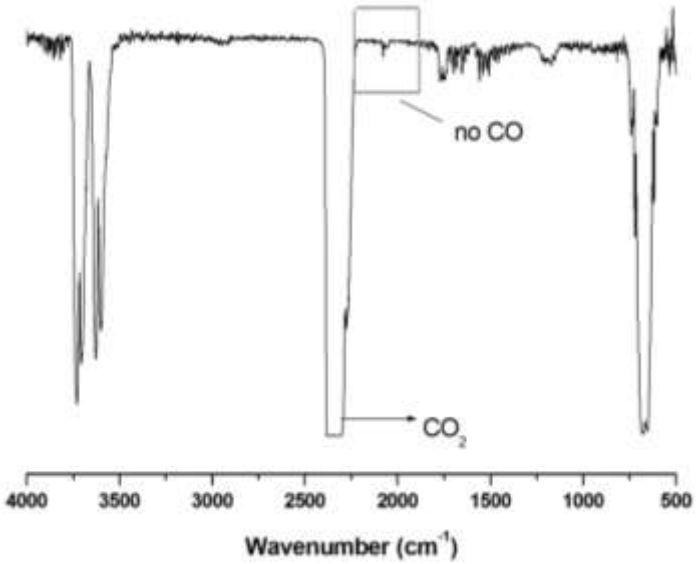

Figure 5.24 FTIR spectrum of gaseous product.

Elemental analysis revealed that the isolated black material consist of 57.0 % iridium, 15.06 % carbon, 3.76 % nitrogen an 1.85 % hydrogen. The elemental analysis results do not match with any of expected structures. The unexpectedly high iridium content let us suggest that the black material is a mixture of Ir carbonyl complexes and Ir particles rather than a pure compound.

Integrated FA dehydrogenation and hydrogen/air fuel cell

A glass pressure tube reactor was coupled with a hydrogen/air fuel cell in order to demonstrate that the selective decarboxylation of FA can provide an appropriate gas feed for a hydrogen/air fuel cell to produce electricity. Since the FA is not used directly in a fuel cell, this integrated system can be considered as an indirect FA fuel cell requiring the consecutive FA decomposition and utilization of the H_2/CO_2 mixture for power generation. The integrated system is illustrated in Figure 5.25.

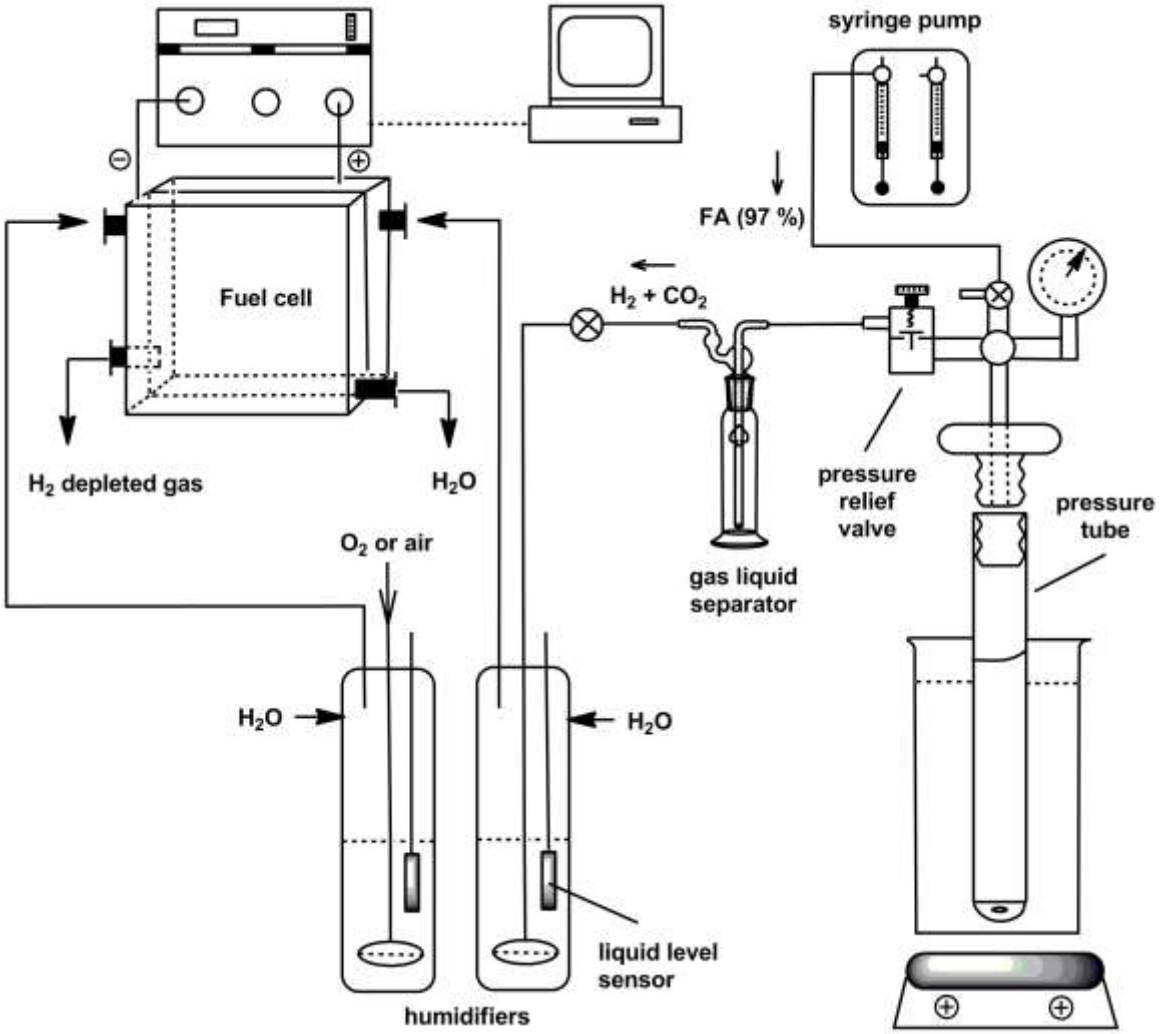

Figure 5.25 Integrated FA decomposition unit and H_2/air fuel cell.

Although catalyst particles could be recovered from the separator, the loss of catalyst in the reactor could not be prevented, resulting in decreasing reaction rates (Figure 5.26).

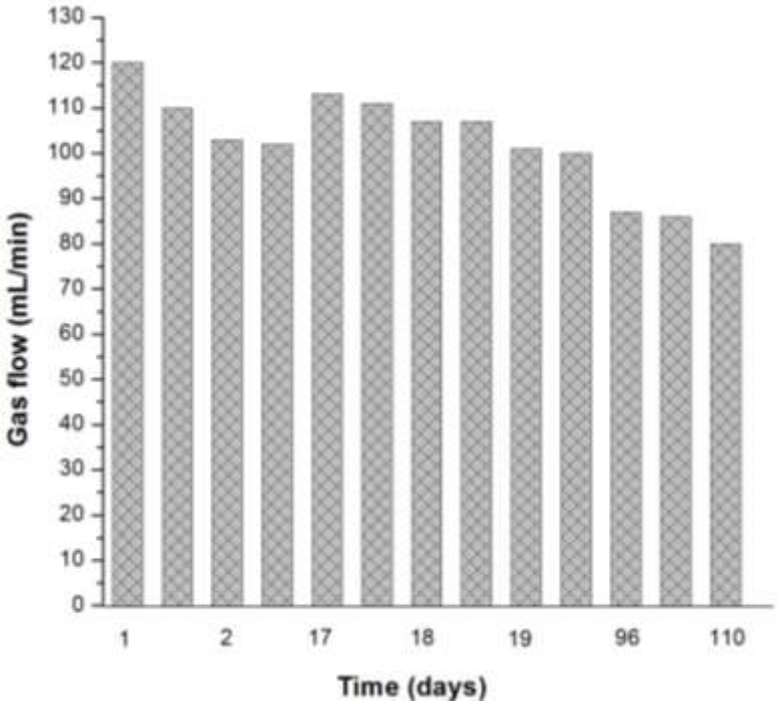

Figure 5.26 Gas flow (H_2/CO_2) *versus* time diagram. $[IrCl_3]_0$= 9.987 mM, [IndH]= 9.987 mM, $[FA]_0$= 3.50 M, $[HCO_2Na]$= 0.40 M, t=100 °C.

The stable performance of the fuel cell was first verified by monitoring the cell voltage as a function of time at constant current (I= 1.0 A) using pure hydrogen from a cylinder as a fuel. These measurements were considered benchmarks to compare the performance of the fuel cell after extensive use under various conditions as shown below. As it can be seen in Figure 5.27, the cell voltage was stable (0.85 V) for the time of the measurement using either O_2 or air as the cathode feed gas.

The fuel cell was then connected to the FA decomposition unit and tested at a current of 1.0 A. A comparison is given in Figure 5.28 between the performances of the fuel cell using different membranes. While the cell voltage was very similar at the beginning (≈ 0.85 V) the former membrane suffered from a significant decline in voltage (0.2 V after an hour) but the new one did not show any loss of performance.

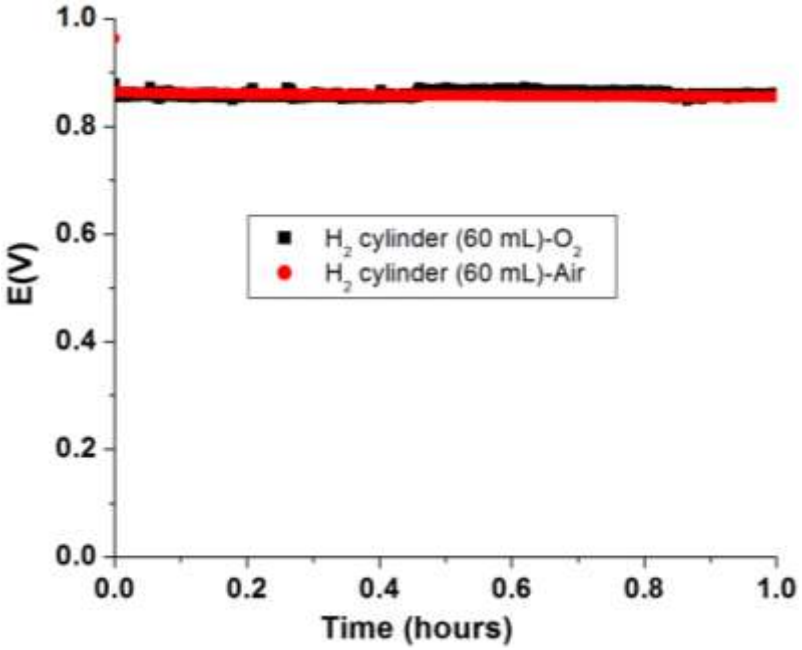

Figure 5.27 Cell voltage as a function of time at constant current (I=1.0 A).
H_2 flow=60 mL/min. Cathode feed gas: 240 mL/min air or oxygen, humidifier temp: 85 °C, fuel cell temp: 65 °C.

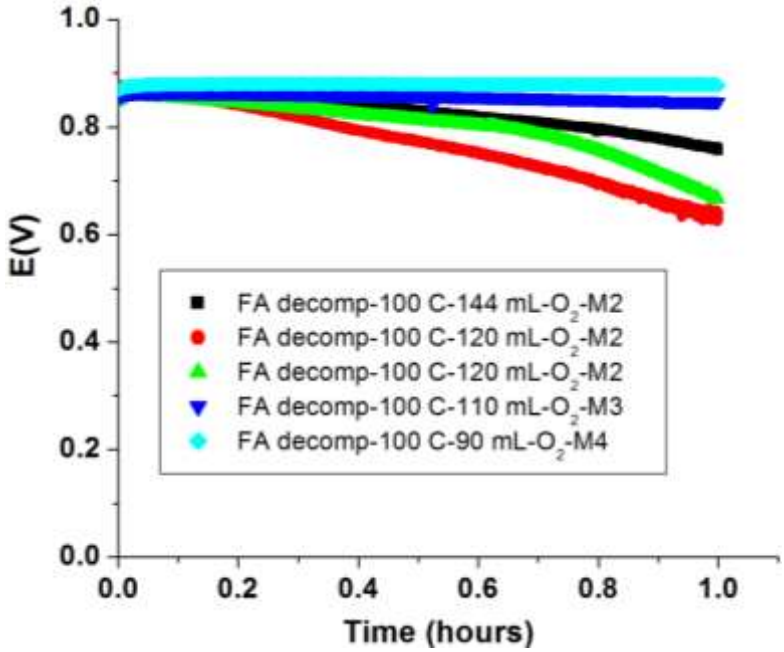

Figure 5.28 Cell voltage as a function of time.
Anode feed gas: 144-90 mL/min H_2/CO_2, Cathode feed gas: 240 mL/min O_2, humidifier temp: 85 °C, fuel cell temp: 65 °C. *Note*: M2, M3 and M4 stand for second, third and fourth MEA.

In order to design a practical energy storage system based on FA as an energy carrier the ultimate oxidant (cathode feed gas) should be preferably air rather than oxygen. The integrated FA decomposition-fuel cell system was tested using air as cathode feed gas and no difference in

performance could be observed under the given experimental conditions (Figure 5.29). It can also be seen in Figure 5.29 that the former systems (M2) lost 33 % of the original voltage (0.85 V) in the first 40 minutes and the experiments suffered from poor reproducibility (see black, green and red lines in Figure 5.29).

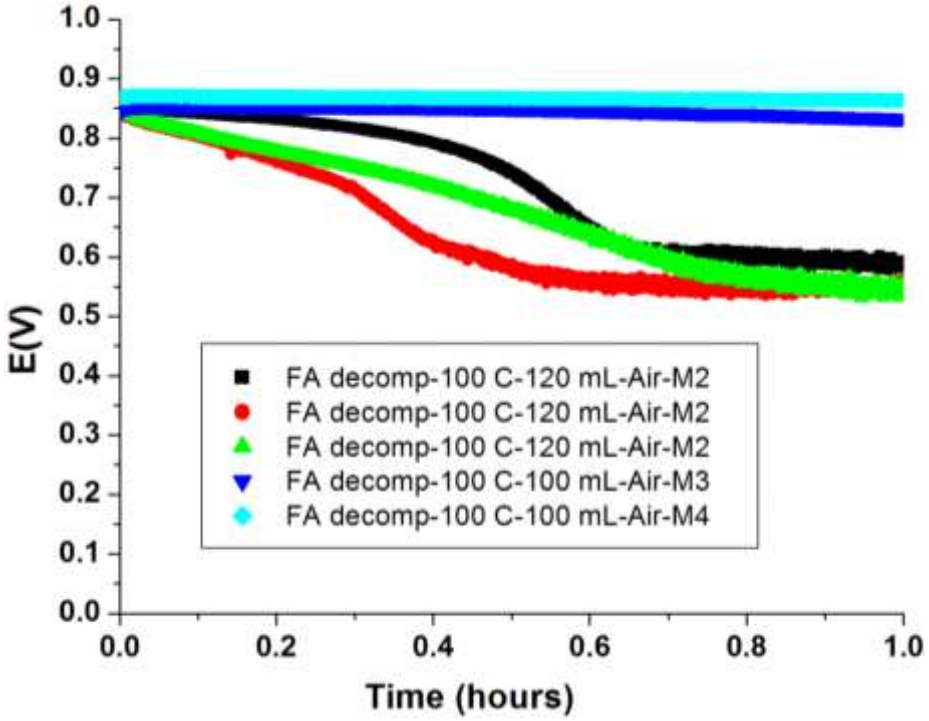

Figure 5.29 Cell voltage *versus* time. Anode feed gas: 120-100 mL/min H_2/CO_2, Cathode feed gas: 240 mL/min air, humidifier temp.: 85 °C, fuel cell temp: 65 °C.

The poor reproducibility in the measurements using the former MEA (M2) in the original experimental setup is also supported by the current *versus* time diagram (see black, green and red lines in Figure 5.30). The results using the new membrane and the modified experimental setup showed better stability and the cell responded to higher flow rate with higher current value (see blue and aquamarine lines).

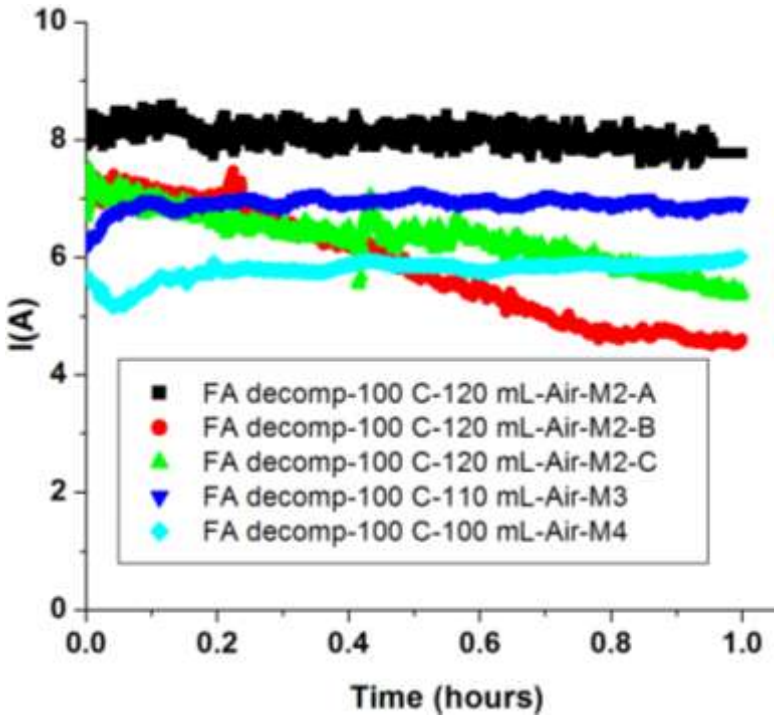

Figure 5.30 Cell current as a function of time. Anode feed gas: 120-100 mL/min H_2/CO_2, Cathode feed gas: 240 mL/min air, humidifier temp: 85 °C, fuel cell temp: 65 °C.

Comparing the fuel cell performance using pure hydrogen as a feed gas with those obtained using a H_2-CO_2 mixture from the decomposition unit, it could be assumed that purification of the gas mixture can be avoided and this mixture can be used directly in the fuel cell. In order to support this assumption, the fuel cell was run using a feed from the decomposition reactor after trapping the FA vapor and CO_2 with NaOH (See Figure A4 in Appendix 5.1).

As it is illustrated in Figures 5.31 and 5.32, practically no difference could be observed in the performance using FA and CO_2 free feed.

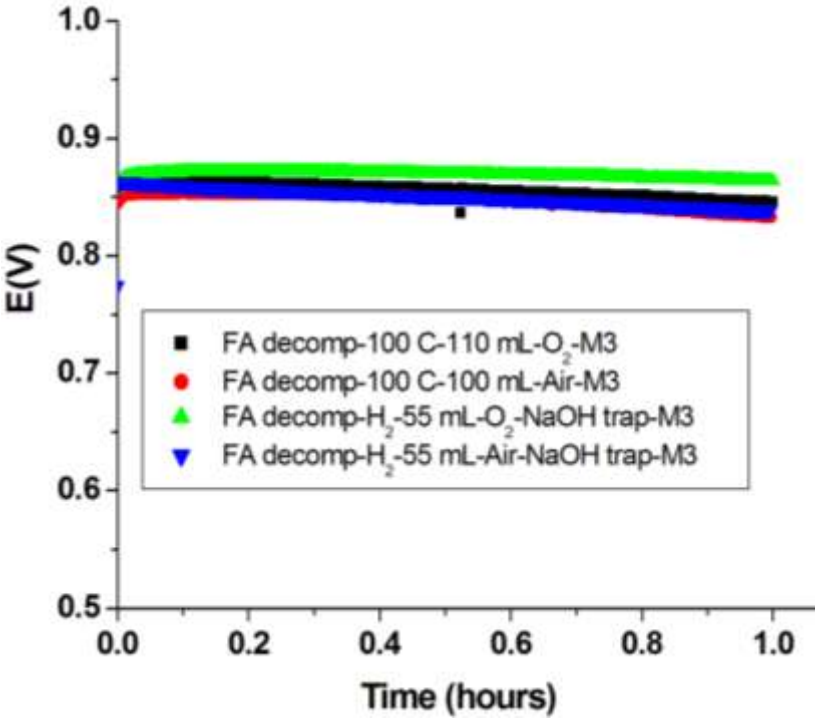

Figure 5.31 Cell potential as a function of time. Anode feed gas: 110-100 mL/min H_2/CO_2 or 55 mL/min H_2. Cathode feed gas: 240 mL/min air or oxygen, humidifier temp.: 85 °C, fuel cell temp: 65 °C.

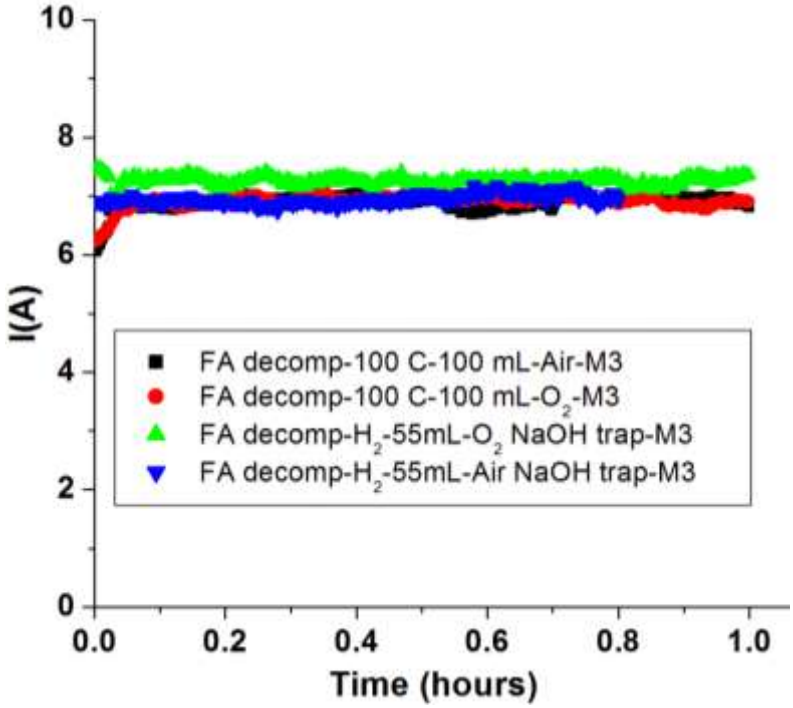

Figure 5.32. Cell current as a function of time. Anode feed gas: 110-100 mL/min H_2/CO_2 or 55 mL/min H_2. Cathode feed gas: 240 mL/min air or oxygen, humidifier temp.: 85 °C, fuel cell temp: 65 °C.

Decarbonylation of FA in the presence of heterogeneous catalysts

Even though the decomposition of FA to carbon monoxide and water was not part of the original proposal its decomposition pathway over supported metal catalysts was evaluated. Generation of CO from FA combined with dehydrogenation of FA provides an alternative way to produce syngas/metgas from renewable sources such as CO_2 derived FA.

In a typical experiment a plug of quartz wool was placed into the quartz reactor tube to hold the catalyst (Figure 5.33). The reactor tube was then inserted into the furnace and 30 mL/min N_2 was passed through the catalyst. When the temperature reached 250 °C, 0.1 mL/min FA was introduced into the reactor using a syringe pump. The gaseous products were analyzed by gas chromatography using a TCD detector while the FA content of the condensed products was determined by ^{1}H NMR spectroscopy.
Blank experiment

In order to compare the performance of supported metal catalyst, first a blank experiment, using a quartz reactor tube and quartz wool plug (but no catalyst) was carried out. Table 5.9 shows the FA conversion values and selectivity data as a function of temperature. In the absence of any catalyst, no conversion was observed at 250 °C while at 300 °C, 41.88 % CO selectivity was observed at 24.2 % conversion. The conversion increased as a function of temperature until it reached a plateau at 100 % at 450-500 °C. The CO selectivity decreased from 41.88 % to 1.4-2.8 % as the temperature increased from 300 to 500 °C. Interestingly no CO_2 was detected at 300 °C and the H_2/CO ratio was 1.39.

Table 5.9 FA conversion and chemical composition of gaseous products at different temperatures in the absence of metal oxide catalyst (quartz wool, blank experiment).

	Temperature (°C)					
	250	**300**	**350**	**400**	**450**	**500**
H_2 %	*-*	*58.12*	*43.26*	*44.96*	*45.73*	*48.40*
CO %	*-*	*41.88*	*10.53*	*3.81*	*1.43*	*2.81*
CO_2 %	*-*	*0*	*46.21*	*51.24*	*52.84*	*48.78*
CH_4 %	*-*	*0*	*0*	*0*	*0*	*0*
H_2/CO_2	*-*	*-*	*0.94*	*0.88*	*0.87*	*0.99*
FA Conv. (%)	-	24.21	36.0	44.14	100	99.67

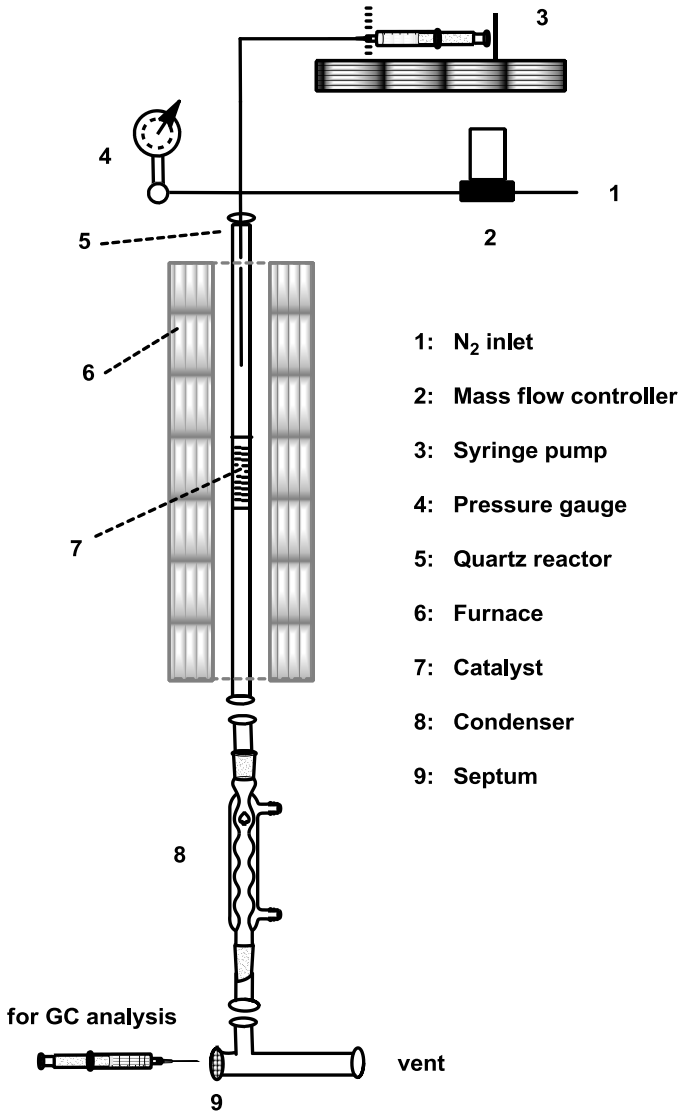

Figure 5.33 Tubular flow reactor for the decomposition of FA using heterogeneous catalysts.

Performance study on supported metal oxide catalysts

Nickel oxide on fumed silica

Selectivity and conversion of FA decomposition over NiO (20%) /fumed silica was studied using a tubular reactor shown in Figure 5.33. A conversion of 30 % was observed at 250 °C and it rapidly increased as a function of temperature and finally it reached practically 100 % at 400 °C. At 30 % conversion, the CO selectivity reached 96.7 %, which is one of the highest selectivity that was observed in the present study. However, the catalyst did not maintain this high value at higher conversions (e.g. 1.96 % selectivity at 99.4 % conversion at 400 °C). Methane formation as a concurrent reaction accounts for the low H_2 and CO yields (14.4 % and 1.96 %, respectively).

At 250 °C, the formation of methane was not observed but as the temperature the methane yield also increased and reached a maximum (18 %) at 400 °C. In order to find evidence for the occurrence of any side reactions (e.g. carbon formation) H_2 balance and C balance were added to Table 5.10. For example: H_2 balance (300 °C)=44.01+4×0.05+13.71=57.92, C balance (300 °C)=13.71+42.23+0.05=55.99. The small difference between the H_2 balance and C balance let one conclude that the occurrence of side reaction(s) is not significant.

Table 5.10 FA conversion and chemical composition of gaseous products at different temperatures for NiO (20%) on fumed silica.

	Temperature (°C)					
	250	**300**	**350**	**400**	**450**	**500**
H_2 %	*3.34*	*44.01*	*29.03*	*14.40*	*14.68*	*20.21*
CO %	*96.66*	*13.71*	*20.81*	*1.96*	*2.86*	*5.80*
CO_2 %	*0*	*42.23*	*44.49*	*65.62*	*64.99*	*59.98*
CH_4 %	*0*	*0.05*	*5.66*	*18.02*	*17.47*	*14.02*
H_2/CO_2	*-*	*1.04*	*0.65*	*0.22*	*0.23*	*0.34*
FA Conv. (%)	30.23	92.87	97.40	99.43	99.85	100
H_2 balance	100	57.92	72.50	88.44	87.42	82.09
C balance	96.66	55.99	70.96	85.60	85.34	79.80

Nickel oxide on fumed alumina

In the presence of NiO (15%) on fumed alumina catalyst (FAl), a slightly lower conversion (24.1%, Table 5.11) was observed than that on NiO (20%) on fumed silica (30.2%). A lower CO yield (90.8 %) was also observed. Similarly to NiO/fumed silica catalyst, NiO/fumed alumina did not catalyze methanation at lower temperatures (250-300 °C) and the temperature dependence of methane formation was less pronounced (12-16%) in the temperature range from 350-500 °C.

Table 5.11 FA conversion and chemical composition of gaseous products at different temperatures for 15% NiO on fumed alumina.

	Temperature (°C)					
	250	**300**	**350**	**400**	**450**	**500**
H_2 %	*9.16*	*43.00*	*19.47*	*16.89*	*18.5*	*23.46*
CO %	*90.84*	*14.87*	*2.65*	*3.10*	*4.23*	*7.79*
CO_2 %	*0*	*42.00*	*62.81*	*63.84*	*61.94*	*56.80*
CH_4 %	*0*	*0.13*	*15.06*	*16.16*	*15.33*	*11.95*
H_2/CO_2	*-*	*1.02*	*0.31*	*0.26*	*0.30*	*0.41*
FA Conv. (%)	24.09	97.11	99.67	100	100	100

Nickel oxide on magnesium oxide

NiO/MgO was less active (Table 5.12) than NiO/fumed silica or NiO/fumed alumina at the lower temperature region giving only 45.9 % conversion at 300 °C. Following the general trend among the studied catalysts the H_2/CO_2 ratio decreased as a function of temperature and stabilized around 0.3 while the methane yield increased (13.5-15.2 %).

Table 5.12 Chemical composition of gaseous product and FA conversions at different temperatures for 35% NiO/MgO.

	Temperature (°C)					
	250	**300**	**350**	**400**	**450**	**500**
H_2 %		*45.19*	*42.54*	*18.91*	*18.32*	*20.64*
CO %		*10.61*	*13.62*	*2.95*	*3.99*	*6.11*
CO_2 %		*44.2*	*43.57*	*63.06*	*62.43*	*59.78*
CH_4 %		*0*	*0.27*	*15.07*	*15.26*	*13.47*
H_2/CO_2	-	*1.02*	*0.98*	*0.3*	*0.29*	*0.34*
FA Conv. (%)	-	45.85	95.60	100	100	100

Cobalt oxide on fumed alumina

CoO (20%)/fumed alumina (FAl) was tested under similar conditions. The catalyst provided moderate activity (27.5%) with good CO selectivity (97.5 %) at 250 °C (Table 5.13). The relatively low methane contents (0.2-1.4) indicate the low methanation activity of this catalyst. This is in good agreement with the previous results in which CoO/MgO showed high activity as a catalyst for dry/bireforming of methane giving low residual methane content.

Based on the data summarized in Table 5.13 it can be concluded that CoO/FAl catalyst provides an excellent CO selectivity (96.3 %) even at 300 °C and the formation of methane was not observed up to 400 °C. Even at 450-500 °C the methanation reaction was not significant resulting in 1.4 % methane. The low methanation activity of CoO/FAl is also confirmed by the H_2/CO_2 ratio, which remained almost constant (≈ 1).

Table 5.13 Chemical composition of gaseous product and FA conversions at different temperatures for CoO 20% on fumed alumina.

	Temperature (°C)					
	250	**300**	**350**	**400**	**450**	**500**
H_2 %	*2.5*	*3.74*	*41.59*	*41.74*	*41.21*	*40.36*
CO %	*97.5*	*96.26*	*18.32*	*16.85*	*16.85*	*14.91*
CO_2 %	*0*	*0*	*40.1*	*40.35*	*41.89*	*43.34*
CH_4 %	*0*	*0*	*0*	*1.07*	*0.17*	*1.39*
H_2/CO_2	*-*	*-*	*1.04*	*1.03*	*0.98*	*0.93*
FA Conv. (%)	27.49	Not measured	100	99.65	99.33	99.92

Since the decomposition of FA to carbon monoxide and water was not part of the original proposal techno economical analysis of this decomposition pathway was not performed.

Conclusions

1) It was found that $RuCl_3$ in the absence of any ligand has good catalytic activity for the decarboxylation of FA and the reaction rate is first order with respect to the catalyst concentration. A tetranuclear Ru-complex, $[Ru_4(CO)_{12}H_4]$ formed in the course of the reaction and this complex was found an active and selective catalyst.

2) It was demonstrated that FA can be decomposed in the presence of $RuCl_3/PPh_3$ derivatives in emulsions with good selectivity to H_2 and CO_2. The *in situ* formed Ru species ($[Ru(HCO_2)_2(CO)_2(PPh_3)_2]$, $[Ru_2(HCO_2)_2(CO)_4(PPh_3)_2]$, $[Ru(CO)_3(PPh_3)_2]$ and $([Ru_{12}C_{30}H_{14}Na_2O_{50}\cdot 6(C_{18}H_{15}OP)\cdot 2(C_7H_8)\cdot 4(H_2O)]$)were isolated and structurally characterized. Kinetic measurements proved that these isolated complexes have moderate catalytic activity indicating that other species account for the overall catalytic activity for FA decomposition.

3) The performance of $IrCl_3$/*N*-donor ligand systems was also explored. The catalyst that formed from $IrCl_3$ and IndH ligand in the presence of FA showed excellent activity and selectivity (to H_2 and CO_2) in long term.

4) The decomposition reactor loaded with $IrCl_3$/IndH catalyst was coupled with a hydrogen/air fuel cell in order to demonstrate the long term stability of this integrated system. This system, which can be considered as an indirect formic acid fuel cell showed high performance.

5) Supported metal were used as heterogeneous catalyst for the decomposition of FA to carbon monoxide and water. Although conversions were moderate catalyst such as CoO on fumed alumina, NiO on fumed silica showed high selectivity to CO formation (96-98 %).

References

(1) Boddien, A.; Loges, B.; Junge, H.; Beller, M. *ChemSusChem* **2008**, *1*, 751.
(2) Laurenczy, G.; Fellay, C.; Yan, N.; Dyson, P. J. *Chem. Eur. J.* **2009**, *15*, 3752.
(3) Ahmad, N.; Levison, J. J.; Robinson, S. D.; Uttlky, M. F.; Wonchoba, E. R.; Parshall, G. W. In *Inorganic Syntheses*; John Wiley & Sons, Inc.: 2007; Vol. 15, p 45.
(4) Morris, D. J.; Clarkson, G. J.; Wills, M. *Organometallics* **2009**, *28*, 4133.
(5) Johnson, B. F. G.; Johnston, R. D.; Lewis, J.; Williams, I. G. *J. Chem. Soc. A* **1971**, 689.

Direct Formic Acid Fuel Cells

Background

Since the mid-late 20^{th} century, much focus has been has been dedicated to the development of new power sources that are environmentally benign and more energetically efficient than internal combustion engines. Early interest focused on the hydrogen fuel cell as the center of an infrastructure known as the "Hydrogen Economy", but complications quickly arose with respect to the hazards of working with hydrogen gas and the necessity for an ultra-pure hydrogen source, which ultimately led to the program's scale-back. The subsequent development of the methanol fuel cell provided a simpler solution by storing hydrogen in the chemical bonds of a liquid, which could be used as the power source under the appropriate conditions. However, complications of its own have prevented the methanol fuel cell from reaching wide-spread commercialization. The high costs of noble metal catalysts along with methanol cross-over to cathode resulting in parasitic loss of methanol due to chemical oxidation. Performance losses due to surface deactivation also results since methanol and its associated intermediates must then compete with the oxygen for active sites on the platinum cathode. Hence, elaborate circulation systems must be devised in order to mitigate this problem.

Direct formic acid fuel cells (DFAFCs), while still in need of further optimization to compete with methanol or hydrogen fuel cells, have generated considerable interest in recent years due to the inherent advantages, over methanol or hydrogen, that come with using formic acid as a fuel source. The complete oxidation of formic acid (eqn. 1) is a two electron transfer, vs. a six electron transfer for methanol (eqn. 2), thus should proceed in fewer steps with a smaller number of potentially reactive intermediates that could introduce strongly bound surface species. Although the energy density of neat formic acid is lower than methanol (2104 Wh L^{-1} vs. 4900 Wh L^{-1}), electrostatic repulsions between the formate anions formed in aqueous solution and the sulfonate functionalities on the backbone of Nafion, the polymer electrolyte membrane most commonly employed in hydrogen powered fuel cells, lowers parasitic cross-over.

$$HCOOH \rightarrow CO_2 + 2H^+ + 2e^- \quad (1)$$
$$2\ CH_3OH \rightarrow CO_2 + +6H^+ + 6e^- \quad (2)$$

As a result, formic acid can be used in concentration up to and exceeding 10M whereas methanol is limited to 1-2M so as to minimize the negative effects of crossover. Moreover, DFAFCs exhibit a high theoretical maximum cell voltage at 1.48V (eqn. 3-5), which is ~ 200 mV greater than either methanol or hydrogen fuel cells. The optimal catalyst for the formic acid oxidation (FAO) also introduces an inherent advantage to these cells, in that Pd is considered more effective than Pt since the formation of CO is largely avoided. This is beneficial since palladium is about half the price of platinum (1420 USD/oz vs. 675 USD/oz) at the time of this report.

$$\text{Anode: } HCOOH \rightarrow CO_2 + 2H^+ + 2e^- \qquad E^0 = -0.25 \quad (3)$$
$$\text{Cathode: } \tfrac{1}{2}\ O_2 + 2H^+ + 2e^- \rightarrow H_2O \qquad E^0 = 1.23V \quad (4)$$
$$\text{Net Rxn: } HCOOH + \tfrac{1}{2}\ O_2 \rightarrow CO_2 + H_2O$$
$$E^0 = E_{cathode} - E_{anode} = 1.48V \quad (5)$$

Nonetheless there remain several obstacles to be cleared before commercial DFAFCs can be realized. Although Pd is markedly cheaper than Pt, rapid deactivation and corrosion limits its ability for long-term operation in a DFAFC. Hence, the problem of developing high efficiency, powerful fuel cells lies in the optimization of the anode catalyst. Platinum employed at the cathode to facilitate the oxygen reduction reaction (ORR) presents another hurdle toward commercialization due to its high cost, although this is not as crucial as finding an improved catalyst for the FAO. In the project, two approaches were undertaken to develop improved DFAFCs; **1** Alloy palladium with other metals to find a more FAO active composition that is less susceptible to surface deactivation and corrosion. **2** Support catalysts on a high surface material to better utilize the metal by exposing more electrochemically active surface area (ECSA). Together, these approaches have allowed the achievement of the goal of developing DFAFCs with greater than 40% voltage efficiency.

Palladium Alloys

Initial efforts were focused on developing PdSn and PdAu alloys supported on high surface area active carbon, namely vulcan XC-72R. It was found that the optimal compositions for the respective materials were PdAu (unsupported) and $Pd_{20}Sn$(60wt%)/C. The results from

the fuel cell polarization curves are shown in Figure 5.34. At 80mA/cm^2, $Pd_{20}Sn$(60wt%)/C operates at 0.54V and generates 43mW/cm^2, corresponding to 36.5% voltage efficiency. Drawing the same current densities from the fuel cell incorporating unsupported PdAu, a higher operating potential (0.64V) is achieved and 51.9mW/cm^2 is produced, increasing the voltage efficiency to 43.8%.

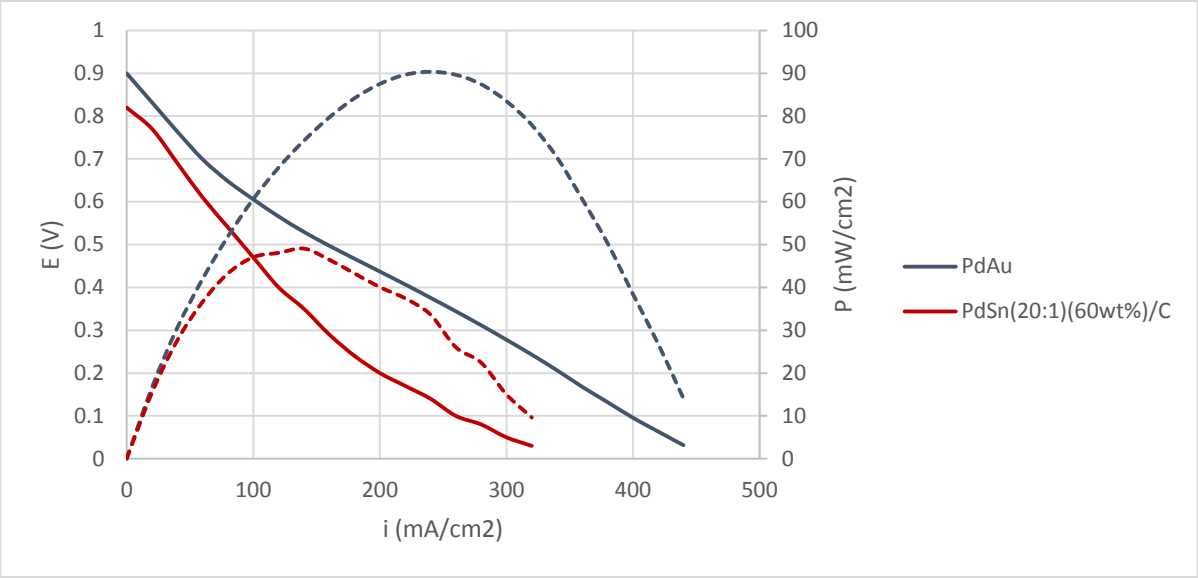

Figure 5.34 Cell Voltage Polarization Curves of the Optimal PdAu and PdSn Catalysts. 2M HCOOH, O_2 flow at cathode, T=90˚C. Dotted lines correspond to the power density axis.

In an effort to move away from gold, PdFe and PdSb alloys were prepared and compared with some previously prepared PdSn catalysts. The following materials were prepared at 60wt% on XC-72:

1. $Pd_{20}Sn$/C
2. PdSn/C
3. PdFe/C
4. PdSb/C

As seen in Figures 5.35 and 5.36, PdFe/C exhibited the highest open circuit voltage whereas $Pd_{20}Sn$/C yielded the highest power density. Despite significant activation polarization, PdFe/C ultimately reaches the second highest maximum current density, which shows promise for the development of catalysts incorporating significant amounts of inexpensive and abundant materials.

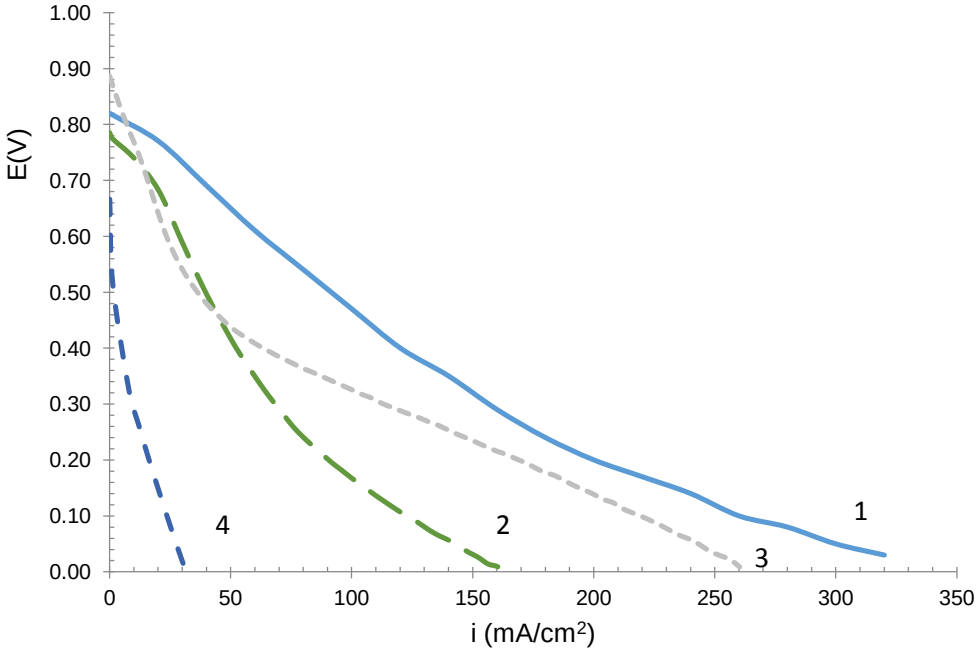

Figure 5.34 Cell Voltage Polarization Curves. 2M HCOOH, O_2 flow at cathode, T=90˚C

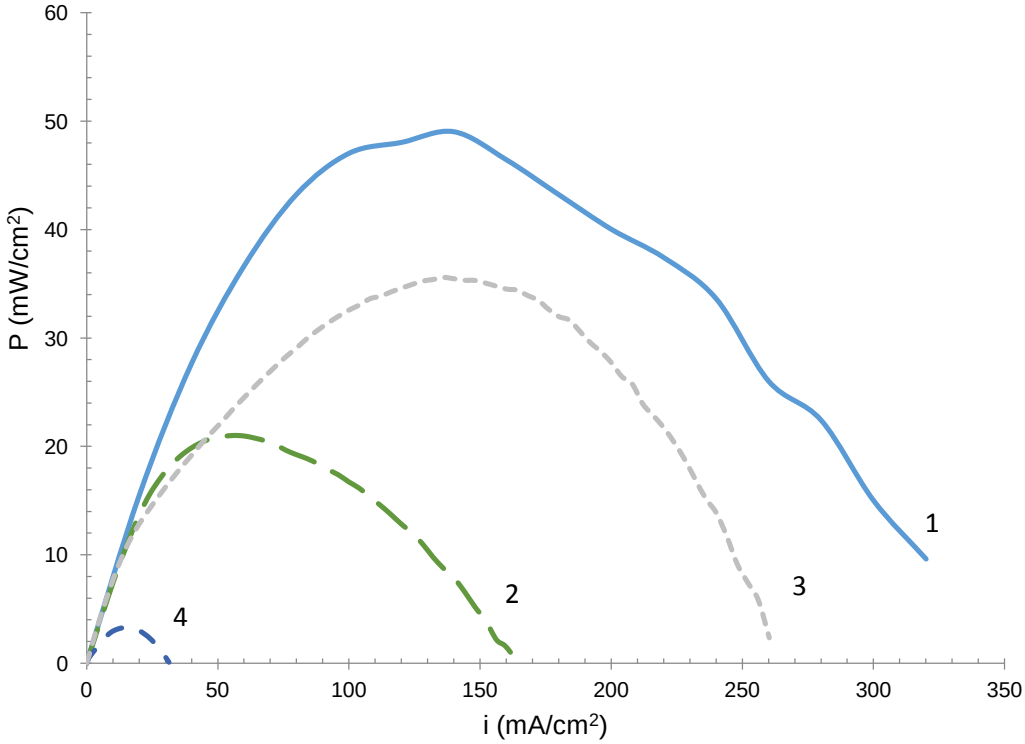

Figure 5.35 Power Density Polarization Experiments. 2M HCOOH, O_2 flow at cathode, T=90˚C

To further reduce cost while maintaining sufficient performance, a ternary and quaternary catalyst were also investigated. The following compositions were prepared at 20wt% loading and subjected to fuel cell testing:

1. Pd/C
2. PdAuSnFe/C
3. $Pd_{20}Sn/C$
4. PdFe/C
5. PdAuSn/C

Figure 5.36 shows the cell voltage polarization plots for the various catalysts compared to Pd/C, in terms of specific current. All catalysts outperformed Pd/C regardless of composition. Interestingly, at 20wt% metal loading, PdFe/C outperformed $Pd_{20}Sn/C$, contrary to what was observed with 60wt%. Unfortunately, at 50mA/cm^2 voltage efficiency dropped to 16% and 9.5% voltage efficiency for PdFe/C and $Pd_{20}Sn/C$, respectively. Although, combining Au with Pd and Sn to obtain PdAuSn/C resulted in an improvement in performance respective to the other catalysts in this series, achieving 21.6% voltage efficiency at 50mA/cm^2.

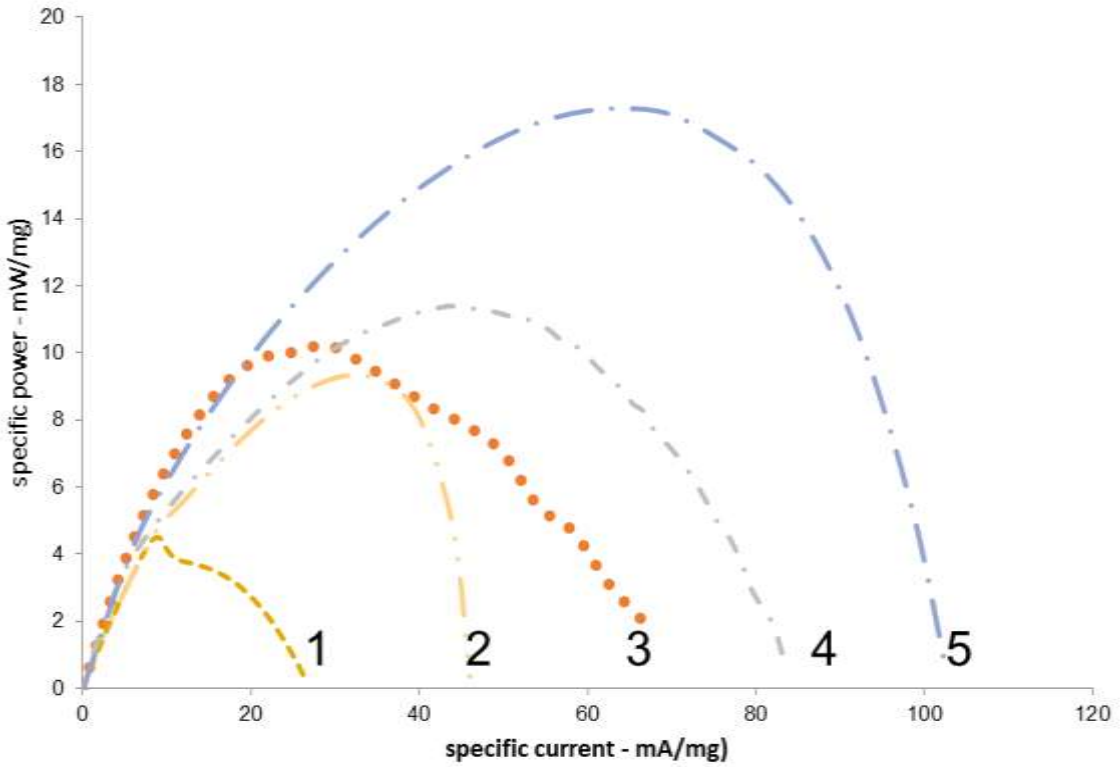

Figure 5.36 Cell Voltage Polarization Curves for Binary, Ternary and Quaternary Catalysts. Pd/C (catalyst 1) was tested to serve at the "state-of-the-art" example. 2M HCOOH, O_2 flow at cathode, T=90˚C.

Additional work was carried out to gain a better understanding of PdFe alloys and to determine the effect on FAO activity from varying the iron-content. Pd_3Fe/C is especially interesting since it is also known to be active for the oxygen reduction reaction (ORR).

Investigations began by preparing Pd_3Fe/(C+TaC) at 20, 40 and 60wt% and testing their efficacy towards FAO. The results of chronoamperometry experiments are shown in Figure 5.37. As expected, the catalysts with the largest precious metal loading gave the highest current density and were deactivated more slowly.

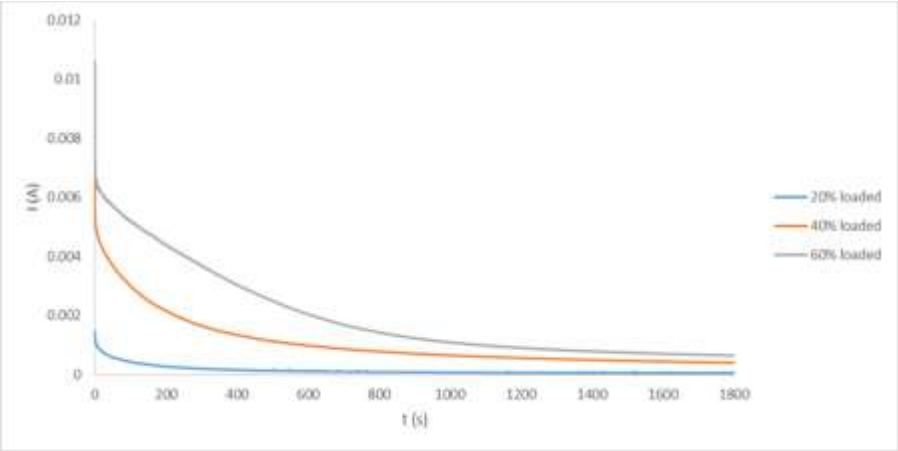

Figure 5.37 Chronoamperometry of Pd_3Fe/(C+TaC). Performed at 0.51V vs. NHE.

After several unsuccessful fuel cell tests using these materials, it was hypothesized that iron, which readily dissolves in acidic media, could be leaching from the catalyst surface and becoming lodged in the proton-exchange membrane, increasing cell resistance. To test this hypothesis, the catalyst in question was boiled in dilute sulfuric acid to remove corrodible surface species prior to being incorporated into a membrane electrode assembly (MEA). The results shown in Figure 5.38 demonstrate an increase in efficiency from 30% to 36%, respectively, at about 35mA/cm^2 after pretreatment of the Pd surface. In addition, a mass transport limitation is observed ca. 130mA/cm^2 if pretreatment is not performed, suggesting increased membrane resistance from Fe-blocked proton transport channels.

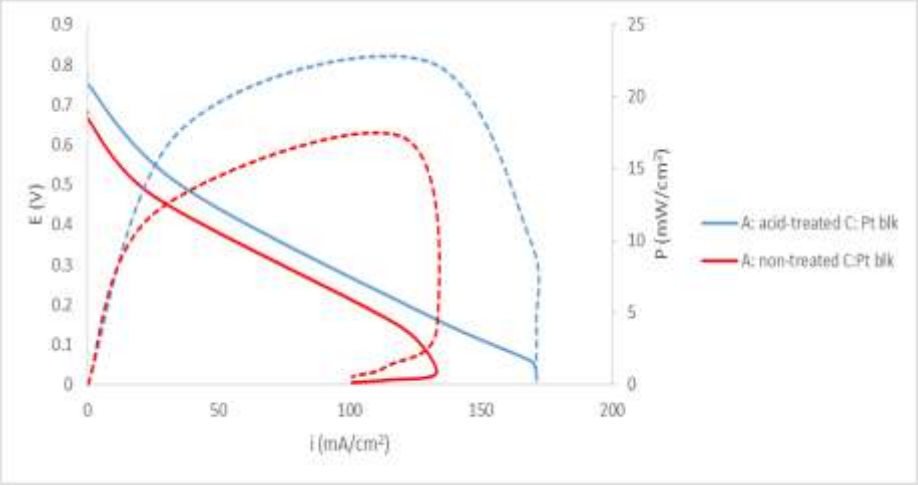

Figure 5.37 Cell Voltage Polarization Curves Post and Prior acid treatment. Dotted lines correspond to the power density. 2M HCOOH, O_2 flow at cathode, T=60˚C

These catalysts were also tested for FAO using chronoamperometry (Figure 5.38), and compared to the previously prepared 40 and 60% loaded Pd_3Fe/(C+TaC). Interestingly, PdFe(20%)/C outperforms the 40% loaded Pd_3Fe and exhibits current densities comparable with the 60% example. This result further demonstrates that Fe has great potential as a component in FAO catalysts, by achieving competitive current densities at a low precious metal loading. A 1:1 atomic composition may be less susceptible to deactivation by strongly binding intermediates due to an electronic effect from the presence of Fe in the palladium lattice.

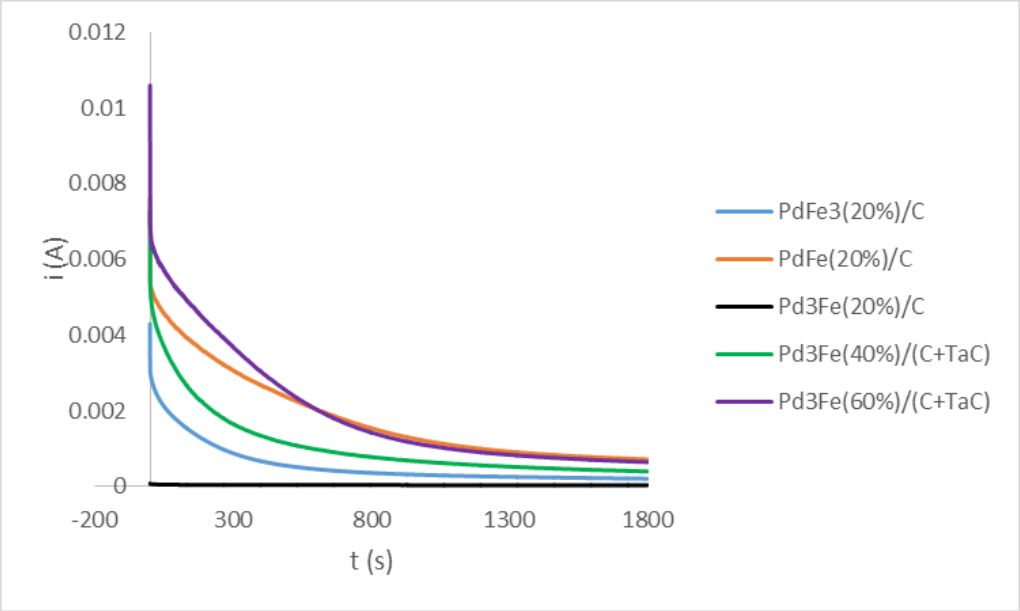

Figure 5.38 Chronoamperometry of various PdFe catalysts.

To gain a better understanding of the nature of the interaction between these catalyst surfaces and the intermediates formed during formic acid oxidation, CO-stripping was performed, as shown in Figure 5.39. This experiment was initially performed with Pd black to obtain a reference potential against which a shift caused by the incorporation of iron could be compared, which was measured as 0.248 V vs. MSE. It was found that CO oxidation in catalysts with calculated stoichiometric Pd:Fe ratios of 1:1 and 3:1 exhibited very similar peak stripping potentials of 0.228 V and 0.221 V, respectively, ~0.2 V more negative compared to Pd black. Hence, less energy will be required to accomplish oxidation of a reaction intermediate that might otherwise have become irreversibly bound. On the contrary, a positive shift of 0.45 V is observed when a small amount of iron is incorporated into the matrix, as in the case of $PdFe_3$ (20wt%)/C. Thus, surface species will likely bind more strongly and be more difficult to remove from this catalyst than the others.

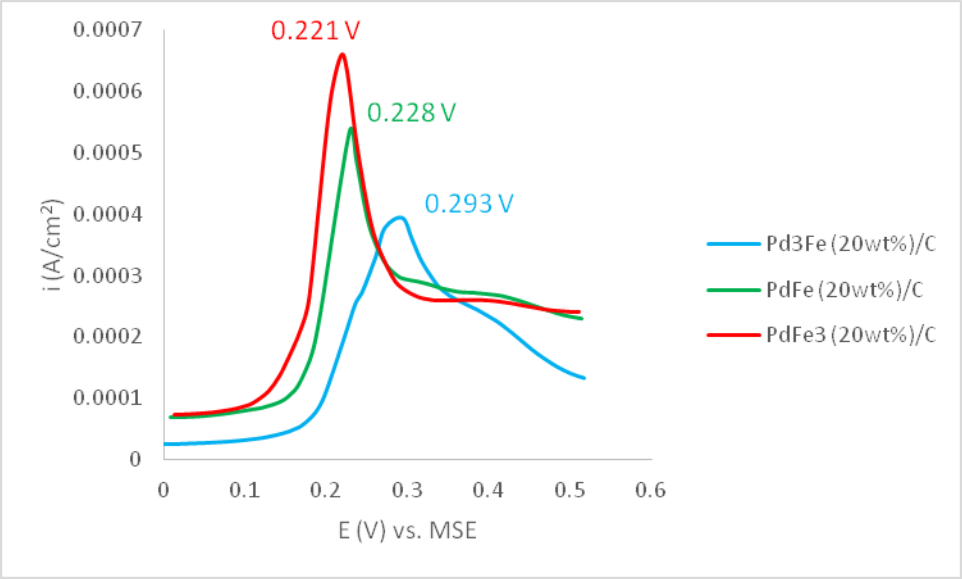

Figure 5.39 CO-stripping Cyclic Voltammograms. Peak CO oxidation potentials are given in the same color as the corresponding curve. Current densities are normalized to electrochemically active surface area. Experiments were performed to determine this value for Pd black as well, which was found to be 0.248 V vs. MSE (curve not shown).

Applying the knowledge obtained from CO-stripping, one can come to a better understanding of what occurred with the chronoamperometry experiments shown in Figure 5.38. The catalyst that exhibited the highest CO oxidation potential (i.e. strongest binding energy) also gave the poorest performance (blue curve). As the formic acid oxidation proceeds on Pd_3Fe (20wt%)/C, a strongly binding intermediate rapidly covers the surface such that formic acid molecules can no longer react with the catalytically active sites. Conversely, the catalysts with the lowest CO-stripping potentials were also the ones with the highest performance. Although the other two catalysts exhibit similar CO-oxidation potentials, suggesting similar surface binding properties, PdFe (20wt%)/C exhibits higher current than $PdFe_3$ (20wt%)/C. This can be understood by fact that the 1:1 PdFe catalyst has a greater number of catalytically active sites than 1:3 PdFe when both are loaded at 20 wt% on Vulcan carbon. Since poisoning species likely adsorb and desorb to the same degree on each surface, the catalyst with a greater amount of palladium will retain a greater number of active sites as strongly binding intermediates build up throughout the course of the formic acid oxidation.

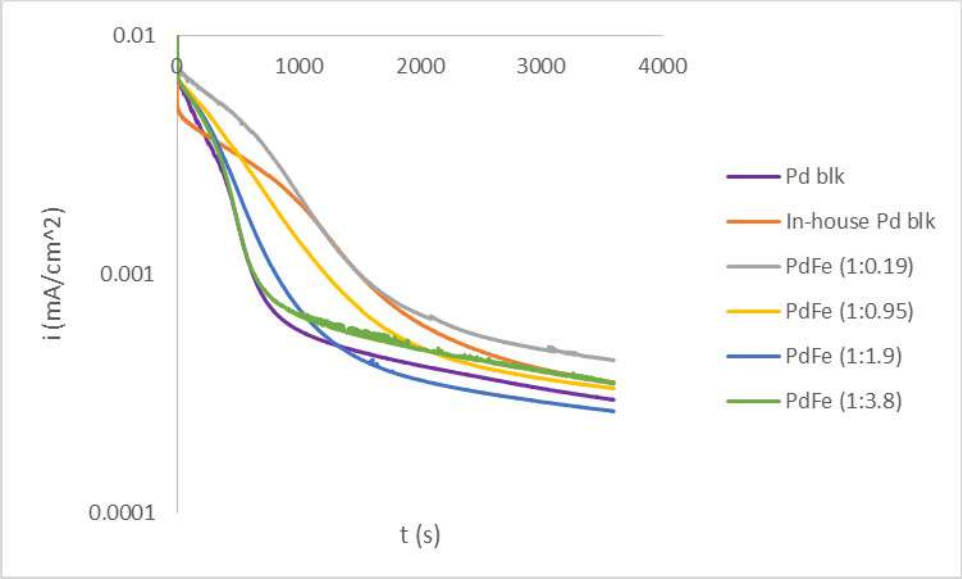

Figure 5.40 Chronoamperometry of Unsupported PdFe Catalyst.

Further studies have been carried out with PdFe catalysts by varying the Pd:Fe molar ratio, as shown below:

1. $Pd_1Fe_{0.19}$
2. $Pd_1Fe_{0.95}$
3. $Pd_1Fe_{1.9}$
4. $Pd_1Fe_{3.8}$

This series of materials was tested against Pd prepared by $NaBH_4$ reduction of ammonium tetrachloropalladate and commercially available Pd black.

As shown in Figure 5.40, the catalyst with the least amount of iron exhibited the highest current density and stability after 1 h of FAO at 0.51 V vs. NHE in 0.1 M $HClO_4$ and 0.5 M HCOOH. Increasing iron content resulted in a concomitant decrease in performance, but all materials exhibited better stability than the commercial Pd black. Interestingly, the Pd prepared from $NaBH_4$ reduction of ammonium tetrachloropalladate outperformed the commercial catalyst, probably due to differences in their catalytic sites. Work is continuing towards the incorporation of the aforementioned materials into functioning DFAFCs and the development of novel catalyst formulations that may exhibit improved FAO performance.

Supported Catalysts

Carbon powder has long been known as an effective catalyst support for its high conductivity and surface area, as well as its chemical inertness. All of these properties are necessary for any catalyst operating in the reactive and sometimes corrosive fuel cell environment. To expand on our previous results, we have prepared a series of PdAu catalysts supported on both carbon and tantalum carbide (TaC); TaC is a hard, conductive, and corrosion-resistant material well suited for incorporation into fuel cell electrocatalyst layers. Tantalum metal has a very low toxicity and has been deemed biocompatible. Catalysts on the 1:1 by

weight C:TaC support system were found to perform even better than those supported solely on carbon. It was found that supporting $Pd_{99}Au$ at 20wt% (labeled as PdAu-A in Figure 10) on 1:1 C:TaC resulted in a drastic increase in specific power, as shown in Figure 5.41.

Figure 5.42 shows a TEM image of PdAu-A/(C+TaC) in which the metal nanoparticles are easily resolved, measuring from 3 to 6 nm in diameter. Small particle sizes, such as those seen here, are very desirable for increasing the exposed surface area and therefore reducing the necessary precious metal content.

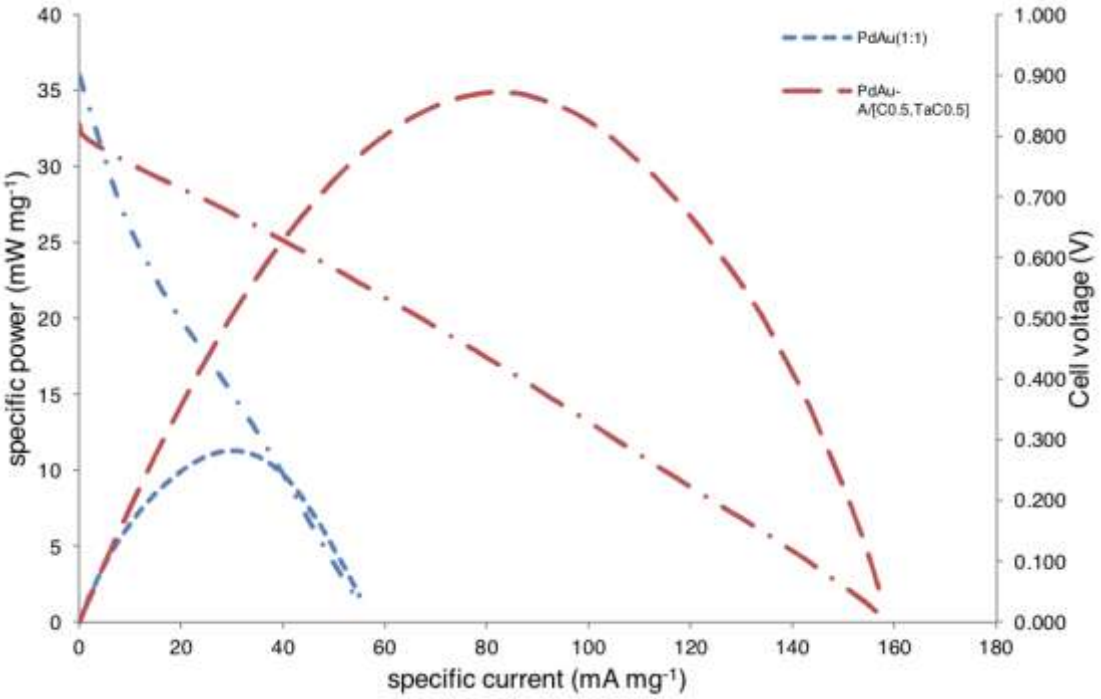

Figure 5.41 Specific Power Polarization Curve of a Catalyst incorporating 1:1 C:TaC. The parabola-shaped curves correspond to the specific power. 2M HCOOH, O_2 flow at cathode, T=90˚C.

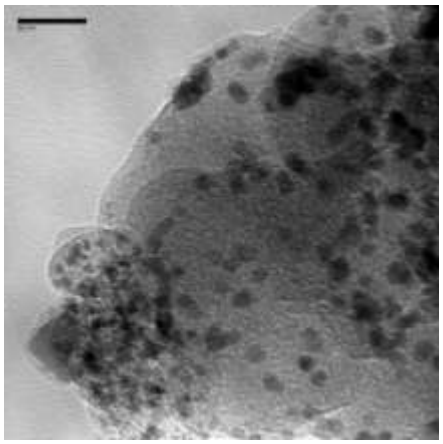

Figure 5.42 *TEM image of $Pd_{99}Au/[0.5C+0.5TaC]$ at 160,000x magnification.* Scale bar = 20nm.

Very recently, much interest has arisen towards using graphene as a catalyst support, due to its excellent conductivity and extremely high surface area. However, graphene is difficult to obtain in sufficient quantities, thus reduced graphene oxide is employed, which retains many of graphene's desirable properties. Graphene oxide, a sheet of sp^3 bonded carbons covered in a multitude of oxygen functionalities, is produced from the oxidation of graphite powder. This material is an insulator, so it must be partially reduced to regenerate the conductive graphitic surfaces. The simultaneous reduction of graphene oxide in the presence of the appropriate metal salts resulted in the deposition of metal nanoparticles onto reduced graphene oxide (rGO). To our knowledge, this is the first example of the borohydride reduction method to obtain rGO-supported metal catalysts.

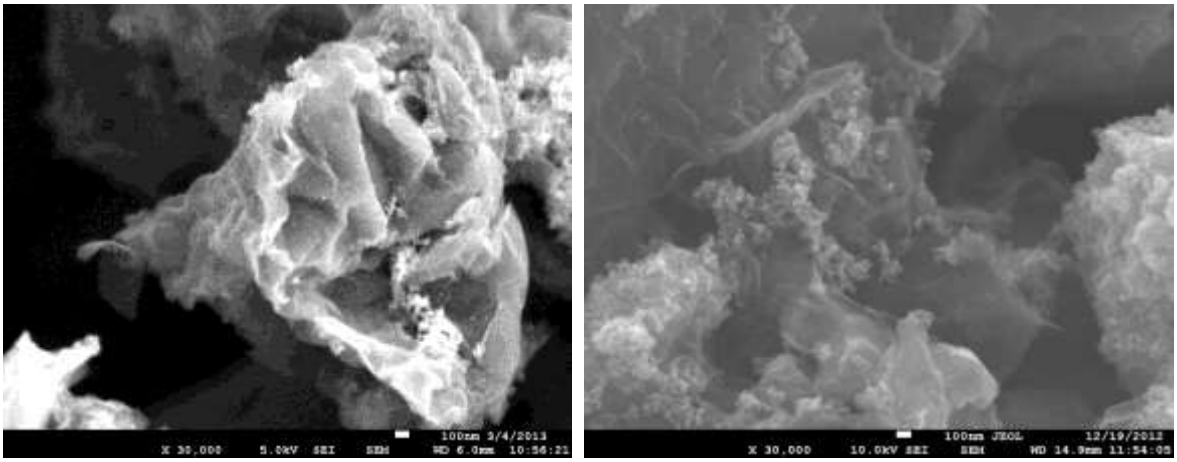

Figure 5.43 *SEM images of Pd/rGO and Pd_3Fe/rGO at 30,000x magnification*

Pd and Pd_3Fe catalysts were successfully supported on rGO at 20 wt%. As shown in the SEM images in Figure 5.43, there appears to be a better dispersion of metal catalysts in Pd_3Fe/rGO than in Pd/rGO, which may explain the its higher activities observed in the CV in Figure 5.44.

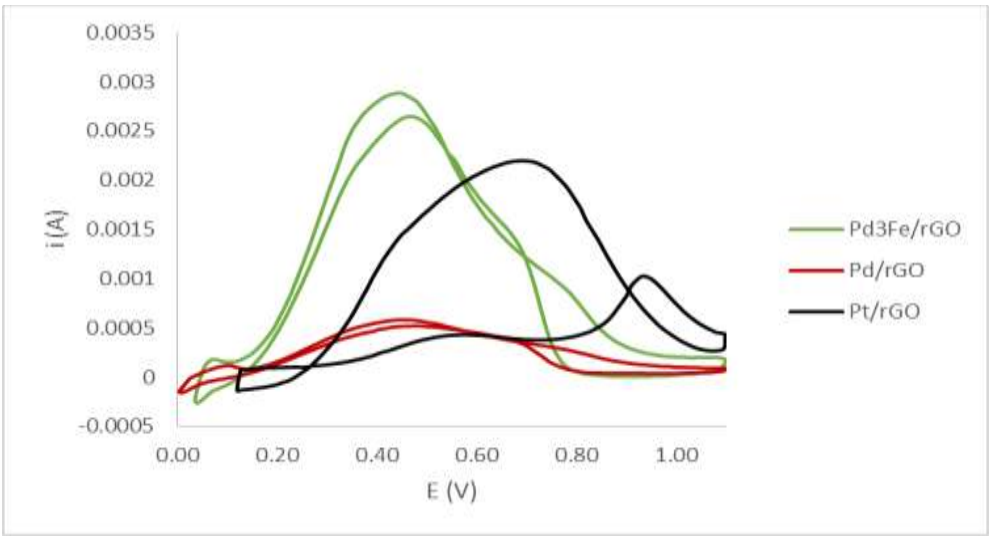

Figure 5.44 Cyclic Voltammetry of rGO-supported Metal Catalysts. The difference in FAO mechanism can be seen between the Pt and Pd catalysts.

The aforementioned rGO supported catalysts were tested against Pt supported on rGO, and important differences in reactivity towards formic acid were observed. As is evident in Figure 5.45, there are two oxidation peaks on Pt while only one on the Pd catalysts. This difference arises from the presence of the dehydration pathway on Pt, which generates a significant amount of CO. Since the dehydrogenation pathway (in which CO_2 is formed rather than CO) is dominant at high potentials, the oxidation peak current is higher in the reverse scan.

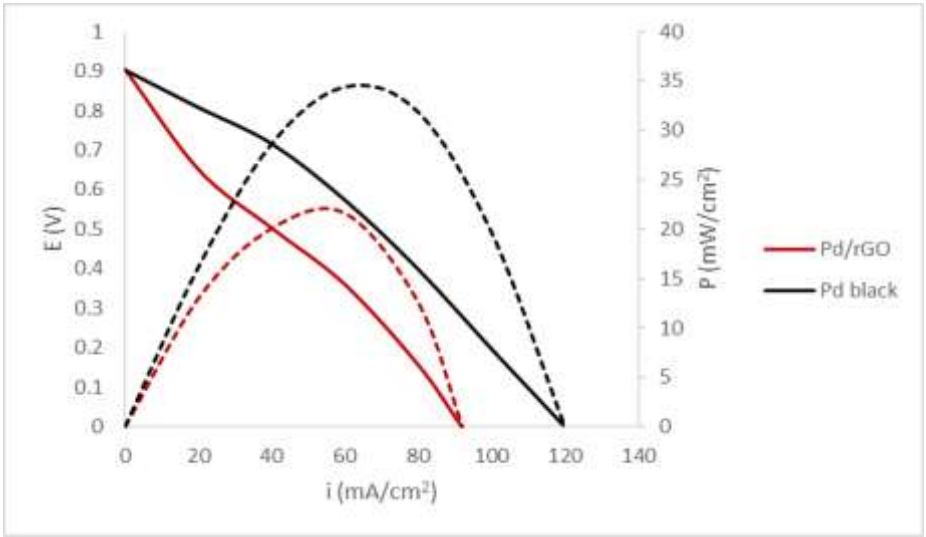

Figure 5.45 Fuel Cell Polarization Curves for Pd/rGO and Pd/black. 2M HCOOH, O_2 flow at cathode, T=60˚C.

A Pd black fuel cell was prepared and tested so as to set a benchmark against which future catalysts can be compared. As seen in Figure 14, At 40mA/cm^2 the DFAFC with Pd black at the anode achieved 48% voltage efficiency. With Pd/rGO, an efficiency of 34% was achieved while operating at the same current density. This result is significant because it demonstrates the effective utilization of a smaller amount of precious metal by employing the rGO support to

achieve performance comparable to state-of-the-art Pd black. Work will be continued in this area

Table 5.14 The best performing formic acid oxidation catalysts at 40 mA/cm^2.

Catalyst	**Voltage Efficiency at 40 mA/cm^2 ($V_{operating}/V_{max. theoret.}$)**	**Operating Potential(V)**
Pd Black	48%	0.7
PdAu	52%	0.77
PdFe(60wt%)/C	34%	0.5
PdSn(20:1)(60wt%)/C	47%	0.7
Pd(20wt%)/rGO	42%	0.62

In summary, and as listed in Table 5.14, five catalysts were found that have approached or exceeded the goal of operating a DFAFC at 40% voltage efficiency. Of the supported catalysts that were tested, PdAu is the only catalyst that outperforms state-of-the-art Pd black, but PdFe and PdSn on carbon supports perform comparably well and show promise for the development of non-precious metal based catalysts. In addition voltage efficiencies higher than 40% were achieved with Pd on rGO, demonstrating its utility as a catalyst support and further reducing the amount of precious metal required for an effective catalyst. Work is ongoing to understand the electronic effects that the incorporation of Fe may have on the catalytic surfaces of Pd. Future work will investigate other catalyst materials and combinations for the FAO and examine the effects of hetero-atom doped graphene and graphene-based nanostructures as supports. By utilizing the benefits of high-surface area supports and alloying Pd with non-precious metals, and through their subsequent characterization and testing, future research will result in the discovery of more optimal fuel cells and a better understanding of the processes involved therein.

Task 6: Techno-Economic Analysis of Various Projects

Techno- Economic Analysis: Production of Methanol from the Bromination of Methane (Task 2)

Methanol is currently produced on a large scale using the high temperature and cost intensive steam reforming of methane to produce synthesis gas (CO and H_2), which is subsequently converted to methanol at 250^o C and 50 bar. A new route for the production of methanol was developed at modest reaction conditions (atmospheric pressure and below 600^o C) using bromine as an oxidant. The catalytic cycle involves three major steps (Figure 6.1):

1- Bromination of methane to methyl bromide
2- Hydrolysis of methyl bromide to methanol and dimethyl ether
3- Oxidation of hydrogen bromide to bromine.

The analysis will concentrate on the costs of the chemicals necessary to produce 1 ton of methanol. Recycling of chemicals will significantly reduce the initial costs while adding costs related to the recycling. The methanol production rate will dictate the size of the equipment and the related costs; this aspect of the process is not included in this analysis.

Bromination of Methane to Methyl Bromide

Of the many catalysts tested, SAPO-34 exhibited a good activity, stability, and an excellent selectivity to methyl bromide. In fact, methyl bromide was the sole product of the bromination of methane over SAPO-34 at 365^o C under atmospheric pressure with a conversion of bromine close to 50 mol % for a methane-bromine molar ratio of 10 to 1, a total flow rate of 7.2 mL/min, and 3 g of catalyst. With 10 g of catalyst, the conversion of bromine increased to 62 mol % and the selectivity to methyl bromide decreased to 36.4 mol % with the formation of higher hydrocarbons and the formation of carbon deposits. Due to the corrosive nature of bromine and hydrogen bromide, we think that it is advantageous to consume all the bromine in the bromination reactor, which will limit its presence beyond that step while hydrogen bromide thanks to its high solubility in water will be absorbed in water at the exit of the reactor.

The thermal bromination of methane using an empty 9 mm ID quartz tube at 525^o C under atmospheric pressure led to the total conversion of bromine for a methane/bromine/nitrogen molar ratio of 10 : 1 : 17 and a total flow rate of 26 mL/min. The selectivity of methyl bromide dropped to 82 mol %; methylene bromide selectivity was 17 mol% and 0.01 mol % of methane produced carbon deposits. The thermal bromination has several additional advantages: (i) no catalyst is necessary, therefore costs of catalyst replacement and regeneration are avoided, especially under severe oxidative conditions that always limit the catalyst lifetime; (ii) the total flow rate is almost 4 times higher; and (iii) the reaction conditions can be easily optimized to improve the yields and avoid carbon deposits. Thus, the results of the non-catalytic thermal bromination are used in this analysis.

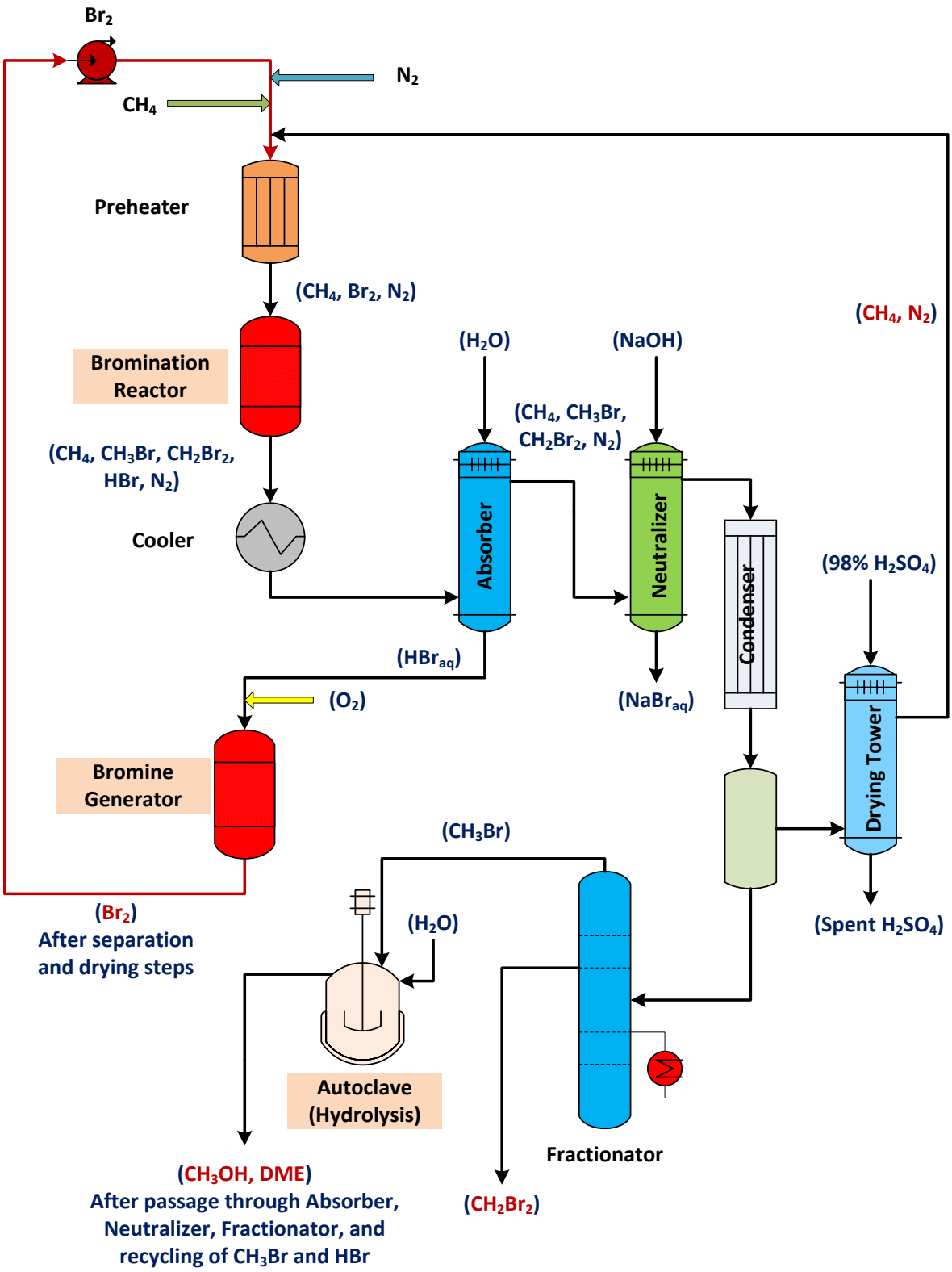

Figure 6.1: Simplified schematic of the production of methanol from the bromination of methane

Hydrolysis of Methyl Bromide to Methanol and Dimethyl Ether

The hydrolysis of methyl bromide (b.p. 4 ^{o}C) reactions were carried out at the millimole level in a 20 mL-pressure glass tube at 100^{o} C and about 8 bar of autogeneous pressure (the maximum pressure rating of the glass tube was 10 bar). For a contact of 5 hours, the conversion of methyl bromide was 16.3 mol % for a molar ratio of water and methyl bromide of 12 to 1 in the absence of a catalyst. The selectivity of methanol was 52.4 mol % and that of dimethyl ether 47.6 mol %. In the presence of a catalyst the conversion of methyl bromide was lower, 13 mol % and the selectivity of methanol increased to 73.7 mol %. Lower conversions in the presence of a catalyst were due to the volume occupied by the catalyst compared to the reactants and the large dead volume of the reactor that favors long residence times of methyl bromide in the gas phase. Higher conversions are expected at higher pressures and smaller reactor dead volumes. The techno-economic analysis is based on the results obtained in the absence of a catalyst.

Oxidation of aqueous Hydrogen Bromide to Bromine

The oxidation of hydrogen bromide solutions to bromine was not investigated in this work. However, the costs of the chemicals necessary to carried out the reactions were included in the analysis. Several catalysts are known to efficiently convert aqueous HBr to Br_2.[2] A proprietary catalyst named 'BROCAT' from Catalytica, Inc.[2] showed a high activity and stability at temperatures as low as 275^{o} C. However, the price of the catalyst was not available. The price of CuO/Al_2O_3 catalyst, less active and less stable, especially above 325^{o} C, was used in the analysis.

Initial Costs of Chemicals for the Production of 1 ton of Methanol (DME)

The production of 1 ton of methanol will require 18 ton of methyl bromide at 16.3% conversion of methyl bromide. 44 ton of bromine and 2,397 Mcf (Thousand cubic feet) of methane are needed to produce the 18 ton of methyl bromide. At $2,970/ton for bromine and $4.48/Mcf for methane, the costs of bromine and methane are $129,986 and $10,737, respectively. If an additional 1 percent of methane used for the reaction is to provide the energy for the bromination, the hydrolysis and the oxidation of hydrogen bromide, the cost of methane becomes $11,274. 4,074 Mcf of nitrogen will be needed. At $6/Mcf, the cost of nitrogen is $24,456. If 99.9 percent of the 25 ton of HBr produced could be recovered from the absorber; the remaining 0.1 percent will be neutralized by NaOH in the neutralizer unit. The cost of NaOH will be $0.73. 0.1 ton of sulfuric acid is used in the dehydration unit at a cost of $25. 1.1 ton of oxygen and 1 ton of CuO/Al_2O_3 (about $424/ton) are required for the oxidation of HBr; the cost of oxygen is $3.6. Water usage, estimated at 19,800 cf, will cost $1,386. Therefore, the total initial cost of the chemicals amounts to **$167,452** per ton of methanol (dimethyl ether). Table 6.1 summarizes all the costs of chemicals. The next section shows the effect of recycling on the costs of the chemicals.

[2] P. F. Schubert, R. D. Beatty, and S. Mahajan, Environmental Catalysis; Amor, J.; ACS Symposium Series, 1994

Table 6.1 Initial costs[1] of chemicals for the production of 1 ton of methanol (dimethyl ether) from the bromination of methane

Chemical	Usage	Cost/unit	Total cost
Br_2	44 ton	$2,970/ton	$130,680
Natural Gas for reaction	2,400 Mcf	$4.48/Mcf	$10,752
Natural Gas for energy	24 Mcf	$4.48/Mcf	$108
N_2 gas	4,076 Mcf	$6.0/Mcf	$24,456
CuO/Al_2O_3	0.1 ton	$424/ton	$42.4
O_2	1.2 ton	$3.0/ton	$3.6
NaOH	0.012 ton	$60.4/ton	$0.73
98% H_2SO_4	0.1 ton	$250/ton	$25
H_2O	19,800 cf	$0.07/cf	$1,386
Total			**$167,452**

[1] **Calculations for the usage of chemicals**: 1 ton CH_3OH (31.3 Kmol) will require 31.3 Kmol of CH_3Br. At 16.3% conversion, the initial amount of CH_3Br is 31.3/0.163 = 192 Kmol (18.2 ton). Amount of Br_2 needed = 192*1.17/0.82 = 274 Kmol (44 ton) [Balanced equation for the bromination of methane: **$CH_4 + 1.17\ Br_2 = 0.82\ CH_3Br + 0.17\ CH_2Br_2 + 0.01\ C + 1.19\ HBr$**]. At a CH_4/Br_2 molar ratio of 10 to 1; the amount of CH4 = 2740 Kmol (2,400 Mcf). For energy requirement, 1% of 2,400 Mcf is used = 24 Mcf. N_2/CH_4 molar ratio is 1.7; amount of N_2 = 2740*1.7 = 4,658 Kmol (4,076 Mcf). HBr produced from bromination and hydrolysis = (1.19*274/1.17)+31.3 = 311 Kmol (25 ton). 99.9% of HBr will be recovered in the absorber unit and the rest will be neutralized by NaOH. 0.1 ton of catalyst will be used for the oxidation. Amount of O_2 for the oxidation = (311*0.999)/4 = 310.7 Kmol (67 Mcf, 1.2 ton). NaOH for neutralization = 0.001*311 = 0.311 Kmol (0.012 ton). In the dehydration unit 0.1 ton 98% H_2SO_4 is used. Assuming water usage equivalent to 100 times the amount of HBr, amount of water required = 100*311 = 31,100 Kmol (19,800 cf).

Cost of Chemicals with Recycling of methane, bromine, methyl bromide, methylene bromide, water, and exclusion of nitrogen from the Reaction Mixture

Assuming an efficient recycling of methane, bromine, methyl bromide, methylene bromide, and the exclusion of nitrogen from the reaction mixture, the costs of the chemicals will be limited to the use of methane necessary to produce 1 ton of methanol and for heating purposes. Thus, the cost of methane from the reaction will be reduced to $123. The total costs of the chemicals could be as low as **$400** per ton of methanol, including the costs of water, sodium hydroxide, catalyst for the oxidation of HBr, oxygen and sulfuric acid. These costs can further decrease at higher production levels. However, even if all NaBr is oxidized to Br_2, there will still

be some lost of bromine in the system which will require some bromine makeup, which can increase the production costs since bromine is too expensive.

Comparison with the Steam Reforming Route

At a 10,000 to 15,000 ton of methanol/day plant, methanol could be produced at 30 cents a gallon,[3] which is approximately $100/ton. Higher production costs are expected for a 5,000 ton/day plant which could make the bromination a viable route for the conversion of methane to methanol. For this route to become competitive, the recovery of bromine should be very efficient and the overall space time yield should increase, especially that of the hydrolysis of methyl bromide. Methylene bromide ($5,500/ton) is more expensive than bromine ($2,970/ton); it can be sold instead of recycling it, which will provide funds for the bromine makeup.

Future Works

More research is necessary to optimize both the bromination and the hydrolysis steps assuming that the 'BROCAT' catalyst of Catalytica Inc. remains efficient and stable for long reaction periods at a production level of 5,000 ton of methanol per day and more. Lorkovic et al.[4] found that for the methane bromination (CH_4/Br_2 molar ratio of 1, diluted with nitrogen) at 525^o C, the conversion of methane and the selectivity of methyl bromide reached 73.5% and 69.5%, respectively, after 60 s time for reproportionation of methane with methylene bromide. The carbon balance and carbon deposits were not reported in this study. We found that hydrolysis of methanol in a 100 mL Monel-type autoclave, which can sustain up to 2000 psi of pressure led to higher methyl bromide conversions but as the body of the reactor significantly interferes with the reaction, tests were not pursued under these conditions. Higher conversions of methyl bromide (greater than 50 mol %) can be obtained in the reaction with methanol to dimethyl ether (methanolysis of methyl bromide).

The high corrosiveness of bromine and aqueous hydrogen bromide solutions bring other challenges associated to the lifetime of the equipment. Resistant materials to corrosion are necessary for long production periods.

[3] R. Vikram, Research Triangle Energy Consortium, http://rtec-rtp.org/2012/04/27/methanol-is-pro-choice/
[4] I. M. Lorkovic et al., J. Phys. Chem. A 2006, 110, 8695-8700

Techno-Economic Analysis: Production cost of methanol from syn-gas through bi-reforming of natural gas with steam and CO_2 (Task 3)

Synthesis gas (syn-gas), a variable composition mixture of hydrogen, carbon monoxide and carbon dioxide, is the basis for the production of a variety of chemicals. Syn-gas is produced by oxidation with steam and oxygen from virtually any carbon source including biomass.[1] However, natural gas and methane are generally the preferred feedstocks. It is also the source for the large scale production of synthetic fuels and chemicals such as methanol, dimethyl ether and hydrocarbons.[2] The synthesis of methanol requires a syn-gas with a H_2/CO ratio of about 2.[3] The most commonly used reforming technology for methane, steam reforming, produces a syn-gas with a H_2/CO ratio close to 3. This means that additional steps are needed to adjust the H_2/CO ratio. Carbon dioxide reforming, called dry reforming, produces a syn-gas with a H_2/CO ratio close to 1, which is too low and has also to be adjusted.[4] On the other hand, methane partial oxidation with oxygen can produce an ideal ratio of 2 but is difficult to control and can lead to local hot spots in the catalyst bed and associated dangers of explosions.[5] The combination of steam reforming and partial oxidation (autothermal reforming) also always produces a H_2/CO ratio higher than 2.[1]

The production of a syngas mixture with a H_2/CO ratio suitable for methanol synthesis in which dry reforming is combined with steam reforming in a single step process called *bi-reforming* was therefore proposed.[6, 7] In bi-reforming, a ratio of methane, steam and CO_2 of 3/2/1 produces a gas mixture with essentially a 2/1 ratio of hydrogen to carbon monoxide, which we have suggested be called "metgas" to underline its difference from the widely used syn-gas mixtures of varying H_2/CO ratio This specific 2/1 H_2/CO gas mixture is for the sole purpose of preparing methanol (a clean burning, high octane rated fuel) with complete utilization of the hydrogen in the gas feed. The conversion of methane with CO_2 and water is:

Steam reforming	$2CH_4 + 2H_2O \longrightarrow 2CO + 6H_2$	$\Delta H_{298K} = 49.1$ kcal.mol^{-1}	Eq. 1
Dry reforming	$CH_4 + CO_2 \longrightarrow 2CO + 2H_2$	$\Delta H_{298K} = 59.1$ kcal.mol^{-1}	Eq. 2
Bi-reforming	$3CH_4 + 2H_2O + CO_2 \longrightarrow 4CO + 8H_2 \longrightarrow 4CH_3OH$		Eq. 3

Bi-reforming is also advantageous in the use of natural gas sources containing significant CO_2 concentrations. CO_2 would, otherwise, have to be removed and vented to the atmosphere to allow further processing of the natural gas. Some natural gas as well as biogas sources contain CO_2 in concentration up to 50% or even higher.[8] Bi-reforming could also be used to recycle CO_2 emissions from sources such as flue gases from fossil fuel (coal, petroleum, natural gas, etc.) burning power plants, exhaust of cement factories and other industries.

Bi-reforming to metgas is adaptable for reforming varied natural gas (containing hydrocarbon homologues) and CO_2 sources.

$$3\ C_nH_{(2n+2)} + (3n\text{-}1)H_2O + CO_2 \longrightarrow$$

$$(3n+1)CO + (6n+2)H_2 \longrightarrow (3n+1)CH_3OH \quad \text{Eq. 4}$$

Metgas can also be generated from other carbon sources including coal bed methane, methane hydrates as well as biomass. Recent findings of significant shale gas (methane) deposits considerably increased the overall reserves of natural gas. Shale gas production is made possible by horizontal drilling and rock fracking using high pressure water and chemical additives although the environmental consequences of these techniques is still unclear.[9]

The two reactions in bi-reforming could be performed in two separate steps, one for the dry reforming and another for steam reforming, combining both effluent streams before sending them to the methanol synthesis unit. However, it is much preferable to combine these in a single step to lower capital and operational cost as well as complexity of the system. The catalyst for such a reaction should therefore be active and stable over extended durations for both reactions.

The preparation of metgas from natural gas using bi-reforming should have a comparable cost to the production of syn-gas from natural gas using conventional technologies (steam reforming and autothermal reforming). It uses the same type of technologies, catalysts, temperature range, pressure range, etc. The fact that a hydrogen/carbon monoxide ratio of 2/1, ideal for methanol synthesis, is obtained with the bi-reforming reaction could however be an advantage as no additional steps are needed to adjust the H_2/CO ratio potentially lowering the costs of methanol production. In the case of natural gas sources containing high concentrations of CO_2, the use of bi-reforming could avoid the need to first separate the CO_2 prior to processing, eliminating a costly step. Due to the lower excess of steam in the gas feed compared to steam reforming and autothermal reforming the choice of material for the reforming reactor should be adapted to handle potential metal dusting problem by either passivating the metallic surfaces or lining the reactor with an inert material. This could affect the construction costs of the plant negatively.

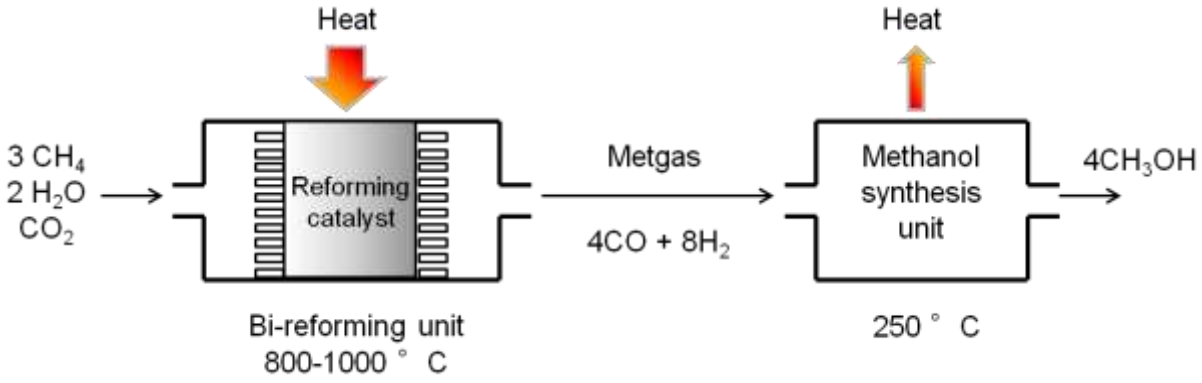

A methanol plant with natural gas feed can be divided into three main sections. In the first part of the plant natural gas is converted into synthesis gas. The synthesis gas reacts to produce methanol in the second section, and methanol is purified to the desired purity in the tail-end of the plant.

The synthesis gas preparation and compression typically accounts for about 60% of the investment, and almost all energy is consumed in this process section. Therefore, the selection of reforming technology is of paramount importance, regardless of the site where the plant will be installed.[10]

Given the fact that most of equipment and technology used are similar to existing technologies for methanol production (via steam and autothermal reforming), the cost of methanol should be relatively close to the one obtained with these processes. Usually, increasing the size of the plant will lead to considerable economies of scale and the norm are now so-called Mega-Methanol plants with capacities of 5000 to 10000 metric tonnes per day (MTPD). This is of particular importance not only to improve the economics but also to provide the feedstock for the Methanol-to-Olefin (MTO) processing plants.

Regardless of the technology used, a large part of the cost of methanol will be tied to the cost of natural gas itself. Mega-methanol plants based on bi-reforming, like the ones based on other technologies, will be placed overwhelmingly in locations having some of the most inexpensive natural gas supplies such as the Middle East and thanks to the boom in shale gas production, the United States of America. Considering cheap natural gas resources, the production cost for methanol in mega-methanol plants has been estimated to be below \$200 t^{-1}methanol.[11] In the case of the Middle East the cost has even be estimated to be below \$100 t^{-1} methanol. This is well below the current sale prices of methanol between \$400 and \$600 in the last 3 years.

The capital cost of a Mega-methanol plant with a capacity of 10000 MTPD (3.3 million metric tonnes) consuming 170 billion scf natural gas per year (about 5 billion m^3, 3.5 million metric tonnes) has been estimated at about \$700 million (2003 dollars).[11]

Oxidative bi-reforming

A further advance in the exclusive conversion of natural or shale gas (methane) to metgas for methanol synthesis is using a process we have named *oxidative bi-reforming*. Oxygenation (i.e. oxygen functionalization) is a substitution of oxygen into a hydrocarbon that is different from varied conventional oxidations.[12] Bi-reforming[13, 14] itself is highly endothermic, necessitating substantial external energy. The complete combustion of a single equivalent of methane (natural or shale gas) with O_2 from the air gives the needed reaction heat. Furthermore, it also provides the required CO_2 -$2H_2O$ feed mixture which is captured and mixed with 3 equivalent of methane (natural gas) giving the needed specific feed for bi-reforming to produce exclusively metgas for the subsequent methanol synthesis step.

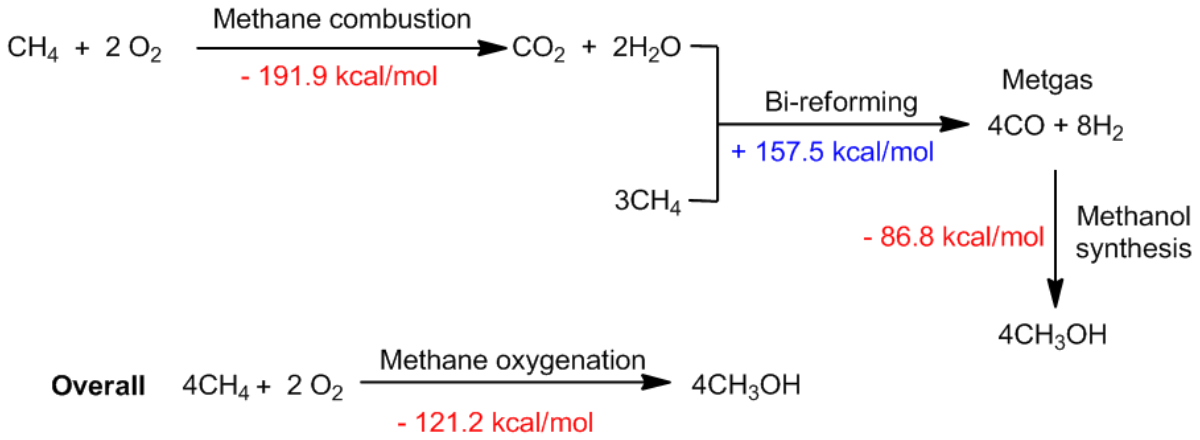

A single reactor is needed for the oxidative bi-reforming of methane (and its source materials). In the first part of the reactor methane is burned with pure oxygen to produce a heat and a gas mixture composed of CO_2 and H_2O in a 1 to 2 ratio. Further in the reactor, more methane is added to this CO_2/H_2O mixture and reacted over a catalyst to obtain a syngas with a H_2/CO ratio of 2 ideal for methanol synthesis. The need for a single reactor substantially decreases the complexity and thus potentially the cost of preparing metgas for subsequent methanol synthesis while also providing the needed reaction heat for the reaction in-situ.

Oxidative bi-reforming is actually very close to the autothermal reforming (ATR) of natural gas already practiced on a large scale, which uses a single refractory lined pressure vessel as reactor for syngas preparation.[10] In that case a part of the natural gas is first burned with oxygen to produce CO and water, which then further react with methane to form syngas. For ATR as well as for oxidative bi-reforming, the cost of an air separation plant to produce the needed oxygen has to be factored in. The presence of large amounts of inert gas such as nitrogen is not acceptable in the syngas as well as methanol synthesis step. There are three types of technologies used commercially for producing oxygen from air: cryogenic distillation, polymer membranes and pressure or vacuum swing adsorption on beds of zeolites. In mega-methanol plants, cryogenic separation is usually the technology of choice. For a 10000 MTPD methanol plant about 5000 MTPD oxygen in 99.5 % purity are needed in an ATR based plant. The cost for oxygen on such a large scale is about \$50/metric ton O_2 and depends mostly on the electricity cost to run the cryogenic distillation plant. About 300 KWh are needed per metric tonne of oxygen produced.[11]

Given their close similarity, the production of methanol by oxidative bi-reforming of methane should therefore have similar production cost to ATR based methanol plants. Considering cheap natural gas resources, the production cost for methanol in a mega-methanol plants using oxidative bi-reforming should therefore also be below \$200 t^{-1}methanol and probably below \$100 t^{-1} in the Middle East.[11]

It has been shown by Haldor Topsoe that for large scale plants Autothermal Reforming (ATR) at a steam-to-carbon (S/C) ratio of 0.6 combined with boiling water reactors optionally with an adiabatic top layer for the synthesis represents the superior choice for low investment.[10] They have estimated in a case study that a plant with this technology will have a higher single line capacity and a 15-20% lower cost compared to plants based on combinations of steam

reforming and Autothermal (or secondary) Reforming. The ATR based plants at low S/C-ratio may be designed to produce either fuel grade or high purity methanol. They also added that further development of the syngas and methanol synthesis technologies can further improve economics. The reduction of the S/C-ratio in particular could increase the single line capacity. This is important because in the case of oxidative bi-reforming the overall S/C ratio is 0.5 (below the S/C ratio of 0.6 used in current plants) as determined by the ratio of $H_2O/(CH_4 + CO_2)$ before the reforming catalyst.

Autothermal reforming always provides a syngas deficient in hydrogen (H_2/CO lower than 2). The ratio must be adjusted to a value of about 2 before the synthesis gas is suitable for methanol production. The adjustment is usually done either by removing carbon dioxide from the synthesis gas or by recovering hydrogen from the synthesis loop purge gas and recycling the recovered hydrogen to the synthesis gas.[15] In the case of oxidative bi-reforming such an adjustment is not necessary.

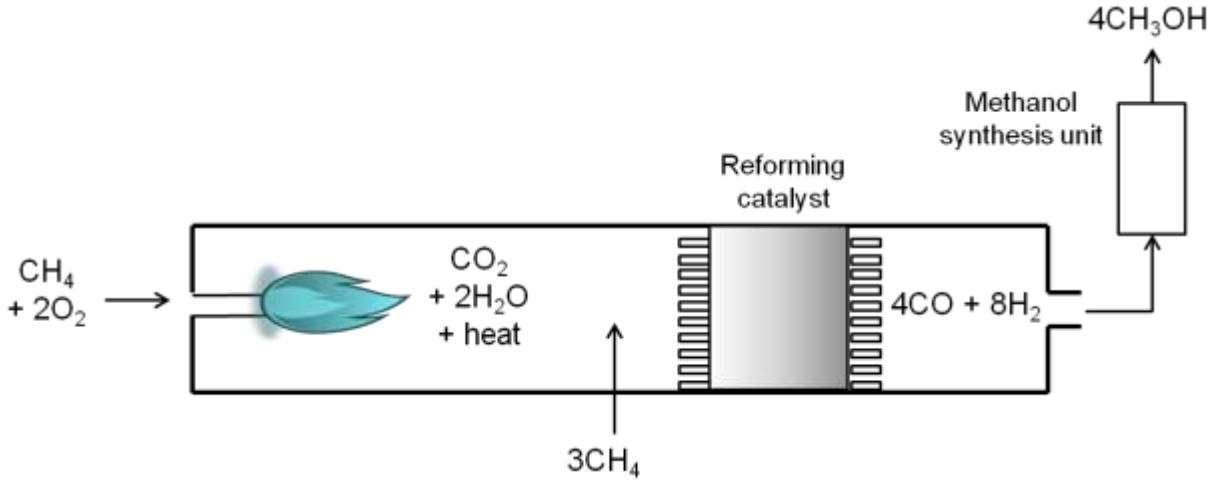

In the methanol synthesis loop cost savings could be obtained by operating the reactor below the methanol dew point. This removes methanol from the gas phase and allows a higher reactant conversion. The result is a once through process with substantial cost reductions.

References

1 J. Rostrup-Nielsen and L. J. Christiansen, *Concepts in Syngas Manufacture*, Imperial College Press, London, 2011.

2 H.-J. Arpe, *Industrial Organic Chemistry*, Wiley-VCH, 2010.

3 G. A. Olah, A. Goeppert and G. K. S. Prakash, *Beyond Oil and Gas: The Methanol Economy, 2nd edition*, Wiley-VCH, Weinheim, 2009, and references therein.

4 M.-S. Fan, A. Z. Abdullah and S. Bhatia, *ChemCatChem*, 2009, **1**, 192-208.

5 T. V. Choudhary and V. R. Choudhary, *Angew. Chem. Int. Ed.*, 2008, **47**, 1828-1847.

6 G. A. Olah, A. Goeppert and G. K. S. Prakash, *J. Org. Chem.*, 2009, **74**, 487.

7 G. A. Olah, G. K. S. Prakash and A. Goeppert, *J. Am. Chem. Soc.*, 2011, **133**, 12881-12898.

8 D. Seddon, *Gas Usage & Value: The Technology and Economics of Natural Gas Use in the Process Industries*, PebbWell, Tulsa, Oklahoma, 2006.

9 R. A. Kerr, in *Science* 2010, vol. 328, pp. 1624-1626.

10 K. Aasberg-Petersen, C. Stub Nielsen, I. Dybkjaer and J. Perregaard, *Large Scale Methanol Production from Natural Gas, A report by Haldor Topsoe* Haldor Topsoe, Denmark.
11 A. Pavone, *Mega Methanol Plants, Report No. 43D*, Process Economics Program, SRI Consulting, Menlo Park, California, 2003.
12 G. A. Olah and Á. Molnár, *Hydrocarbon Chemistry, 2nd ed.*, Wiley-Interscience, Hoboken, N.J., 2003.
13 G. A. Olah, A. Goeppert, m. Czaun and G. K. S. Prakash, *J. Am. Chem. Soc.*, 2013, **135**, 648-650.
14 G. A. Olah and G. K. S. Prakash, U.S. Patent 7,906,559, March 15, 2011; 8,133,926, March 20, 2012; 8,440,729, May 14, 2013.
15 J. Haugaard and H. Holm-Larsen, *Recent Advances in Autothermal Reforming Technology - Reducing Production Costs to Prosper in a Depressed Market*, World Methanol Conference, San Diego, USA, 1999.

Techno-Economic Analysis: Cost of CO_2 from air (Subtask 4.1)

CO_2 adsorption processes are dependent on numerous factors such as CO_2 concentration in the source, temperature of the CO_2 source, relative humidity, cost of the adsorbent, capacity of the adsorbent, regeneration method (TSA, VSA, TVSA, MSA, etc.)[5] and conditions, stability of the adsorbent, and if the separated CO_2 will be sequestered or used as a feedstock or not.

In terms of costs of CO_2 adsorption, two of the most important parameters are probably the cost of the adsorbent itself and the regeneration conditions. In general, the lower the cost of the adsorbent, the better the economics of the process. Upfront capital cost will be greatly reduced by using a cheaper adsorbent. Of course the adsorbent should also to be stable for extended periods of time under the adsorption/desorption conditions to avoid the need to change the adsorbent bed too often and the associated costs of such a replacement. On the other hand, the regeneration conditions will also be of primary importance to determine the operation costs. Using temperature swing adsorption (TSA) for example, it is preferable to keep the desorption temperature as low as possible to reduce the cost of heating the adsorbent bed. Higher temperature (e.g. 100 °C) will allow for faster CO_2 desorption but will incur an energy penalty compared to lower temperature adsorbent regeneration (e.g. at 60 °C). Therefore a compromise has to be found between reasonable desorption kinetics and temperature of desorption. Lower regeneration temperatures could also allow the use of waste heat from numerous processes, thus reducing the operating cost of the system.

To try to access cost, we have to look at a more specific example; in our case the adsorbent based on silica and polyethylenimine, used in our DOE sponsored project.

Cost of the adsorbent based on silica and polyethylenimine (PEI)

The cost of the adsorbent based on silicas and PEI (HMW) are presented in the Tables (6.2 and 6.3) below. Two different "nano" silica sources are compared; fumed silica (Aerosil 380) from Evonik and precipitated silica, also from Evonik. PEI (HMW) with a molecular weight of 25000 g/mol is produced by BASF. The prices indicated are the ones obtained from the manufacturers for a quantity of about a tonne of each material. With both fumed and precipitated silica adsorbents with a silica/PEI (HMW) ratio of 1/1 were prepared. The adsorption/desorption characteristics of these two adsorbents are relatively similar.

[5] TSA: Temperature swing adsorption; VSA: Vacuum swing adsorption; TVSA: Temperature-vacuum swing adsorption; MSA: moisture swing adsorption.

Table 6.2. Cost of adsorbent prepared on a large scale (1 tonne) based on fumed silica / PEI (HMW) 1/1

	Price per kg	To produce 1 kg of adsorbent
PEI (HMW) Branched Mw = 25000 g/mol	~$30	$15
Aerosil 380 from Evonik	~$20	$10
Material cost		~$25

Table 6.3 Cost of adsorbent prepared on a large scale (1 tonne) based on precipitated silica / PEI (HMW) 1/1

	Price per kg	To produce 1 kg of adsorbent
PEI (HMW) Branched Mw = 25000 g/mol	~$30	$15
Precipitated silica from Evonik	~$5	~$2.5
Material cost		~$17.5

The cost of precipitated silica was significantly lower than the cost of fumed silica. This is probably due to their very different way of production and the costs associated with each of them. Fumed silica is made by the vapor-phase hydrolysis of silicon chlorides in a hydrogen-oxygen flame at very high temperature to produce silicon dioxide, which falls down as "fumes". Precipitated silica on the other hand is prepared in aqueous solution by the reaction of sodium silicate with an acid resulting in the precipitation of silica.

PEI (HMW) has a cost of about $30 per kg. PEI with lower molecular weight have generally a lower cost, so there should also be some room to reduce the cost on the polyamine side. Of course oligomers of ethyleneamines such as pentaethylenehexamine (PEHA) or tetraethylenepentamine (TEPA) are much cheaper than PEI but suffer from extensive leaching over time when supported on silica. They are therefore not the most adapted for this application. Because precipitated and fumed silica based adsorbents showed similar adsorption characteristics it is logical in our case to go with the least expensive one, i.e. precipitated silica, at a cost of about $17.5 per kg.

Capture of CO_2 from the air

Various techniques can be applied for the separation of CO_2 from relatively concentrated sources such as flue gases from fossil fuels burning power plants and cement factories Capturing and concentrating CO_2 from the air is however more challenging. Due to its very low CO_2 concentration (~ 400 ppm), the presence of moisture, necessity to operate close to room temperature and ambient pressure, many of the technologies applied to gases containing higher CO_2 concentration can be ruled out. At atmospheric pressure, physical adsorbents such as zeolites, activated carbon and alumina can be excluded due to their low selectivity for CO_2 in the presence of moisture and very low heat of adsorption, which result in low adsorption capacities.

The Selexol process for the capture of CO_2 at rather high pressure can also not be applied. MEA based sorbents suffer from stability problems when contacted with air as well as evaporation issues due to the large volume of gas to be handled.

Despite its very low concentration of only 400 ppm, the capture of CO_2 directly from the air is technically feasible. Theoretically, CO_2 capture from the atmosphere would only require about 2 to 4 times as much energy as capture from flue gases, which is relatively modest considering that at the same time the CO_2 concentration is decreased by roughly a factor of 250-300. Strong bases such as NaOH, KOH and $Ca(OH)_2$ can effectively scrub CO_2 out of the atmosphere. However, their regeneration is energy intensive and requires very high temperatures.

The use of K_2CO_3 as an absorbent offers to considerably lower the regeneration temperature but the bonding energy with CO_2 remains high. This excessive bonding with CO_2 requires a considerable energy input for the regeneration step.

The use of solid adsorbents to capture CO_2 from the air such as the ones studied in this DOE sponsored project require only mild regeneration conditions and offer an attractive solution.

Some of the most important characteristics for an ideal adsorbent for CO_2 adsorption from the air are presented in Figure 6.2.

Figure 6.2 Characteristics of ideal adsorbent for CO_2 capture from the air
- High adsorption capacity for CO_2 capture from the air
- Fast CO_2 adsorption kinetics close at room temperature (15-35°C)
- Fast CO_2 desorption kinetics at relatively low temperature (50-60 ºC) under a flow of air or under vacuum.
- Able to work under humid conditions
- Long term stability under working conditions
- Active part of the adsorbent should not leach out
- Low cost
- Easy to produce

Precipitated silica / PEI (HMW) 1/1 (PS-PEI-50) and comparable solid adsorbents satisfies most of the requirements of Figure 6.2. If we assume a conservative adsorption capacity of about 50 mg CO_2/ g adsorbent for PS-PEI-50 (0.05 kg CO_2 per kg adsorbent) over 1000 adsorption/desorption cycles, the cost of capturing 1 tonne of CO_2 is about $350 taking into account only the adsorbent cost (Table 6.4). However, if this adsorbent is used over 10000 cycles, the cost of capturing 1 tonne of CO_2 will be about 10 times less ($35/t CO_2). In the current experiments, a decrease in adsorption capacity over 110 cycles was not seen using this type of adsorbent. 1000 cycles should therefore not be a major problem and 10000 cycles or ideally much more is probably achievable. The higher the number of cycles, the lower the cost of the adsorbent per cycle will be. Of course, the cost per cycle would also be greatly reduced if the cost of the adsorbent could be lowered further. Further studies using lower cost polyamines are underway to potentially reduce the cost of the adsorbent in the range of $3-$6 per kg, translating

into a cost of \$6-\$12/t CO_2 assuming 10000 cycles of operation. As a comparison, the adsorbent cost of capturing CO_2 from a source containing 10% CO_2 instead of 400 ppm is shown in Table 6.5. It can be seen that the cost only increased by a factor of 2 (from \$17.5 to \$35/t CO_2 captured) going from a CO_2 concentration of 400 ppm to 10%. This is a relatively minor increase considering the dramatic 250 fold increase in CO_2 concentration.

Table 6.4 Adsorption of CO_2 from the atmosphere (~400 ppm CO_2)

Number of cycles	Total amount of CO_2 adsorbed over x cycles (kg CO_2 per kg adsorbent)[a]	Adsorbent cost per t of CO_2 captured over x cycle
1000	50 kg	\$350/t CO_2
10000	500 kg	\$35/t CO_2

[a] Assuming a conservative adsorption capacity of about 0.05 kg CO_2 per kg adsorbent using precipitated silica / PEI (HMW) 1/1 adsorbent

Table 6.5 Adsorption of CO_2 from a source containing 10% CO_2

Number of cycles	Total amount of CO_2 adsorbed over x cycles (kg CO_2 per kg adsorbent)[a]	Adsorbent cost per t of CO_2 captured over x cycle
1000	100 kg	\$175/t CO_2
10000	1000 kg	\$17.5/t CO_2

[a] Assuming a conservative adsorption capacity of about 0.1 kg CO_2 per kg adsorbent using precipitated silica / PEI (HMW) 1/1 adsorbent

Of course beside the cost of the adsorbent, numerous other costs including capital costs to build the capture unit and operating costs (electricity, heat, vacuum, etc.) have to be added to obtain the total cost of CO_2 adsorption. These will however greatly depend on the intended application. Even considering only CO_2 capture from the air, there are a number of possible applications. Silica/PEI adsorbents could be utilized to purify gas streams from CO_2 in submarines and other closed environments as well as for applications such as alkaline fuel cells for which it is important to have an air source free of CO_2 to avoid formation of carbonates by reaction with the strongly basic electrolyte (generally NaOH or KOH). Supply of CO_2 free air is equally important for inexpensive and robust iron-air batteries being currently developed in our laboratory under ARPA-E support for large-scale energy storage for grid applications, which also necessitate basic electrolytes for their operation. In the above mentioned applications the CO_2 captured is generally released and not sequestered or used. However, these same adsorbents could be used to capture CO_2 from the air for sequestration underground (carbon capture and sequestration, CCS) or recycling (carbon capture and recycling, CCR) to fuels and materials. The total cost of capture will depend on the intended use.

Total cost of CO_2 capture from the air reported in the literature

The cost of direct CO_2 capture from air will highly influence the overall economic feasibility of the utilization of atmospheric CO_2 as a carbon feedstock. Using current technologies the cost to remove a ton of CO_2 from point sources such as a coal burning power plant that contain 10-15 % CO_2 has been estimated between \$30-100. The cost of direct air

capture (DAC) on the other hand varies vastly from about $20 to more than $1000 per ton of CO_2.[1-7]

The technology developed by Steinberg and co-workers and CoAway LLC[8,9] using the K_2CO_3 /$KHCO_3$ cycle is described as being able to capture CO_2 from air for less than $20/ton. The total cost including sub-surface injection was estimated to be slightly above $20/ton. A significant improvement in the feasibility is due to using waste heat from existing power plants, oil refineries, etc.

An air capture system designed by Keith et al. using a Na/Ca cycle was estimated to cost approximately $500/ton-C (140 $/ton CO_2).[10,11] The authors added that about a third of this cost was related to capital and maintenance cost. Further development and optimization of the system by Carbon Engineering Ltd. for the effective extraction of CO_2 from air resulted in the decrease of the estimated cost to 49-80 $/tonne CO_2.[12] To test the critical aspects of their full-size contactor design, a prototype working under real outdoor conditions was constructed in 2011.

Lackner et al. in an analysis of a system using $Ca(OH)_2$ as adsorbent material in a convection tower suggested that the cost of the process would be only on the order of 10-15 $ per ton of CO_2. As expected a major cost of such a process would be in the recovery step.[13] It was also found that the additional CO_2 generated in the calcination process due to methane combustion would be substantially less than the amount of CO_2 captured and would be captured by the same unit.

More recently, Lackner and co-workers developed an anionic exchange resin able to release CO_2 in a moisture–swing process. The cost of only the energy required per ton of CO_2 collected was around $15.[14,15] The initial cost of air capture including manufacturing and maintenance can be estimated at about $200 /ton of CO_2. However, this cost is expected to drop considerably as more collectors are built, possibly putting CO_2 capture in the $30 per ton range in the long term.

The direct capture of CO_2 from air also received some degree of criticism mostly due to its potentially very high cost. The DAC schemes proposed by Lackner and Keith have been labeled by some as overly optimistic. In 2003, Herzog pointed out that the former authors had potentially significantly underestimated the overall cost of air capture, which would be in excess of $1700/ton CO_2 using a CaO-$CaCO_3$ cycle. Critical assumptions that give rise to such a large differences are the following according to Herzog et al: (a) Authors assume a dry kiln with 80 % thermal efficiency while Herzog assumes a kiln with wet feeds giving about 33 % efficiency, (b) authors used lower natural gas and oxygen prices for the calculations, (c) authors do not take into account other cost components such as compression, recycling flue gas from calciner and (c) the extra CO_2 associated to the energy requirements of oxygen production, CO_2 compression and process auxiliaries. More recent publications by House et al.[2] and the American Physical Society estimated that the cost of DAC using hydroxide absorbents was in the order of $1000/ton and $600-800/ton, respectively.[16]

Direct CO_2 capture from the air is still in its infancy. The cost of a commercial plant will depend upon many factors including the process used as well as cost of labor, materials and

energy. While there is no question that the capture of CO_2 from the air is possible, more research and development is clearly needed to optimize this technology and determine its economic viability. Only with the construction of demonstration and pilot plants will we have a clearer understanding of the total cost associated with DAC. A few start-up companies including Carbon Engineering,[17,18] Kilimanjaro Energy,[19-21] Global Thermostat and Climeworks[22] have started such efforts.[8] Some of the proposed devices and prototypes for the capture of CO_2 from the air are shown in Figure 6.3. It should also be pointed out that the costs associated with DAC units are not "stand alone". Once captured, the CO_2 will be used for applications such as enhanced oil recovery (EOR) or recycling into chemicals and fuels including synthesis of methanol, DME and hydrocarbons (CCR). This will give an economic value to the captured CO_2, lowering the *de facto* cost of DAC and provide a more favorable overall picture of the process. Water (moisture) could also be separated from the air at the same time as CO_2, which could provide clean water as an added value.

Regardless of the technology used, the overall cost of CO_2 capture from the air remains a highly debated question which will probably get clearer answers only after the construction of demonstration and pilot plants.

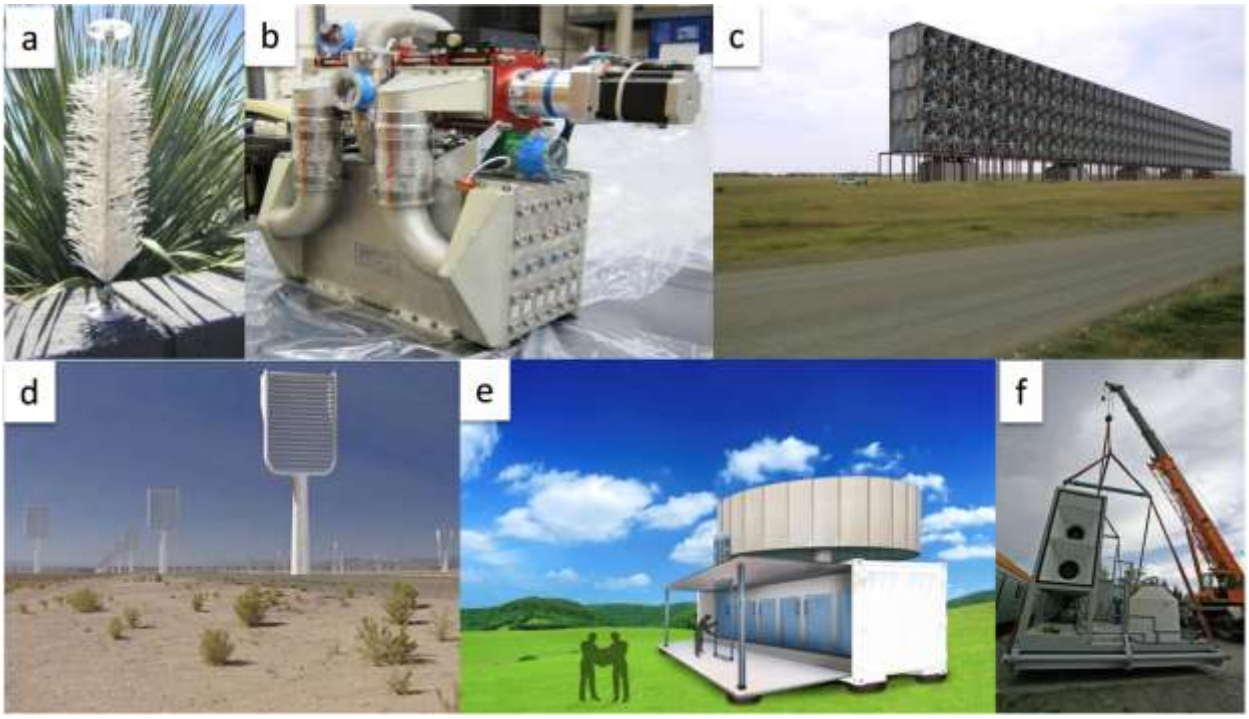

Figure 6.3 Examples of prototypes and proposed designs for the separation of CO_2 from the air. (a) Prototype for CO_2 capture from the air (Kilimanjaro Energy). (b) Solid amine based swing bed for CO_2 removal in human spaceflights. Currently undergoing tests in the International Space Station (ISS). (c) Artist rendering of an atmospheric CO_2 capture contactor (Carbon Engineering). (d) Artist rendering of an array of atmospheric CO_2 capture units also known as Synthetic Trees (Stonehaven Production). (e) Artist rendering of a prototype for CO_2 capture from the air using an anionic exchange resin and regeneration by moisture swing (Kilimanjaro

Energy). (f) Construction of a prototype for CO_2 capture from the air in Alberta, Canada (Carbon Engineering).

References

(1) Simon, A. J.; Kaahaaina, N. B.; Friedmann, S. J.; Aines, R. D. *Energy Procedia* **2011**, *4*, 2893.

(2) House, K. Z.; Baclig, A. C.; Ranjan, M.; van Nierop, E. A.; Wilcox, J.; Herzog, H. J. *Proc. Nat. Acad. Sci.* **2011**, *108*, 20428.

(3) Ranjan, M.; Herzog, H. J. *Energy Procedia* **2011**, *4*, 2869.

(4) Pielke Jr., R. A. *Environ. Sci. Policy* **2009**, *12*, 216.

(5) *Negative Emissions and Carbon Recycling - Air Capture, Environment Policy Statement 11/01*, UK Institution of Mechanical Engineers, IMechE: 2011.

(6) Ranjan, M. *Feasibility of Air Capture, Master of Science in Technology and Policy Thesis*; Massachusetts Institute of Technology, 2010.

(7) McGlashan, N.; Nilay, S.; Workman, M. *The Potential for the Deployment of Negative Emissions Technology in the UK*; a report by AVOID, Avoiding Dangerous Climate Change, Imperial College London, 2010.

(8) Goeppert, A.; Czaun, M.; Prakash, G. K. S.; Olah, G. A. *Energy Environ. Sci.* **2012**, *5*, 7833.

(9) Polak, R. B.; Steinberg, M., *Carbon Dioxide Removal System* Pat. Appl. US 2012/0003722A1, **2012**.

(10) Keith, D. W.; Ha-Duong, M.; Stolaroff, J. K. *Climatic Change* **2006**, *74*, 17.

(11) Stolaroff, J. K. *Capturing CO_2 from Ambient Air: a Feasibility Assessment, PhD Thesis*; Carnegie Mellon University: Pittsburgh, PA, 2006.

(12) Heidel, K.; Holmes, G.; Singh, A.; Keith, D. W. *Process Design and Costing of an Air-Contactor for Air-Capture, Information Sheet*; Carbon Engineering Ltd., Calgary, Canada, 2011.

(13) Lackner, K. S.; Grimes, P.; Ziock, H. J. In *Proceedings of the First National Conference on Carbon Sequestration* Washington, DC, 2001.

(14) Lackner, K. S. *Eur. Phys. J. Special Topics* **2009**, *176*, 93.

(15) Lackner, K. S. *Scientific American* **2010**, *June*, 66.

(16) *Direct Air Capture of CO_2 with Chemicals. A Technology Assessment for the APS Panel on Public Affairs*, American Physical Society (APS),**2011** available at www.aps.org/policy/reports/assessments/upload/dac2011.pdf

(17) Keith, D. W.; Mahmoudkhani, M., *Carbon Dioxide Capture*, US Pat. Appl. 2010/0034724, **2010**.

(18) Keith, D. W.; Mahmoudkhani, M.; Biglioli, A.; Hart, B.; Heidel, K.; Foniok, M., *Carbon Dioxide Capture Method and Facility*, US Pat. Appl. 2010/0064890 A1, **2010**.

(19) Wright, A. B.; Lackner, K. S.; Wright, B.; Wallen, M.; Ginster, U.; Peters, E. J., *Removal of Carbon Dioxide from Air*, US Pat. 8,088,197, **2012**.

(20) Wright, A. B.; Peters, E. J., *Air Collector with Functionalized Ion Exchange Membrane for Capturing Ambient CO_2*, US Pat. 7.993,432, **2011**.

(21) Lackner, K. S.; Wright, A., *Laminar Scrubber Apparatus for Capturing Carbon Dioxide from Air and Method of Use*, US Pat. 7,833,328, **2010**.

(22) Gebald, C.; Wurzbacher, J. A.; Steinfeld, A., *Structure Used for Adsorption and Desorption of Carbon Dioxide from Gas Mixture, Comprises Fiber Filaments, and Sorbent with*

Amine Groups which Captures Carbon Dioxide from Gas Mixture by Adsorption and Desorption Cycles., Eur. Pat. Appl. 2266680A1, **2010**.

Techno-Economic Analysis for Electrochemical Reduction of CO_2 to CO or Formic Acid (Subtask 4.2)

Introduction

Electrochemical conversion of CO_2 to either formic acid or carbon monoxide is a promising technology that may alleviate some of the world's problems with anthropogenic CO_2 emissions while simultaneously generating useful materials. The main goal has been to demonstrate a scalable electrolyzer that would be capable of producing large amounts of CO_2 reduction products and compare the projected cost of these products with their current market value. In addition to electrochemical CO_2 reduction, a cost analysis of electricity produced has been included using a direct formic acid fuel cell using results from the experiments operating these devices in the laboratory. These two processes (CO_2 reduction to formic acid and formic acid fuel cells) can be combined to form a very simple CO_2 recycling strategy for energy storage and use.

Assumptions

The only industrial scale process that resembles CO_2 electrolysis is water electrolysis. With alkaline water electrolysis, it has been estimated that over 80% of the cost is due to electricity prices.[6] Although there are significant differences between water electrolysis and CO_2 electrolysis, we will assume that the cost of electricity will remain the major associated cost with the products produced. Other costs, such as the cost to build and maintain the reactor, finance, etc. have not been considered. Since CO_2 is likely to either be free or even have a negative cost, i.e. that there will be a monetary incentive to use it, we will not consider it in our analysis.

A major difference between the present system and water electrolysis is that less than 1% of the CO_2 that flows across the cathode is consumed. Perhaps this would not be a significant issue upon scale up, or perhaps conditions could be found to convert a much larger percentage of the incoming gas. At the very least, it seems that a significant investment in CO_2 recycling equipment would be necessary for large-scale electrochemical CO_2 reduction. The program did not focus on any method for increasing the conversion of CO_2 during the experiments because it was never a parameter that was considered, but it may prove to be a significant barrier to industrial application.

For the purposes of this analysis, an assumption has been made that electricity generation will take place on site or very close so that the cost of electricity can be brought down to what it costs to generate electricity, rather than what it costs to buy electricity from the grid. Rather than selecting a particular strategy for electricity generation, a cost of 4 ¢/kWh was selected, which falls in the range of electricity produced from coal, natural gas, wind, and is more expensive than nuclear.[7] While it would probably not be advantageous to the environment to use coal or natural gas to power a CO_2 electrolyzer, wind and nuclear power would be good choices given that they

[6] Simbeck, D. R.; Chang, E. *Hydrogen Supply: Cost Estimate for Hydrogen Pathways - Scoping Analysis*; National Renewable Energy Laboratory NREL/SR-540-32525: Golden, Colorado, 2002.

[7] *Projected Costs of Generating Electricity*; Nuclear Energy Agency, International Energy Agency: Paris, 2005.

do not emit CO_2. The cost of solar power is currently too high to be considered for electrochemical CO_2 reduction.

Conditions for Formic Acid Production

Through a great deal of testing various catalysts and conditions, a conservative estimate for the operating conditions and expected product distribution that could be expected for a large scale production facility was generated. To begin with, data from a single experiment was selected as a baseline for CO_2 reduction to formate using the conditions specified in Table 6.6.

Table 6.6 Formic Acid Baseline Conditions

Controlled Variables	Working Electrode	100 mesh Tin powder
	Membrane	Nafion-H
	Counter Electrode	Platinum black
	Catholyte	Pure CO_2
	Anolyte	0.1 M LiOH
	Cell Potential	3.6 V
	Cathode Pressure	300 psig
	Anode Pressure	305 psig
	Cathode Flow	30 mL/min
	Anode Flow	2 mL/min
	Temperature	50 °C
Measured Values	Average Current Density	24.2 mA/cm^2
	Formate Faridaic Efficiency	39.3 %
	CO Faradaic Efficiency	51.0 %
	Faradaic Efficiency	10.2 %
Assumed	Cost of Electricity	4 ¢/kWh
Cost of Electrochemical Formic Acid		**$427/tonne**

Using these conditions as a baseline, the only other piece of information that was taken as input was the price of electricity. The cost to heat up the electrolyzer to 50 °C has not been considered because the energy efficiency of the electrolysis is low enough that it would almost certainly heat itself up to and beyond 50 °C and may require cooling rather than heating. One additional step in the process that was not considered is the acidification of the resulting lithium formate to formic acid. This may well be a significant cost, but was not considered. One could instead determine the production cost per metric ton of lithium formate, but since this would almost certainly be a very small volume product, it seems unlikely to be the end point for the process.

With these input values, an initial conservative estimated value for production of formic acid at $427 per metric ton was calculated. Figures 6.4-6.6 illustrate the dependence of the cost on various factors including operating voltage (Figure 6.4), faradaic efficiency (Figure 6.5), and cost of electricity (Figure 6.6), with the baseline conditions indicated with a red square. Faradaic

efficiency is the only factor, which does not follow a linear trend. One point to make about the faradaic efficiency, however, is that the other two products (CO and H_2) could also be sold and a certain amount of the cost could be recovered in that way. There is no silver lining for the cost of cell voltage, however, and a more energy efficient system would probably have the biggest impact on the cost of producing formic acid from CO_2 using electrolysis. Although there is no control over the cost of electricity, it plays a major role in the cost of formic acid produced through electrolysis.

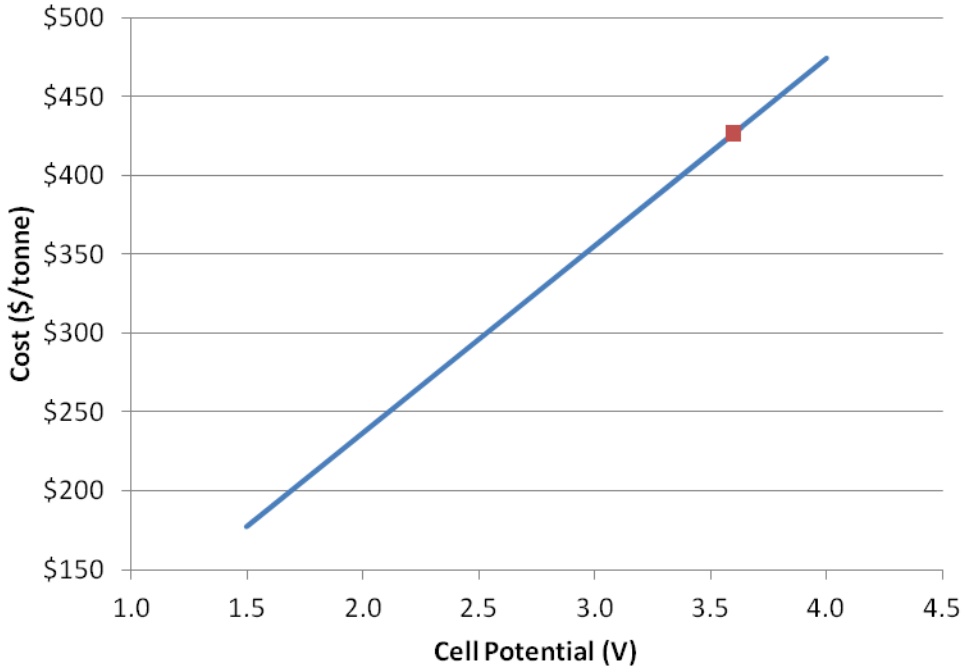

Figure 6.4 Cost of Formic Acid as a Function of Cell Voltage

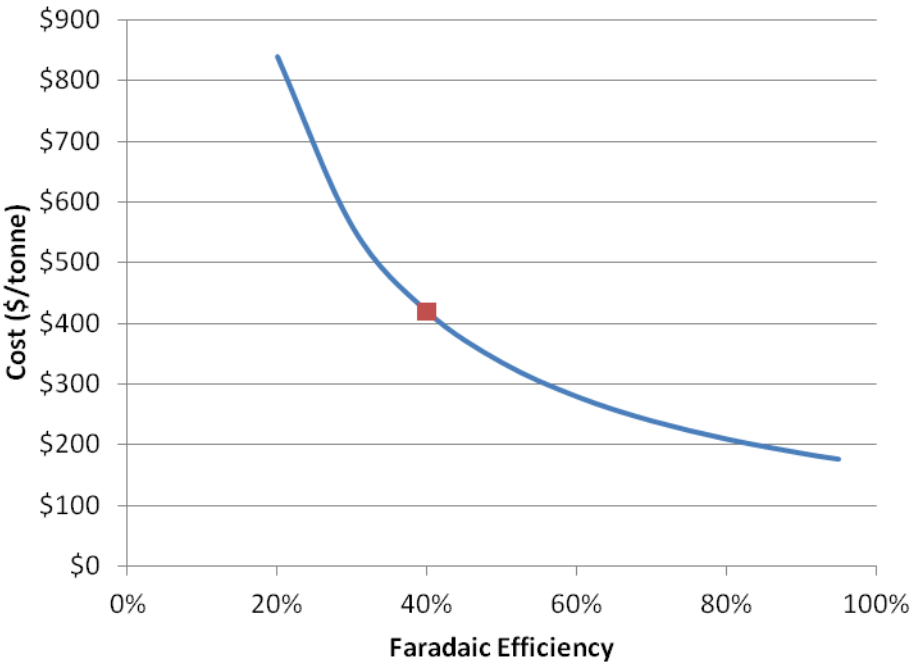

Figure 6.5 Cost of Formic Acid as a Function of Faradaic Efficiency

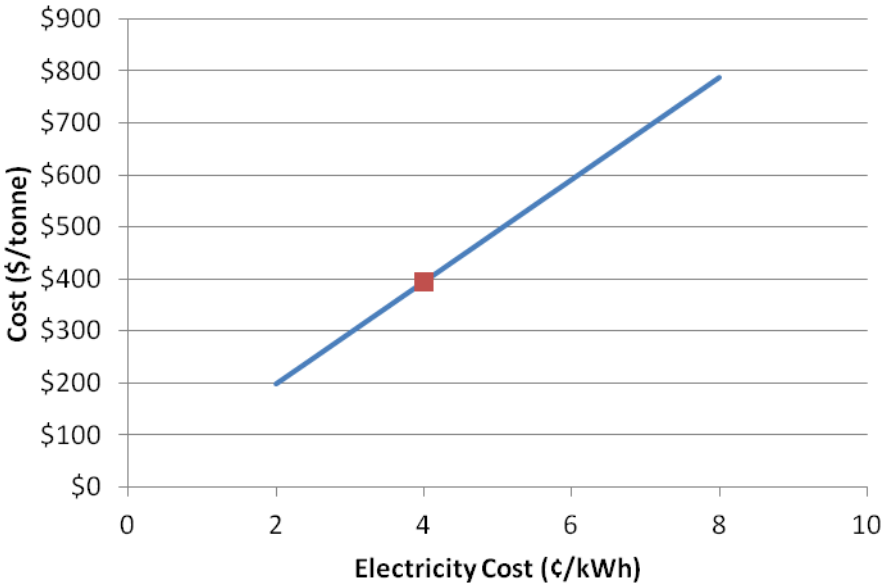

Figure 6.6 Cost of Formic Acid as a Function of Electricity Cost

Although lithium formate isn't an item that is typically sold in large volumes, sodium and potassium formate are, and one can directly compare electrochemically produced sodium formate to commercially available sodium formate since there is no acidification step. Using the same "baseline" conditions of Table 6.6, a cost of $553 per metric ton of sodium formate produced electrochemically from CO_2 can be estimated. This includes the cost of sodium hydroxide, which has been estimated to be $450 per metric ton. The baseline conditions call for LiOH as the anolyte, which would produce lithium formate rather than sodium formate, but these

are relatively conservative estimates, so it seems plausible that conditions could be found to generate similar values while using NaOH as an anolyte instead.

Based on reports in the literature, it seems that faradiac efficiency could be improved significantly, potentially up to 90%, while current density could also increase to above 100 mA/cm^2. Cell potential should also drop with improved design and cell components, as much of our cell potential is likely being lost to resistance since we typically measure ~1 Ω across the cell. Reducing the cell potential to 3.0 V seems like a reasonably achievable goal without resorting to exotic catalysts or methods. Given 90% faradaic efficiency and 3.0 V instead of 39% faradaic efficiency and 3.6 V gives us a cost of formic acid of $155 per metric ton, which is a huge improvement from $427 per metric ton that was estimated on a conservative basis. Again, it should be emphasized that this does not take into account acidification, but the price/tonne will be quite similar for production of sodium formate, so one can use that number as a basis for comparison.

Conditions for CO Production

A large portion of the work on this project has been related to the production of CO and H_2, or syngas, using similar conditions to our formate reactor but with a different catalyst. Table 6.7 gives a summary of the conditions used and the measured values for a conservative electrolysis experiment using a gold electrode to generate CO and H_2. Since sodium ions move from the anode to the cathode and regenerate sodium hydroxide, the cost of sodium hydroxide was not included since it is not consumed, and thus could be recovered and reused. Currently, all the estimates for CO production use gold electrodes, which degrade in a matter of hours of CO_2 reduction. This issue must be addressed; either with a new catalyst or conditions prior to consideration of an industrial process. One possible solution to poisoning would be to use tin instead of gold as a catalyst for syngas. It was shown that conditions can be found to generate ~90% syngas in ~2:1 ratio of H_2:CO at 4.0 V and 100 mA/cm^2. Rather than suggest tin, however, it has been assumed that a solution to gold poisoning can be found and stick with gold since it is the best known catalyst for the reduction of CO_2 to CO.

Table 6.7 CO Baseline Conditions

Controlled Variables	Working Electrode	Gold powder
	Membrane	Nafion-Na
	Counter Electrode	Platinum black
	Catholyte	Pure CO_2
	Anolyte	0.1 M NaOH
	Current Density	30 mA/cm^2
	Cathode Pressure	600 psig
	Anode Pressure	605 psig
	Cathode Flow	90 mL/min
	Anode Flow	2 mL/min
	Temperature	40 °C
Measured Values	Average Cell Potential	2.92 V
	CO Faradaic Efficiency	56.0 %
	H_2 Faradaic Efficiency	43.8 %
Assumed	Cost of Electricity	4 ¢/kWh
Cost of Electrochemical CO		**$399/tonne**

For Table 6.7, a set of experimental conditions was selected that gave the highest percentage of CO measured, rather than the lowest cell potential at a given ratio of H_2:CO. The gold catalyst has the characteristic of producing both H_2 and CO in varying quantities depending on the conditions, so one can fine-tune the ratio to the desired composition for downstream processing. For methanol synthesis, a ratio of 2:1 H_2:CO would be desirable, so these conditions might not be ideal for that application. An alternative would be to use a commercial electrolyzer or other source of H_2 to make up the H_2 deficiency because it may prove cheaper overall; however it would increase the complexity of the system by adding another step. The values given in Table 6.8 and represented graphically in Figure 6.7 assume that conditions can either be found for simultaneous production of H_2 and CO in a ratio of 2:1 (very close to our observations), or a system capable of sustaining 95% faradiac efficiency for CO (not something that has been observed).

Table 6.8 Syngas Hypothetical Conditions

		Simultaneous Production	Separate H_2O Electrolysis	Separate H_2 from Methane
Hypothetical Values	Cell Potential	3.0 V	3.0 V	3.0 V
	CO Faradaic Efficiency	32 %	95 %	95 %
	H_2 Faradaic Efficiency	63 %	0 %	0 %
Assumed	Cost of H_2	n/a	$2700/tonne	$750/tonne
	Cost of Electricity	4 ¢/kWh	4 ¢/kWh	4 ¢/kWh
Cost of Syngas		**$634/tonne**	**$551/tonne**	**$306/tonne**

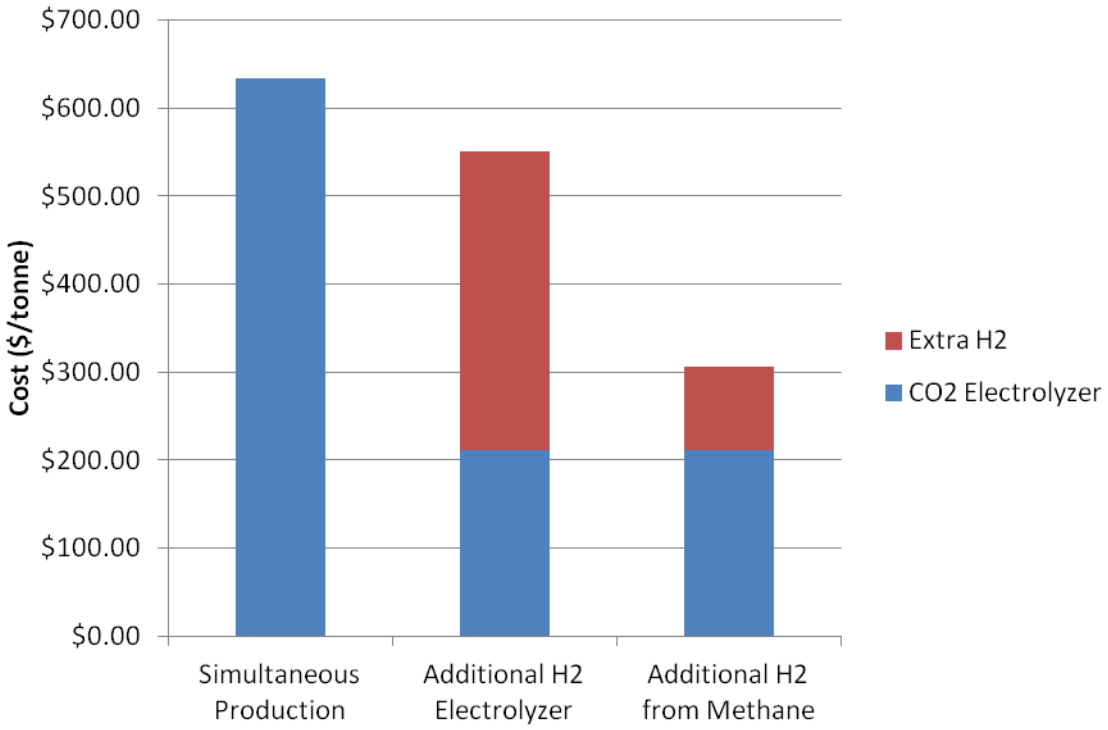

Figure 6.7 Production of Syngas in a 2:1 H_2:CO Ratio by Various Methods

Commercial water electrolyzers produce exclusively hydrogen at a price of $2560-2970 per metric ton, while hydrogen from natural gas can be produced for an even lower price of $750 per metric ton. Taking these values into account, it does not appear that the price per metric ton of syngas is significantly reduced by using H_2 from electrolysis. On the other hand, H_2 from methane lowers the cost by approximately 50% compared to simultaneous production of CO and H_2. Using H_2 from methane produced by steam reforming would not solve any environmental problems, however, since the methane used to generate H_2 would release CO_2 back into the environment. An alternative to this approach would be to use H_2 generated by the Carnol process, where methane is converted into H_2 gas and elemental carbon. Although this approach costs more than methane steam reforming, which is commonly practiced, it has the advantage of avoiding CO_2 emissions.

The trends for the cost per tonne of CO are the same as for formate production, so figures 1-3 will not be replicated for CO production here. Suffice to say that cell potential and cost of electricity have the same linear influence on the cost of CO, while the faradaic efficiency follows an exponential trajectory. There would be much less incentive to increase faradaic efficiency toward CO in this case, however, since it is more likely that a plant operator would want to achieve a specific ratio of H_2:CO rather than eliminate H_2 entirely. Therefore, the most important performance metric to improve in this case is the cell potential. Since gold is a slightly better catalyst for CO_2 reduction than tin, it is already feasible to operate the cell at ~3.0 V and achieve reasonable current densities of ~30 mA/cm^2. Getting values higher than this and closer to 100 mA/cm^2 may require higher cell potentials, but it is not unreasonable to assume that improved system design (less resistance, etc.) could achieve 100 mA/cm^2 with $\leq$ 3.0 cell voltage.

Comparison to Commercial Producers

Figure 6.8 compares the cost of formic acid and syngas produced from CO_2 electrochemically to the price of the same products produced commercially. Although accurate and current prices for bulk chemicals are not readily available, rough prices for formic acid and methanol have been determined, which will be used as a basis for comparison. On a large scale, it has been reported that formic acid ranges from $890 per metric ton in Western Europe to $1,250 per metric ton in the United States.[8] Both of these values compare favorably to the conservative estimate of $426 per metric ton, although the electrochemical cell is producing formate rather than formic acid and acidification has not been accounted for, among other costs. Assuming that the other costs and the acidification step would double the cost, a revised estimate of $852 would still be competitive with Western Europe and significantly cheaper than the US price. If improvements such as lower resistance and improved efficiency could be realized upon scale up, this price would drop further to be more competitive on the world market.

Whether or not there is a large enough market for formic acid to make this feasible at the moment is not something that was considered because simply producing formic acid to sell on the current formic acid market was never the end goal of this project. Instead, this formic acid would ideally be converted into methanol for use as a fuel, or used directly in formic acid fuel cells, or indirectly in hydrogen fuel cells using formic acid decomposition catalysts. Given the size of the energy market, it seems that the challenge would be to produce enough to make even a small dent in the energy landscape.

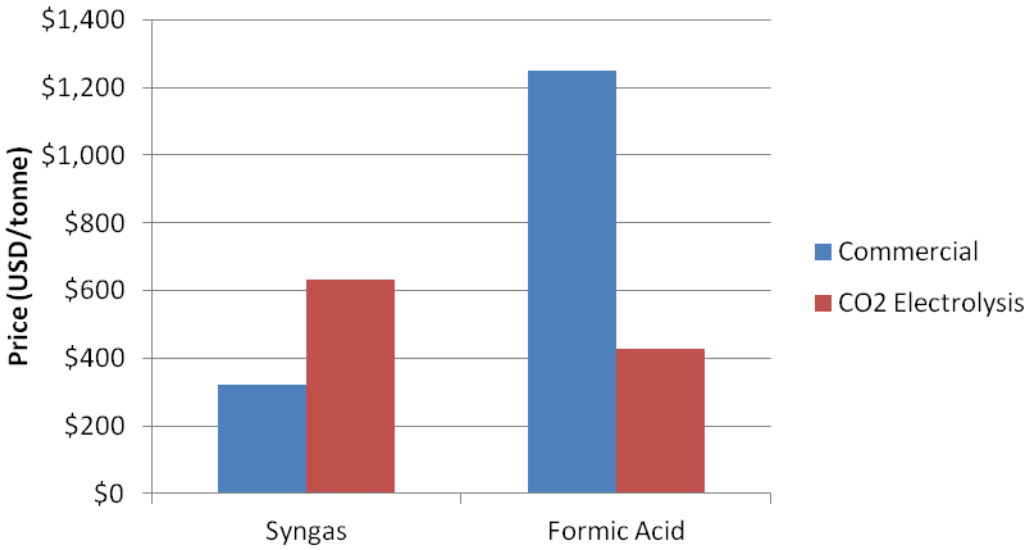

Figure 6.8 Costs Compared

Since syngas is not sold commercially, the price of methanol has been used as a substitute for it. Although this may seem a bit strange given that the goal of the project is the production of

[8] S. N. Bizzari and M. Blagoev (june 2010). "CEH Marketing Research Report: FORMIC ACID". *Chemical Economics Handbook*. SRI consulting, http://www.sriconsulting.com/CEH/Public/Reports/659.2000/

methanol from syngas, ~80%[9] of the cost of a methanol production plant is taken up by the process to produce syngas. Thus, if 80% of the cost of methanol is taken, a rough guide for how much syngas costs industrially can be obtained. If methanol is assumed to be ~$1.20 per US gallon, a price of $400 per metric ton of methanol can be calculated and, using the 80% assumption, $320 per metric ton of syngas. Since this syngas is clearly intended for methanol production, the ratio is likely close to 2:1 H_2:CO, which compares to the calculated value of $634 per metric ton above. Using water electrolysis instead of simultaneous generation of CO and H_2 would cut our cost to $551 per metric ton, or using hydrogen from methane would cut the cost to $306 per metric ton.

While there would not be much benefit in producing CO electrochemically only to combine it with H_2 produced from methane, it is interesting how close the cost of this last scenario is to the estimated cost for syngas directly from methane. The cost for either of the non-methane routes is significantly higher and would naturally lead to methanol with a much higher price than what is available now, but with the benefit of being completely fossil fuel free if one assumes that electricity would be from non-CO_2 producing sources.

If one assumes that syngas generation would still account for 80% of the total cost of methanol, then methanol produced from electrochemically generated syngas would cost $793 per metric ton, or $2.38 per US gallon. This translates into $4.85 per US gallon for the equivalent amount of energy contained in one gallon of gasoline. Although this is higher than the cost of gasoline at the pump in the US today, it is not that much higher, especially in states like California and Hawaii. It should also be emphasized that this price would be for methanol produced exclusively from CO_2, rather than methanol produced from natural gas or methane. Of course this price does not include the taxes and various other fees, which are levied on gasoline prices at the pump, so the comparison is not entirely correct.

Conclusions

Based on data obtained from experiments in the current project, an estimate has been made for the cost to produce either formic acid or syngas from CO_2 electrochemically. Using these data, the estimates are $427 per metric ton for formic acid and $634 per metric ton of syngas. The major assumption for both of these processes is that the vast majority of the cost comes from the electricity requirement. This assumption is based on the fact that commercial water electrolyzers report that >80% of their cost is associated with the electricity requirement. Given the similar design to the present system, it appears that the same should hold true for CO_2 electrolysis. Improvements in catalyst and engineering could bring the estimated costs down significantly, and there is good reason to believe that such improvements are feasible given the literature reports.

In the case of syngas generation, another significant assumption is that a solution can be found to the poisoning problem that has been observed on gold catalysts. Currently, one can only run electrolysis experiments for a few hours before gold poisoning becomes a serious issue. This is not the case for tin, which was primarily used as the formic acid catalyst. While regeneration

[9] Pavone, A. *Mega Methanol Plants*, Process Economics Program, SRI Consulting, 2003.

may be a possibility, the useful lifetime would still have to be significantly improved to be considered for an industrial process.

Compared to industrial costs, formic acid produced via electrolysis appears to be very competitive already at less than half the cost of commercially available formic acid. Syngas produced electrochemically is not nearly as economical compared to syngas produced from natural gas, at roughly double the price based on the current estimates. Even at this relatively high cost, however, a case could be made to produce methanol from electrochemically generated syngas since it could be carried out using non-fossil fuel based electricity sources.

Techno Economical Analysis of Utilization of Formic Acid as a Feed-stock and Fuel in Fuel Cells (Task 5)

Techno Economical Analysis of H_2 Generation from Formic Acid

Introduction

According to the Bloomberg New Energy Finance [1] the global new investment in renewable energy was $ 244 billion in 2012 of which, $ 4.1 billion, was an investment from private sector. It has been predicted that renewable energy sources will have an increasing contribution to the energy production in the coming centuries. Although renewable energy is available on a large scale and the utilization of these energy sources would provide enough energy for the future generations, energy production is not the only problem we face. Due to the intermittent nature of renewable energy sources, energy storage is also a real challenge.

Quite a few materials have already been suggested as chemical energy storage media such as ammonia borane, alkali borohydrides, hydrous hydrazine, methane and formic acid (FA).

Formic acid is a low volatility, low toxicity organic acid, which can be synthesized by decomposition of biomass, catalytic hydrogenation or direct electrochemical reduction of carbon dioxide. Subsequently, FA can be decomposed to a mixture of H_2 and CO_2 resulting in an overall "carbon neutral" energy storage cycle (Figure 6.9). The required CO_2 can also be captured from industrial streams or even directly from air.

The main goal of this analysis was to calculate the cost of hydrogen obtained by formic acid decomposition and compare the price with already existing technologies such as steam reforming of methane, coal gasification, biomass pyrolysis and electrolysis.

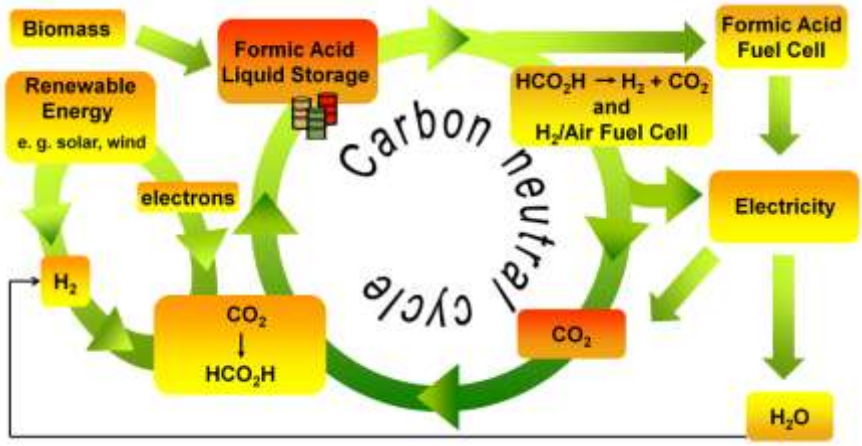

Figure 6.9 "Carbon neutral" energy/hydrogen storage system.

This estimation considers the endothermicity of the decomposition reaction only and does not take into account the heat loss and other factors that may affect the cost of hydrogen generated from formic acid. Decomposition reactions were carried out in a pressure tube equipped with pressure gauge and pressure relief valve as shown in Figure 6.10.

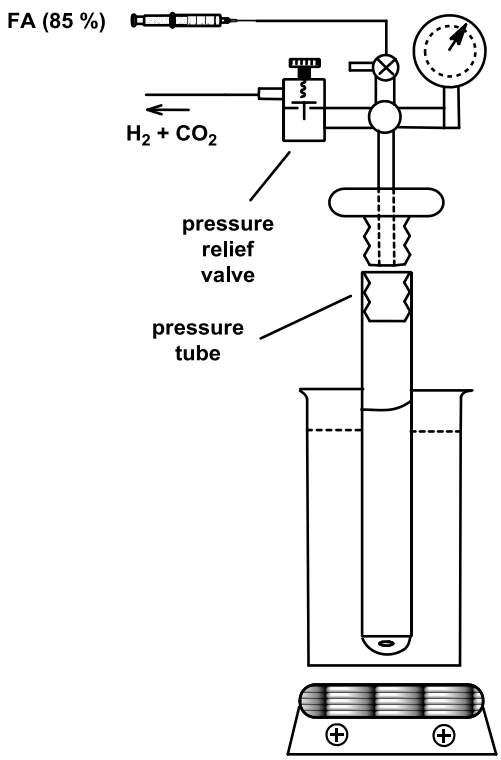

Figure 6.10 Schematic representation of the experimental reactor for FA decomposition.

FA feed for the experimental reactor

$T_{reactor}$= 100 °C, gas flow (H_2+CO_2)=145 mL/min, H_2 flow= 72.5 mL/min, $t_{burette}$=25 °C

The formic acid flow which is necessary to provide 145 mL/min gas flow can be calculated according the differential form of the general gas equation (Eq.1). Note: "0.5" factor accounts for the stoichiometry of the decarboxylation reaction (Eq. 2), namely the decomposition of 1 mole of formic acid gives 2 moles of gas.

$$\left(\frac{\partial V}{\partial t}\right) \times p = \left(\frac{\partial n}{\partial t}\right) \times RT$$

$$\boxed{\left(\frac{\partial n}{\partial t}\right)_{FA} = \frac{1}{2}\left(\frac{\partial V}{\partial t}\right) \times \frac{p}{RT}}$$

Eq. 1

FA flow = 0.5 × 145 × 10^{-6} m^3/min × 101325 N/m^2 / (8.314 Nm/molK × 298 K) × 60 = 0.178 mol/h

This FA flow corresponds to 8.19 g/h and 11.75 mL/h (85 % FA) if one considers the density and the concentration of the technical grade formic acid.

Cost of 1 kg hydrogen by FA decomposition

The decomposition takes place according to the following equation (Eq. 2):

$HCO_2H \rightarrow H_2 + CO_2$ ΔG= - 48.4 kJ/mol (Eq.2)

Taking into account the molecular weight of the hydrogen (2 g/mol) and the formic acid (46.03 g/mol) the production cost which accounts for the hydrogen storage medium can be estimated as follows (Table 6.9 shows the market price of the necessary materials):
FA cost: 1.25 $ / kg × (500 mol × 0.04603 kg/mol)/0.85 = $33.8/kg H_2
FA cost if FA is produced by direct electrochemical reduction of CO_2: 0.427 $ / kg × (500 mol × 0.04603 kg/mol)/0.85 = 11.56 $ / kg H_2

Table 6.9 Price of starting materials.

	Cost ($)	Cost of 1 gram	Source
$IrCl_3 \times H_2O$	51.2 $/g	51.2 $/g	Strem Chemicals
phthalonitrile	142 $/kg	0.142 $/g	Aldrich
2-amino-pyridine	38 $/100g	0.38 $/g	Aldrich
IndH[a]		0.4 $/g	-
Formic acid (85 %)	1250 $/ton	-	[2]
Formic acid (electrochem. red. of CO_2)	427 $/ton	-	*b*

[a]Note: cost was calculated based on material cost only, [b]See techno-economic analysis for electrochemical reduction of CO_2

Electricity cost

Electricity price for industry: 4¢/kWh
Energy needed: 500 mol × 48.4 kJ/mol= 24200 kJ
Electricity cost: (24200 kJ/3600h^{-1}) × 4 ¢/kWh= 26.9 ¢/kg H_2
Total cost (FA+electricity) = $33.8 + $0.269= $ 34.1 / kg H_2 (considering 100 % efficiency)
Total cost if FA is produced by direct electrochemical reduction of CO_2 = $11.56 + $ 0.269 = 11.8 $/kg H_2

Catalyst cost for the experimental reactor

Although numerous catalysts have been tested for formic acid decomposition, for this calculation one of the most promising catalysts was selected, which was synthesized from iridium chloride and IndH ligand (Eq. 3).

$IrCl_3 \bullet xH_2O$ + IndH → Catalyst 1 (Eq. 3)
0.1965 g 0.158 g
Cost: 0.195 g × 51.2 $/g + 0.158 g × 0.4 $/g = $ 10.0 (for producing ≈73 mL/min H_2).
For producing 1 kg/h of H_2 under similar conditions and using similar reactor the catalyst cost is $28,248.

Note 1: Even though the catalyst cost is very significant due to the high price of iridium, the catalyst is robust and can be recycled and further optimization of the system on catalyst loading would result in a more feasible method.

Note 2: Techno economical analysis of the H_2/air fuel cell and direct formic acid fuel cell was not done due to the fact that these devices and technologies are already commercial or subject of extensive development.

Comparison of cost of hydrogen by FA decomposition with other technologies

Table 6.10 summarizes the cost of hydrogen production from different sources. As it can be seen, the approach presented here produces hydrogen at a much higher price than the ones shown in Table 2 (0.54 -2.97 $/kg) mainly due to the high price of FA, which is presently used mainly on a relatively small scale as a chemical and not as an energy carrier. Production increase would lower the price of FA significantly. On the other hand, the production of FA by direct electrochemical reduction may reduce the cost of FA significantly, thereby lowering the cost of hydrogen produced this way.

Table 6.10 Cost Comparison of Selected Hydrogen Production Technologies (*source: Office of Fossil Energy - Hydrogen Program Plan; Hydrogen from Natural Gas and Coal: The Road to a Suistainable Energy Future*; *Hydrogen Coordination Group, 2003*.)

Resource	Technology	Hydrogen Cost ($/MMBtu) / ($/kg)	Year Technology is Available
Natural Gas*	Steam Methane Reforming, PSA, No Sequestration	5.54 / 0.75	Current
Natural Gas*	ITM Synthesis Gas Generation, Advanced Membrane Separation, CO_2 capture	4.15 / 0.56	2013
Coal	Gasification, Shift, PSA, No Sequestration	6.83 / 0.92	Current
Coal	Advanced Gasification, Membrane Separation, CO_2 Sequestration	5.89 / 0.79	2015+
Coal**	Advanced Gasification, Membrane Separation, Co-Production of Power, CO_2 Sequestration	3.98 / 0.54	2015+
Biomass	Pyrolysis to bio-oil followed by steam reforming	(9 – 16) / (1.21 – 2.16)	2015+
Nuclear	Sulfur-Iodine Cycle (Thermochemical Process)	9.70 / 1.31	2020+
Electrolysis	Electricity Cost at 4 cents/kWh	(19 – 22) / (2.56 – 2.97)	Current
FA (industrial)	FA Decomposition	34.1 $ / kg	research
FA (electrochemical CO_2 reduction)	FA Decomposition	11.8 $ / kg	research

References

[1] Global trends in renewable energy investment, Frankfurt School, United Nations Energy Policy Collaborating Centre for Climate & Sustainable Energy Finance, 2013.
[2] S. N. Bizzari et al.”CEH Marketing Research Report: Formic Acid” Chemical Economics Handbook, SRI Consulting, 2010 June.

Direct Formic Acid Fuel Cells

Here, the goal was to evaluate the capacity of the developed formic acid fuel cells to produce electricity at prices competitive within the current market. As such, gauging the current progress of state of the art technology and predicting how further improvements may affect the cost of energy production may not be straightforward. The anode and cathode reactions for a formic acid fuel cell are given below:

Equation 1: Anode: $HCOOH \rightarrow CO_2 + 2H^+ + 2e^-$ $E^0 = -0.25V$

Equation 2: Cathode: $\frac{1}{2} O_2 + 2H^+ + 2e^- \rightarrow H_2O$ $E^0 = 1.23V$

Equation 3: Net Rxn: $HCOOH + \frac{1}{2} O_2 \rightarrow CO_2 + H_2O$ $E^0 = E_{cathode} - E_{anode} = 1.48V$

At 100% faradaic efficiency, 2 moles of electrons may be produced per mole of formic acid. The metals used in these devices are intended to be *catalytic*, that is, not consumed by the reaction and able to be regenerated almost completely after deactivation. However, it has been observed that the current state-of-the-art-catalyst, Pd, dissolves in the presence of formic acid, so continued operation will eventually result in the failure of the cell due to loss of the active material. Moreover, a controversial surface intermediate builds up rapidly on the catalyst as the fuel is continually oxidized that prevents these devices from operating efficiently for more than a few hours. But assuming that these challenges can be overcome by finding a more robust anode catalyst, the operating cost of this technology may be evaluated as a function of the *price of fuel* and the *potential at which the cell operates*. The catalysts considered are shown in Table 6.11, which have been found to give the best voltage efficiencies ($V_{operation}/V_{theory}$) at 40mA/cm^2. V_{theory} is 1.48V, the maximum open circuit voltage attainable in a formic acid fuel cell. Performance is evaluated 40 mA/cm^2 because at this current density fuel cells are capable of supplying 1 A of current, if 25 cm^2 working electrodes are used.

Table 6.11 The best performing formic acid oxidation catalysts at 40 mA/cm^2

Catalyst	Voltage Efficiency	Operating Potential(V)
Pd Black	47%	0.7
PdAu	52%	0.77
PdFe(60wt%)/C	34%	0.5
PdSn(20:1)(60wt%)/C	47%	0.7
Pd(20wt%)/rGO	42%	0.62

Currently, the market value for formic is estimated to be $1250/metric ton, and the cost to produce grid-scale electricity for various sources is about $0.04/kWh on average. Table 6.12 displays the cost of electricity with formic acid fuel cell technology using the best-performing catalysts and commercially available fuel. It is quite evident that even with Pd black, which is considered to be the state-of-the-art anode catalyst, the cost to produce electricity is markedly higher than the grid-scale cost. Using PdAu reduces the cost of energy due to the improved oxidation performance, but this may be offset by the price of gold, which is expected to continue rising in the future. However, the PdSn catalyst shows promise for this technology because it only requires 60% metal loading to achieve the same cost/kWh as pure Pd.

Table 6.12 Cost to produce electricity at the current market value of formic acid

Catalyst	Price of Formic Acid ($/ton)	Cost of Electricity ($/kWh)
Pd Black	1250	1.53
PdAu		1.39
PdFe(60wt%)/C		2.15
PdSn(20:1)(60wt%)/C		1.53
Pd(20wt%)/rGO		1.74

The result obtained with Pd supported on reduce graphene oxide (rGO) is even more promising. Although the cost/kWh of electricity is 14% higher than with state-of-the-art Pd black ($1.74/kWh vs. $1.53/kWh), precious metal content is five times lower in the rGO catalyst, which would markedly reduce the costs associated with constructing these devices. At the moment, energy produced from PdFe catalysts costs the most since voltage efficiency is the lowest. Efforts are currently being made to improve their performance such that electricity may be produced at prices comparable to the other, more successful catalysts. Moreover, coupling efficient energy production with the abundance and low price of Fe may allow for the fabrication of fuel cells that exhibit a balance between the costs of their initial manufacture and subsequent operation.

The program has demonstrated CO_2 reduction to sodium formate at 3.6V and a faradaic efficiency of 39%, however. Supposing that the acidification of formate to formic acid is a trivial step, then the cost of formic acid produced by this method drops from $1250/metric ton, by commercially available routes, to $427/metric ton. The results from figuring this new price into current calculations for the production of energy from formic acid are shown in Table 6.13. Using the CO_2 reduction method to provide the fuel not only drives the operation costs down significantly, but suggests the possibility of introducing an anthropogenic carbon cycle to the energy infrastructure. CO_2 and water are the only waste products of formic acid fuel cells, and the program has developed an array of compounds that are able to capture CO_2 from the air. A device could be imagined in which CO_2 is captured from the fuel cell exhaust, then reduced to sodium formate via the flow cell method. After acidification, the recycled formic acid could be fed through the fuel cell, subsequently the cycle could be repeated with waste CO_2.

Table 6.13 Cost to produce electricity using formic acid from our CO_2 reduction method

Catalyst	Price of Formic Acid ($/ton)	Cost of Electricity ($/kWh)
Pd Black	427	0.52
PdAu		0.48
PdFe(60wt%)/C		0.73
PdSn(20:1)(60wt%)/C		0.52
Pd(20wt%)/rGO		0.60

Since the aforementioned technologies are still evolving, improvements are expected for all aspects of the anthropogenic carbon cycle. It is predicted that further research into the CO_2

reduction technology will result in the discovery of a better catalyst that will further lower the large overpotential associated with CO_2 reduction and allow for the reaction to occur at 3V. If conditions are optimized such that faradaic efficiency can be increased to 90%, it would further lower the cost of formic acid produced in-house to $155/metric ton. The projected cost of electricity using formic acid from the optimized CO_2 reduction system is shown in Table 6.14. It should be noted that these values are based on performance data from fuel cells as they actually function at time of this writing. Hence, it is evident that by improving just one aspect of the carbon cycle, costs associated with electricity production can be minimized so that it is more competitive with grid-scale energy.

Table 6.14 The best performing formic acid oxidation catalysts at 40 mA/cm^2

Catalyst	Price of Formic Acid ($/ton)	Cost of Electricity ($/kWh)
Pd Black	155	0.19
PdAu		0.17
PdFe(60wt%)/C		0.73
PdSn(20:1)(60wt%)/C		0.19
Pd(20wt%)/rGO		0.28

The estimated energy costs may be reduced even further if one considers the inevitable improvements that are to come with the fuel cell technology itself. Formic acid fuel cells have the potential to exhibit an open-circuit voltage (OCV) of 1.48V. But to date, the highest OCV that has been observed with the catalysts discussed in this analysis is about 0.9V, so there is ample room for this technology to advance as research continues. Table 6.15 shows the potential cost of electricity if catalysts are found that are capable of operating at higher voltages (and hence, higher voltage efficiencies) as a function of the source of formic acid.

Table 6.15 The cost to produce electricity from various sources of formic acid with better catalysts

Operating Voltage (Efficiency) of Future Catalyst	Cost/kWh at current formic acid market value ($1250/ton)	Cost/kWh with formic acid from current CO_2 reduction capabilities ($427)	Cost/kWh from formic acid at projected CO_2 reduction capabilities ($155)
0.89V (60%)	$1.21	$0.41	$0.15
1.04V (70%)	$1.03	$0.35	$0.13
1.18V (80%)	$0.91	$0.31	$0.11
1.33V (90%)	$0.81	$0.28	$0.10

With the present level of fuel cell performance and current market value for formic acid, the cost to produce electricity per kWh is markedly larger than for grid scale electricity, even if more optimal anode catalysts were to be discovered. Applying the CO_2 reduction system to produce formic acid could bring this cost sufficiently closer to the current grid price, and even more so if that technology were also optimized ($0.15-0.10/kWh vs. $0.04/kWh). Formic acid

fuel cells may find the largest application in the market of portable power since they could act as instantly rechargeable batteries, since refueling is all that may be required to restart the device (supposing that no other problems have developed during operation). Moreover, if sufficiently robust catalysts are discovered, fuel cells could exhibit much longer lifetimes than conventionally used batteries, thereby further reducing costs associated with replacing the device. Ultimately, progress in this field is expected to continue up to and beyond the point where formic acid can be efficiently utilized as a fuel and its major waste product, CO_2, will be captured, converted, and recycled back into the fuel cell, thereby resulting in a technology that is clean, efficient, and both economically and environmentally sustainable.

Conclusion

For direct formic acid fuel cells, it has been determined that electricity could be produced for as low as $1.39/kWh using the current catalysts when buying formic acid from commercial sources. Coupling the formic acid produced by electrochemical CO_2 reduction (assuming that formate can be easily acidified to formic acid) with the best conditions for a formic acid fuel cell, however, the cost of electricity would come down to as low as $0.48/kWh. These estimates assume that robust formic acid fuel cells can be developed. Further improvements in either electrochemical CO_2 reduction or direct formic acid fuel cells could bring this value down further to more competitive values. A very simple cycle can be envisioned using these two processes to support one another, where CO_2 released by the direct formic acid fuel cell could be directly converted back into formic acid by electrochemical reduction.

Appendix 3.1
High pressure tubular reactor : Problems of reactor material dusting – *A technical report* –

After a few month of initial usage, small holes have been observed on the surface of the 6.5" spool, thermowell as well as the inside wall of the tubular reactor. This "dusting" of the metal is mostly located between 7" and 8" from the bottom of the thermowell (see photo 1 to 5).

Photo 1. 6.5 " spool from reactor #3

Photo 2.1. 6.5 " spool from reactor #3, detail

Photo 2.2. 6.5 “ spool from reactor #1, detail

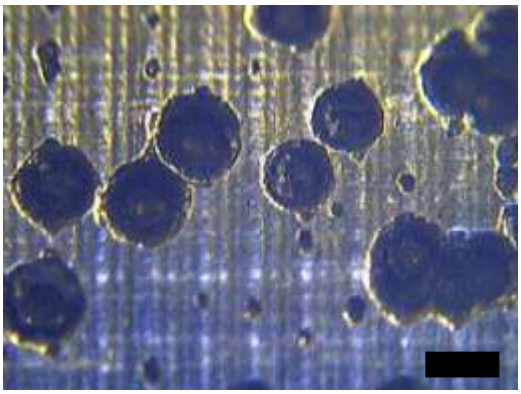

Photo 3. 6.5 “ spool from reactor #3 (Magnification: 5 X, scale bar=10 micron)

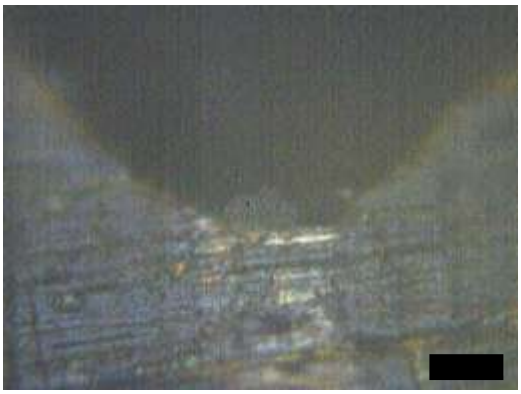

Photo 4. 6.5 “ spool from reactor #3 (Magnification: 50 X, scale bar=1 micron)

Photo 5 thermowell from reactor # 2

Although it is difficult to see, a similar dusting seems to have occurred on the walls of the tubular reactor itself in the same region.

This phenomenon occurred in all three pressure reactor. It favors side reactions and the formation of coke. In photos 6.1 and 6.2 taken after a typical reaction we can see the presence of a coke "ring" around the 6.5" spool. The formation of coke progressively impedes the gas passage which results in reactor clogging and an increase in pressure.

Photo 6.1. 6.5" spool with carbon "ring" after reaction (exp. TR-51)

Photo 6.2. 6.5" spool with carbon "ring" after reaction (exp. TR-59)

Before this “dusting” started to appear, reactions were relatively stable (see TR36 below as a typical example). After the dusting was observed, however, the activity and stability of the same catalyst was greatly reduced (see TR56 below). After less than 40 hours the reactor was clogged. The gas mixture after the catalyst bed is composed of the following gases:

Gas	% of total
H2	30.92
N2	18.61
CO	39.29
CH4	6.67
CO2	4.51

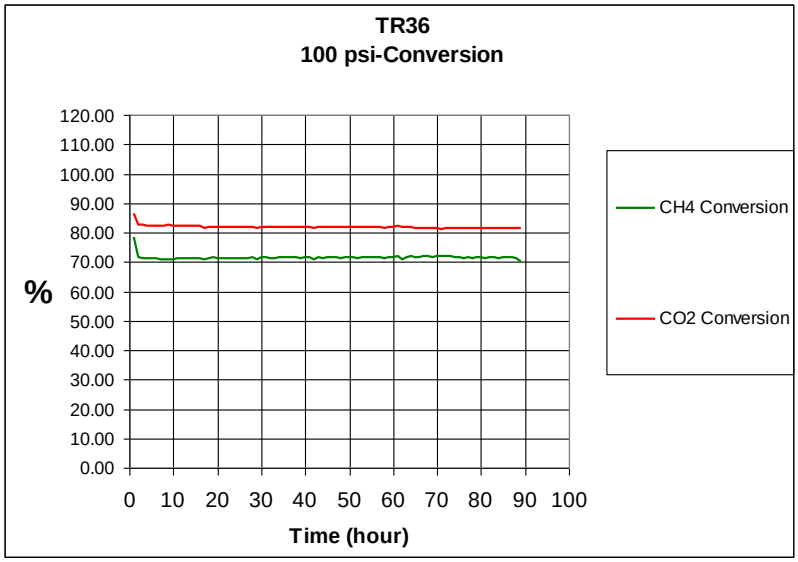

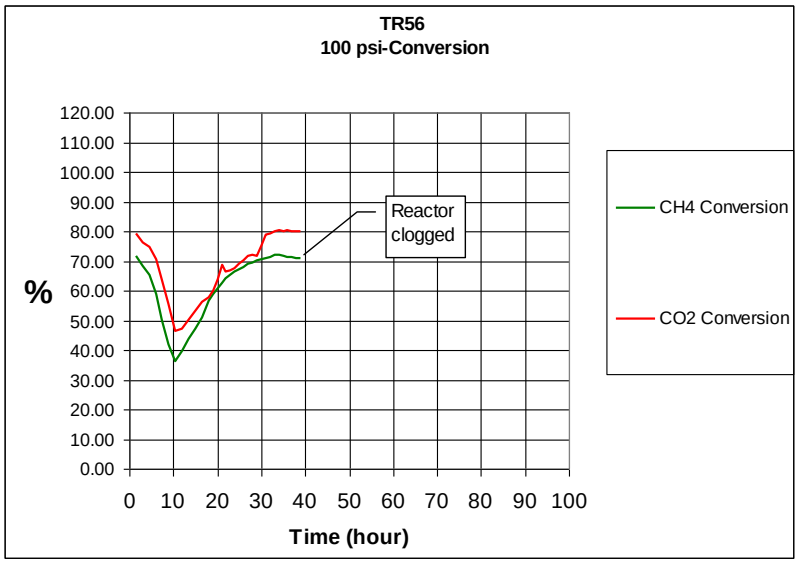

The dusting appeared mostly in the part of the tubular reactor where the temperature ranges from 550 °C to 700 °C. At higher as well as lower temperature there does not seem to be

much pitting. Intuitively one would expect the phenomenon to be more pronounced at higher temperatures.

A similar but less pronounced dusting seems to have also occurred on the reactor walls in the upper part of the tubular reactor. It is however hard to determine visually the extend of the damage inside the reactor. Here again the phenomenon seems to be very localized in a specific temperature range.

The feed gas is composed of equal amounts of CH_4, CO_2 and N_2. Total flow is 100 mL/min.

The material used for the reactor (Haynes 230) is supposed to be very resistant to grain growth and carburization so it seems odd that pitting would occur especially at temperatures of only 550 °C to 700 °C.

Table Haynes 230 composition

Ni	Cr	W	Mo	Fe	Co	Mn	Si	Al	C	La	B
57[a]	22	14	2	3*	5*	0.5	0.4	0.3	0.10	0.02	0.015*

*Maximum [a]As balance

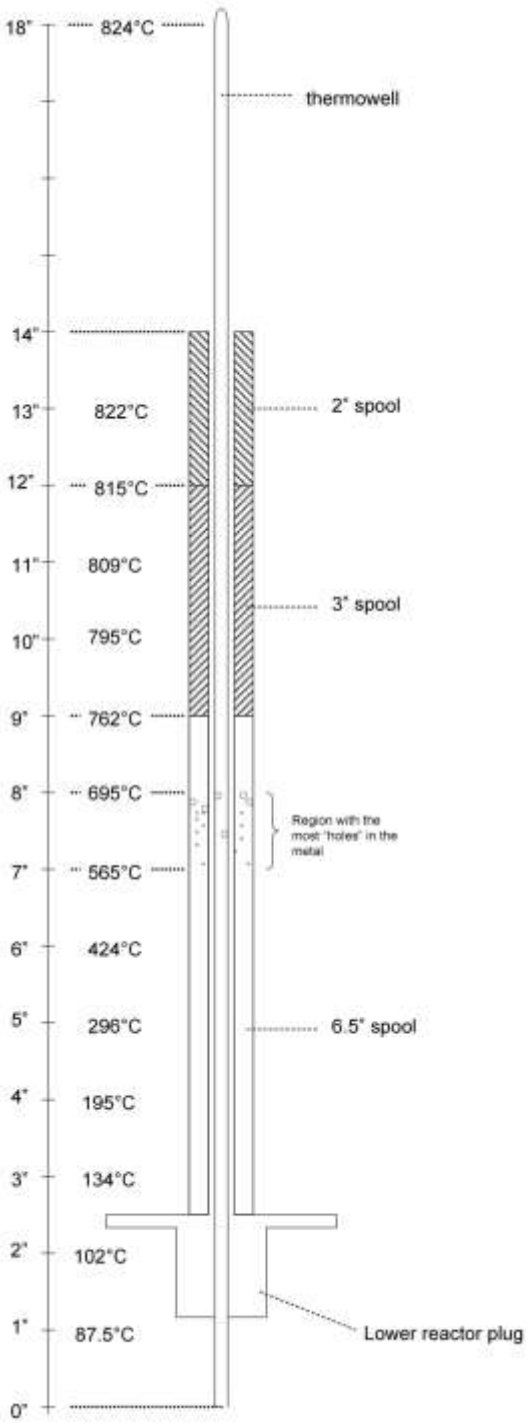

Temperature profile of the tubular reactor during a reaction.

To get more insight into the observed degradation of the reactor the Haynes company was contacted which manufactures the Haynes 230 (H230) alloy used for this tubular reactor. As it

turns out this metal "dusting" phenomenon is apparently a known problem. It occurs in high carbon activity environments (ac >>1) in a temperature range of 450 °C to 800 °C. H230 is known to have a good metal dusting resistance. However, all metals are susceptible to dusting in aggressive environments. According to Klarstrom et al.[1] HR-160 alloy shows a better resistance to dusting than H230 (see table and figure hereafter from ref[1]. The same was observed by other groups even at higher pressure.[2]. Some alloys showed a better dusting resistance at atmospheric pressure but degraded faster at higher pressure.

Final Metal Wastage Rates Obtained for Exposures In 49% CO-49% H_2-2% H_2O at 650°C

Alloy Designation	UNS No.	Total Exposure Time, Hours	Final Metal Wastage Rate, mg/cm²h
HR-120	N08120	190	4.1×10^{-2}
800H	N08810	925	2.7×10^{-3}
214	N07214	5,707	1.0×10^{-3}
601	N06601	10,000	2.5×10^{-3}
230	N06230	10,000	3.2×10^{-4}
HR-160	N12160	10,000	0.0*

*Attack Too Small for Analysis

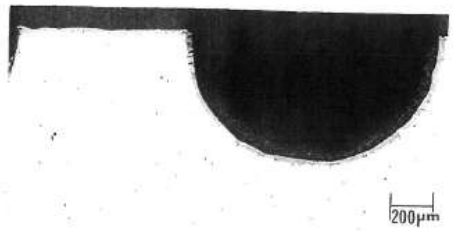

(a) 601 alloy

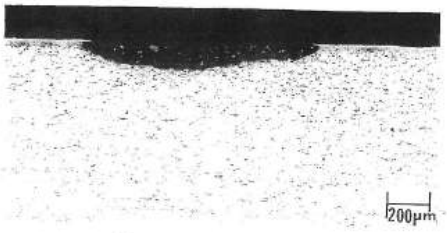

(b) 230 alloy

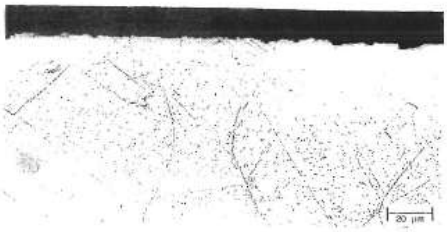

(c) HR-160 alloy

Figure 3. Metal Dusting Attack Observed in 601, 230 and HR-160 alloys After 10,000 Hours of Exposure.

Table 5.6 Surface conditions of alloys after testing at 593 °C (1100 °F) for 246 h in H_2-18.4CO-5.7CO_2-22.5H_2O at 1, 14.3, and 40.8 atm pressures

	Condition at pressure		
Alloy	1 atm	14.3 atm	40.8 atm
601	Clean surface	Pits	Pits
690	Clean surface	Pits	Pits
617	Clean surface	Pits	Pits
602CA	Clean surface	Clean surface	Clean surface
214	Clean surface	Pits	Pits
45TM	Clean surface	Clean surface	Clean surface
HR160	Clean surface	Clean surface	Clean surface

Source: Ref 95

The HR-160 alloy is ASME rated (VIII-1 code) and is therefore acceptable for the construction of pressure vessels. HR-160 has however other characteristic that makes it less

suitable in the current application. Its typical strength is considerably lower than H230 and the maximum permissible temperature is 815 °C (see table below). This high temperature limit is too low for our application.

Temp F	Haynes 230 Max allowable strength, ksi	Haynes 160 Max allowable strength, ksi
100	30.0	23.3
1500	4.1	2.5
1800	0.45	Not perm

Other possible solution to the dusting problem

Another way to deal with the dusting issue is to try to avoid contact of the reaction gases with any metallic parts in the tubular reactor. The idea is to introduce an alumina tube inside the H230 reactor over most of its length (see Figures below). The reaction mixture will flow over the catalyst through the alumina tube form the top. A separate flow of nitrogen was also introduced between the alumina tube and the inside wall of the tubular reactor. This nitrogen blanket will avoid contact of the reactive gases with the reactor walls at temperatures promoting metal dusting. The nitrogen and gaseous product are combined at the bottom of the alumina tube and exit the reactor from the side. The seal of the alumina tube with the tubular reactor wall is made in the top part using a Teflon cone machined to the exact dimensions of the given space. The alumina tube has to remain open on one side to avoid large pressure differentials between the inside and outside of the alumina tube and possible breaking due to the increased pressure. The spools, filling material and diluent will also be pure alumina so the only metal present will be the one on the catalyst. Photos of the alumina tube and spools as well as the Teflon cone can be seen hereafter. Testing of this new configuration showed indeed a complete suppression of the dusting problem. This configuration was therefore used for all further reactions.

References

1 D. L. Klarstrom, H. J. Grabke, L. D. Paul, in *The Metal Dusting Behavior of Several High Temperature Alloys*, Paper No. 1379, Corrosion/2001, NACE International, 2001.

2 G. Y. Lai, *Carburization and Metal Dusting*, in *High-Temperature Corrosion and Materials Applications*, ASM International, Materials Park, Ohio, **2007**, p. 97 to 145.

Appendix 3.2
Materials and Chemicals

Solid supports:

- Fumed alumina, Aeroxide Alu C, hydrophilic fumed alumina 100± 15 m^2/g, Degussa (now Evonik).
- Fumed silica, Aerosil 300, hydrophilic fumed silica 300± 30 m^2/g, ~50 g/L, Degussa 9now Evonik).
- MgO, Magnesium oxide, Strem chemicals, 99.5% Mg, (Cat. # 93-1243), 325 mesh, CAS 1309-48-4, MW 40.31
- PURAL MG30 and PURAL MG70, hydrotalcite samples provided by SASOL Germany. These hydrotalcites (aluminum magnesium compounds) were obtained by hydrolysis of heterometallic alcoholates.

Compared to alumina hydrates (pH 8-9) hydrotalcites are even more alkaline by nature. Basicity is adjustable by increasing the Mg/Al ratio and/or incorporating anions other than OH^-. As shown below, hydrotalcites have a double-layered metal hydroxide structure consisting of magnesium and aluminum hydroxide octahedrons interconnected via the edges. Additional interstitial anions between the layers compensate the charge of the crystal and determine the size of the interlayer distance (basal spacing)

Product Name:		**PURAL MG 30**	**PURAL MG 70**
Product No.		595030	595070
Chemical Data:			
$MgO : Al_2O_3$	%	30 : 70[1)]	70 : 30
L.O.I.	%	40 max.	45 max.
Carbon	%	0.5 – 3	0.5 – 3
SiO_2	ppm	350 max.	350 max.
Fe_2O_3	ppm	200 max.	200 max.
Na, Ca, Ti each	ppm	50 max.	50 max.
Physical Properties:			
Surface Area [2)]	m^2/g	250 min.	180 min.
Pore Volume [2)]	ml/g	0.5 min.	0.2 min.
Loose Bulk Density	g/l	350 – 550	350 – 550
Particle Size Distribution:			
< 25 µm	%	20 min.	30 min.
< 45 µm	%	40 min.	50 min.
< 90 µm	%	85 min.	90 min.

1) Due to the high aluminum content, PURAL MG 30 contains a significant amount of boehmite (alumina monohydrate).
2) After activation 3h at 550°C

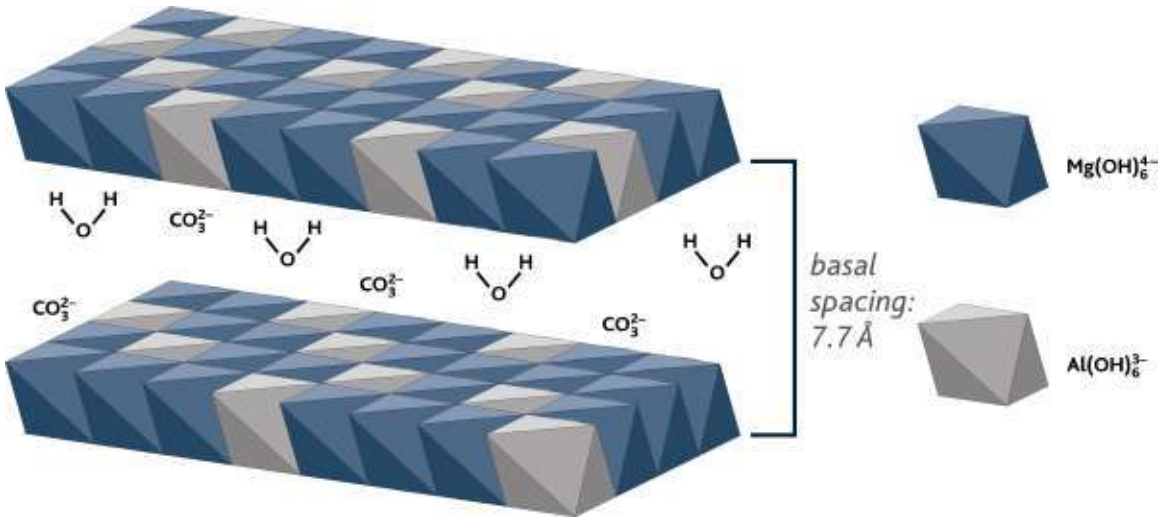

Chemical Formula: $Mg_{2x}\,Al_2\,(OH)_{4x+4}\,CO_3 \cdot n\,H_2O$

CAS-Number: 11097-59-9

Metal precursors:
Nickel (II) nitrate hexahydrate $Ni(NO_3)_2 \bullet 6H_2O$, Aldrich (203874-100G), CAS 13478-00-7, MW 290.81 g/mol.
Cobalt (II) nitrate hexahydrate $Co(NO_3)_2 \bullet 6H_2O$, Aldrich (230375-100G), CAS 10026-22-9, MW 291.03 g/mol, mp 55°C, d 1.88.

Reaction gases:
CO_2 (Instrument grade), H_2 UHP (99.999%), Nitrogen pre-pure grade. Methane labeled UHP (99.97%).

Appendix 3.3 GC analysis of the natural gas used

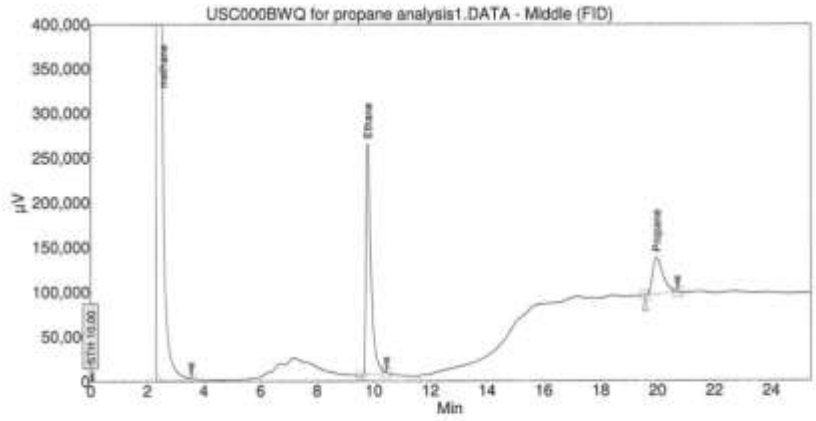

Peak results :

Index	Name	Time [Min]	Quantity [% Area]	Height [µV]	Area [µV.Min]	Area % [%]
3	methane	2.33	96.50	21812082.2	1948321.4	96.497
2	Ethane	9.78	2.64	258563.7	53257.7	2.638
1	Propane	19.96	0.87	41004.2	17465.6	0.865
Total			100.00	22111650.1	2019044.6	100.000

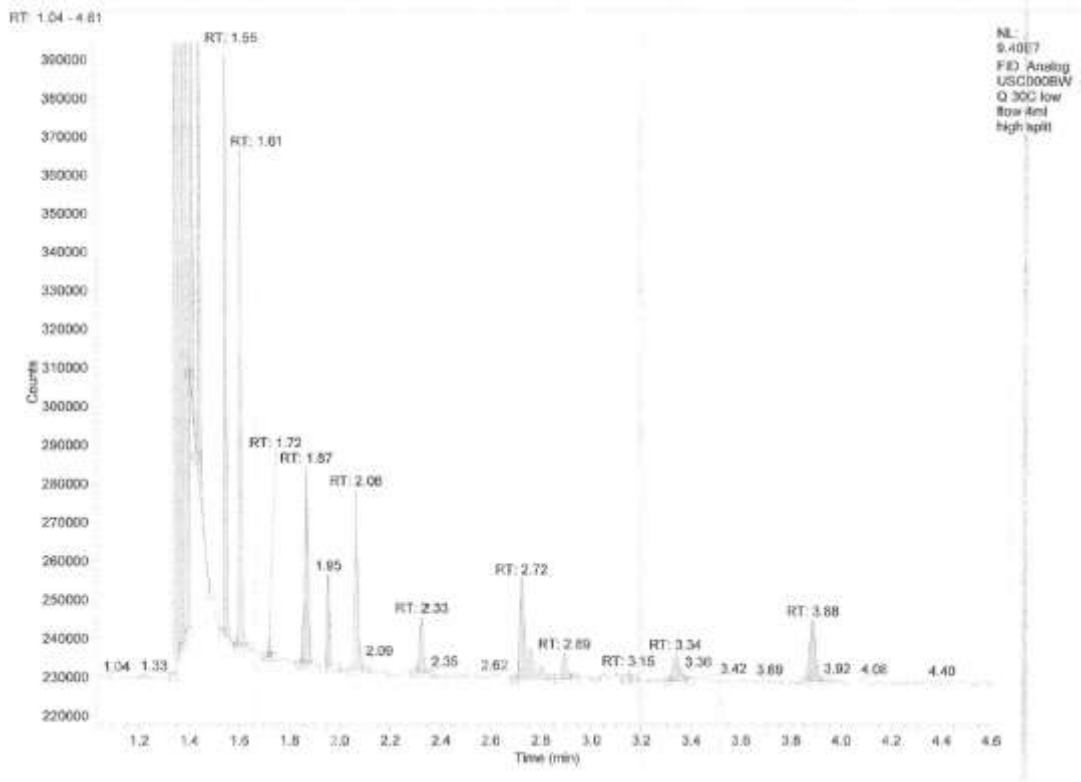

Higher hydrocarbons contained in natural gas. GC analysis.

Appendix 4.1: Experimental section for the adsorbents based on amines impregnated on solid supports

Reagents and Supports

The amines, PEI (LMW) low molecular weight (Mw ca. 800), PEI (HMW) high molecular weight (Mw ca. 25000), PEI (linear) (Mw ca. 423), tetraethylenepentamine (TEP), pentaethylenehexamine (PEH), 2-amino-2-methyl-1,3-propanediol (AMP), 2-(2-aminoethylamino)-ethanol (AEAE), diisopropanolamine (DIPA), imidazole, MEA, DEA, triethanolamine (TEA) were purchased from Aldrich. Fumed silica (average primary particle size 7 nm), poly(4-vinylpyridine) (PVP, 2% cross-linked) and polyvinylpyrrolidone (povidone) cross-linked were obtained from Aldrich. Silica gel (60-200 mesh) and aluminum oxide were purchased from J.T. Baker. Precipitated silica (Hi-SiL® T-600) was obtained from PPG industries. Aerosil® 150 (hydrophilic), Aerosil® 380 (hydrophilic), Aerosil® 300 (hydrophilic) and Aerosil® R106 (hydrophobic) are fumed silicas that were provided by Evonik (formerly Degussa).

Preparation of the sorbents

The following example illustrates the preparation of a supported amine sorbent composed of 50 wt. % polyethylenimine and 50 wt. % fumed silica.

4 g of polyethylenimine (LMW) was dissolved in 25 mL of methanol. This solution was then added stepwise under stirring to 4 g fumed silica in suspension in 100 mL methanol to ensure a good dispersion of the polyethylenimine on the support. The solution was then mixed for an additional hour. After that, the solvent was removed from the mixture by heating at 50°C under vacuum on a rotary evaporator followed by vacuum treatment overnight (< 1 mm Hg). The supported amine sorbent was obtained as a white solid.

In the case of adsorbents containing both PEI and PEG the preparation of the materials was carried out by impregnation of the supports in two steps: in the first step a methanolic solution of polyethyleneglycol (about 10%) was added stepwise under stirring to a suspension of the support in methanol (proportion 1 g / 20 mL). After mixing for an hour at room temperature the solvent was removed from the mixture by heating at 50 °C under vacuum on a rotary evaporator followed by dynamic vacuum treatment overnight (< 1 mmHg). The obtained polyol / support was subsequently crushed and sieved (< 60 mesh) and the obtained powder mixed in methanol (proportion 1 g / 10 mL). To this mixture, a methanolic solution of polyethylenimine (about 10 %) was added stepwise to ensure a good dispersion of the polyethylenimine on the polyol / support. The amount of both the polyol solution and the polyethylenimine were calculated according to the required concentrations of both in a given sample. The solution was then mixed for an additional hour. After this treatment, the solvent was removed from the mixture by heating at 50 °C under vacuum on a rotary evaporator followed by dynamic vacuum overnight (< 1 mmHg). This procedure was the same for all the adsorbents prepared and only the support and the final concentrations in PEI and PEG were changed.

Measurement of CO_2 adsorption and desorption capacity

The adsorption capacity of the adsorbents was measured by two techniques: CO_2 adsorption under static conditions and adsorption measurement by thermogravimetry (TGA).

Static conditions

CO_2 adsorption data were obtained using glass tubes capped with a septum and connected to the gas delivery and vacuum system via needles inserted though the septum. 0.5 gram of the adsorbent was loaded in the glass tube and a layer of glass wool placed over it to avoid possible loss of small particles. The sample was pre-treated by heating at 80-100°C under vacuum (0.1-0.5 mm Hg) for 1-3 h to desorb CO_2 and water that could be present on the solid. The sample was then cooled down to room temperature and re-pressurized with nitrogen. The weight of the tube was measured. The temperature was then adjusted to the desired adsorption temperature. After evacuation of the tubes (0.1-0.5 mm Hg), CO_2 was added until the atmospheric pressure was reached. After a defined adsorption time under CO_2 at atmospheric pressure, generally 1 h, the weight of the glass tube was measured. The amount of CO_2 effectively adsorbed on the solid was determined by the difference in weight of the glass tube before and after CO_2 adsorption (taking into account the correction factor due to molecular weight difference between CO_2 and N_2).

Following the CO_2 adsorption measurements, the glass tubes were exposed to vacuum (0.1-0.5 mm Hg) at 80-100°C for 1-3 h to perform the desorption of CO_2 freeing the amine groups present on the solid.

TGA measurements

The TGA tests were performed using a thermogravimetric analyzer (Shimadzu TGA-50 Thermogravimetric Analyser). Samples previously treated for at least two hours under vacuum at 110 °C were loaded (5-20 mg) in a platinum crucible and placed on the instrument's balance under a N_2 flow. After the sample / furnace reached the desired temperature, the gas flow was switched to either CO_2 or a mixture of CO_2 in different proportions with other gases (N_2, O_2, etc). The change in mass of the sample was recorded over time to determine the adsorption capacity. To test the adsorption/desorption cycles over time the gases were switched automatically between N_2 and CO_2 using a valco multiposition valve controlled by the "Labview" software.

CO_2 adsorption from the air

CO_2 adsorption data were obtained using an all-glass grease free flow system. The adsorbent, generally 3 g was placed in a U-tube between two glass wool plugs. The inner diameter of the tube was 8 mm. The height of the adsorbent bed for FS-PEI-50 was about 10 cm. The U-tube was then evacuated (~65 mTorr) at 85°C for 3 hours. The weight of the adsorbent after this treatment was measured. The weight loss due to CO_2 and water desorption, depending on the adsorbent, was generally between 2 and 10%. The FS-PEI-50 used to obtain Figure 1 had for example a weight of 2.72 g after vacuum treatment due to a weight loss of 9.45%. The

adsorbent weight after pretreatment was used for the later calculation of the CO_2 adsorption capacities. After pretreatment the adsorbent containing U-tube was placed in a thermostated oil bath at 25 °C. Air from the laboratory atmosphere was dried (over silica gel), filtered and compressed to 150 psi and used directly for the adsorption measurements. For the adsorption measurements a Horiba VIA-510 CO_2 analyzer equipped with an IR detector specifically intended for CO_2 measurements was placed in-line with the adsorption setup. The concentration range used was 0-2000 ppm. Before each run, the analyzer was calibrated with reference gases; CO_2 in air and ultra zero grade air for the zero. After calibration, the initial CO_2 concentration in air was determined and was generally between 410 and 420 ppm; somewhat higher than the average global atmospheric CO_2 concentration of 390 to 395 ppm. The air-flow (335 mL/min) was then opened on the adsorbent bed. Almost immediately the CO_2 concentration in the gas outlet fell to 0 ppm, signaling complete CO_2 adsorption from the air. The CO_2 concentration was recorded as a function of time via LabView 8.6. After saturation of the adsorbent, when the CO_2 concentration reached the inlet value (410-420 ppm), the gas flow was stopped.

Desorption was performed using two different methods

a) By applying vacuum (~65 mTorr) at 85 °C for 3 hours

b) By heating the adsorbent containing U-tube to 85 °C and then passing a flow of air (335 ml/min) through it. In this case the outlet gas was analyzed on a Horiba VIA-510 CO_2 analyzer with a range of 0-20% CO_2. The CO_2 concentration was recorded as a function of time via LabView 8.6. Immediately after opening of the air-flow onto the saturated adsorbent the concentration in CO_2 spiked to 3-5% CO_2 and then slowly decreased until reaching the inlet CO_2 concentration (410-420 ppm).

For CO_2 adsorption measurements under humid conditions, a part of the air feed was saturated with water by bubbling through a water-containing saturator maintained at 25 °C. This moisture saturated feed was then combined with a dry air feed in order to obtain a gas flow with a relative humidity of 67%. The obtained humid air was flown through the adsorbent.

Surface area and pore volume analysis

The supports were characterized by N_2 adsorption/desorption isotherm measurements on a Quantachrome NOVA 2200e instrument. The surface area was determined by the multipoint BET method. The total pore volume was evaluated at a P/P_0 close to 0.995. Pore size distribution was derived from the desorption branch of the isotherm using the BJH method.

SEM and TEM Measurements

SEM pictures were taken on a Cambridge 360 model. The samples were previously covered by a thin gold layer sputtered coated. Samples for TEM were embedded in EPO-fix (from Electron Microscopy Sciences), sectioned and viewed on a Philips EM 420 Transmission Electron Microscope.

Density measurements

The tapped density of each sorbent was measured by placing a known amount of the sorbent into a graduated cylinder, which was tapped continuously during 2 minutes. The volume occupied by the sorbent was then noted and the density of the solid in g/mL calculated.

Adsorption efficiency determination

The "Adsorption Efficiency" (AE) was defined as the amount of CO_2 adsorbed divided by the theoretical maximum adsorption value in percentage. It was calculated considering that the polyethylenimine is composed of (-NH-CH_2-CH_2-) monomers with a molecular weight of 43 g/mol and that 2 amino groups are expected to react with one CO_2 (vide infra). A pure sample of PEI with 100 % AE would theoretically adsorb 511.63 mg CO_2 / g amine. The following equation can be derived from these assumptions:

AE (%) = { [CO_2] / [PEI] } * 19.55

Where:

AE = Adsorption Efficiency (in %)

[CO_2] = Adsorption of CO_2 (mg of CO_2 / g of sample)

[PEI] = Amount of PEI in the sample before the adsorption (%)

Calculation of the maximum theoretical adsorbable amount of CO_2 for adsorbents containing PEI

The number of amino groups per g of solid adsorbent was calculated considering that PEI is composed for a large part of (-NH-CH_2-CH_2-) units with a molecular weight of 43 $g.mol^{-1}$. In 1g of adsorbent containing equal amounts of PEI and support (amine/support ratio of 1), the PEI represents 50% of the weight or 0.5g. This amounts to 11.6 mmol of amino groups per gram of sorbent. One should however keep in mind that PEI contains a mixture of primary, secondary and tertiary amino groups, which will react at different rates with CO_2. The theoretical maximum adsorbable amounts of CO_2 in mg, CO_2 per gram sorbent, reported in table 1, were calculated considering that each molecule of CO_2 will be complexed by two amino groups to form a carbamate. Of course, in the presence of water, the carbamate could further react to form a bicarbonate, meaning that only one amino group is necessary to complex one CO_2 molecule, effectively increasing the amount of CO_2 adsorbable on the sorbent.

Appendix 5.1

Synthesis of 1,3-bis(2'-pyridyl-imino)-isoindoline

IndH ligand was synthesized in the reaction between phthalonitrile and 2-aminopyridine at 200 ºC according to a literature procedure.

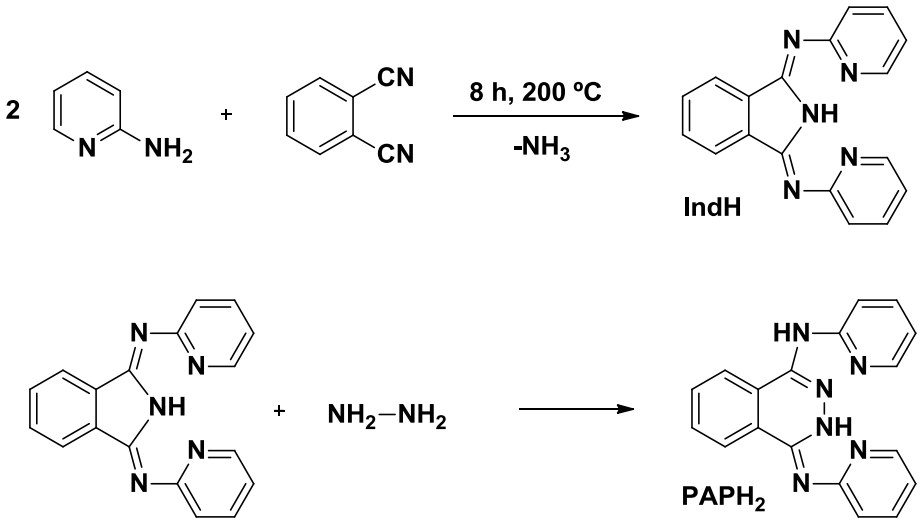

Figure A1. Synthetic route for IndH and $PAPH_2$.

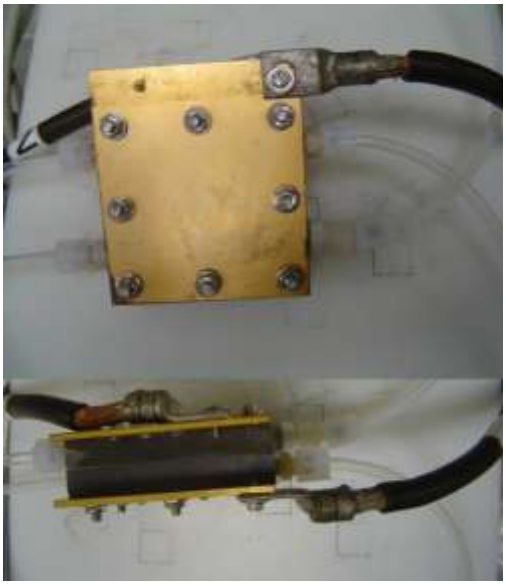

Figure A2. Hydrogen/air fuel cell.

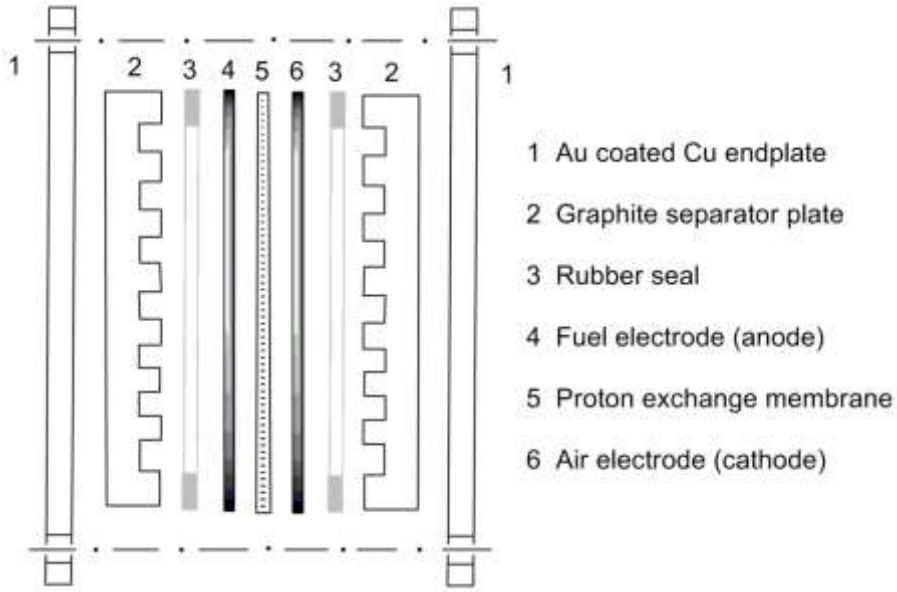

Figure A3. Structure of the fuel cell. Part 4-5-6 form an electrode membrane after heating in the press.

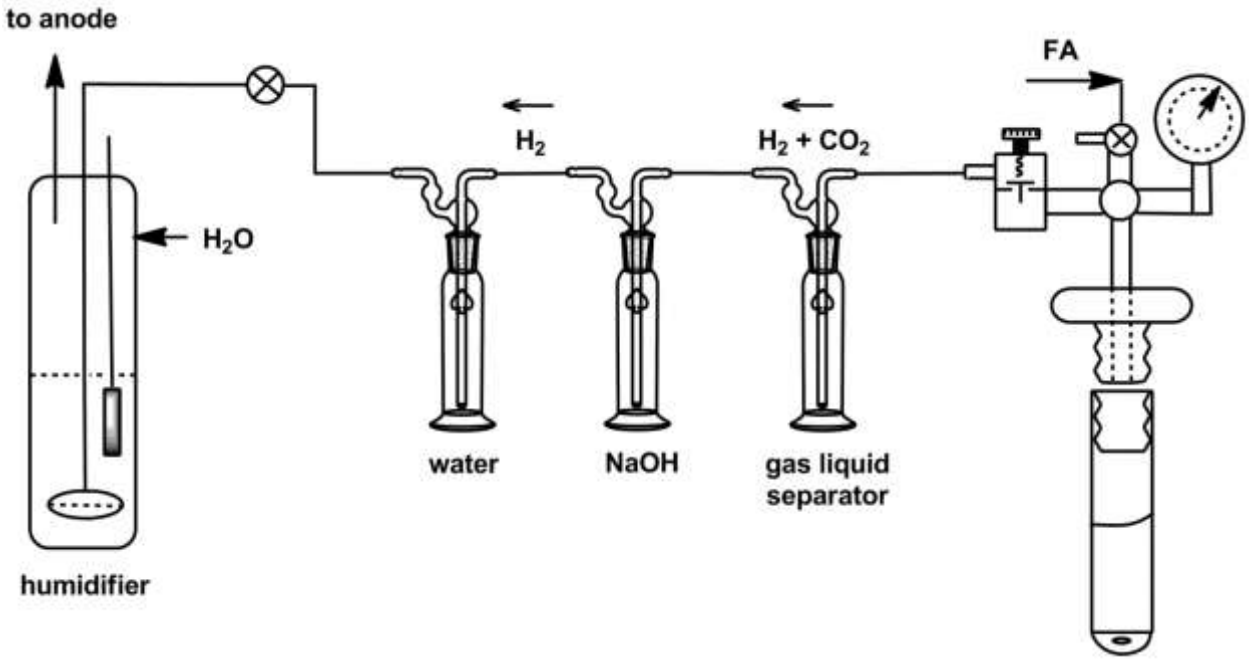

Figure A4. Modified experimental setup for an integrated FA decomposition and a H_2/air fuel cell unit with a NaOH trap to remove CO_2. Other parts of the system are omitted for clarity.

Papers Presented at the Meetings (2009-2013)

[1] Selective bromination of methane over solid acid catalysts and poly (4-vinyl pyridine) catalyzed hydrolysis and methanolysis of methyl bromide, G. K. S. Prakash, P. Batamack, J. C. Colmenares, T. Mathew, G. A. Olah, 2011 *AICHE Spring meeting*, Chicago, March 13-17, 2011.

[2] Regenerable high capacity organo-amine based CO2 sorbents using nano structured silica as a support, A. Goeppert, M. Sergio, G. A. Olah, G. K. S. Prakash, *Abstracts of Papers, 241st ACS National Meeting & Exposition*, Anaheim, CA, March 27-31, 2011: *Prep. Pap.-Am. Chem. Soc., Div. Fuel Chem.* **2011**, *56 (1)*, 270.

[3] Decomposition of formic acid to H_2 and CO_2 in the presence of 1,3-bis(2'-pyridyl-imino)-isoindoline iridium complex, M. Czaun, A. Goeppert, R. May, G. K. S. Prakash, G. A. Olah, *Abstracts of Papers, 241st ACS National Meeting & Exposition, Anaheim, CA, March 27-31, 2011*: *Prep. Pap.-Am. Chem. Soc., Div. Fuel Chem.* **2011**, *56 (1)*, 476.

[4] Palladium-Gold electrocatalysts for efficient formic acid oxidation, G. K. S. Prakash, F. C. Krause and G. A. Olah, A1-55, Presented at the 219th ECS Meeting, Montreal, QC, Canada, May 1-6, 2011.

[5] Ruthenium carbonyls as active catalysts for the decomposition of formic acid to H_2 and CO_2, M. Czaun, A. Goeppert, R. May, J. J. Zhang, M. Sax, G. K. S. Prakash , G. A. Olah, and R. Haiges, Paper No. 51, Presented at the Division of Fuel Chemistry. 242nd ACS National Meeting, Denver, CO, United States, August 28-September 1, 2011.

[6] Methanol and acetals synthesis through a two-step bromination of methane and hydrolysis/alcoholysis of methyl and methylene bromides, G. K. S. Prakash, P. T. Batamack, J. C. Colmenares, R. Jog, S. K. Ganesh, T. Mathew, I. Bucsi and G. A. Olah, Paper No. 163, Presented at the Division of Fuel Chemistry. 242nd ACS National Meeting, Denver, CO, United States, August 28-September 1, 2011.

[7] Polyamine based regenerable solid adsorbents for the capture of CO_2 from the air, A. Goeppert, M. Czaun, R. B. May, G. K. S. Prakash, G. A. Olah and S. R. Narayanan, Presented at the 243rd ACS National Meeting, San Diego, CA, March 25- 29, 2012, Fuel- 482.

[8] Beyond oil and gas: The Methanol Economy, G. K. S. Prakash, Presented at the 243rd ACS National Meeting, San Diego, CA, March 25- 29, 2012, Fuel- 475.

[9] In situ formation of tetra-ruthenium dodecacarbonyl tetrahydride from ruthenium (III) chloride in the catalytic decomposition of formic acid to hydrogen and carbon dioxide, M. Czaun, A. Goeppert, R. May, M. Sax, J. Zhang, R. Haiges, G. K. S. Prakash, and G. A. Olah, Presented at the 243rd ACS National Meeting, San Diego, CA, March 25- 29, 2012, INOR-1067.

[10] Selective decomposition of formic acid to hydrogen and carbon dioxide in the presence of ruthenium hydrido carbonyl complexes , Kothandaraman, J; Czaun, M; Goeppert, A; May, R;

Prakash, G. K. S; Olah, G A., 244th ACS National Meeting & Exposition, Philadelphia, PA, United States, August 19-23, 2012, INOR-533.

[11] Bireforming of Methane and Natural Gas under High Pressure, A. Goeppert, M. Czaun, R. B. May, G. K. S. Prakash and G. A. Olah, Paper No. 491e, Presented at the 12th AIChE Annual Meeting, Pittsburgh, PA, October 31, 2012.

[12] Hydrogen generation by selective decomposition of formic acid in the presence of ruthenium pincer ligand complexes, J. Kothandaraman, M. Czaun, A. Goeppert, G. K. S. Prakash and G. A. Olah, Paper No. 1025, Presented at the INORG Division, 245th American Chemical Society Meeting, New Orleans, LA, April 7-11, 2013.

[13] Ruthenium-catalyzed hydrogen generation from formic acid, M. Czaun, A. Goeppert, J. Y. Zhang, R. May, M. Sax, G. K. S. Prakash and G. A. Olah, Paper No. 1024, Presented at the INORG Division, 245th American Chemical Society Meeting, New Orleans, LA, April 7-11, 2013.

[14] Regenerable Solid Polyamine based absorbents for CO_2 capture from the air, H. Zhang, A. Goeppert, M. Czaun, R. May, G. K. S. Prakash and G. A. Olah, Paper No. 568, Presented at the ENFL Division, 245th American Chemical Society Meeting, New Orleans, LA, April 7-11, 2013.

[15] Combined steam and carbon dioxide reforming of methane and natural at high pressures: Bi-reforming, A. Goeppert, M. Czaun, R. B. May, G. K. S. Prakash and G. A. Olah, presented at the Division of Energy & Fuels, Paper No. ENFL-56, 246th American Chemical Society Meeting, Indianapolis, IN, September 8-12, 2013.

[16] Insight into hydrogen generation from formic acid in the presence of ruthenium pincer ligand complexes, M. Czaun, A. Goeppert, J. Kothandaraman, R. B. May, G. K. S. Prakash and G. A. Olah, presented at the Division of Energy & Fuels, Paper No. ENFL-191. 246th American Chemical Society Meeting, Indianapolis, IN, September 8-12, 2013.

Peer-Reviewed Papers Published (2009-2013)

[1] Poly(4-vinylpyridine) catalyzed hydrolysis of methyl bromide to methanol and Dimethyl ether, G. K. S. Prakash, J. C. Colmenares, P. T. Batamack, T. Mathew and G. A. Olah, *J. Mol. Catalysis A: Chemical* **2009**, *310*, 180-183.

[2] Poly(4-vinylpyridine) catalyzed selective methanolysis of methyl and methylene bromides, G. K. S. Prakash, J. C. Colmaenares, P. T. Batamack, T. Mathew and G. A. Olah, *Tetrahedron Lett.* **2009,** 6016-6018.

[3] Nano Structured Silica as a support for regenerable high capacity organo-amine based CO_2 sorbents, A. Goeppert, S. Meth, G. K. S. Prakash and G. A. Olah *Energy & Environmental Science*, **2010**, *3(12)*, 1949-1960.

[4] Hydrogen Generation from Formic Acid Decomposition by Ruthenium Carbonyl

Complexes. Dodecacarbonyl-Ruthenium- Tetrahydride as an Active Intermediate, M. Czaun, A. Goeppert, R. May, R. Haiges, G. K. S. Prakash, and G. A. Olah, *Chem.Sus. Chem.* **2011**, *4*, 1241-1248.

[5] Carbon Dioxide Capture from the Air Using a Polyamine Based Regenerable Solid Adsorbent, A. Goeppert, M. Czaun, R. May, G. K. S. Prakash, G. A. Olah and S. R. Narayanan, *J. Am. Chem. Soc.* **2011**, *133*, 20164- 20167. *This paper received enormous attention from public media (For example it was covered by Science, Scientific American, Los Angeles Times, Christian Science Monitor, etc.)*

[6] Silica Nanoparticles as Support for Regenerable CO_2 Sorbents, S. Meth, A. Goeppert, G. K. S. Prakash and G. A. Olah, *Energy & Fuels*, **2012**, *26(5)*, 3082-3090.

[7] Air as the renewable carbon source of the future: An overview of CO_2 capture from the atmosphere, A. Goeppert, M. Czaun, G. K. S. Prakash and G. A. Olah, *Energy and Environmental Science*, **2012**, 5, 7833-7853 (a comprehensive and timely review).

[8] Electrochemical reduction of CO_2 over Sn-Nafion® coated electrode for a fuel-cell-like device, G. K. S. Prakash, F. Viva and G. A. Olah, *J. Power Sources*, **2013**, *223(1)*, 68-73.

[9] Organoamines-Grafted on Nano-Sized Silica for Carbon Dioxide Capture, M. Czaun, A. Goeppert, R. B. May, D. Petier, G. K. S. Prakash and G. A. Olah, *J. CO_2 Utilization*, **2013**, 1, 1-7.

[10] Carbon dioxide recycling to methanol, dimethyl ether and derived products for a sustainable future, A. Goeppert, G. K. S. Prakash and G. A. Olah, Actualite Chimique, 371-372, 78-83 (2013).

[11] Bi-reforming of methane from any source with steam and carbon dioxide exclusively to metgas ($CO\text{-}2H_2$) for methanol and hydrocarbon synthesis, G. A. Olah, A. Goeppert, G. K. S. Prakash, *J. Am. Chem. Soc.* **2013**, *135*, 648-650.

[12] Self-Sufficient and Exclusive Oxygenation of Methane and Its Source Materials with Oxygen to Methanol via Metgas Using Oxidative Bi-reforming, G. A. Olah, G. K. S. Prakash, A. Goeppert, M. Czaun and T. Mathew, *J. Am. Chem. Soc.* **2013**, *135*, 10030-10031.

[13] CO_2 capture and recycling to fuels and materials: towards a sustainable future, A. Goeppert, M. Czaun, G. K. S. Prakash and G. A. Olah, in An Introduction to Green Chemistry Methods, R. Luque and J. C. Colmenares (Eds.), E-Book, Future Science, London, pages 132-146, **2013**.

[14] Formic acid as a hydrogen storage medium: Ruthenium-catalyzed generation of hydrogen from formic acid in emulsions, M. Czaun, A. Goeppert, J. Kothandaraman, R. May, R. Haiges, G. K. S. Prakash and G. A. Olah, *ACS Catal*. **2014**, *4*, 311-320.

[15] Easily Regenerable Solid Adsorbents Based on Polyamines for CO_2 Capture from the Air, A. Goeppert, Z. Zhang, M. Czaun, R. May, G. K. S. Prakash and G. A. Olah, *Chem. Sus. Chem*, in press (DOI: 10.1002/cssc.201301114).

Related patents issued during the period (2009-2013), these concept patents were conceived before the beginning of the program and have priority dates between April 15, 2005 and July 13, 2007.

[1] Electrolysis of carbon dioxide in aqueous media to carbon monoxide and hydrogen for production of methanol, G. A. Olah and G. K. S. Prakash, US Patent, 7,704,369, April 27, 2010 (priority date: July 13, 2007).

[2] Nanostructured solid regenerable absorbents for reversible absorption of carbon dioxide from gases, including air, G. A. Olah, A. Goeppert, S. Meth and G. K. S. Prakash, US Patent 7,795,175, September 14, 2010 (priority date: August 10, 2006).

[3] Conversion of carbon dioxide to methanol and/or dimethyl ether using bi-reforming of methane or natural gas, G. A. Olah and G. K. S. Prakash, U.S. Patent, 7,906,559, March 15, 2011 (priority date: June 21, 2007)

[4] Electrolysis of carbon dioxide in aqueous media to carbon monoxide and hydrogen for production of methanol, G. A. Olah and G. K. S. Prakash, U.S. Patent, 8,138,380, March 20, 2012 (priority date: July 13, 2007)

[5] Conversion of carbon dioxide to dimethyl ether using bi-reforming of methane or natural gas, G. A. Olah and G. K. S. Prakash, U.S. Patent, 8,133,926, March 20, 2012 (priority date: June 21, 2007)

[6] Efficient and selective chemical recycling of carbon dioxide to methanol, dimethyl ether and derived products, G. A. Olah and G. K. S. Prakash, U.S. Patent, 8,212,088, July 3, 2012 (priority date: April 15, 2005)

[7] Conversion of carbon dioxide to methanol using bi-reforming of methane or natural gas, G. A. Olah and G. K. S. Prakash, U.S. Patent, 8,440,729, May 14, 2013 (priority date: June 21, 2007).

Awards and Recognition to the PI (George A. Olah) and Co-PI (G. K. Surya Prakash), during the period

Professor Prakash received the ***CRSI Medal*** from the Chemical Research Society of India (2010).

Professor Olah received Hungary's highest Prize, **Széchenyi-nagydíj Grand Prize** for academic achievement affecting all of Humanity. He also received an **Honorary Doctoral Degree** from the Obuda University in Hungary (2012).

Professor Prakash was honored with **Albert S. Raubenheimer Senior Faculty Award** for exemplary contributions in the areas of teaching, research and service from the Dornsife College of Letters, Arts and Sciences at the University of Southern California (2012).

Professor Prakash received the ***Mellon Mentoring Award*** from the University of Southern California (2013).

Professor Prakash was elected as a ***Fellow of the European Academy of Sciences*** (2013).

Professor Olah received the ***Semmelweis Budapest Award*** from the Semmelweis Medical University, Hungary (2012).

Professor Prakash was elected as a ***Foreign Fellow of the National Academy of Sciences***, India (2013).

Professors Olah and Prakash were jointly recognized by the ***Inaugural $ 1M 2013 Eric and Sheila Samson Prime Minister's Prize for Innovation in Alternative Fuels in Transportation*** from the State of Israel.

Timeline for the Methanol Economy Project – DE-FE0000435

Project Value Milestones

Milestone	Date	Description	Status
M1 – Subtasks 2.1, 3.1 and 3.2	FY10-Q3	Building of Pressurized reactor and testing of dry-reformimg of methane and CO_2 to syngas as a prelude to testing Bireforming.	Completed
M2 – Subtasks 2.1 and 2.2	FY10-Q4	Optimizing Bromination of Methane and Hydrolysis of Methyl Bromide to Methanol/DME with >95% selectivity. Provide most favorable parameters.	Completed
M3 – Subtasks 3.1 and 3.2	FY11-Q2	Identify suitable catalyst compositions for Bireforming of methane (or higher hydrocarbons)/CO_2/H_2O to syngas.	Completed
M4 – Subtasks 3.1, 3.2 and 4.1	FY11-Q4	Demonstrate Bireforming using the pressure reactor under optimized conditions. Identify most suitable CO_2 adsorbents for capture and regeneration.	Completed
M5 – Subtasks 4.2 and Task 5.0	FY12-Q2	Electrochemical reduction of CO_2/H_2O to syngas. Demonstrate a factor of 5-10 improvement in current densities obtained from operation under pressure (up to 100 psi) and with improved cell design.	Completed
M6 – Task 5.0	FY12-Q4	Electrochemical reduction of CO_2 to formic acid under pressure with high Faradic efficiencies (> 95%) and current densities.	Completed (target efficiencies not achieved)
M7 – Task 5.0	FY13-Q2	Build formic acid fuel cells with improved Membrane Electrode Assemblies with efficiencies close to 40% with ambient air at modest temperatures. Select suitable decomposition catalysts for formic acid to CO_2 and H_2.	Completed
M8 – Task 6.0	FY13-Q4	Complete techno-economic analysis based on all achievements and milestones with a wrap up report.	Completed